AUSTENITE GRAIN GROWTH BEHAVIOUR OF HSLA STEEL DURING REHEATING TREATMENT

by

FEI WANG

A thesis submitted to the University of Birmingham for the degree of

DOCTOR OF PHILOSOPHY

School of Metallurgy and Materials

College of Engineering and Physical Sciences

University of Birmingham

December 2016

Abstract

The grain growth behaviour during reheating between 950 ºC and 1300 ºC of as-cast Al-Nb steel (containing 0.019 wt% Nb and 0.057 wt% Al) and rolled Nb-containing steel (containing 0.028 wt% Nb and 0.031 wt% Al) have been investigated. In particular the role of microalloying element segregation during casting and, hence the spatial distribution of microalloying precipitates, on grain boundary pinning during reheating has been considered. The Al-Nb containing steel has been examined in separate initial conditions, including as-cast (segregated structure), homogenised and forged (reduced separation of segregated bands) samples. It was found that microalloy segregation occurred between the dendritic and interdendritic regions, where the secondary dendrite arm spacing (SDAS) was 150 ± 50 μm. Nb showed strong segregation into the interdendritic regions resulting in a higher number density of Nb(C,N) precipitates (2.64×10^4 /mm^2) compared to the dendritic region (0.73×10^4 /mm^2). However, Al did not show strong segregation resulting in relatively well-distributed AlN precipitates in the matrix (1.29×10^4 /mm^2 in the interdendritic region and 1.89×10^4 /mm^2 in the dendritic region). After forging, the separation between the segregated bands was reduced to 65 ± 10 μm from the previous 150 ± 50 μm in the as-cast sample. The increased Nb content in the rolled Nb-containing steel compared to the Al-Nb steel gave a greater extent of segregation in the solute-enriched regions resulting in a larger number density of Nb(C,N) present (5.9×10^4 /mm^2), whilst the separation between in the segregated bands in the as-rolled Nb-containing steel was 35 ± 10 μm.

The composition profile of Mn (due to microsegregation) predicted by DICTRA at the proeutectoid reaction temperature is generally close to the measured experimental results (cumulated profile of Mn from ranking data obtained by SEM-EDS) of the concentration (Mn) at dendritic-centre and interdendritic-centre regions. The precipitation behaviour of Nb(C,N) and AlN was then predicted by Thermo-Calc for the as-cast Al-Nb steel in the interdendritic and dendritic regions (with the segregated Nb and Al levels predicted by DICTRA at the complete solid stage) and for the homogenised Al-Nb steel (with the average composition as input). The measured volume fraction of precipitates agreed well with the predicted values. The particle dissolution temperature was then predicted by Thermo-Calc to determine the reheating temperatures where abnormal grain growth might occur.

During heat treatment, abnormal grain growth was seen on reheating the homogenised Al-Nb steel to 1170 ºC (predicted dissolution temperature of AlN with 0.057 wt% Al). Normal grain growth was observed on reheating to higher temperature at 1200 ºC, agreeing with the literature reports. However, bimodal grain growth occurred on reheating the as-cast (segregated composition) Al-Nb steel to temperatures of 1160 ºC - 1200 ºC, i.e. above the predicted dissolution temperature of the most stable precipitates in the dendritic region (1160 ºC for dendritic AlN with 0.059 wt% Al) but below the predicted dissolution temperature of the most stable precipitates in the interdendritic regions (1230 ºC for interdendritic Nb(C,N) with 0.062 wt% Nb). The bimodal grain structure was characterised by bands of coarse grains and fine grains, with the separation of the bands being similar to the SDAS, whereas abnormal grain growth was characterised by very large grains randomly distributed and surrounded by finer

grains. Bimodal grain size distributions have been reported in the literature for as-cast material due to Nb segregation; in this work the results indicate that the addition of Al, and hence formation of AlN in the dendritic region, can be used to reduce the temperature range over which bimodal grain growth occurs in a similar Nb-only containing steel (presumably < 1160 ºC), as the AlN in the dendritic region had a higher dissolution temperature than the Nb(C,N) in that region. It was found that the severity of bimodal grain growth (defined as the ratio between the coarse and fine grains) depends on the segregation spacing (i.e. SDAS). However, no bimodal grain growth has been observed in a forged Al-Nb steel, where the separation between the segregation bands had been reduced to 65 ± 10 µm, which means the uniform grain structure occurred in the narrower SDAS (forged). No abnormal grain growth was seen in the as-cast or forged Al-Nb steels for any reheating conditions.

Abnormal grain growth occurred on reheating the rolled Nb-containing steel at 1090 ºC, which had a segregation band spacing of 35 ± 10 µm. A larger grain size ratio (largest grain size to mode grain size) of around 7 was seen in the homogenised Al-Nb steel (at 1170 ºC) compared to a ratio of 3 in the rolled Nb-containing steel (at 1090 ºC), this is believed to be due to random particle dissolution in the homogenised steel resulting in local unpinning such that when the abnormally large grains grow, they do so relatively unimpeded, compared to unpinning in the rolled Nb-containing steel in the ‘dendritic solute-depleted’ regions with the reduced thickness and spacing of the segregated regions being insufficient to pin the growing grains (hence abnormal grains can form) but giving some pinning to limit the resulting large grain size.

In summary, the grain growth behaviour (normal-abnormal-normal or normal-bimodal-normal) and temperature ranges can be predicted, based on knowledge of the segregation distance (related to the solidification rate) and segregated composition, from the particles' dissolution temperatures. The results are novel to science that have systematically compared and distinguished the abnormal grain growth (AGG) and bimodal grain growth (BGG) in terms of morphology (AGG: localised phenomenon with large grains having isolated nature; BGG: microstructure consisting of bands of large grains and bands of small grains) and grain size distribution (AGG: a significantly skew size distribution; BGG: double mode grain size distribution). The occurrence of these non-uniform grain growth behaviours has been successfully predicted at the reheating temperatures by Thermo-Calc and DICTRA, and suggestions to avoid them have also been made which most previous research work has not discussed.

Acknowledgements

I would like to express my deep sense of gratitude to my main supervisor Prof. Claire Davis, for her guidance and encouragement through my Ph.D. study. I am so proud that I can have this opportunity to work with Claire, who is always in patience like a friend, to inspire me in many aspects. The memory of her constant support will never fade, and her spirit of exploration will be inherited for my future.

I also would like to thank Dr. Martin Strangwood, for his valuable academic advices and support for the experimental work, and for his time and patience when he corrected my thesis. It is my honour that I can learn from Martin, who is knowledgeable and friendly, always help me to carry out the research work sensibly.

I gratefully acknowledge to the School of Metallurgy and Materials for the departmental scholarship and provision of research equipment, and TATA steel, UK for providing the materials for research.

I sincerely thank to every individual from the school of Metallurgy and Materials, the University of Birmingham, especially for Anne Cabezas, Kay Jones, Paul Stanley, Teresa Morris.

Massive thanks my friend in department of Metallurgy and Materials, to help and support me, especially Dayue Zhang (for assistance with Thermo-Calc), Avril Rogers (for help with furnace), Jasbinder Singh (for help with sample preparation), Mo Ji and Shanshan Si (for help with SEM)

My sincere gratitude to my friends especially Dr. Lei Zhou, Dr Jinlong Du, Dr Kaijie Lin, Mr Qi Chen, Guowei Zhang and all the members of 1B20, for their constant support to help me overcome the hard time.

I sincerely thank my wife Yulin Ju. Without her encouragement and support, it would not be easy to complete my thesis writing.

Finally, I would like to express my enormous gratitude to my parents (Baba and Mama), who have always been the source of strength throughout my life. I sincerely thank for their selfless love and constant support. I am so proud to be their son, to be their ‘longlong’ and I would like to dedicate my thesis to them.

Contents

List of Figures

List of Tables

chapter 1 Introduction

Carbon steels are the most widely applied structural alloys globally due largely to their excellent property mixes and competitive price. In order to meet ever stricter requirements for a greater range of applications, there has been much research work carried out over the years, to design and improve carbon steels with better properties mixes (mostly mechanical). Most studies have focused on changing the composition and microstructure to improve the final mechanical properties which are strongly influenced and mainly determined by grain size, precipitates and secondary phases. High Strength Low Alloyed (HSLA) steels are designed to provide better mechanical property mixes, such as greater strength and higher toughness than conventional carbon steels. Their designed properties are derived from grain refinement and precipitates strengthening from minor additions of V, Ti, and/ or Nb (less than 0.1 wt%), which also give grain pinning during processing by casting, reheating and thermo-mechanically controlled rolled (TMCR) process. HSLA steels have been widely used in industrial sectors, such as construction industry, oil and gas industrial equipment, automotive and other areas where the high strength and toughness are required [1-9].

The general processing route for HSLA steel [10] is shown in Figure 1-1, including three important processes:

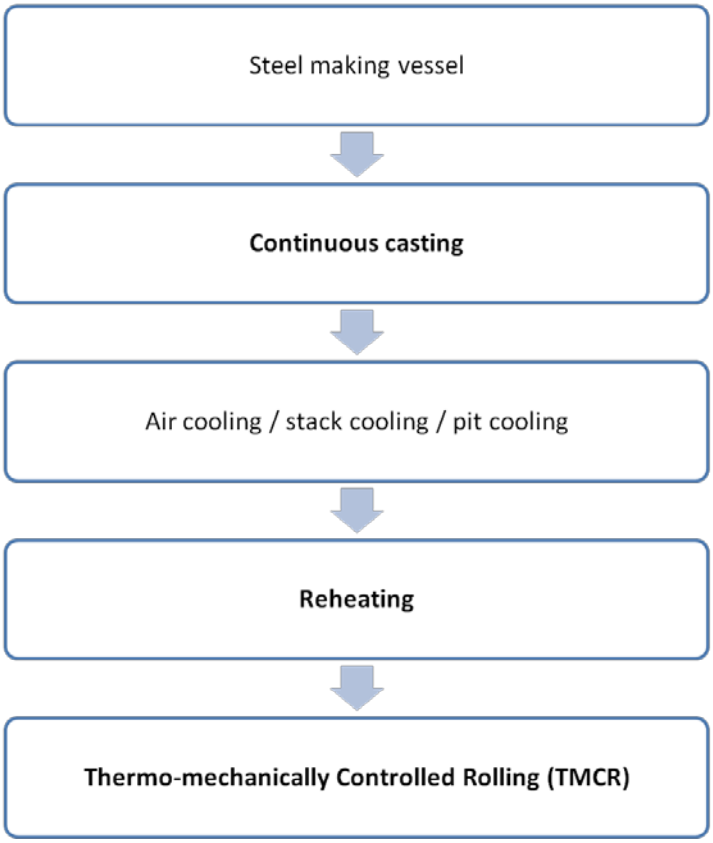

Figure 1-1 Flow graph showing the common route of HSLA steel making in a simple process with continuous casting, reheating and TMCR highlighted [10].

1. Continuous casting is widely applied during steelmaking as it can improve the quality of steel with a higher productivity and lower energy cost than batch ingot casting routes. The common process of continuous casting [11] is shown in Figure 1-2, the molten steel is poured into the water cooled copper mould and a thin shell is formed to support the liquid steel through the primary cooling zone. The strand then passes through the secondary cooling zone with water sprays to give completed solidification, and subsequently goes to radiative cooling process. Generally, three morphological crystal zones are observed in casting of an ingot, including fine grained chilled zone at the surface then followed by a columnar zone and central equiaxed zone [12-15]. Dendrite structures with interdendritic

segregation (as the solubility of alloyed elements in the solid are usually lower than in the liquid) are observed in the columnar zone, which results in a non-uniform precipitates (mainly are carbide, nitride and carbonitride) distribution in the cast steel. (e.g. Nb (C,N) show a large population in the interdendritic region) [16, 17].

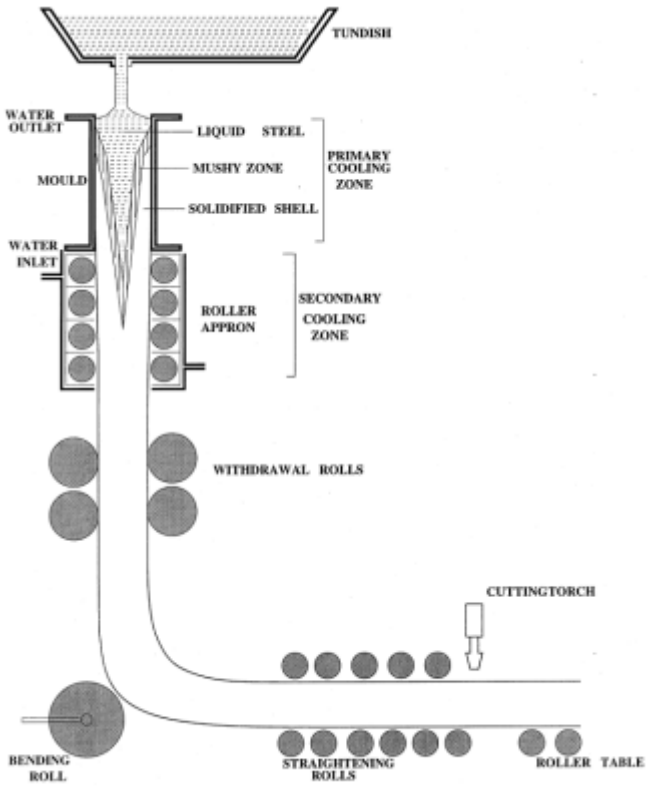

Figure 1-2 Basic process of continuous casting [11].

2. After casting, the slabs are often cooled and stored before being reheated to the chosen re-austenite temperature prior to rolling, in order to make the steel soft enough for the desired reduction in thickness to be achieved during the hot rolling stages. It is very important to control the prior austenite grain structure during the reheating process, as the grain size distribution of the final refined microstructure after deformation depends on the starting austenite grain size [18]. The kinetics of

austenite grain formation and growth are influenced by chemical composition, initial microstructure, heating parameters [19-21] and pinning effect from grain boundary microalloying precipitation. A non-uniform grain growth has been observed mainly due to the particles having an inhomogeneous distribution in HSLA steel. A bimodal grain structure (with the bands of fine and coarse grains) is observed in Nb-containing cast slabs, as the grain growth in the solute-enriched region (with higher segregated Nb contents) is prevented markedly by the particle pinning force which is stronger than that in the solute-depleted region [22-26]. Abnormal grain growth which gives a relatively large grains surrounded by smaller ones, has been studied by many researchers [27-33], identifying the phenomenon as being associated with reheating temperatures at/or close to the particle's dissolution temperature resulting in a different local pinning force, as discussed fully in section 2.4.3.1. It has also been reported that these non-uniform grain structures can affect the recrystallised grains in the final product after the thermo-mechanically controlled rolling (TMCR) process [34].

3. Thermo-mechanically controlled rolling (TMCR) process makes a contribution to the improvement in both the strength and toughness of the HSLA steel by refinement of final grain size. With microalloying element being dissolved in solution, strain induced precipitates are formed during deformation which can effectively restrict the recrystallised grain growth [35]. However, it has been reported that any non-uniform parent austenite structures (e.g. bimodal grain size distribution) can result in a non-uniform final recrystallised grain size, Figure 1-3, and increase scatter in toughness properties [36].

Therefore, selection of an appropriate reheating schedule requires a better understanding of the austenite grain growth behaviour during the reheating process to generate a more uniform structure from hot rolling and/or thermo-mechanically controlled rolling processes. In this study, the development of austenite grain size distributions in HSLA steels (with different initial conditions) has been studied, which is based on the prediction of precipitates thermodynamic stability by Thermo-Calc.

In this thesis, microsegregation during solidification, microalloying precipitation and austenite grain growth behaviour are reviewed in the chapter 2. The methodology and experimental design for the investigated HSLA steels is described in the chapter 3. In the chapter 4, the initial microsegregation and precipitate distributions are characterised, while the composition profile and microalloying precipitate thermal stabilities are simulated in the Al-Nb steels for the as-cast and homogenised conditions. Then the experimental results after reheating treatments are analysed for the homogenised (chapter 5), as-cast (chapter 6), and forged (chapter 7) conditions. Additionally, the modelling predication and experimental results of as-rolled Nb-containing steel are also discussed in the chapter 7. Finally, the conclusions and the future work for designing advanced steel are given in chapter 8 and chapter 9 respectively.

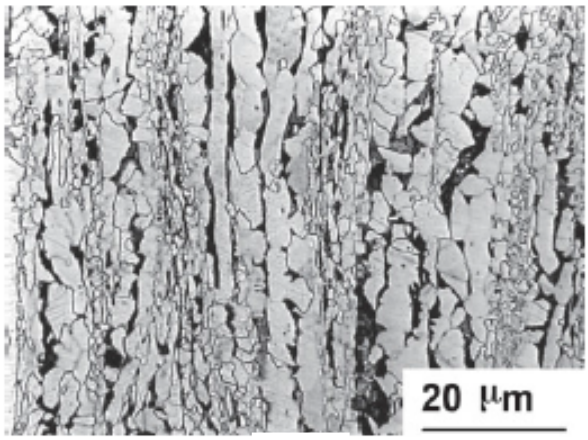

(a)

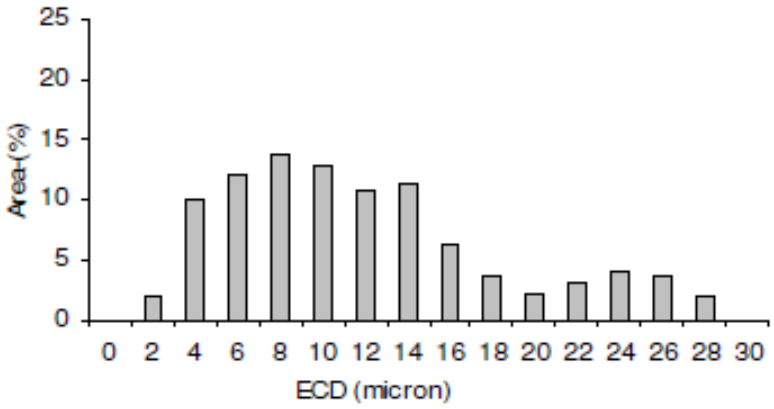

(b)

Figure 1-3 (a) Microstructure of ferrite and pearlite; and (b) bimodal grain size distribution of a TMCR plate in 0.1 C-0.045 Nb [36]. ECD: equivalent circle diameter.

chapter 2 Literature review

As mentioned in chapter 1, the development of grain structure and precipitates during casting and reheating is significant to the subsequent TMCR process. The distribution of microalloying particles is strongly linked to the segregation behaviour during solidification which may result in an inhomogeneous pinning effect on grain growth after reheating. In order to obtain the desired uniform microstructure prior to subsequent rolling, this study is carried out which includes segregation and precipitation in a solidification structure during the casting process, and prior austenite grain growth behaviour during the reheating. The chemical compositions of investigated microallyed steels from the literature report are summarised in Table 2-1.

Table 2-1 Chemical compositions of steels reported from literature (wt %).

	Pipeline [16, 37]	Structural [16, 37]	Ship build [16, 37]	Slab-1 [16, 24, 25, 37]	Slab-2 [24, 25, 38]	Slab-3 [24, 25]	Slab-A [39, 40]	Slab-B [39, 40]	Al-steel [30]	Nb-V steel [40]
C	0.03	0.06	0.14	0.1	0.1	0.09	0.09	0.07	0.2	0.09
Si	0.25	0.3	0.38	0.31	0.28	0.38	0.33	0.18	0.2	0.28
Mn	1.7	1.52	1.35	1.42	1.41	1.52	1.42	1.2	0.8	1.22
P	0.008	0.01	0.015	0.017	0.013	0.011	0.01	0.012	0.015	0.01
S	0.005	0.003	0.007	0.005	0.001	0.002	0.003	0.005	-	0.01
Cr	-	0.021	0.027	-	-	-	-	-	-	-
Mo	-	-	0.001	-	-	-	-	-	-	-
Ni	-	-	0.01	0.32	0.3	0.51	-	-	-	-
Al	0.052	0.036	0.039	0.046	0.029	0.036	0.035	0.034	0.04	0.03
N	-	-	-	0.008	0.008	0.007	0.007	0.007	0.006	0.008
Nb	0.063	0.052	0.002	0.045	0.027	0.02	0.05	-	-	0.05
Ti	-	-	0.004	0.002	0.001	0.009	0.019	0.041	-	-
V	0.082	-	0.003	0.052	0.05	-	0.05	-	-	0.06

2.1 Dendrite structure

2.1.1 Dendrite structure development during solidification

The crystals in the chill zone which grow fastest are those with preferred crystallographic orientation (e.g. <100> for the cubic metals) linked to the direction of heat flow, such as perpendicular to the mould walls and parallel to the maximum temperature gradient [12]. Due to heat being able to be removed more effectively at the tip of the protrusion (the increasing effectiveness of heat conduction as the radius of curvature decreases) than from the surrounding regions in the supercooled liquid, growth of elongated grain shape (dendritic structure) is favoured in the columnar region [12, 13]. The dendritic solid structures with branched or tree-shaped crystals form into columnar zone grains, as shown in Figure 2-1 below.

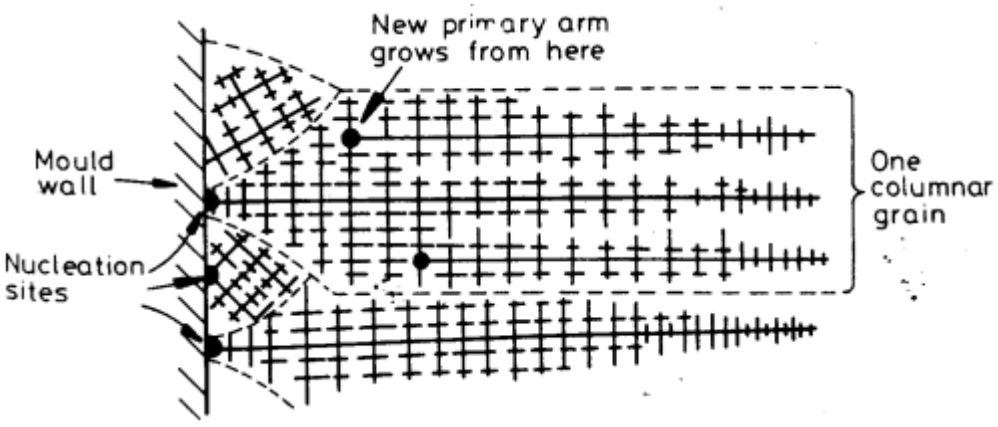

Figure 2-1 Dendritic structure develops in columnar grains which contains many primary dendrite arms [13].

In Figure 2-2 below, several length values have been used to characterise the dendritic structure, such as the distance of the primary dendritic structure, λ_1; and the secondary

arm spacing (SDAS) of λ_2 which is more significant to the microsegregation as will be fully discussed in section 2.2 [41].

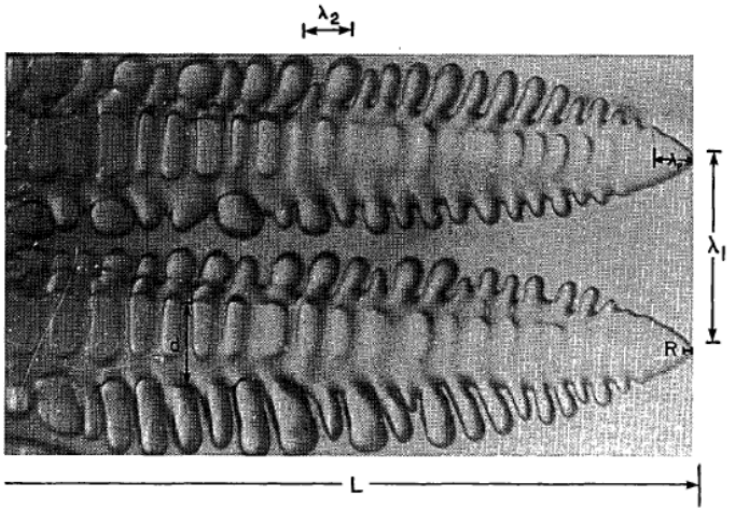

Figure 2-2 Dendritic structure with important length scales: λ_1-Distance of primary dendrite arm space; λ_2-Secondary arm space distance [41].

The development of dendritic structures is mainly due to the nucleation rate of dendrite correlating to constitutional supercooling and the coarsening of dendritic solid within the freezing time. It has also been found that an increased cooling rate resulted in a decrease of the dendritic arm spacing (which is consistent with the observation of lower dendrite arm spacing towards the cold mould wall) , due to there being less time for dendrite coarsening and requiring smaller cell or arm spaces to avoid constitutional supercooling.

2.1.2 Phase transformation during solidification

Solidification process in steels starts as δ ferrite or austenite (γ-Fe), depending on the alloying element contents (e.g. carbon contents) and the cooling rate. Figure 2-3 below shows a Fe-C phase diagram in an equilibrium condition, where a peritectic reaction

can be observed for a low carbon content, theoretically in the range of 0.09 wt% to 0.17 wt%, as indicated in the range of 'b', and the low carbon (< 0.09 wt%) steel would be expected to solidify as the δ phase, as indicated in the area of 'a'.

In general, HSLA steels which contain low carbon at around 0.1 wt% may be expected to have a peritectic reaction during solidification. The solidification route may be changed if a non-equilibrium state has been given. It has been reported that peritectic reaction could occur in a lower carbon steel (0.06 wt%) if segregated compositions were achieved during solidification [37].

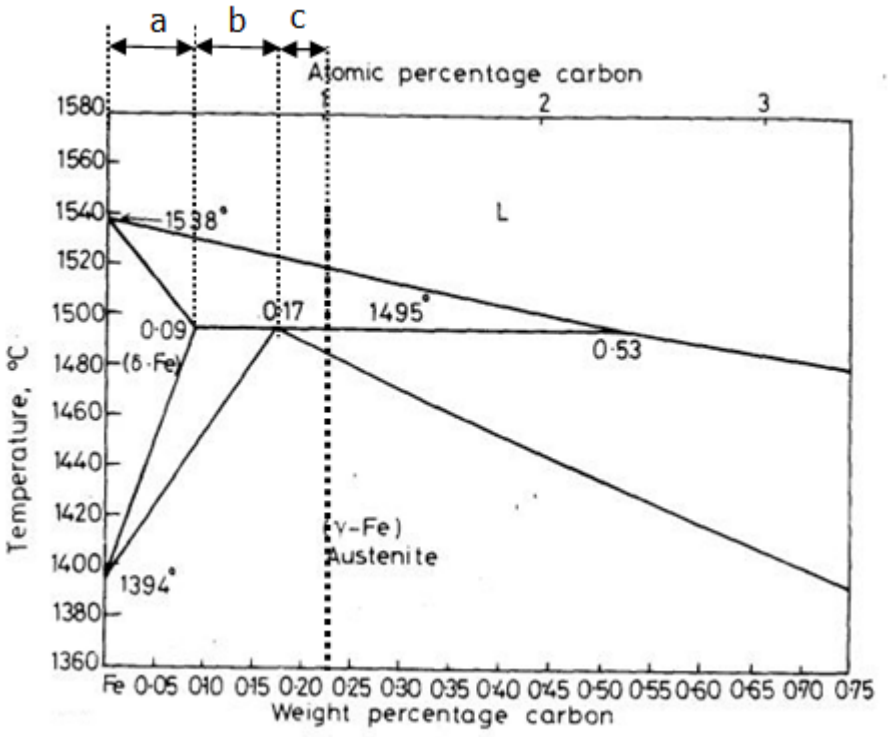

Figure 2-3 Part of an Fe-C phase diagram in an equilibrium condition [13].

During dendrite solidification through the peritectic reaction, the γ-austenite forms at the interface of the pre-formed δ-dendrite solid and liquid phase, therefore coating at the dendritic structure, then growing into both the δ-ferrite and liquid phase during cooling, as shown in Figure 2-4 below [42]. The thickening rate of the γ-austenite can be influenced by the diffusion of carbon through the layer [43, 44]. The peritectic reaction temperature has been reported as being a few degrees below the peritectic temperature, due to the addition of substitutional dissolved alloying elements to the Fe-C system [45]. The peritectic reaction temperature decreases with the addition of the alloy elements of S, P, Ti, Si, Mo, and W, whilst it can be increased if the alloy elements of Mn, Co, Ni and Cu are added [46]. It has been shown experimentally that the peritectic temperature can be expected to decrease with an increased cooling rate [47].

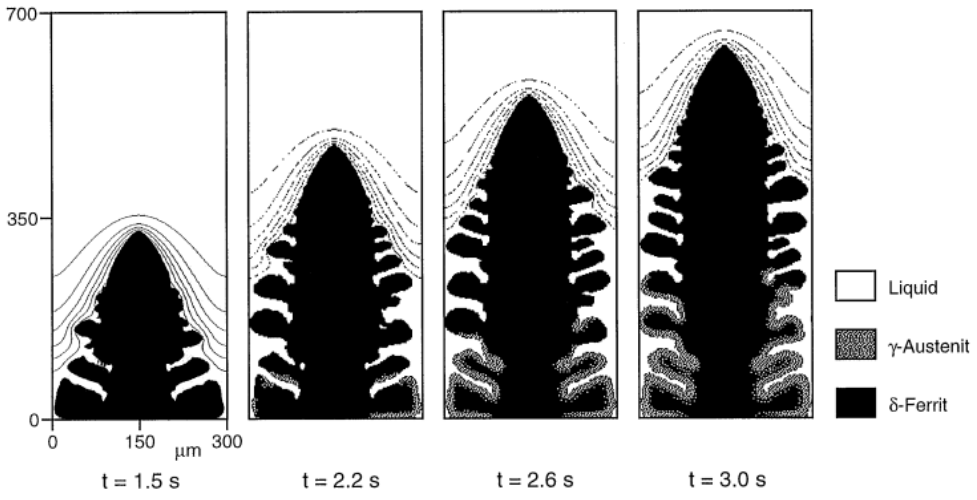

Figure 2-4 Simulation of austenite development in the interface of liquid and ferrite during peritectic solidification [42].

2.1.3 Dendrite structure in HSLA steel

With further cooling under A_3, the ferrite phase is formed from prior austenite grains [48, 49], whilst pearlite (the lamellar structure of ferrite and cementite) is also formed when the carbon steel is subjected to slow cooling under A_1 [50-52]. It has been reported that the transformation of pearlite occurred at the regions which inherited a higher content of Mn in solution (such as solute-enriched regions) [30]. The grey dendritic ferrite and dark interdendritic pearlite can be observed in HSLA steel (Figure 2-5), corresponding to the original dendritic structures during solidification, as will be discussed fully in section 2.2.2.

The mean value of the secondary dendrite arm spacing (SDAS) in the microstructures of ferrite and pearlite can be measured by the centre to centre distance of the interdendritic (pearlite) regions, as seen in Figure 2-5 (a) [38]. The measured SDAS values of HSLA steels (reported in the open literature for the chemical compositions shown in Table 2-1) with various carbon contents can be seen in Table 2-2, which demonstrates that the reduced SDAS has been observed in the steels containing more carbon contents (e.g. a narrower SDAS (90 ± 15μm) has been seen in ship building steel (C: 0.14 wt%, as seen in Table 2-1) [37] than that in a Slab-B steel (SDAS: 170 μm; C: 0.07 wt%, as seen in Table 2-1) [39]).

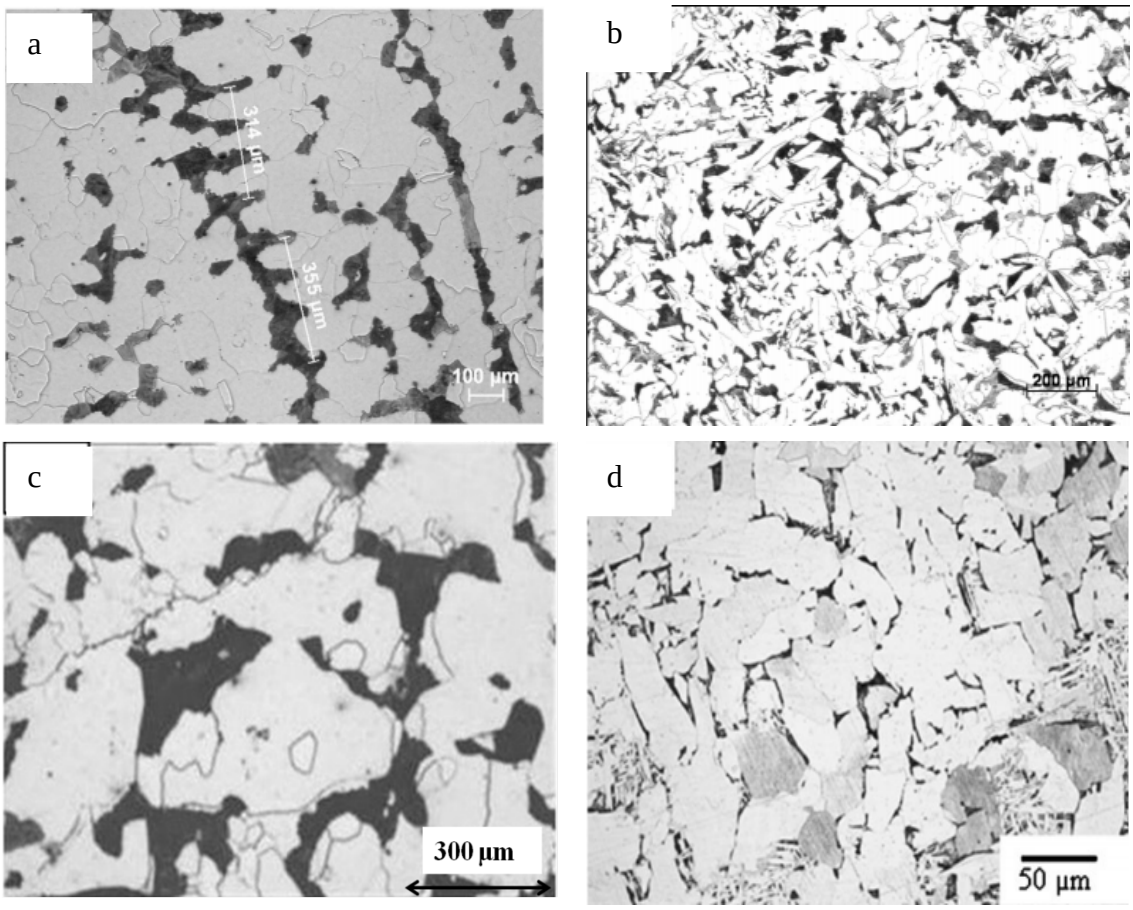

Figure 2-5 Dendrite structures consisting of grey dendritic ferrite and dark interdendritic pearlite at 1/4 position of width and depth in the HSLA steel: (a) cast Slab-2 steel [38]; (b) ship building steel [37]; (c) cast Slab-1 steel [24]; (d) cast Slab-B steel [39].

Table 2-2 Secondary dendrite arm spacing is shown with various carbon contents at the quarter position of width and depth in HSLA steels.

	Carbon content/ wt%	SDAS/ µm
Slab-2 [38]	0.1	117±15
Ship building[37]	0.14	90±15
Slab-1 [24]	0.1	211±36
Slab-A[39]	0.09	160
Slab-B[39]	0.07	170

The solidification rate can be expected to influence the SDAS, as seen in Figure 2-6, where the SDAS is reduced with an increased cooling rate in the low carbon steel [53]. Therefore, in a cast steel, the SDAS can be expected to increase from the chill surface to the quarter and centre positions (Figure 2-7 [39, 54]), with the decreased cooling rate [14, 53-58]. Using the data from Figure 2-6 and Figure 2-7 below, the cooling rate (of around 500 ºC/ min) in subsurface regions (at 10 mm from the surface with SDAS of approximately 50 µm) is nearly ten times quicker than that at the 1/4 thickness position (of around 50 ºC/ min with SDAS of approximately 150 µm). The clear typical dendrite structure can be seen in the quarter position (see Figure 2-5), therefore, many investigations of precipitation and grain growth behaviour correlated microsegregation were carried out at this region [18, 24, 37, 38].

Consequently, an empirical equation has been proposed by Won [59]; equation 2-1, which can be used to predict the SDAS for a low carbon steel, and takes into account the cooling rate and carbon content, as discussed above.

$$\lambda_{SDAS} = \left(169.1 - 720.9\ (\%C)\right) \times C_R^{-0.4935} \qquad \text{for } 0 < (\%C) \leq 0.15$$

$$= 143.9 \times C_{\mathrm{R}}^{-0.3616} \times (\%C)^{(0.5501 - 1.996(\%\mathrm{C}))} \quad \text{for } 0.15 < (\%C) \qquad \text{2-1}$$

Where C_R is the cooling rate (ºC/s) and (%C) is the carbon content in wt%. This empirical equation is also frequently used to roughly calculate the cooling rate with a given carbon content and the measured value of SDAS. With the same carbon content (0.1 wt%, see Table 2-1) given in Slab-2 [38] and Slab-1 steel [24] (see Table 2-2), a larger SDAS has been observed in the Slab-1 steel (211±36 µm) than that in the Slab-2 steel (SDAS: 117±15 µm). This has been ascribed to the cooling rate (0.2 ºC/s)

calculated in the Slab-1 steel being lower than that in the Slab-2 steel (0.68 ºC/s). Generally, a narrower SDAS can be expected in the HSLA steel which has larger carbon content and/ or a greater cooling rate.

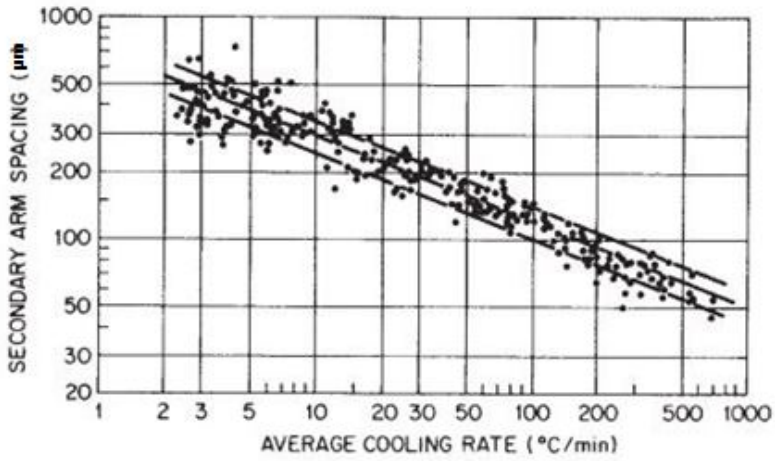

Figure 2-6 Secondary dendrite arm spacing against the cooling rate for the steels with C: 0.1-0.9 wt% [53].

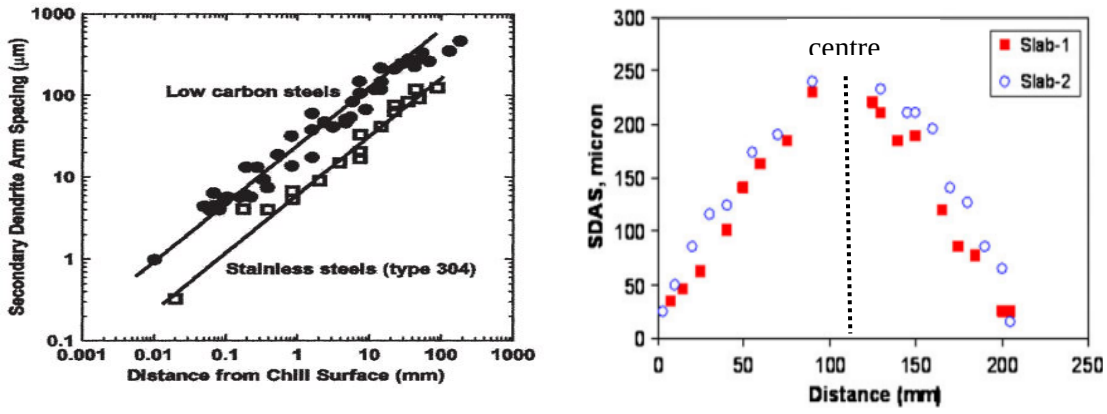

(a) (b)

Figure 2-7 SDAS against the distance from the surface to the centre position of the as-cast slab: (a) low carbon steels and 304 stainless steels [54]; (b) Slab-A and Slab-B steels [39].

2.2 Segregation during solidification

Solute segregation occurs mainly during solidification, which results in a non-uniform composition distribution in the slab. There are two types of segregation that can be observed: macrosegregation resulting in composition variation over distances relative to the size of the specimen, and microsegregation giving a composition change on the scale of the secondary dendrite arm spacing. There are several types of macrosegregation indicated in Figure 2-8, which is mainly due to the fluid flow in and the slow cooling of a large ingot of steel [60]. Macrosegregation is not significant for a small ingot of steel (thick< 300 mm) which has a faster cooling rate and less fluid flow [18, 24, 37-40]. Therefore, microsegregation (e.g. dendritic segregation) can be investigated during solidification which strongly affects abnormal (bimodal) grain growth, as will be fully discussed in section 2.4.

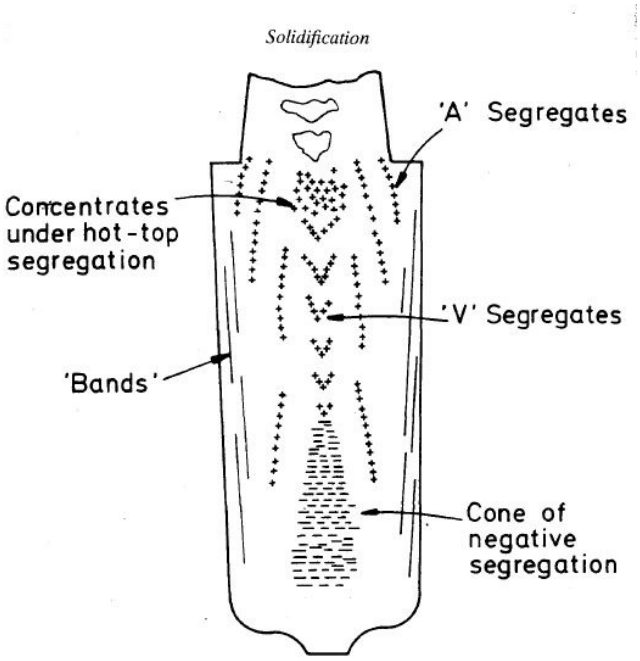

Figure 2-8 Different types of macrosegregation observed in large ingots. Positive segregation is denoted "+"; and negative segregation is represented by "-" [61].

2.2.1 Theory of segregation

Solute can be partitioned between two adjacent phases during the phase transformation. Within a solid-liquid two-phase field, solute atoms are re-distributed during solidification following the equilibrium partitioning of chemical elements. At a given temperature, C_S is described as the equilibrium composition of solute in the solid phase, and the solute concentration of liquid can be referred to C_L. The equilibrium partition coefficient k, as shown in equation 2-2, describes the partitioning behaviour of each element between the solid and liquid phases [12, 14].

$$k=C_S/C_L \qquad 2\text{-}2$$

During segregation in the solidification process, if k <1, then the solute prefers to enrich in the liquid, otherwise, the solute partitions to the solid phase. Furthermore, the degree of element segregation into liquid is higher in steel when a lower partition of the coefficients (k<1) is given. k can also be characterised as k_δ and k_γ if there is a direct solidification as a δ or γ solid phase. Partition coefficient values can be determined from the concentrations of elements at the interface of two different phases (e.g. in a phase diagram). In a multicomponent system, phase diagrams can be obtained through Thermo-Calc calculation (as will be fully discussed in section 2.2.4). Table 2-3 shows the summarised equilibrium partition coefficients of k_δ [38, 58, 62-67] and k_γ [64, 66-68]. In general, it can be assumed that these values are independent of temperature and are determined from the binary phase and/ or multi-phase diagram (e.g. from Thermo-Calc calculation).

Most alloying elements prefer to enrich the interdendritic liquid region, especially Nb which has a stronger segregation tendency than any other microalloying element to enrich in the liquid phase. Some substitutional elements, such as V, have low tendency to enrich the liquid region (as k is close to 1), which shows a nonsignificant segregation behaviour during solidification compared to Nb. Al demonstrates a different partition behaviour (k >1) compared to other substitutional elements, which indicates that a slight enrichment can be expected in the solid phase. Different partition behaviours have been seen in δ-ferrite and γ-austenite, as shown in Table 2-3, which indicates that some elements have a lower partition ratio in austenite than in δ-ferrite, such as V, Al, Ti and Nb. This means that these elements have more severe segregation in the interface of liquid-austenite than that of liquid-δ-ferrite; whilst other elements, such as Mn and Ni, have a greater partition coefficient in austenite than in δ-ferrite, indicating that more solutes can be expected in austenite than in the δ-ferrite during solidification process.

Table 2-3 Equilibrium partition coefficients of solute elements in δ-ferrite [38, 58, 62-67] and in γ-austenite [64, 66-68].

Elements	Kδ [38, 58, 62-67]	Kγ [64, 66-68]
C	0.13-0.20	0.30-0.36
Si	0.63-0.83	0.50-0.52
Mn	0.68-0.90	0.75-0.95
P	0.13-0.29	0.06-0.13
S	0.02-0.05	0.02-0.05
N	0.25-0.28	0.48-0.54
Al	0.92-1.26	0.60
Nb	0.19-0.4	0.22
V	0.90-0.93	0.63
Ti	0.25-0.61	0.30-0.33
Ni	0.79-0.83	0.95
Cr	0.33-0.95	0.85-0.86

It is known that the elements have a fast diffusion rate in the liquid phase. Therefore, a uniform composition can be expected after the atoms have been rejected from the solid phase. However, a low diffusion rate exists in the solid phase which may result in a composition profile that occurs from the solute-depleted region (early formed solid) to the solute-enriched region (solid develops from the last remaining liquid phase) after the solidification is completed. The diffusion of elements driven by the composition gradient in the solid phase continues to minimise the segregation level towards a relative homogenised composition (close to the bulk composition). The diffusion constant (D_0) and activation energies (Q) are the determined parameters to describe the diffusion behaviour for microalloying elements; D (in cm^2/s) is calculated from

equation 2-3, with temperature of T (in Kelvin) and universal gas constant of R, 8.314 $Jmol^{-1}K^{-1}$.

$$D=(D_0)\exp(-Q/RT) \quad 2\text{-}3$$

$$X=(D \cdot t)^{1/2} \quad 2\text{-}4$$

The diffusion distance, X depends on the diffusion coefficient, D, and diffusion time (t) in equation 2-4 [18, 69], which means that the homogenised distribution can be expected at a high temperature (faster diffusion rate) with a long reheating time. For example an homogenisation treatment was carried out at 1225 ºC for 4 days for Nb atoms to diffuse 100 µm, hence removing microsegregation to be a homogenised condition in a Slab-1 steel [18]. Table 2-4 shows the various parameters of (D_0) and Q based on previous research work on the austenite and ferrite phase [18, 24, 59, 66, 68-71], indicating that the diffusion rates of C and N are much higher than other alloying elements in the austenite. Therefore, the uniform distributions of C and N are expected to be close to the bulk composition. Using the parameters in Table 2-4, a lower diffusion rate is observed (according to equation 2-3) in austenite for most elements (except C and N) than that in the ferrite, which means that the segregated elements may have a slow diffusion behaviour at the austenite temperature. Therefore, a final microsegregation may be expected at room temperature during the re-distribution of the elements in the transformation of austenite to ferrite below A_{c3} temperature.

Table 2-4 The diffusion constant *(D_0)* and activation energies *(Q)* for the alloying elements in the ferrite and austenite phases [18, 24, 59, 66, 68-71]. The maximum value of *D* in ferrite (at 800 ºC) and in austenite (at 1200 ºC)

Element	(D_0) (cm^2/s) in ferrite	Q (kJ/ mol) in ferrite	D cm^2/s at 800 ºC	(D_0) (cm^2/s) in austenite	Q (kJ/ mol) in austenite	D cm^2/s at 1200 ºC
C	0.0127-0.062	80.4-81.3	6.83E-06	0.1-0.15	134.6-143.5	2.53E-06
Si	8.0	248.9	6.11E-12	0.3	251.5	3.61E-10
Mn	0.76	224.4	9.04E-12	0.055	249.4	7.87E-11
P	2.9	230.1	1.82E-11	0.01	182.8	3.29E-09
S	4.56	214.6	1.63E-10	2.4	223.4	2.87E-08
N	0.008-0.5	77-79.1	8.92E-05	0.91	168.5	9.62E-07
Al	5.9-30	234.5-241.4	1.15E-10	5.9	241.4	1.62E-08
Nb	1.3-50	240-251.9	1.04E-10	0.83-5.3	266.5-344.6	2.94E-10
V	0.61-4.8	240.0-267.1	9.94E-12	0.25-0.284	259.0-264.2	1.85E-10
Ti	3.15	247.7-248	2.66E-12	0.15	251.0-251.2	1.88E-10
Ni	1.6	240.0	3.31E-12	0.34	282.4	3.28E-11
Cr	2.4	240.0	4.97E-12	0.0012	219.0	2.06E-11

2.2.2 Dendritic segregation

During dendrite solidification, microsegregation occurs due to the most of the alloying elements having the partition ratio k <1. Therefore, more solute is expected to be rejected from the dendrite solid to the interdendritic liquid, as shown in Figure 2-9; the dark shade around the solidifying dendrites represents the solute rejected to the liquid [72]. Pottore reported that steel with the carbon content 0.08-0.012 wt% confirmed to this dendritic segregation scheme. Figure 2-10 shows that two-phase mushy structures consist of the last liquid during solidification corresponding to the solute-enriched region which can be etched out preferentially [73]. At temperatures below A_{c3}, α-ferrite can be formed in the previous solute-depleted (dendritic solid) region, whilst the

pearlite originates from the solute-enriched (interdendritic liquid) region due to the high content of Mn appearing (as was explained in section 2.1.3) [30]. Generally, the composition profile can be obtained by following the distance of secondary dendrite arm spacing which includes to the regions of dendritic ferrite and interdendritic pearlite [58], as discussed in section 2.1.3. A greater space of solute-depleted region can be expected if a larger SDAS is obtained during solidification.

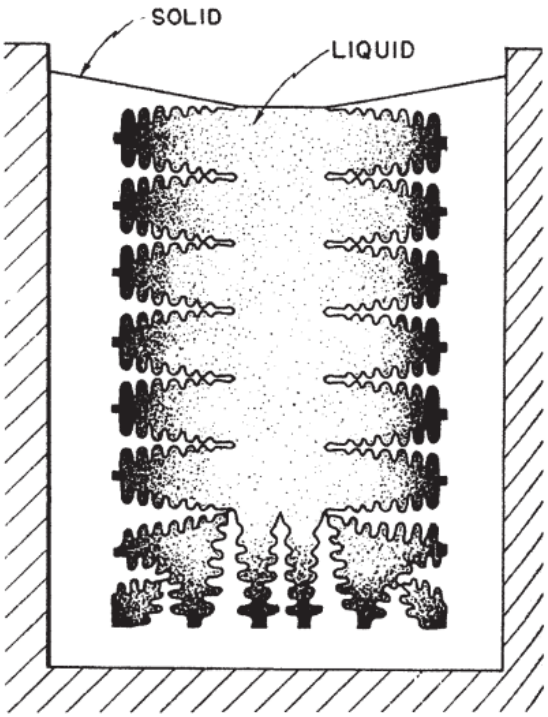

Figure 2-9 Schematic of the dendritic solidification with the solute rejected from solid to liquid. [72].

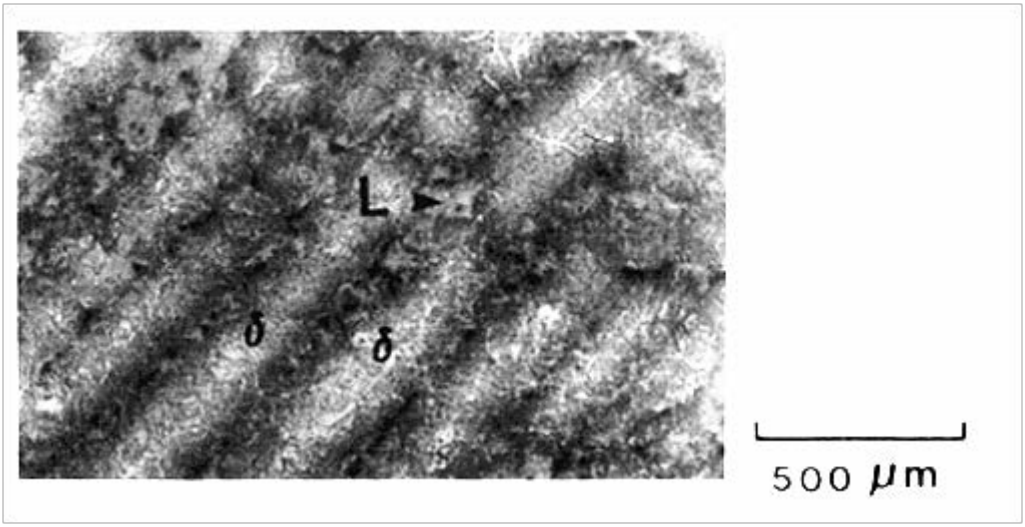

Figure 2-10 Micrograph consist of two-phase mushy structure existing prior to the quench. The deeply etched microstructure represents the liquid phase (L) and the coarse grey dendrites represent the solid phase (δ ferrite) at the condition: steel with 0.12 wt% carbon had been melted at 1600ºC, control-cooled at 12 ºC/ min, isothermally held at 1500 ºC for 15 minutes, then subjected to water quench (quench rate was approximately 600 ºC/s) to room temperature [73].

Microsegregation can be analysed through element distribution which can be characterised by equipment such as scanning electron microscope-energy dispersive spectroscopy (SEM-EDS). The precision of EDS detection is approximately ± 5% [37], and a calibration is required for the experimental data obtained from EDS analysis. Generally, the microsegregation is characterised in a 2D section with a quantitative data being obtained from a large investigated region, which can be used to describe a spatial element distribution in the 3D material [37].

Line-scan analysis is used to characterise the composition changes along a selected line, for example through areas containing solute-enriched (interdendritic pearlite) and solute-depleted (dendritic ferrite) regions. A general segregation trend can be observed to analyse any non-uniform distributed elements within the selected line. Figure 2-11

shows that the typical measurements of C and Mn cross the SDAS to characterise the segregation, which indicates that a greater value of Mn is observed in the solute-enriched region compared to that in the solute-depleted region. Carbon shows a relatively uniform composition, which means that a uniform distribution of C can be expected during the cooling process as fast diffusion of carbon occurs in the solid phase [74] (discussed in section 2.2.1). Measurements for the elements in HSLA steel were carried out by Zhang [37], as shown in Figure 2-12. It indicates that Mn shows an obvious segregation behaviour (two content peaks have been seen in Figure 2-12 (b)) across the dendritic ferrite and interdendritic pearlite regions, compared to other elements such as Ni and Si in a slab measured at room temperature. However, the line-scan method cannot establish an accurately measured composition profile for a 3D dendrite structure, as segregated contents in the regions of dendritic centre and interdendritic centre may be missed in the line-scan analysis, which may not be on a plane that passes through these.

The cumulative profile is a method that ranks the measured contents for an element from grid-mapping detection (area scan technique) to build the composition profile describing segregation behaviour [75]. Grid-mapping was used by Zhang in a continuously cast steel Slab-1[37], by carrying out EDS analyses on a grid of 200-400 points with a spacing greater than the SDAS, to provide the elemental concentrations across the regions of pearlite (interdendritic solute-enriched region) and ferrite (dendritic solute-poor region). Then the cumulative profiles were obtained by ranking the composition data from the grid points in ascending order ($k < 1$ of Nb) or descending ($k > 1$ of Al) against the segregated distance from centre to centre regions

of dendrite and interdendrite (such as the half value of SDAS). The cumulative profile can provide more accurate segregation data than that from the line-scan method, as the subjective selection of a line (through the solute-enriched and solute-depleted regions) can be avoided when describing a composition profile from the 3D structure [76].

Banding structure can be observed in a rolled or forged steel, as shown in Figure 2-14, containing alternating ferrite (the bright region) and pearlite (the dark region) phases which are parallel to the rolling direction [77]. Solute segregation can be expected across a band structure which corresponds to the ferrite and pearlite phases, as seen in Figure 2-15, and it shows that a large content of Mn is present in the pearlitic regions whilst the concentration of Mn in the ferrite regions is low for an Al-rolled steel (Table 2-1) [30, 78]. However, after this Al-rolled steel was homogenised at 1300 ºC for three hours, a nearly uniform distribution of Mn was observed in the structure with randomly distributed ferrite and pearlite, Figure 2-16. This is due to full diffusion of Mn occurring when holding at a high temperature with a sufficient time, as discussed in section 2.2.1.

Segregation ratio for the elements is commonly used to describe a microsegregation level in the steel, which can be defined as C_{max}/C_{min}, where C_{max} is the maximum element concentration; and C_{min} is the minimum element concentration. This has been widely used to characterise the segregation level in HSLA steel, to give a ratio describing the experimental results and the predicted values [18, 24, 37].

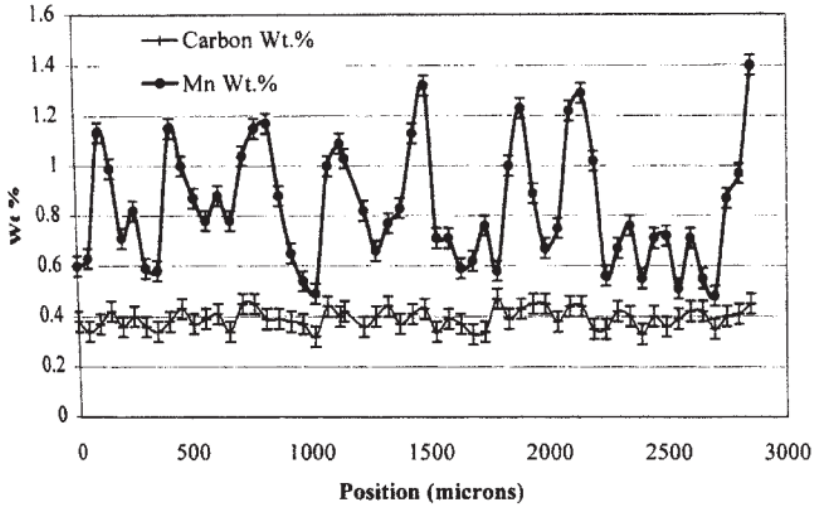

Figure 2-11 Variations in the concentration of C and Mn (measured by EDS) cross the SDAS (200-300 µm) in the quenched and tempered 4140 low alloy steel bar [74].

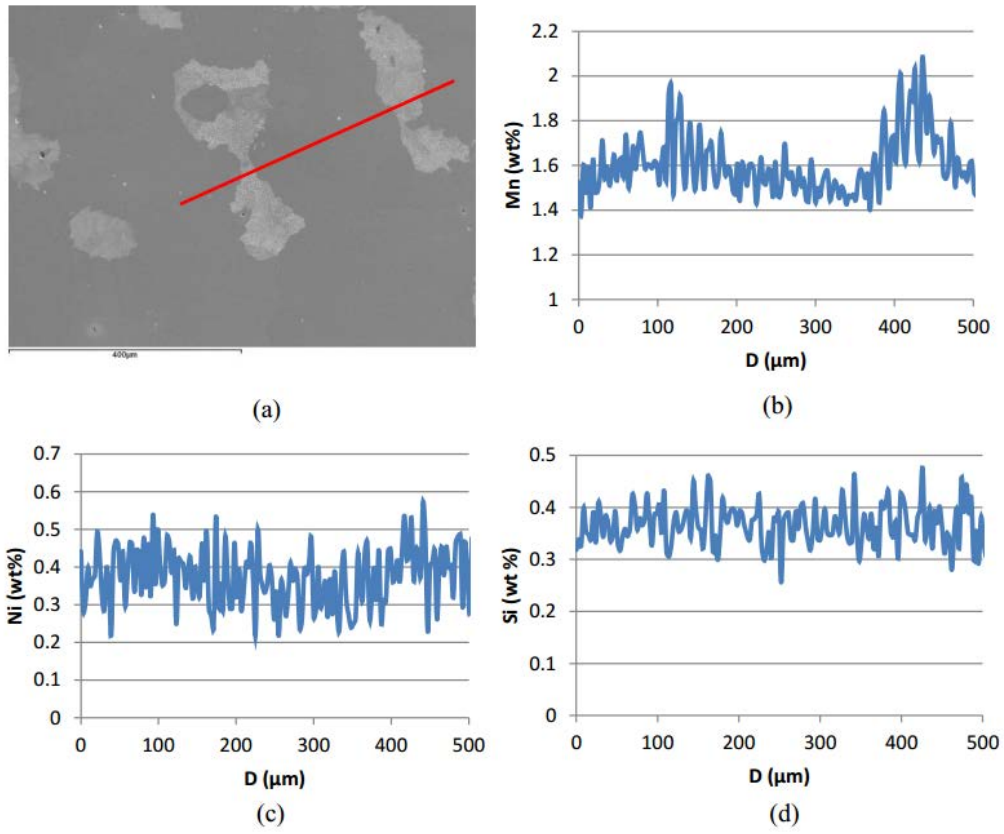

Figure 2-12 Line-scan for Slab-1 steel at 1/4 position crosses dendrite structure: (a) SEM image show the dendrite arm structure with a line-scan trace and the content distribution of (b) Mn, (c) Ni, and (d) Si along the red line [37].

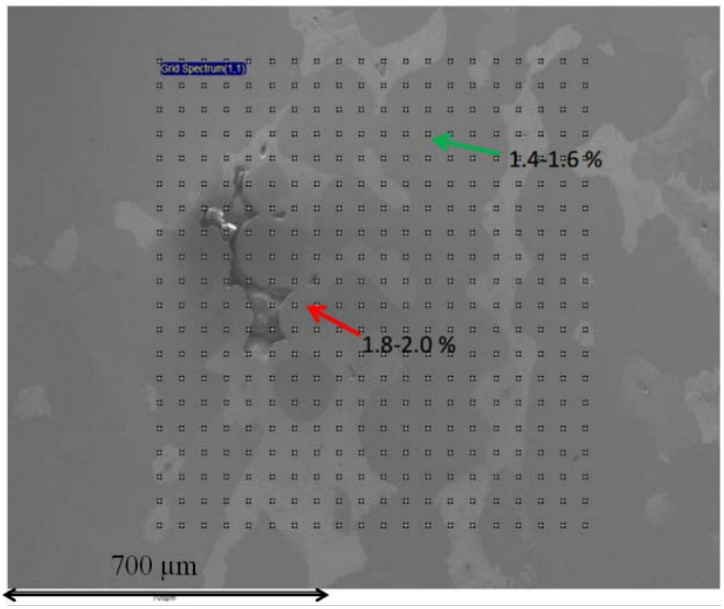

Figure 2-13 SEM image of as-cast Slab-1 steel indicates the grid-mapping covering the dendritic ferrite and interdendritic pearlite regions [37].

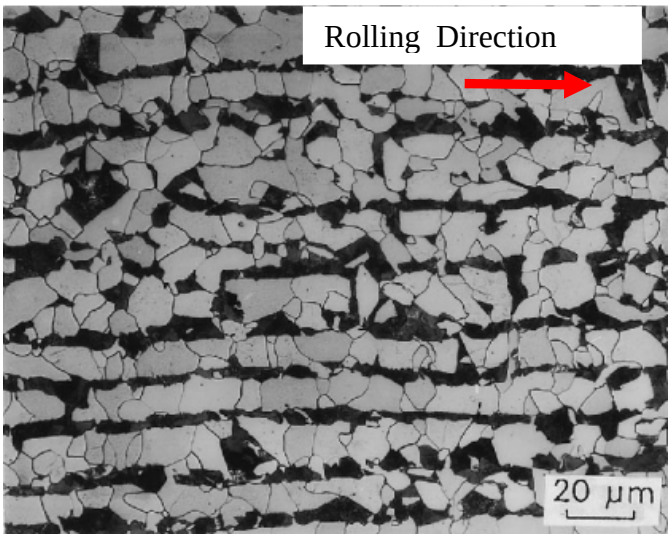

Figure 2-14 Banded structures consist of ferrite (light grey) and pearlite (dark black) phases in the 1020 hot-rolled steel [77].

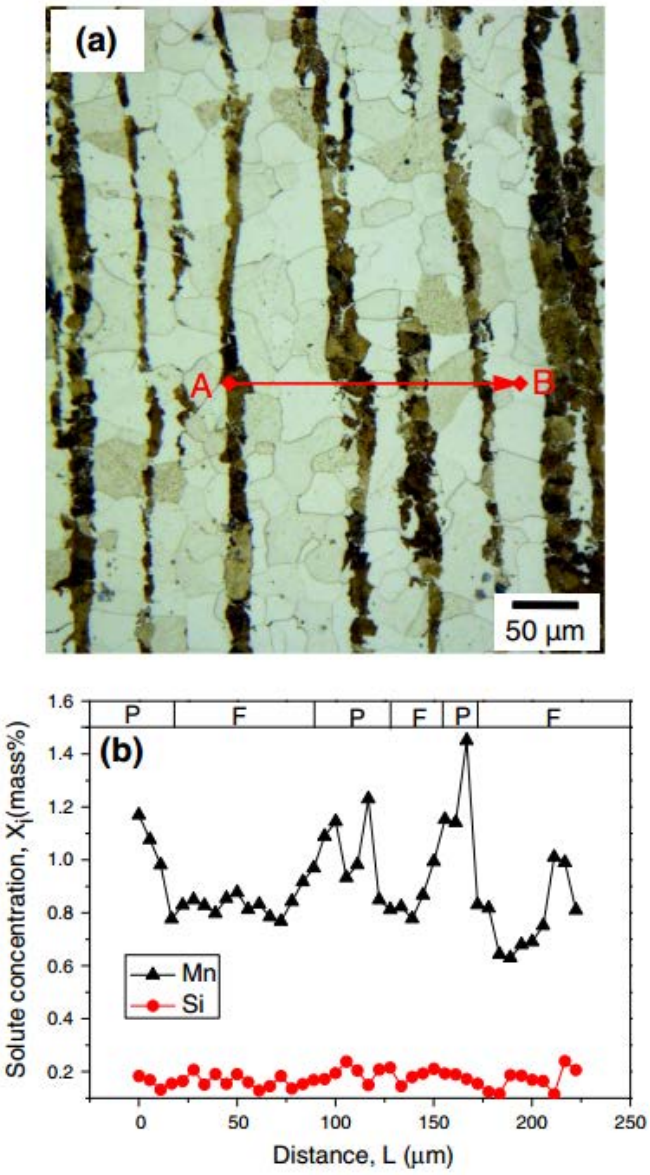

Figure 2-15 The segregations of alloying elements related to the banded structure: (a) alternating ferrite and pearlite phases present in a banded sample for the Al-containing steel after hot rolling; (b) the content distribution of Mn and Si along the selected line AB in a range between pearlite and ferrite [30, 78].

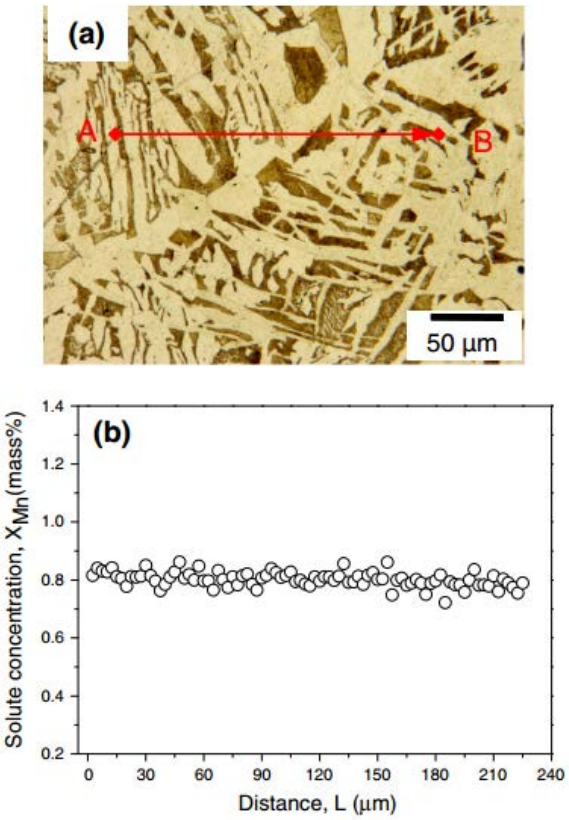

Figure 2-16 Correlation between (a) ferrite-pearlite structures in an Al-containing steel (Al: 0.04 wt%, Table 2-1) after homogenisation treatment at 1300 ºC for three hours followed by air cooling to room temperature and (b) the distribution of Mn content along the selected line of AB [30, 78].

2.2.3 Prediction of dendrite segregation

Generally, the principle of most microsegregation models is the relationship between solute concentration and solid fraction, producing a composition profile across two adjacent phases, which takes into account the solute partition and elements diffusion during cooling and transformation. Modelling approaches for microsegregation, involving numerical calculation [37, 59, 79-90] and thermodynamic software (Thermo-Calc and DICTRA) [16, 18, 24, 25, 37, 38, 79, 91-95], have been developed to predict the composition profiles during cooling process.

Table 2-5 shows the suggested equations to predict the composition profile for various liquid and solid diffusion rate assumptions. The lever-rule model has simulated the composition changes, which assumes complete diffusion in the solid and liquid phases. However, the diffusion of elements in the solid phase is slow (as seen in Table 2-4), especially for the substitional solute element such as Nb. Therefore, a complete diffusion assumed in the lever-rule mode is unrealistic in practice.

Figure 2-17 shows the Scheil model [13], which assumes that there is no diffusion in the solid, but fully mixing in the liquid during solidification. The first solid would form with composition k_pC_0 (k_p is the same partition ratio k as mentioned above, Table 2-3) and the solute is rejected in the liquid, which results in the content in liquid being higher than C_0. With continued solidification, the next layer of solid is formed with a richer solute than in the first or previous solid, due to the mixing of rejected solutes in the liquid. Consequently, the concentration of element in the solid gradually increases with the development of solidification, resulting in the composition in the solid at the end stage of solidification being higher than that in the first solid [13, 58], as seen in Figure 2-17. This model can be used to predict the composition profile for a rapid solidification process, for example with cooling rate over 100 ºC/s during laser welding process [86]. In the steel-making process of continuous casting and ingot casting, solidification is mostly different to the Scheil model, where a low cooling rate is expected and the element diffusion in the solid occurs during the cooling process.

The Clyne-Kurz model can be used to predict the composition profile taking into account a modified back-diffusion parameter β, as seen in Table 2-5. The partition coefficient at the solid-liquid interface is assumed to be constant in local equilibrium

condition for this model. Complete diffusion in the liquid phase is assumed in the Clyne-Kurz model which takes into account finite solute diffusion in the solid, making the Clyne-Kurz model more applicable than the lever-rule model and the Scheil model, to predict the microsegregation that is close to the experiment results [37, 59, 79, 82]. Figure 2-18 shows that the prediction from Clyne-Kurz model at solidus temperature is closer to the experimental data, compared to an extreme segregation profile predicted by Scheil model [37]. However, due to the partition coefficient being assumed constant (but being affected by other elements) at the interface of the solid-liquid phase, the Clyne-Kurz model is limited to only simulate the process of solidification under a local equilibrium condition.

Table 2-5 Different numerical equations were used to predict the segregation behaviour during solidification [59].

Model	Lever-rule	Scheil	Clyne-Kurz
Condition	$D_s \to \infty$	$D_s \to 0$	$0 < D_s < \infty$
Equations	$C_s = \frac{kC_0}{1-(1-k)f_s}$ $f_s = \left(\frac{1}{1-k}\right)\left(\frac{T_L - T}{T_f - T}\right)$	$C_s = kC_0(1-f_s)^{(k-1)}$ $f_s = 1 - \left(\frac{T_L - T}{T_f - T}\right)^{1/(k-1)}$	$C_s = kC_0[1 + f_s(\beta k - 1)]^{(1-k)/(\beta k-1)}$ $f_s = \left(\frac{1}{1-\beta k}\right)\left[1 - \left(\frac{T_f - T}{T_f - T_L}\right)^{(1-\beta k)/(k-1)}\right]$ $\beta = 2\alpha\left(1 - \exp\left(-\frac{1}{\alpha}\right)\right) - \exp\left(-\frac{1}{2\alpha}\right)$ $\alpha = \frac{D_s t_f}{X^2}$
Parameters	T: given temperature; C_s: the concentration of element in the solid phase; C_0: average chemical composition k: element partition ratios in equilibrium condition; f_s: solid fraction; T_L: liquidus temperature; T_f: melting temperature of pure material; β: back-diffusion parameter; α: Fourier number of the solute elements; D_s: solute diffusion coefficient in the solid phase; t_f: local solidification time; X: distance of the microsegregation.		

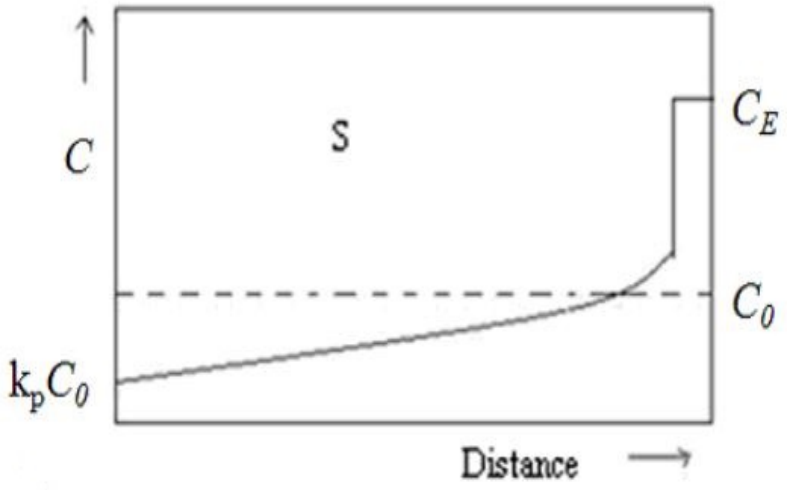

Figure 2-17 Composition profile predicted by Scheil model: the solid with no diffusion and the liquid with full diffusion [13].

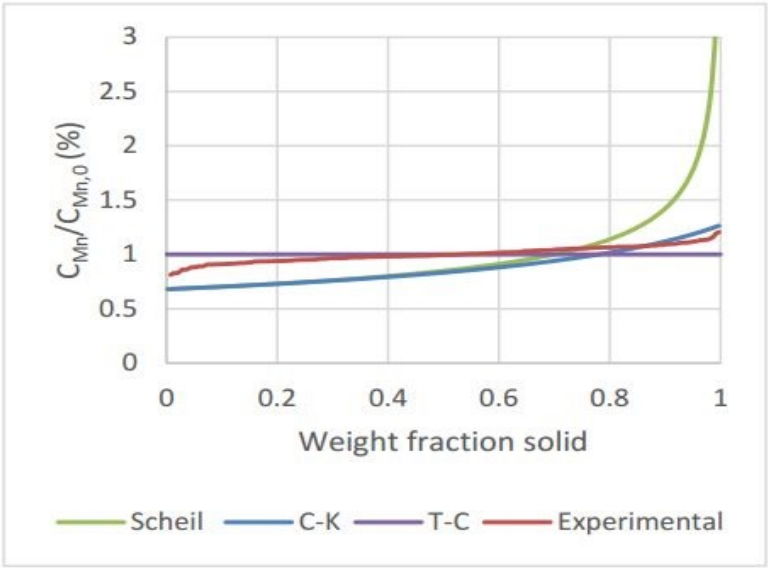

Figure 2-18 Composition profiles of Mn in δ-ferrite at a solidus temperature for structural steel with Mn: 1.52 wt% (Table 2-1) from: (1) Scheil model; (2) Clyne-Kurz model; (3) Thermo-Calc software; (4) and experimental result [37].

Thermodynamic modelling software has been developed to predict the segregation behaviour in a multi-component alloy system. Thermo-Calc is widely applied for analysing a wide range of materials, especially for the steel manufacturing process. It is a flexible commercial software developed with database package for phase equilibrium, phase diagrams, phase transformation calculations and thermodynamic assessments [91, 96-98], to carry out equilibrium simulations for up to 40 components. Simulations have been applied in HSLA steel, including the solidification sequence, phase transformation, composition in a phase, precipitation, and the thermal stability of microalloying precipitates. Segregation behaviour in the HSLA steel was predicted based on Thermo-Calc calculation in literature reports, as will be fully discussed in section 2.2.4.

DICTRA is able to predict the diffusion-controlled phase transformation in multicomponent alloys, which closely links to Thermo-Calc thermodynamic calculations, and combined to the mobility database [92, 95, 98-100]. Many researchers have used it to predict the microsegregation profile in steels [37, 92, 93, 95]. For example, the composition profile of Cr simulated by DICTRA, as shown in Figure 2-19, was consistent with the experimental results of Cr across the secondary dendrite arms spacing [92]. In the simulation of Mn for the structural steel[37], as shown in Figure 2-20, it indicated that the final experimental result (measured at room temperature) agreed with the composition profile simulated by DICTRA after proeutectoid reaction. It indicates that the composition profile at the solid-state can be predicted by DICTRA software which is more useful compared to Clyne-Kurz model.

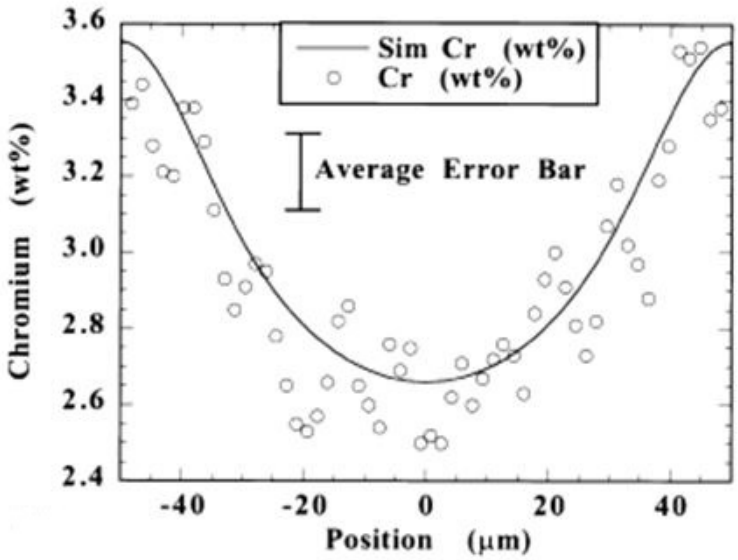

Figure 2-19 Composition profile of chromium simulated by DICTRA compared to experimental result for as-cast AerMet100 across a 100-μm secondary arm spacing [92].

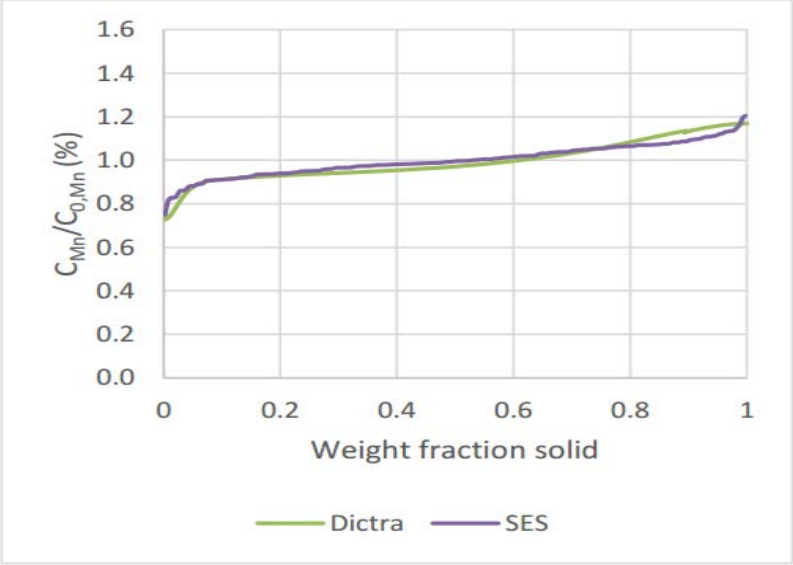

Figure 2-20 Comparison of the experimental result and the DICTRA prediction for Mn composition profile for structural steel (composition is shown in Table 2-1).

2.2.4 Dendrite segregation in HSLA steel

HSLA steel has various carbon contents between 0.04 wt% and 0.2 wt% resulting in different solidification sequences and different final solid phases such as δ-ferrite, or γ-austenite (through the peritectic reaction) [101]. An assumption proposed according to the Fe-C diagram, has been verified by the research on steel with carbon content of 0.08 wt%, 0.12 wt% and 0.16 wt%, which show solidification sequences of L+δ, L+δ+γ and L+γ, respectively [73].

The solidification sequences of four HSLA steels were predicted by using Thermo-Calc (Figure 2-21). The compositions of these steels can be seen in Table 2-1, and they contain various carbon contents[16], where a fully δ-ferrite solidification can be predicted in the pipeline and structural steels (C wt% < 0.06 wt%), whilst the ship building and Slab-1 steel have shown the coexistence of δ-ferrite and γ-austenite before final solidification occurs as austenite (C wt% > 0.1 wt%). These sequences have been simulated under equilibrium condition, which may be different to an actual solidification in steel (as was discussed in section 2.1.2). However, a reasonable description for solidification sequence can be expected from Thermo-Calc prediction [16, 37] as the experimental results are found to follow the assumption generally.

Pipeline steel:	L	→	L + δ	→	δ	→	δ + γ	→	γ
Temperature, °C		1523.2		1492.8		1480		1425.4	
Structural steel:	L	→	L + δ	→	δ	→	δ + γ	→	γ
Temperature, °C		1520.7		1480.7		1477.9		1446.4	
Ship building steel:	L	→	L + δ	→	L + δ+ γ	→	L + γ	→	γ
Temperature, °C		1513.3		1482.8		1478.7		1463.5	
Slab 1 steel:	L	→	L + δ	→	L + δ+ γ	→	L + γ	→	γ
Temperature, °C		1516		1485		1472		1469	

Figure 2-21 Solidification sequences with temperatures for four steels (the compositions are shown in Table 2-1) [16].

Thermo-Calc can be used to predict the partitioning behaviour of elements by calculating the contents in solid and liquid phase during solidification. Figure 2-22 shows that the predicted partition ratio (content of elements in each phase compared to the bulk composition) is generally consistent with the equilibrium coefficient observed in Table 2-3, where Nb shows a strong segregation tendency in the liquid phase, and Al indicates a relatively uniform distribution during solidification [25]. Greater values are seen in δ-ferrite than in γ-austenite for both Nb and Al, which is consistent with the higher partition coefficient observed in the δ-ferrite than that in the γ-austenite (Table 2-3), as discussed in section 2.2.1. The summarised maximum partition ratios at last liquid stage (the content in the last liquid compared to the buck composition) for three slab steels [25], can be seen in Table 2-6; a stable segregation ratio of Al (0.98) can be observed, while Nb shows the similar ratios in the range of 6.45-7, correlating to an increased Nb amount in these slab steels. However, it has been reported that the Thermo-Calc prediction is significantly greater than the experimental result, when using the last liquid composition as input. Evidence for this is shown in a structural

steel [16], which has a lower value (3.12) in measured results than that (7.11) of the Thermo-Calc prediction at the last liquid stage. The maximum segregation ratios have also been reported [16] by using the composition in the last liquid against the contents in the first solid (δ-ferrite), as seen in Table 2-7, which is too extreme as no back diffusion has been taken into account.

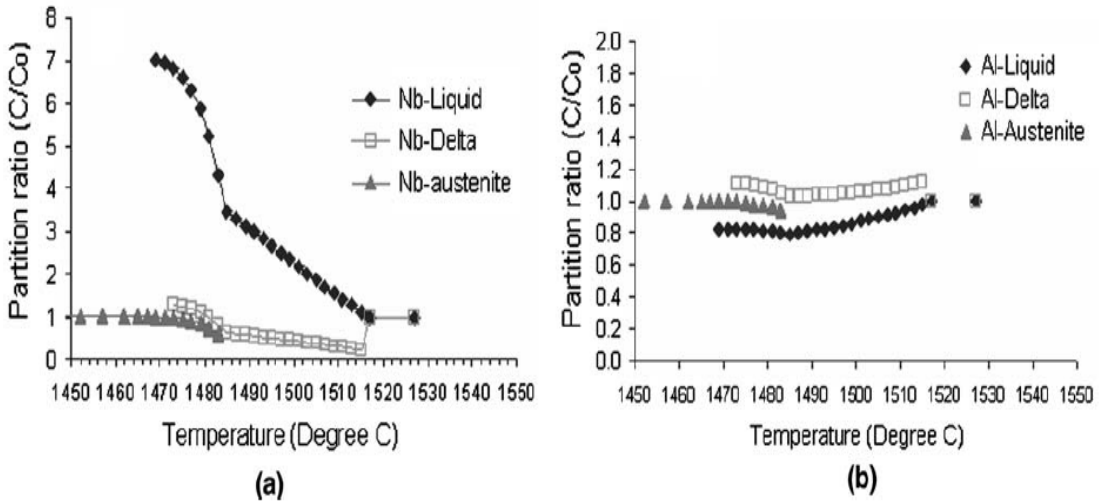

Figure 2-22 Partition ratio during solidification predicted by Thermo-Calc for slab-1 [25] with (a) Nb; (b) Al.

Table 2-6 Partition ratios of content in last liquid compare to average composition, predicted by Thermo-Calc for different slab steels [25].

Element	Slab 1	Slab 2	Slab 3
Mn	1.42	1.41	1.42
Ni	1.21	1.13	1.22
Si	1.58	1.61	1.60
C	3.84	3.80	3.80
Al	0.98	0.98	0.98
Nb	7.00	6.45	6.47
P	5.20	4.50	4.58
Ti	5.36	4.94	5.16
N	2.47	2.47	2.40
S	70.99	60.57	63.90
V	1.78	1.69	0.00

Table 2-7 Maximum ratios of the last liquid composition (wt %) to the first solid composition (wt %) for pipeline steel predicted by Thermo-Calc [16].

	First solid (δ-ferrite)	Last liquid	Max. ratio
C	0·0043	0·2022	47·02
Si	0·159	0·408	2·57
Mn	1·471	2·491	1·69
P	0·0021	0·0290	13·81
S	0·00043	0·22239	517·19
Al	0·0593	0·0403	0·68
V	0·0677	0·1076	1·59
Nb	0·0128	0·3113	24·32

A simple theoretical assumption has been proposed by Zhang [37, 79] to determine the regions of solute-enriched and solute-depleted areas during the peritectic reaction. Figure 2-23 indicates that austenite appears to nucleate at the liquid/δ-ferrite interface, resulting in the formation of a low diffusivity barrier layer of austenite (due to the diffusion rate in austenite being low, Table 2-4) to trap the enriched solutes in the liquid (assuming that very few substitutional elements can transport through the austenite layer [96, 102]). Therefore, the solid phase at the peritectic temperature becomes the solute-depleted region and finally transfers to α-ferrite, whilst the interdendritic liquid becomes the solute-enriched region and finally transfers to the pearlite. It was reported that the volume fraction of a pearlitic structure was close to the predicted volume fraction of the interdendritic liquid at the peritectic point for the HSLA steels, as seen in Table 2-8 [18, 37]. However, a difference of around 5% is seen between the prediction and the measured result, which may arise from the fact that non-equilibrium cooling is expected in the solid state in a slab [38]. It has been reported that the solidification sequence can affect the segregation behaviour [37], for example, a severe segregation of Mn (segregation ratio: 2) was predicted for the steels

which experienced a peritectic reaction (such as ship building steel with 0.14 wt% C and slab-1 steel with 0.1 wt%, Table 2-1) than the steels (e.g. structural steel with C: 0.06 wt% and pipeline steel with C: 0.03 wt%, Table 2-1) solidified without the peritectic reaction (segregation ratio: 1.7) [37]. However, this assumption based on the peritectic reaction cannot predict a complete composition profile describing the segregation behaviour at the final solidification stage, for example if the solute shows significant continued partition from austenite to liquid, then the latter is expected to be enriched gradually after peritectic reaction occurs.

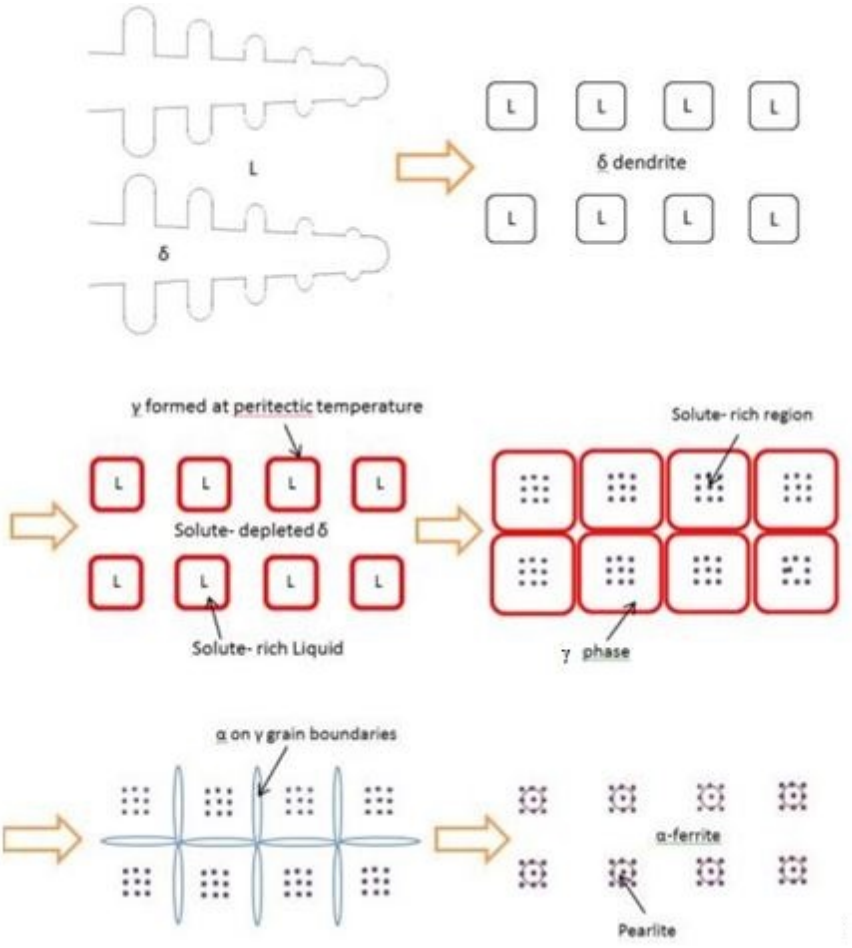

Figure 2-23 Assumed formation of solute-enriched and solute-depleted regions during solidification with the peritectic reaction for the cast slab [37, 79].

Table 2-8 Fraction of the solute-enriched and solute-depleted region predicted by Thermo-Calc at the peritectic temperature compared to the measured experimental result, for the slab-1 steel [18] and slab-2 steel[38], with the same content of C: 0.1 wt% and Mn:1.42 wt%, (Table 2-1).

	Solute-enriched region		Solute-depleted region	
	Thermo-Calc	Measured	Thermo-Calc	Measured
Slab-1	12.5%	19%	87.5%	81%
Slab-2	13%	18%	87%	82%

DICTRA can predict a composition profile, taking into account the diffusion-controlled phase transformation, to deal with the variant partition coefficients and diffusion behaviours (e.g. diffusion of elements in liquid can be calculated) during the process of solidification, and even in the solid-state during cooling. More detailed composition profiles can be predicted as a function of temperature and time. For example in a ship building steel, various composition profiles of Mn predicted by DICTRA at different times can be seen in Figure 2-24 [37], including the distributions of Mn during the solidification process at 80s and 110s, and a profile with diffusion being considered in a longer time of 2500s. A step can be observed in the composition profile at 80s (Figure 2-24) indicating that a higher amount of Mn is observed in the austenite than in the δ-ferrite, which is due to the partition ratio in austenite being greater than in δ-ferrite (Table 2-3). However, the composition profile should be used carefully as it might not be accurate when precipitation has been taken into account (as discussed fully in section 2.3). The composition profile at the final solidification stage, even in the solid-state, can be expected to be predicted by DICTRA due to verified simulation of elemental redistribution and diffusion-controlled phase transformations.

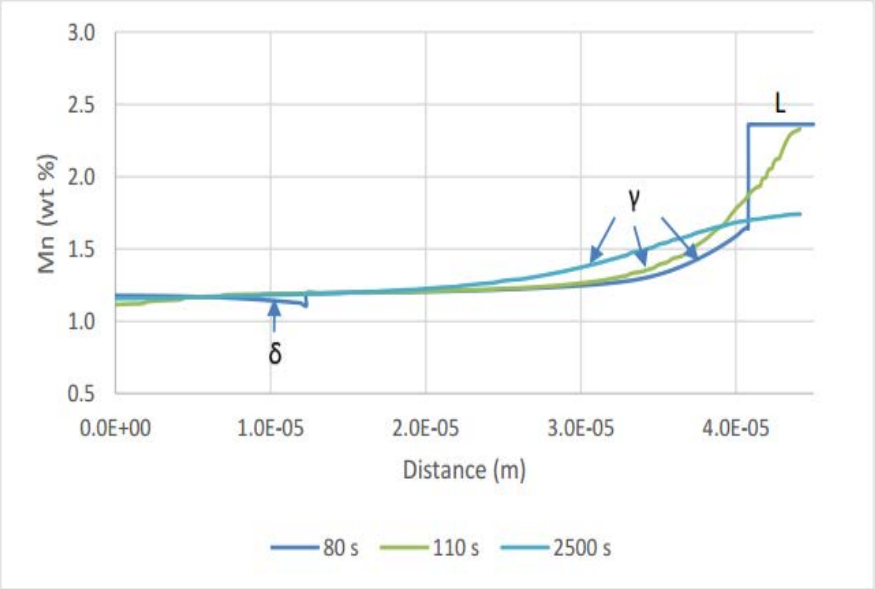

Figure 2-24 DICTRA predictions for Mn distribution as function of distance (half SDAS of 90 μm, as seen in Table 2-2) for ship building steel at different simulated cooling times[37].

2.3 Precipitation during casting and precipitate dissolution during reheating

Precipitates in steel are important to the mechanical properties due to the facts of grain refinement and hardness improvement. The formation of precipitates, related to their nucleation and growth, depends on the supersaturation (amount of solutes above the equilibrium composition) and temperature. The formed particles have different pinning effects on restricting grain growth during steel processing. Different thermal stabilities (which relate to the elements' distribution behaviour) of the particles provide various pinning effects during reheating, such as local unpinning occurring in solute-depleted regions whilst pinning force is still expected in the solute-enriched regions for the same reheating temperatures [24, 25, 103]. Therefore, the distributions and pinning effect of the microalloying precipitates are significant to understanding the grain growth (especially in terms of abnormal grain growth) during reheating treatment in HSLA steel.

2.3.1 Theories of precipitates formation during cooling

During the cooling process, some solute element atoms are assembled, therefore resulting in the precipitation reaction, $[M] + [X] \leftrightarrow (MX)$, where M is the microalloying element and X is the interstitial element (C or N). The microalloying elements mostly prefer to combine with carbon or nitrogen to become carbides or nitrides, reducing the amount of free C and N solutes in the solid solution [104]. Based on the thermodynamic principle, the solubility product describes the equilibrium constant (K_s) for the precipitation reaction and the reverse dissolution reaction. The equilibrium constant refers to the concentration of solutes that are present in the saturated solution, as shown in the equation 2-5

$$K_s = [M] \cdot [X] \qquad 2\text{-}5$$

Here, the [M] and [X] are the concentration in wt%, and the solubility product (K_s) is linked to the temperature, which is described as:

$$ln(K_s) = A - \frac{B}{T} \qquad 2\text{-}6$$

Where A and B are the constants and T is the absolute temperature. Equation of 2-6 indicates that a greater solubility product can be expected at higher temperatures. This equation has been applied to calculate the solute concentrations in many investigations [104-112] in a binary-system, for various microalloying elements, such as Nb, Ti, V and Al under an equilibrium condition (Figure 2-25). However, the formation of more complex precipitate (e.g. carbonitride precipitates) can be predicted by Thermo-Calc,

in a multi-component system within the various compositions, to provide more details such as volume fraction, mole fractions, and the composition of the precipitated phase.

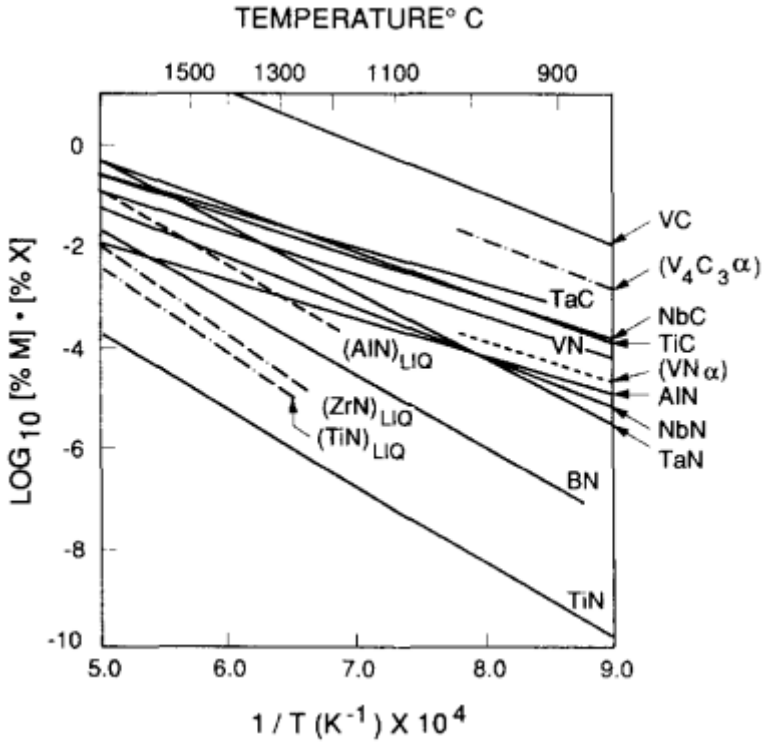

Figure 2-25 Solubility products for different carbides and nitrides of precipitate in microalloyed steel [112].

Due to precipitation occurring in the cooling process, the composition profile predicted by DICTRA for those precipitating microalloying elements (e.g. Ti, Nb, V, Al) should be used carefully, as the composition might not be accurate if precipitation occurs (composition is reduced in the matrix phase) during the cooling process, as discussed in section 2.2.4.

2.3.2 Precipitates in microalloyed steel

Various precipitates formed with the microalloying elements in the HSLA steel have been investigated by applying scanning electron microscopy and transmission electron microscopy (TEM) equipped with an energy dispersive X-ray spectroscopy facility. Precipitates containing microalloying elements of Ti, Nb, V and Al have been characterised in HSLA steel.

Ti: Large cubiform TiN particles (Figure 2-26(a)) form at the high temperatures (> 1350 ºC), with large sizes up to 1 μm (with Ti 0.05 wt% and N 0.028 wt%) [113]. TiN precipitate is generally assumed to be formed in the melt prior to solidification which means that a high thermal stability can be expected during any reheating treatment. Hence, TiN is generally believed to be the most stable microalloying particle which remains in the austenite grain growth at a high temperature [114]. However, it has been found that coarse TiN particles can affect the toughness of steel as they act as a cleavage initiation site in the fracture [115-118]. The precipitation of TiC occurs at the temperature above or close to Ac3 [119], as it has a higher solubility product compared to TiN (and Ti has stronger affinity to nitrogen compared to carbon) at same temperature, as shown in Figure 2-25 above. It has been reported that the pinning effect of TiC on grain boundaries can be expected to increase the yield strength in the Ti-microalloyed steel [120].

Nb: Nb is widely applied in HSLA steel to effectively prevent the austenite grain growth during reheating by Nb(C, N) particle. Generally, it forms as a spherically shaped, or irregular particles, as shown in Figure 2-26(b), at temperatures of around 900 ºC -1200 ºC, which results in a precipitation of fine particle size (60-200 nm) in

large numbers [17, 38, 104], because of the relatively low diffusion rate in a supersaturated austenite solution. Nb is significant in controlling the grain size during recrystallistion due to the strain-induced fine Nb(C, N) particles effectively restricting the recrystallised grains' growth. It has been reported by Cuddy that Nb is the most effective microalloying element to prevent static recovery and recrystallisation and also influences the precipitate strength after deformation [121, 122]. Much research work has been carried out to confirm the strong segregation of Nb in the interdendritic regions [16, 18, 24, 25, 39], resulting in the non-uniform austenite grain growth under the inhomogeneous local pinning force during reheating treatment.

V: V forms to carbide and/ or nitride precipitates during the transformation of austenite to ferrite at around 700 ºC - 900 ºC (with a low diffusion rate), resulting in precipitate strengthening for the steel with a fine particle size of around 5-20 nm [123, 124], as seen in Figure 2-26(c). Due to the instability of V-rich particles during re-austenite heat treatment (> A_{c3}), the pinning effect of V-rich particle is not significant to prevent austenite grain growth, compared to the particles formed with Nb and/or Ti.

Al: Al is not usually classified as a microalloying element, but has been reported to contribute to grain size controlling [18, 30]. Aluminium in HSLA steel does not show strong segregation behaviour compared to Nb, and has a partition ratio, k>1 calculated by Thermo-Calc [16, 18, 24, 25, 38]. It has been found that AlN has no obvious spatial inhomogeneity in an as-cast Slab-1 steel [25]. Faceted AlN precipitates, or with the rod, needle, rounded and irregular shapes are shown in Figure 2-26 (d) [111, 125], appearing in the size range of around 50-400 nm [18]. AlN normally forms at temperatures of around 1000 ºC -1200 ºC, which has a similar thermal stability

compared to Nb-rich particle. It was reported that the presence of AlN particle below 1100 ºC restrained grain growth (grain size of 40 μm after holding at 10 minutes) during an isothermal annealing treatment, whilst fast grain growth was observed when AlN precipitates were dissolved at a high temperature [126]. The addition of Al in Nb-containing steel may provide the pinning effect in the Nb-depleted regions and possibly a uniform pinning force in segregated Nb-containing sample.

Complex particles: Many complex precipitates in a multi-phase can be observed, which indicates a particle of one phase attached to or surrounded by another particle of a second phase [127], for example, Nb (C,N) caps have been found on TiN-based substrates (Figure 2-26(e) [17, 123, 127-130]. Duplex AlN-Nb(C,N) precipitates can also be observed in the microstructure, as shown in Figure 2-26(g), with the formation of AlN wings on a pre-existed Nb(C,N) particle [131]. Figure 2-26(f) shows that the 50 nm AlN plate with Nb- and C-containing cap formed irregular complex particles in an as-rolled steel with 0.036 wt% Al and 0.023 wt% Nb [128]. In Figure 2-26(h), the precipitates present at the interfaces of (Ti,Nb)(C,N) particles were identified as (Nb,Ti,V)C carbides [132]. It has been found that the thermal stability of complex particles was enhanced compared to that of normal precipitates, e.g. a higher dissolution temperature of (Ti,Nb)(C,N) was expected than that for a pure NbC precipitate in the Nb-bearing steel[114].

However, it has been found that the most particles in HSLA steel are simple precipitates containing one microalloying element [18, 24], such as TiN, Nb(C,N), V(C,N) and AlN, which are summarised in Table 2-9: Ti-rich particle forms at high temperatures in a large size, which may correlate the fracture; small V-rich particle

might not have a significant effect on restricting austenite grain growth, due to a lower thermal stability during reheating treatment (< 700 ºC). A similar size can be observed for Al-rich and Nb-rich particles that formed in a similar temperature range, which may have an equivalent pinning effect to restrict the austenite grain growth. However, AlN shows a relatively uniform distribution which is different to the inhomogeneous distribution of Nb(C,N) particle in HSLA steel. Therefore, an investigation on AlN and Nb(C,N) is required for HSLA steel, which includes the distribution during casting with microsegregation (as will be discussed in section 2.3.3) and dissolution during reheating (which will be discussed in section 2.3.4).

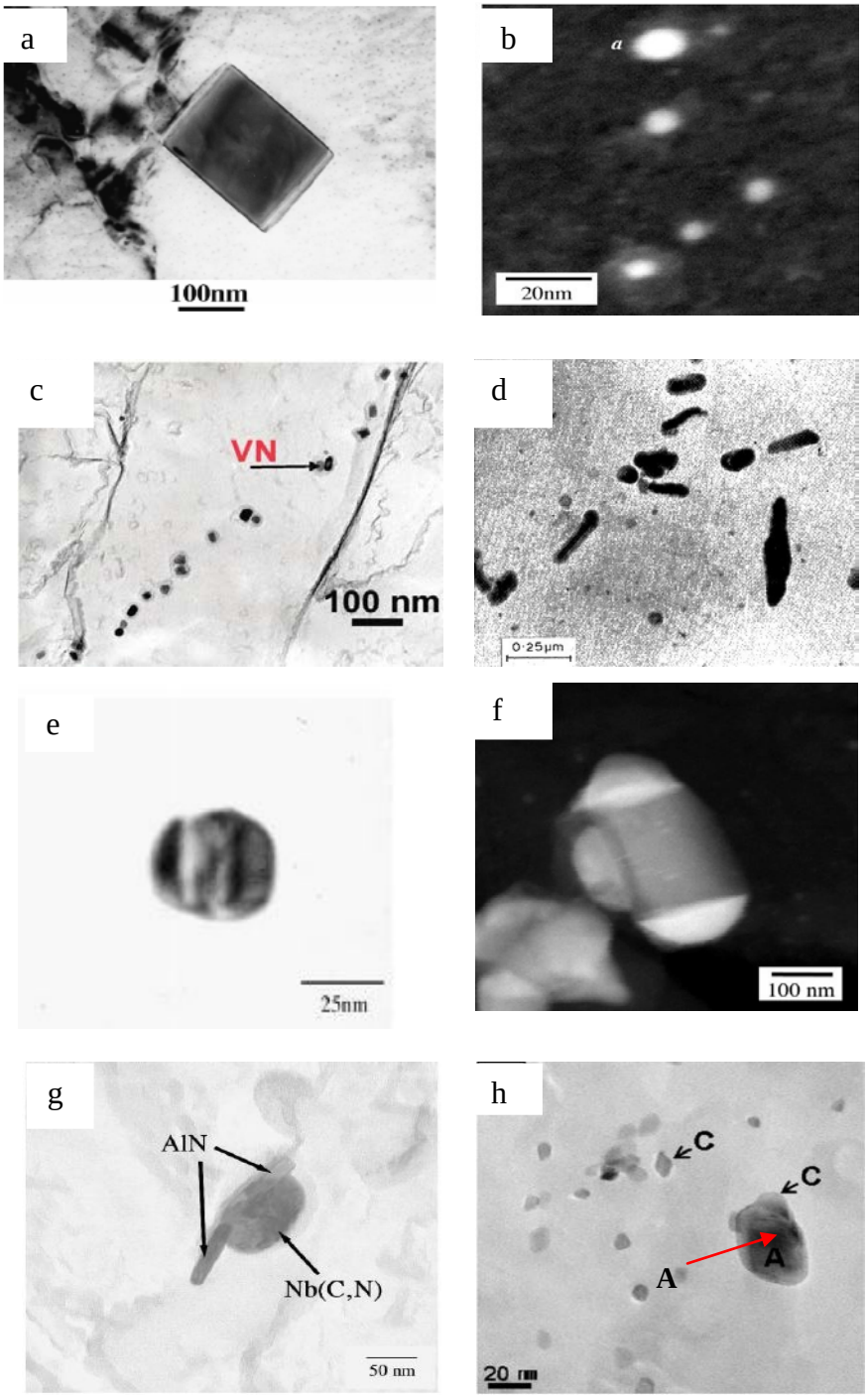

Figure 2-26 Precipitates observed in microalloyed steel: (a) Cubiform shaped TiN [113]; (b) spherical NbC particles [128]; (c) irregular, cuboidal and spherical V-rich precipitates [123]; (d) AlN particles [111]; (e) complex particle of (Ti,Nb)(C,N) [17]; (f) Nb and C coated on a spherical AlN particle [128]; (g) duplex AlN-Nb(C,N) particles [131]; (h) particle 'C' is (Nb,Ti,V)C precipitation and particle A is undissolved (Ti, Nb)(C,N) at 850-900 ºC [132].

Table 2-9 Summarised information for particles contain microalloying elements of Ti, Nb, V, and Al [17, 18, 24, 25, 38-40, 104, 113, 114, 123-125].

	Ti	Nb	V	Al
Precipitate	TiN	Nb(C,N)	V (C,N)	AlN
Shape	cubic	spherical	Irregular, needle	irregular, facet
Size/ nm	>500	60-200	<50	50-400
Temperature/ ºC	>1350	900-1300	700-900	1000-1200
Segregation ratio	5	7	2	1

2.3.3 Precipitation during casting

Due to the various partition behaviours of elements during solidification (discussed in section 2.2), a large proportion of the microalloying elements present in solution is expected to partition to the solute-enriched region. Therefore, more precipitates appear at the previous interdendritic solute-enriched regions. Figure 2-27 shows that the inhomogeneous distribution of precipitates has been observed in the 0.045 wt% Nb containing cast Slab-1, where the precipitate-rich region, indicated as A, B, and C, is separated by regions of precipitates-poor region (D region) [25]. It is reported that the distance between separated precipitate-rich regions is consistent with the second dendrite arm spacing [24, 25]. Nb has been shown to have strong segregation resulting in the large number of precipitates of Nb(C,N) being formed in the solute-enriched regions [16-18, 24, 25, 38-40]. Taking into account the large scale of specimen, there are various local distributions of precipitates where Nb-rich precipitates presenting in the sub-surface region are significantly less than the mid-position (which is formed with final solute-enriched liquid) [17]. AlN particles were found to be distributed uniformly between solute-enriched and solute-depleted regions [25], or slightly more

Al-rich particles were observed in the dendritic ferrite region (solute-depleted regions) [38], corresponding to the partition ratio in Table 2-3.

Table 2-10 reported by Chakrabarti indicates that a greater number density of Nb(C,N) can be seen in the interdendritic region (60×10^4 /mm^2) than that in the dendritic region (12×10^4 /mm^2) in the Slab-1 steel [25]. However, a lower number density (30×10^4 /mm^2) of interdendritic Nb(C,N) is seen in the Slab-3 steel compared to that in the Slab-1 steel (60×10^4 /mm^2), which is due to the lower content of Nb in Slab-3 than that in the Slab-1 steel, Table 2-1.

After homogenisation treatment, it was reported that the volume fraction of particles observed in the homogenised specimens was lower than that in a segregated condition, for example the lower volume fraction of around 3×10^{-4} was observed in the non-banded Al-containing steel (with homogenisation treatment) compared to that (of around 13.16×10^{-4}) in the banded (segregated condition, same composition with no homogenisation treatment) sample [30]. This result indicates that reduced numbers of particles can be expected per unit area as being associated with a well-redistributed solute element in the homogenised specimen.

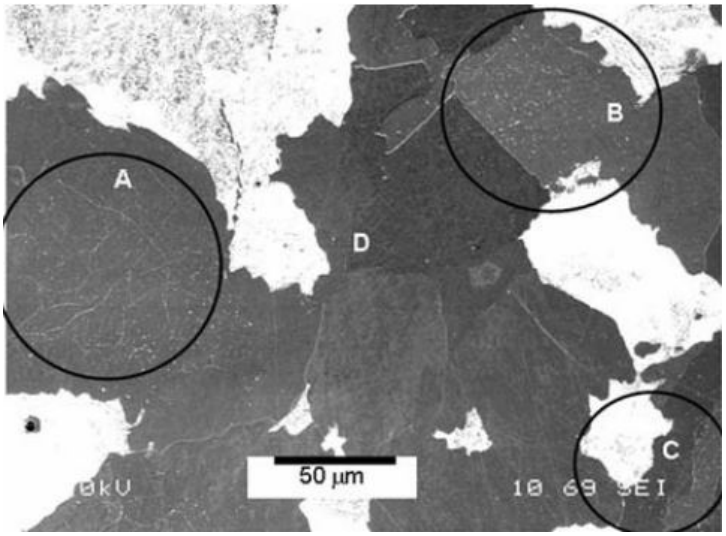

Figure 2-27 SEM analysis of inhomogeneous distribution of precipitates for the cast Slab-1 steel (segregated condition) containing 0.045 wt% Nb with bright pearlite and dark ferrite; the precipitate-rich regions were identified as A, B and C; and the precipitate-poor region was identified as D [25] .

Table 2-10 Precipitate density ($\times 10^4$ /mm^2) in the precipitate-rich and precipitate-poor regions, for the as-cast Slab-1 and Slab-3 steels [25].

	Nb(C,N)	AlN	Total
Slab-1, Interdendritic region	60	4	64
Slab-1, Dendritic region	12	4	16
Slab-3, Interdendritic region	30	5	35
Slab-3, Dendritic region	8	4	12

An isolated ferrite structure surrounded by pearlite phase has been reported in the as-cast microstructure (slab-2, Table 2-1). The isolated ferrite and the EDX results are shown in Figure 2-28, and Nb-rich particles have been found in the isolated ferrite island due to it being an idiomorphic ferrite forming in the interdendritic solute-enriched region [38]. The amount of isolated ferrite was lower (isolated ferrite area fraction is 0.28± 0.05%), compared to the entire interdendritic region with the pearlite

microstructure (the pearlitic area fraction was approximately 18.14±0.5%). The particles characterised in the pearlitic regions containing isolated ferrite have also been taken into account to describe the particle population in the interdendritic solute-enriched region.

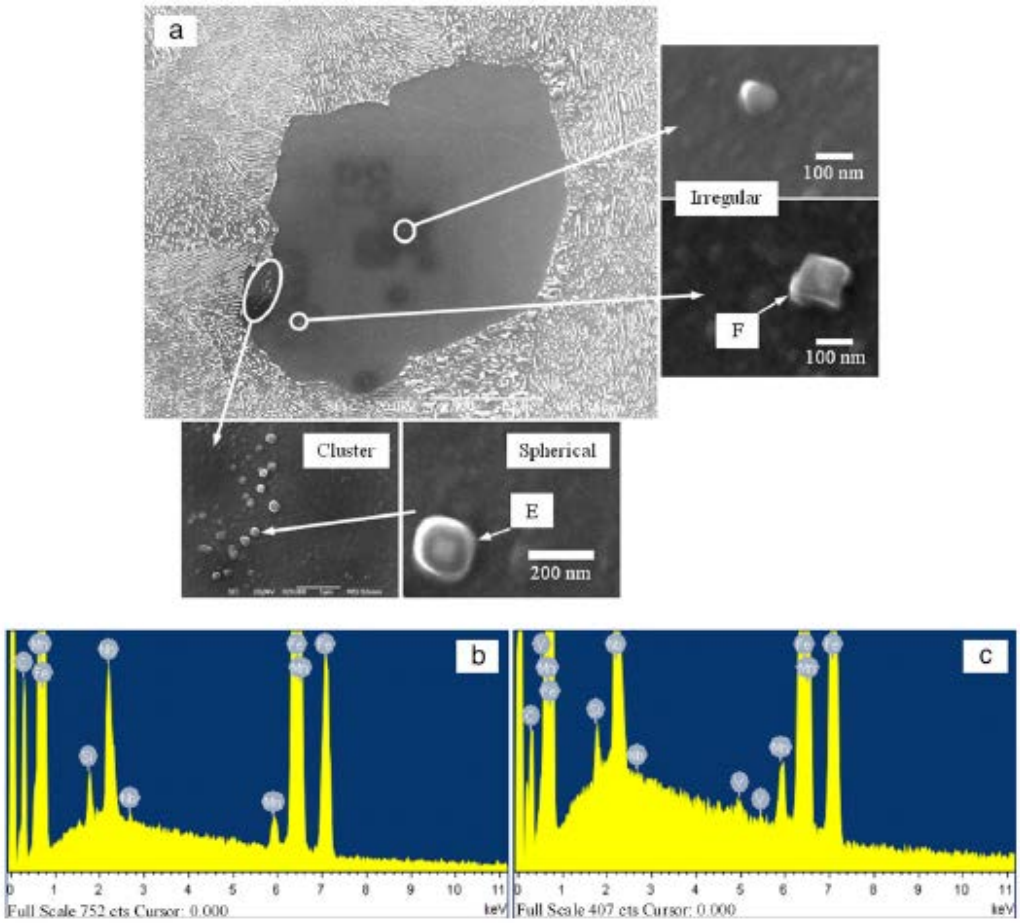

Figure 2-28 (a) SEM image of isolated ferrite with various distribution and shapes of Nb-rich particles, (b) EDS spectrum of precipitate ‘E’ indicating Nb peaks; (c) EDS result of particle ‘F’ indicating V and Nb peaks [38].

2.3.4 Precipitate dissolution and coarsening during reheating

The dissolution of precipitate during reheating (as reduction of number density) is a reverse reaction to the precipitation during the cooling process. The equilibrium

dissolution temperature (T_{diss}) can be given in equation 2-7, which originates from equation 2-6, in section 2.3.1:

$$T_{diss} = \frac{B}{A - ln(K_S)} \qquad 2\text{-}7$$

T_{diss} is the particular temperature for precipitate dissolving completely. However, the application is only limited to a binary system, as discussed previously. Therefore, Thermo-Calc can be used to predict the dissolution temperature for the more complex precipitates (e.g. Nb(C,N)) and alloys under equilibrium condition. With the given compositions, Thermo-Calc can calculate the phase transformation under an equilibrium condition, to predict the dissolution temperatures for the investigated particles in the equilibrium condition [17, 18, 23-25, 133]. However, it has been reported that the Nb-rich particles remained after reheating to a temperature 40 ºC above the complete dissolution temperature of Nb(C,N) predicted by Thermo-Calc [17]. This may be due to the fact that an inhomogeneous distribution of Nb is expected, resulting in different local dissolution temperatures of Nb(C,N).

Therefore, the separated local compositions in the solute-enriched regions and solute-depleted regions have been considered to predict the particle dissolution temperatures in a segregated cast steel [18, 24, 25, 133]. For example, the dissolution temperatures of Nb(C,N) and AlN were predicted separately in the interdendritic (pearlite) region (Nb(C,N): 1210 ºC; AlN: 1120 ºC) and in the dendritic centre (ferrite) region (Nb(C,N): 1090 ºC; AlN: 1125 ºC), as shown in Figure 2-29. And it has been verified by experimental results that the AlN volume fraction was significantly reduced in the dendritic region (close to 0) when reheated at 1150 ºC, whilst the interdendritic

particles (expected to be Nb(C,N)) remained (with a volume fraction of around 0.0005) at this temperature [25].

A higher thermal stability is observed for the interdendritic Nb(C,N) compared to that in the dendritic solute-depleted region, which may be due to the large amount of [Nb] being expected in the interdendritic region. The compositions of different solute-content regions were determined by different assumptions, e.g. the contents in the solid and liquid at the last liquid stage (as discussed in section 2.2.4). However, it has been found that an improved dissolution temperature can be predicted for the carbide or nitride particles, such as Nb(C,N) and AlN, when homogenised compositions of C and N (due to the high diffusion kinetic of C and N in austenite matrix) have been taken into account [38].

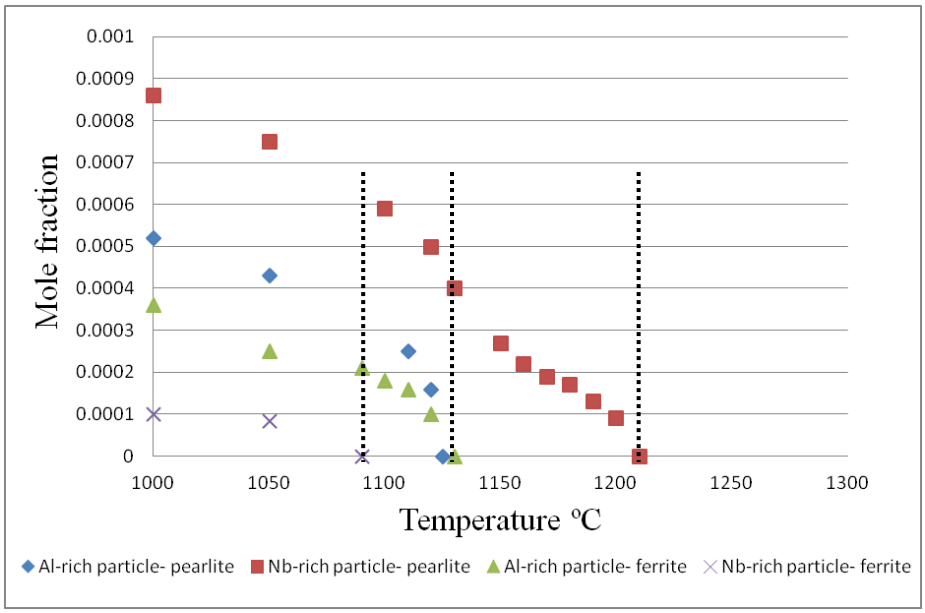

Figure 2-29 Precipitation behaviours were predicted by Thermo-Calc at the interdendritic and dendritic-centre regions for Slab-1. Reheating temperatures are indicated by the dashed lines [25].

During reheating, the large particles are coarsening at the expense of smaller ones, which is due to a partial dissolution resulting in the solute level in the matrix being increased [13, 110, 134]. The factors that control the particles coarsening are expressed in equation 2-8, which has been outlined by Lifshitz and Slyozov [135].

$$r^3 - r_0^3 = \frac{8\sigma VDtC^s}{9RT} \qquad 2\text{-}8$$

Where r is the final particle radius (cm); r_0 is the initial particles radius (cm); σ is the interfacial energy (equal to the grain boundary energy = $800 \cdot 10^{-7}$ J/cm^2 [136, 137]); V is the molar volume of pinning particles, such as Nb (C,N) particles which has been reported to be 6.72 cm^3/mol [138, 139]; C^s is the concentration of the solution in austenite and can be predicted by Thermo-Calc for the given temperatures; t is the particle growth time; R is the universal gas constant (=8.31 J/mol·K); T is absolute temperature (K); and D is the diffusivity of the microalloying element in the matrix. The general growth of particles can be used to predict the limiting grain size, as will be fully discussed in section 2.4.2. It should be noted that the dissolution and coarsening of the particles (discussed above) are also influenced by the holding time at a given temperature.

2.4 Austenite grain growth during reheating

It is well known that cast steel is required to undergo reheating treatment to the temperatures (above A_{c3}) of a full austenitic field, for subsequent industrial processes including hot rolling [19]. The factors of the reheating temperature, carbon content, original microstructure (e.g. initial ferrite and pearlite), and the microalloying elements can be expected to affect the austenite grain growth during the reheating treatment.

2.4.1 Austenite grain growth

Austenite transfers from ferrite and pearlite structure [140], which mostly forms from pearlitic region (with many interfaces between cementite and ferrite), and then experiences growth driven by the reduction of interfacial energy. The ideal austenite grain growth will eventually result in an hexagonal structure with a 120° angle for each boundary junction and straight grain boundaries (Figure 2-30). Due to the fact that the boundaries migrate toward their centres of curvature, the shrinkage of small grains with convex curvature occurs and eventually these disappear during annealing, whereas the grains with concave boundaries are stable and grow to be larger [13]. Therefore, the grain growth during reheating is the process of large grains growth at the expense of smaller grains, which is driven for the minimisation of grain boundary energy [18].

When holding at a certain temperature, the austenite grain growth rate is decreased with holding time, as the driving force of the interfacial energy is reduced for the migration of grain boundaries [141]. In general, normal grain growth is the increase of the grain size corresponding to the decrease in the numbers of grains. Various grain size distributions have been used to describe the grain growth behaviour by many investigations [22-26, 34, 103, 115, 142], including the uniform and non-uniform grain growth, which have taken into account the mode grain size (at peak of distribution), largest grain size (95% accumulated area fraction grain size, as will be discussed later), and the grain size range. The grain growth behaviour can be also depicted using plots of grain size against to the reheating temperatures. One example is shown in Figure 2-31, which indicates the grain growth behaviour of a C-Mn steel (0.18 wt% C; 1.4 wt%

Mn) with the average grain size against the reheating temperatures for holding one hour [143].

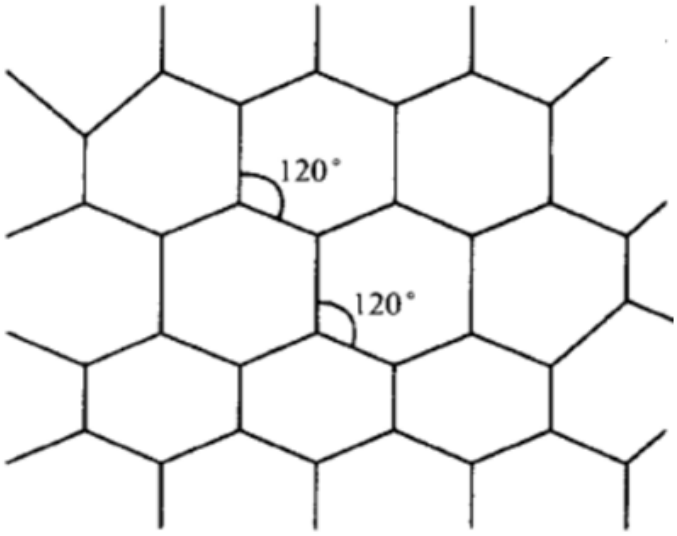

Figure 2-30 Stable structure of grains in binary graph of metal

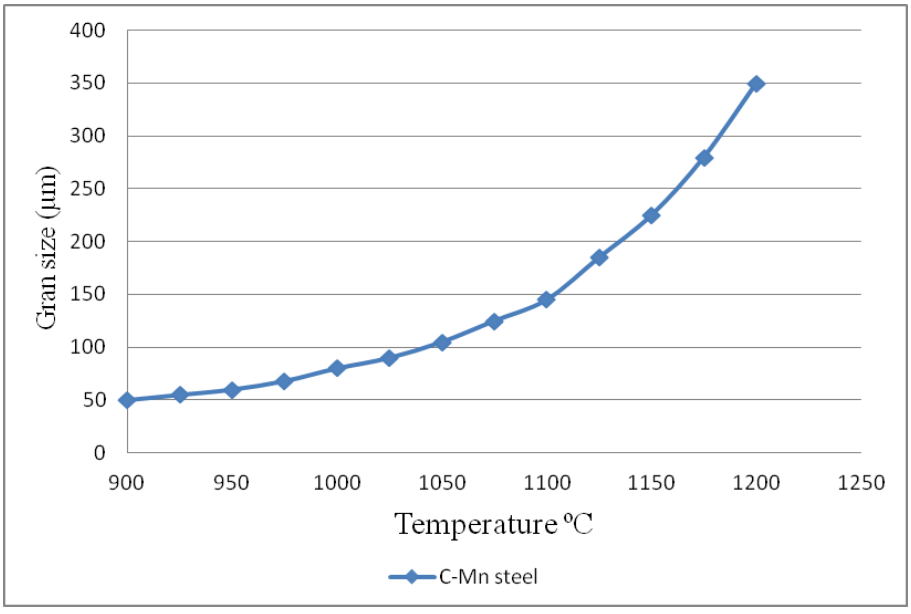

Figure 2-31 Grain size development against the reheating temperatures in a C-Mn steel for one hour [143].

2.4.2 Austenite grain growth inhibition with microalloying precipitates

The addition of microalloying elements in steel can be expected to form into particles which can exert a pinning force to restrict the grain boundary movement, and so prevent grain growth. Figure 2-32 shows the mechanism of the pinning effect where the grain boundary moves from position 'I' to position 'II'. The boundary gradually detaches from the particle and becomes curved, resulting in an increase of the boundary interface, therefore enhancing the surface energy which is in opposition to the austenite grain growth discussed above [144].

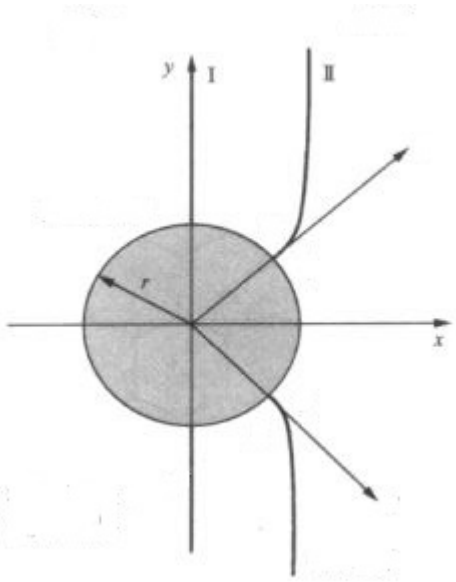

Figure 2-32 Particle pinning effect on grain boundary movement.

Zener considered that there was a relation between the size of the grains, *R*, and the size of the spherical precipitate particles, *r*. The Zener force describing the pinning force per unit area of the boundary P_z [144] is given as:

$$P_z = 3f\sigma/2r \qquad 2\text{-}9$$

Where, σ is the boundary surface energy and f is the volume fraction of the particles. It indicates that an increased pinning effect can be expected when increasing the particle volume fraction and decreasing the particle size. Zener's model [145] has balanced the driving force for grain growth against the pinning force by particles for preventing grain growth, which was corresponding to the limiting grain size:

$$R_c = A\frac{r}{f} \qquad 2\text{-}10$$

Where A is a constant reported by Zener as 4/3; f is the volume fraction of the particles; and R_c is the Zener limiting grain size (the critical maximum grain radius when the driving force for grain boundary movement equals the particle pinning force). However, no information has been given concerning the grain growth rate or the grain size distribution [146].

Many investigations have tried to improve the equation 2-10, considering factors such as the heterogeneity factor of Z describing the size ratio (R/R_0 in radius) of the growing grain size (maximum grains) of R to the adjacent averaged pinned grain size R_0 [144, 147]; the parameter of m has also been used to modify the particle volume fraction [146]. The improved equation can be given as:

$$R_0 = \frac{\pi}{6}\left(\frac{3}{2} - \frac{2}{Z}\right)\frac{r^*}{f^m} \qquad 2\text{-}11$$

It has been reported that grain growth occurred during reheating as some particles are ineffective in pinning the boundary movement, due to the coarsening of particles ($r > r^*$), or the dissolution of particles resulting in a decrease in the volume fraction ($f \approx 0$) [144]. Gladman [148] proposed that grain growth inhibition occurred when the value

of Z was less than or equal to 1.33. However, it has also been found that values of Z between 1.41 and 2 agreed with the experiment results [136, 147-149]. Therefore, the value of A, which corresponds to Z, is between 0.05 and 0.26. m is the exponent of volume fraction f within the range of 0.3-1.

Manohar et al. [146] summarised the modifications mainly in terms of the different values of 'Z' and 'm' being reported in the literature, and examined the critical grain size (R) based on experimental evidence reported in the literature. It has been reported that the coefficient of Z=1.7 enabled the calculation of stable austenite grain growth under any combination of particle sizes and volume fraction [136, 150]. For most of the literature, the value of the exponent m used to modify for 'f' in Zener equation (2-11) is m=1. However, the value of m=0.9 has also been used to predict the limiting grain size in the literature with the small particle volume fraction (f < 0.03) [151-153], which can be expected to modify the '$f^{0.9}$' to be a large value (> 'f'), resulting in an increase in the predicted Zener pinning force (equation 2-10). Therefore, the limiting grain size can be expected to experience no abrupt increase when the volume fraction is effectively decreased. It has been reported that the limiting grain size was successfully predicted in a Slab-3 steel for reheating at 1150 ºC, using the parameters of Z=2 and m=1 (Figure 2-33), where no grain size was larger than the limiting grain size in the interdendritic region (of around 80 μm). The limiting grain size will be predicted by equation 2-11 using appropriate parameters (such as Z and m) in the following investigation to compare with the experimental result for any potential non-uniform grain growth as a reduction in pinning effect.

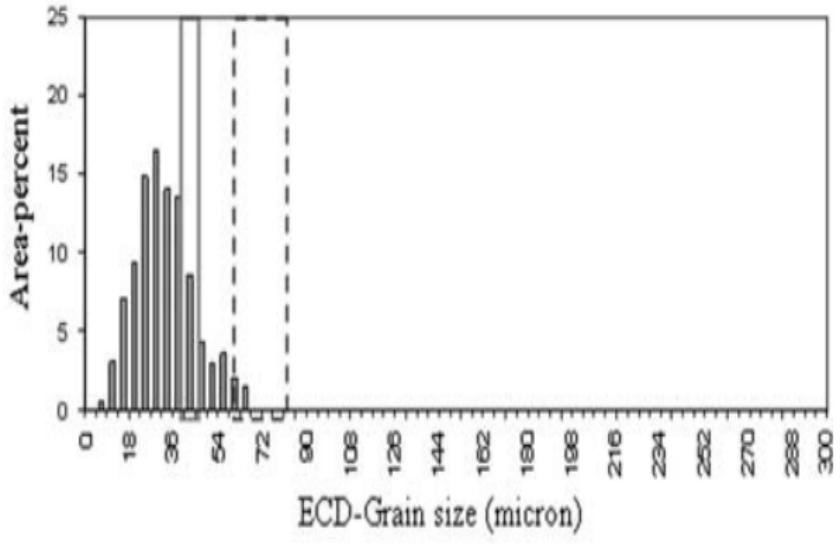

Figure 2-33 Grain size distribution compared to limiting grain size ranges which are predicted in dendritic regions (indicated by the solid lines) and interdendritic regions (indicated by the dotted lines) for Slab-3 reheating at 1150 ºC [25].

2.4.3 Austenite grain growth in HSLA steels

Austenite grain growth in HSLA steel undergoes an inhibition from particles during reheating treatment, where various growth behaviours are to be expected when taking into account the driving force and pinning force. Many researchers have found a typical ‘normal-abnormal-normal’ grain growth behaviour in HSLA steels [24, 25, 30, 31, 39, 40, 154], as shown in Figure 2-34. This includes the normal grain growth (with a uniform grain size distribution) in a finer size when reheating to low temperatures, due to a larger pinning force (supplied by the stable microalloying particles) being expected than the driving force. On reheating close to the particle dissolution temperature, local unpinning occurs resulting in a non-uniform grain growth, such as abnormally large grain growth and bimodal grain growth, which is due to the partial dissolution of the particles. After reheating to a temperature above the particle dissolution temperature, normal grain growth happens once again in a coarsening size,

as there is no pinning effect remaining. The grain growth behaviours of two HSLA steels shown in Figure 2-35 indicate that a similar size development against reheating temperatures can be seen in the steels of Slab-A [40] (compositions are shown in Table 2-1) and EQ70 steel [155] (0.13C-1.09Mn-0.053Al-0.024Nb-0.014Ti). This means that the grain growth in microalloyed steel has been limited to a size which is smaller than that in C-Mn steel (as shown in Figure 2-31). It also indicates that the pinning effect of microalloying precipitates is significant in a steel for the grain size refinement.

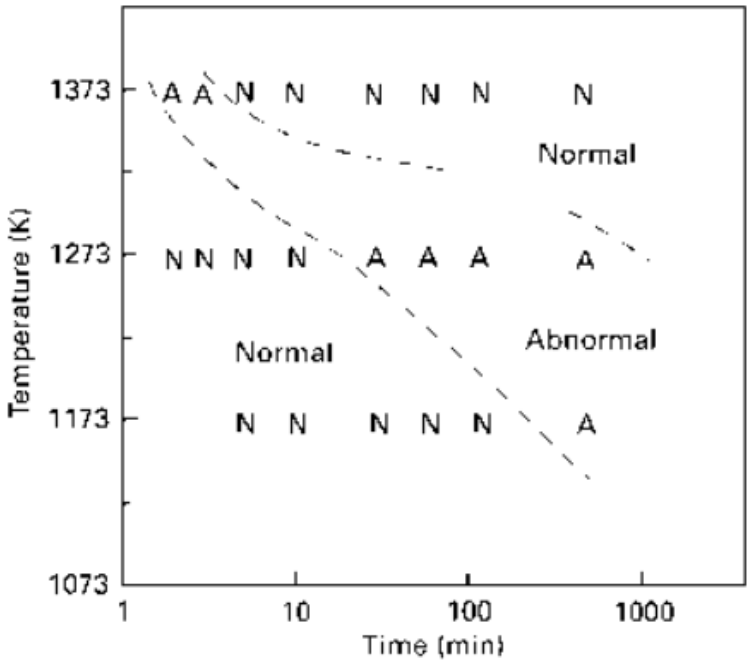

Figure 2-34 Mechanism map of normal and abnormal grain growth zones for 0.3C, 0.036Nb, 0.015V (wt%) steel [31].

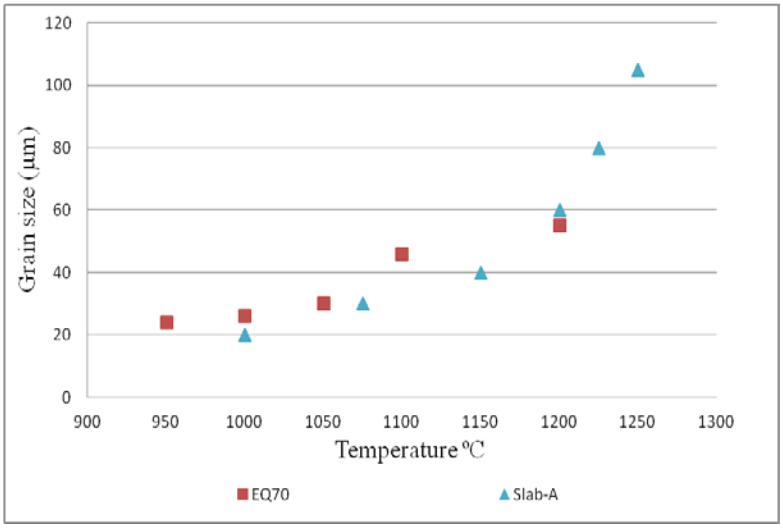

Figure 2-35 Grain size development against the reheating temperatures in EQ70 steel [155] and Slab-A steel [40] for one hour.

2.4.3.1 Abnormal grain growth

Abnormal grain growth has been investigated in various samples during reheating treatments, such as a rolled steel plate [29-31] or in a thin slab [28, 154, 156] (where any segregation was over relatively small distances), which indicates an isolated abnormally large grain surrounded by the small grains, as shown in Figure 2-36 [157]. It indicates that an abnormally large grain with concave boundaries can be expected to grow at the expense of the adjacent small grains (as discussed in section 2.4.1), when local unpinning occurs due to the partial dissolution of the precipitates on the boundaries of the large grains. It has been reported that the particle dissolution depended on the particle type and initial concentration [158], as discussed in section 2.3.4. Abnormal grain growth originating from the former ferrite region has been found in a banded structure [78], which indicates that grain growth from the solute-depleted region can be expected to be abnormally large, if there is no stable pinning effect remaining.

It was reported that on reheating close to the microalloying precipitate dissolution temperature, abnormally large grains were observed in an homogenised steel [30, 40], Figure 2-37(a, b), and in the rolled (with a banded structure) steel [30, 154], as seen in Figure 2-37 (c, d), which were isolated and surrounded by the fine grains. The occurrence of abnormal grain growth results in the grain size distribution expanding to be a wider range of the large grain sizes [159] (Figure 2-37(f)) compared to normal grain growth with a uniform distribution (Figure 2-37 (e)). It has been reported that abnormal grain size was more than 2 standard deviations larger than the normal grain size [159], which approximately was equal to grain size at 95% fraction from a cumulated area diagram [154]. The ratio of large grain size (95% cumulated area fraction mentioned above) to mean grain size is used to determine the occurrence of abnormal grain growth. A larger ratio of abnormal grain size to mean grain size has been observed in homogenised steel (of around 7-9), than that (of around 3) in the rolled steel (with the banded structure), which indicates that abnormal grain growth bebaviour occurs to different extents in a steel with different initial conditions.

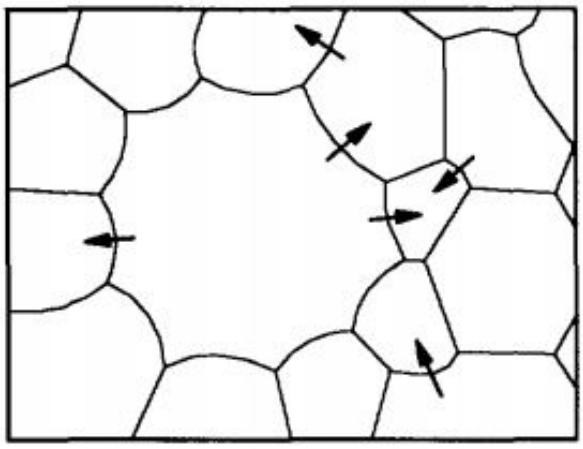

Figure 2-36 Schematic diagram indicating the grain boundary migration (arrows shows the direction) of microstructure consist of polygonous large grains and small grains [157]

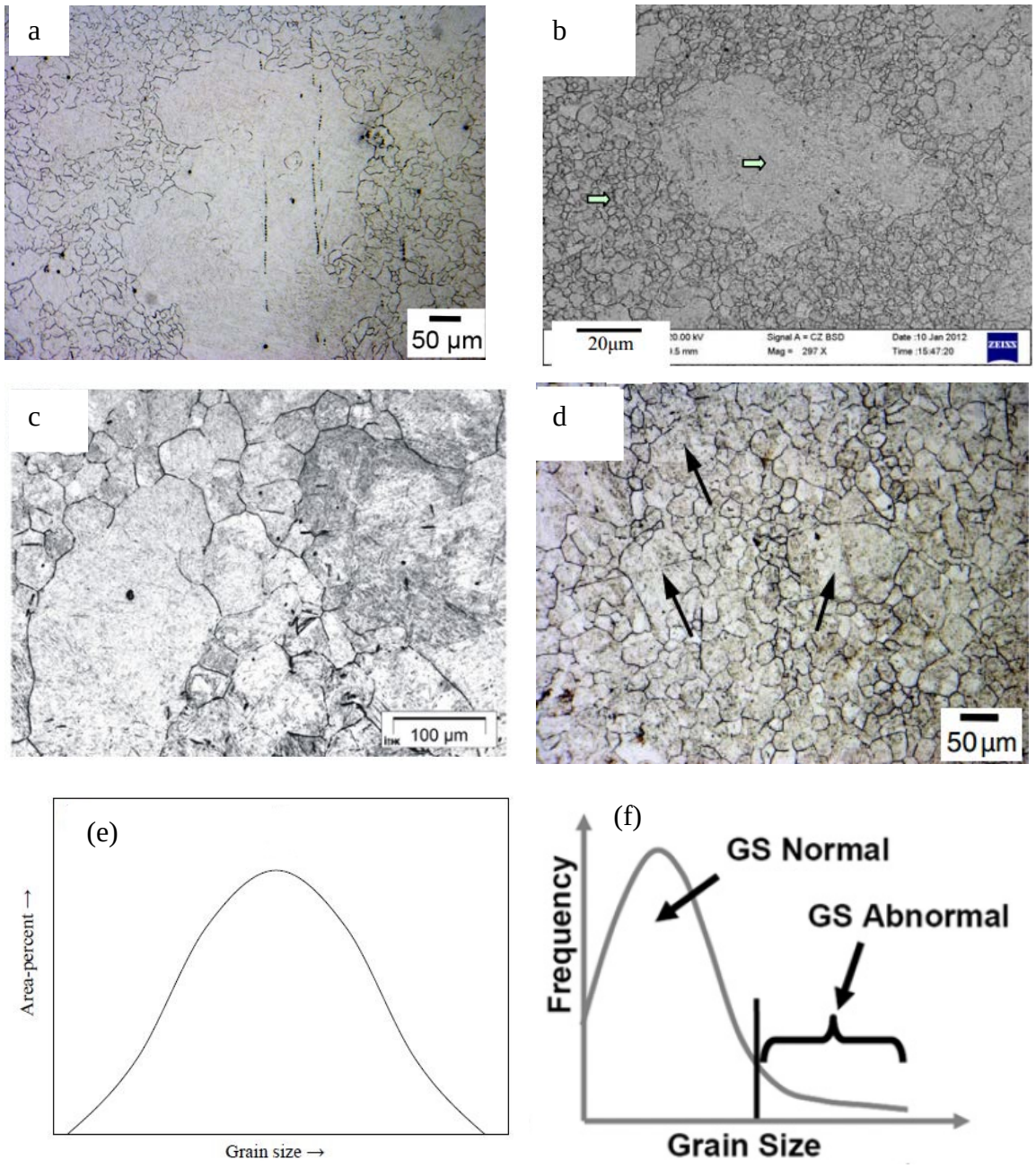

Figure 2-37 Abnormal grain growth occurred in homogenised steel: (a) Al-containing steel with non-banded structure at 1050 ºC [30]; (b) Nb-V steel at 1200 ºC [40]; and occurring in steel with banded structure for: (c) 16MnCr5+ Nb/Ti steel at 1050ºC [154]; (d) Al-containing steel with banded structure at 1000 ºC [30]; (e) theoretical grain size distribution of normal grain growth [24]; (f) grain size distribution of abnormal grain growth [159].

The relative differences (*RD*), shown in equation 2-12, is used to establish the criterion of abnormal grain size [160]:

$$RD = \left[\frac{(GS_{abnormal} - GS_{normal})}{(GS_{normal})}\right] \quad 2\text{-}12$$

Where $GS_{abnormal}$ is the abnormally large grain size, and GS_{normal} is the mean grain size of the normal grains. It was reported that the abnormal grain growth occurred when parameter value (*RD*) exceeded 0.9 [160]. Specifically, the abnormally large grains can be determined if their sizes are greater than approximately 2 times that of the mean grain size [161, 162]. However, this value may be challenged as it is small when describing the abnormal grain growth which occurs in homogenised steel (ratio: 7-9), Figure 2-37 (a, b). Abnormal grain growth was reported to occur at the austenite coarsening temperature which was determined as below the precipitate dissolution temperature by 125ºC in Nb containing steel [106], or slightly less by 40-70ºC in Nb-Al containing steel [163]. On reheating at the particle dissolution temperature for a longer time, those abnormal grains can continue growing to be extremely large by consuming more adjacent smaller grains [27, 30], but they cannot do so to be an arbitrary size [160, 164], as the driving force is reduced (discussed in section 2.4.1), or they encounter pinning forces supplied from other segregated regions.

2.4.3.2 Bimodal grain growth

Due to inhomogeneous precipitate distribution (especially for Nb-rich particles) originating from interdendrite segregation during casting (Figure 2-38), a simple schematic diagram can be produced including the segregation spacing (indicated as ‘L’ corresponding to SDAS) and the thickness of the interdendritic band structure (indicated as ‘d’ in Figure 2-38). The formation of the bimodal grain structure (bands of coarse and fine grains) was found in the reheated continuously cast Slab-1 at 1150

ºC, Figure 2-39(a) [24, 25], which was attributed to the different local pinning force from the dendritic region and the interdendritic region during the reheating process, i.e. at 1150 ºC, the particles with a large population (5.5×10^4 /mm^2, Table 2-11) were remained in the interdendritic solute-enriched region resulting in a strong pinning force to restrict grain growth in a small size; while the coarse grains were originated from the dendritic region with the insufficient pinning effect being expected, due to the particles having been largely dissolved with a low dissolution temperature (as seen in Table 2-11) [103].

Generally, in the histograms, 'mode' is the most frequent (or the peak) value in the grain size distribution. A single mode can be observed in a uniform (log-normal) grain size distribution for normal grain growth (as discussed in section 2.4.3). However, the 'bimodal distribution' is a type of duplex condition with two separate 'mode' values (i.e. two peaks in the grain size distribution), which corresponds to the fine and coarse grain sizes separately in a bimodal grain size distribution, Figure 2-39(b) [22]. The peak grain size range (PGSR) of two mode grain sizes and peak height ratio (PHR) of area fraction for large mode grain size to the area fraction for small mode grain size can be used to characterise the bimodal severity [23-25], for example, Figure 2-39 (b) shows the small mode grain size of 40 μm with area fraction of around 20% and large mode grain size of 220 μm with area fraction of around 9%, giving that the PGSR is around 180 μm and PHR is around 0.45, which can be determined as heavily bimodal, as seen in Table 2-12[25].

On reheating above the interdendritic particles' dissolution temperature, the grains grow normally once again, with a uniform distribution of coarse grains present in the

matrix, as there would be no pinning effect to prevent the grain growth due to all of the particles being expected to have dissolved completely. A uniform coarse grain structure was seen in the Slab-1 steel on reheating at 1225 ºC, with a low number density (0.2×10^4 /mm^2) of Nb(C,N) precipitates being observed in the interdendritic region (Table 2-11), indicating that the pinning effect was insufficient to restrict the grain growth[25].

The bimodal grain growth shows a type of non-uniform grain growth where the bands of coarse and fine grains have been observed, which is different to an isolated large grain (surrounded by smaller grains) occurring in abnormal grain growth. These two abnormal phenomena are associated with local unpinning but with different mechanisms, i.e. a band (area) unpinning is expected in the bimodal grain growth which is associated with interdendritic segregation (form due to the regions of solute-enriched region and solute-depleted region), whilst abnormal grain growth is due to a random particle dissolution (in a homogenised specimen) resulting in the local unpinning for a large grain growth.

It has been found that the non-uniform austenite grain growth formed from reheating can be expected to affect the subsequent recrystallisation in the process of deformation, for example, it was very difficult to achieve a uniform recrystallised grain size from a bimodal grain size distribution[34], while an abnormally large grain was also very difficult to be refined after deformation [40]. It was reported that the presence of larger grains in the bimodal microstructure would decrease the toughness by raising the cleavage initiation, resulting in a high scatter in the fracture stress [103]. The

microhardness in the region of the coarse grain was reported to be lower than that of the fine grain bands [142].

The previous investigations from open literature have tried to avoid bimodal and abnormal grain growth during reheating for the HSLA steels. Chakrabarti and Roy have recommended that an increase of the Ti level in Nb-containing steels can be used to reduce the bimodal grain growth severity, as Ti does not segregate as strongly as Nb, and provides a higher thermal stability during reheating treatment [24, 40]. However, it has been reported that the addition of Ti would influence the toughness [115-118]. And some studies have reported that the addition of Mo would be beneficial to delay the occurrence of abnormal grain growth [149, 165]. A newly designed Al-Nb containing steel will be investigated in this project to explore the effect of Al on alleviation of bimodal grain growth in the Nb segregated steel.

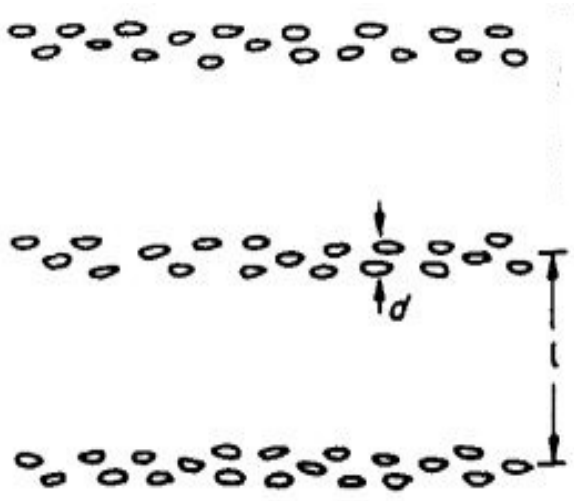

Figure 2-38 Schematic representation of inhomogeneous precipitate distribution due to segregation: ‘d’ is the thickness of the particle-rich (solute-enriched) region; ‘l’ is the distance between two adjacent particle-rich regions, which is similar to SDAS distance [151].

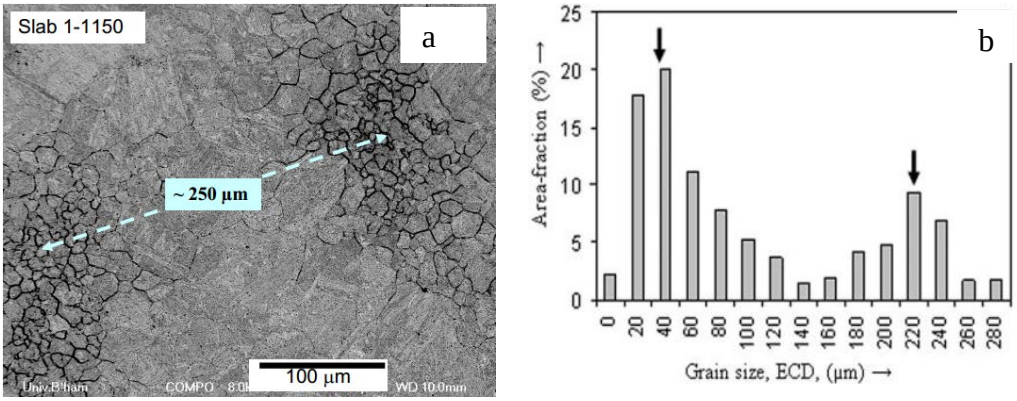

Figure 2-39 Prior austenite grain of Slab-1 (0.1%C, 0.008%N, 0.045%Nb) reheating to 1150 ºC for: (a) Microstructures consisting of coarse and fine grain regions (arrowed); and (b) the corresponding bimodal grain size distribution (peaks indicated by arrows) [24, 25].

Table 2-11 Number density ($\times 10^4$ /mm^2) of the Nb(C,N) and AlN in the interdendritic region and the dendritic region, when reheating the Slab-1 steel at 1075 ºC, 1150 ºC and 1225 ºC in [25].

	1075 ºC		1150 ºC		1225 ºC	
	Nb(C,N)	AlN	Nb(C,N)	AlN	Nb(C,N)	AlN
Interdendritic	16	2	5.5	0	0.2	0
Dendritic	4	2	0	0	0	0

Table 2-12 Severity level of bimodal grain growth is according to peak grain size range (PGSR) and peak height ratio (PHR) [23-25].

Visual Observation	PGSR (µm)	PHR
No bimodal (uniform)	0	0
Low bimodal	0-40	0-0.2
Average bimodal	40-80	0.2-0.35
Quite bimodal	80-200	0.3-0.4
Heavily bimodal	150-300	>0.4

2.5 Summary

Uniform and fine refined grains provide superior strength and toughness that depend on the parent austenite grain size distribution during reheating, associated with the formation of microalloying particles which supply the pinning effect in HSLA steel. Abnormally large grain growth and bimodal grain growth can occur during reheating, taking into account the local unpinning which is attributed to the partial dissolution of precipitates. Previous investigations reported in the open literature have been carried out to reduce the inhomogeneous grain size distribution by applying homogenisation treatment or adding other microalloying elements. However, no investigation has been carried out to establish the comparisons between the abnormal grain growth and bimodal grain growth in HSLA steel with Al addition, taking into account the particle dissolution behaviour predicted by Thermo-Calc.

2.6 Objectives of the present study

In this project, the characterisations of abnormal and bimodal grain growth will be compared and the criterion for determination will be proposed, to establish a clear mechanism for these two types non-uniform grain growth which have discussed in the literature. It is innovative that the grain growth behaviour will be predicted based on precipitate dissolution temperatures simulated by Thermo-Calc and DICTRA, which will be examined and verified to establish a new method (based on modelling prediction) for design of new advanced steel. An Al-Nb steel in different initial conditions (e.g. homogenised, as-cast and forged specimens) and rolled Nb-containing

steel have been investigated to determine grain growth behaviour at the predicted reheating temperatures. To achieve this, the following objectives have been established:

1. To investigate the reheating conditions (such as reheating temperature and holding time) for the occurrence of 'normal (uniform fine grain size distribution)-abnormal (abnormal or bimodal grain size distribution) –normal (uniform coarse grain size distribution)' grain growth in the Al-Nb steel and the rolled Nb-containing steel. To investigate the occurrence of abnormal grain growth and bimodal grain growth under different initial conditions at particle dissolution temperatures (as predicted by Thermo-Calc), taking into account the addition of Al in the Nb-containing steel. To distinguish the differences between these two non-uniform grain growths during reheating and investigate the methods to minimise them in the HSLA steel.

2. To investigate the interdendritic band pinning effect on limiting grain growth. Different segregation spacings have been investigated to examine grain growth behaviour within segregated conditions.

3. To verify the modelling prediction. The grain growth behaviour can be simulated at the particle dissolution temperature predicted by Thermo-Calc, which has taken into account the segregation distance and the segregated compositions. This will be examined by the experimental results, in order to verify the accuracy of the modelling prediction for the future compositions design in HSLA steel.

chapter 3 Materials, modelling and experimental procedure

3.1 Material

A laboratory as-cast ingot of Al-Nb microalloyed steel measuring 340 mm long with a 130 X 130 mm cross-section and an as-rolled (25 mm thick and 150 mm wide) low carbon rolled Nb-containing steel plate were supplied by TATA Steel, UK. The chemical compositions of these two steels are shown in Table 3-1. The schematic diagram in Figure 3-1 shows the sample location in the as-cast ingot Al-Nb steel. 40 samples measuring 10 X 15 X 20 mm were taken at the quarter position (quarter width and depth) of the as-cast Al-Nb ingot steel for investigation on segregated condition. A piece of as-cast steel in size of 20 X 40 X 40 mm was taken from the quarter position in order to achieve the forged Al-Nb steel, which was subjected to 70% deformation from 40 mm to 12 mm at a temperature 1000 ºC (no dissolution of microalloying precipitates) followed by air cooling. 4 specimens of Al-Nb steel in size of 10 X 20 X 60 mm were taken from quarter position of as-cast Al-Nb steel for homogenisation treatment. 20 samples, sized 10 X 15 X 20 mm, were taken from quarter position (in depth and width) for the rolled Nb-containing steel plate, as seen in Figure 3-2

Table 3-1 Chemical composition (wt%) for as-cast ingot (Al-Nb steel) and rolled (Nb steel) steel.

Element	As-cast Al-Nb steel	Rolled Nb-containing steel
C	0.1	0.105
Si	0.29	0.23
Mn	1.42	0.99
P	0.018	0.002
S	0.004	0.001
Cr	0.01	0.005
Mo	0.005	0.005
Ni	0.32	0.005
Al	0.057	0.031
N	0.008	0.006
Nb	0.019	0.028
Ti	0.001	0.001
V	0.052	0.001

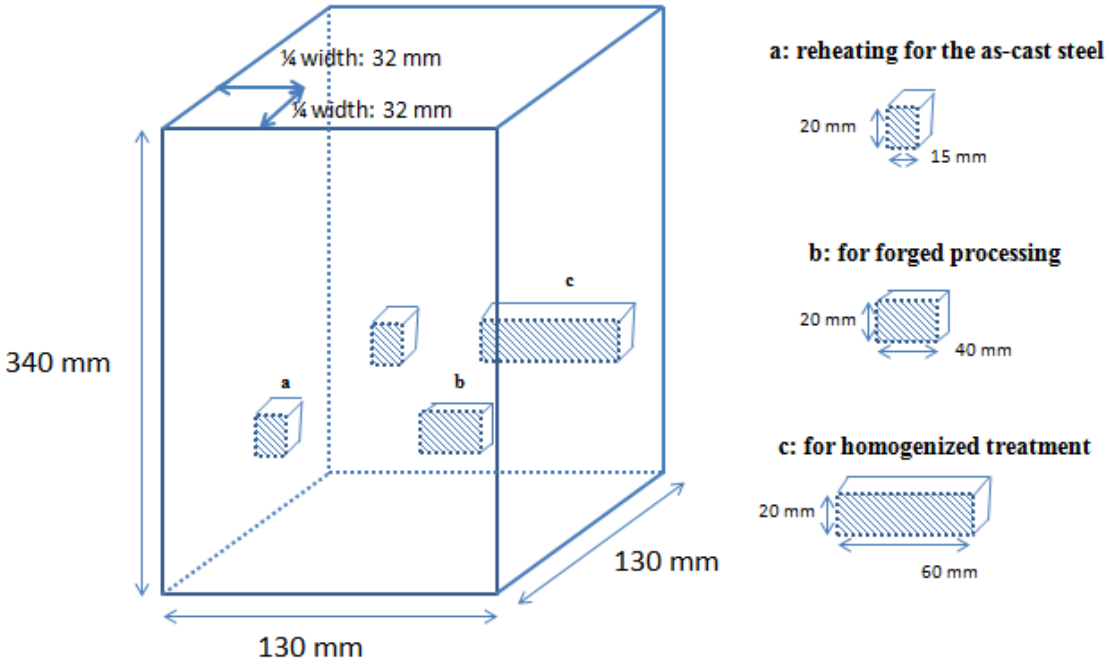

Figure 3-1 Schematic diagram of the sample location in the as-cast Al-Nb ingot. (a) samples for reheating treatment in the as-cast steels; (b) sample for the forged processing at 1000 ºC; (c) samples for the homogenised treatment at 1300 ºC for 24 hours.

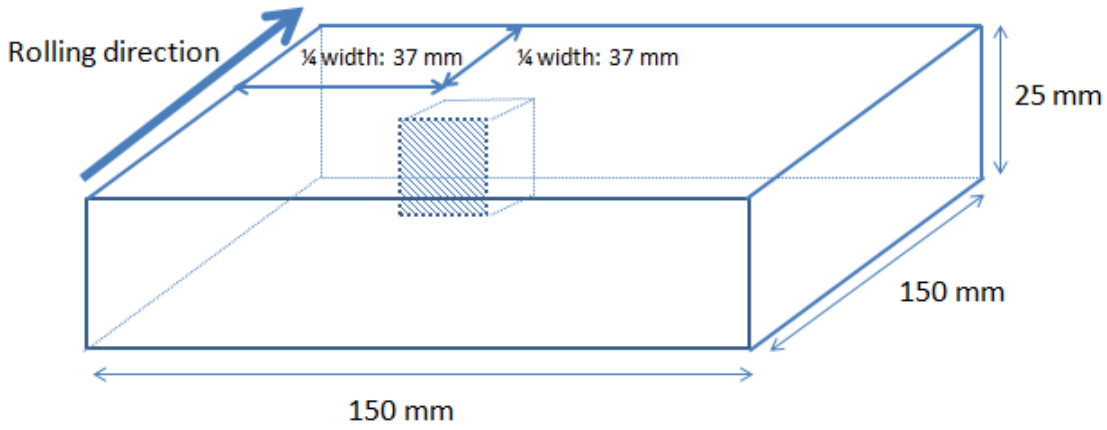

Figure 3-2 Schematic diagram showing the samples were taken from quarter position of as-rolled Nb-containing steel plate.

3.2 Modelling prediction

3.2.1 Thermo-Calc

The chemical composition of the Al-Nb steel (Table 3-1) was taken as the input into Thermo-Calc 4.0 with TCFE-7 database to simulate the solidification sequences during cooling. It was assumed that specimens after the homogenisation treatment (1300 ºC for 24 hours for Al-Nb steel, as discussed in section 3.3.1) had a uniform chemical composition which was also used as the input to predict the dissolution temperatures and volume fractions of precipitates for homogenised Al-Nb steel. The specific phases (liquid, bcc iron, fcc iron, and precipitates (such as AlN) were selected to simulate the phase transformation in temperature intervals of 10 ºC from 1600 ºC to 850 ºC during cooling process.

3.2.2 DICTRA

DICTRA version 27 with MOBFE-2 mobility database and TCFE-7 thermodynamic database was used to simulate the microsegregation levels. The SYS mode was used with a simplified composition of Fe-C-Mn-Nb-Al to save computation time due to the computational limits (computer memory and calculation stability) for DICTRA. The alloying elements of C, Mn, Nb and Al were taken into consideration to predict the segregation behaviour in the as-cast Al-Nb steel and rolled Nb-containing steel, due to insignificant effect of other elements for this simulation because of their low contents (such as Ti-0.001 wt%), or absence of precipitate forming behaviour above A_3 temperature (such as VC). During the casting process, the involved phases of liquid, δ-ferrite (bcc_a2) and γ-austenite (fcc_a1), α-ferrite (bcc_a2) and cementite were included in the simulation with thermodynamic stability (defined by Thermo-Calc)

used to define the appearance and disappearance of any phases. The cooling rate was determined by equation 2-1 for low carbon steel (as both steels had < 0.15 wt% C present) with measured SDAS values (as discussed in section 2.1.3). 1-D linear modelling was carried out to determine the segregation profile over half the SDAS, i.e. from dendrite centre to interdendrite centre. One cell was determined as a closed system with mass conservation, which contained regions of liquid phase, δ-ferrite and γ-austenite according to the solidification sequence of low carbon steel (C: 0.1 wt%). A grid spacing of 1μm was chosen to simulate solidification and the simulation started from 1873K (1600 ºC), when the alloy would be 100% liquid ('active' phase in DICTRA) and homogeneous composition is assumed. The solid phases appeared as noted above (Figure 3-3), and any interfaces were assumed to be at equilibrium. A maximum time step of 10s was chosen to carry out the simulation to ensure simulation stability, which started from liquid phase (1600 º C), to the α-ferrite phase (600 ºC).

The simulation output is the composition profile at a certain time, against to the distance from the dendrite centre to interdendritic centre. The simulated compositions in the dendritic centre and interdendritic centre from DICTRA were taken as the input into Thermo-Calc to predict the stability of precipitates in the solute-depleted region and solute-enriched region separately.

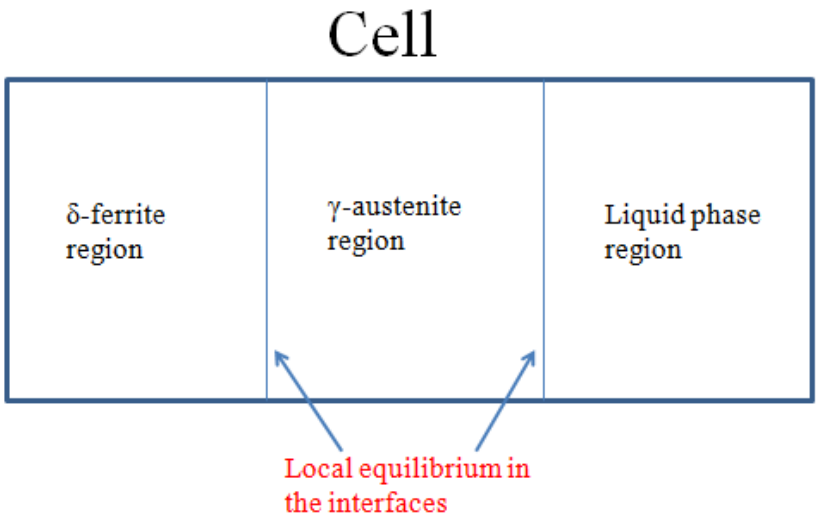

Figure 3-3 Schematic of the DICTRA cell shows the various regions of liquid, δ-ferrite and γ-austenite, with local equilibrium at the interfaces.

3.3 Heat treatment

Three different types of heat-treatments were performed on as-cast ingot Al-Nb samples and rolled-Nb steel: (a) homogenisation treatment to remove segregation and provide a uniform composition; (b) reheating treatment to establish the austenite grain growth behaviour with time and temperature; and (c) tempering treatments to reveal the prior austenite grain boundaries in the as-quenched martensitic microstructure more clearly.

3.3.1 Homogenisation heat treatment for as-cast Al-Nb steel

Specimens of as-cast Al-Nb steel (for homogenisation treatment mentioned early) were encapsulated in silica tubing with argon back-filling, then heated at 1300 ºC (complete dissolution of all precipitates predicted by Thermo-Calc) for 24 hours (calculated based on the diffusion of Nb across a half distance of SDAS of 75 µm according to previous

studies by Kundu [18], as discussed in section 2.2.1) afterwards slowly cooled at the rate of approximately 3.2 ºC/ min in a furnace.

3.3.2 Re-heating treatments

Reheating trials were carried out on homogenised Al-Nb samples at temperatures between 1075 ºC and 1200 ºC for 1 hour (Figure 3-4 shows the homogenisation and reheating treatment). The as-cast Al-Nb samples were reheated at 950 – 1300 ºC (Figure 3-5) for 1 hour followed by water quenching. The reheating temperatures were selected based on Thermo-Calc and DICTRA predictions, which will be discussed in chapter 4. The forged Al-Nb steel samples were reheated at the temperatures from 1160 ºC to 1300 ºC (Figure 3-6, as discussed in chapter 7) and rolled Nb-containing steel samples were reheated at the temperatures of 1090 ºC and 1200 ºC (Figure 3-7), as will be discussed in chapter 7. The temperatures during reheating treatment were monitored by the K-type thermocouple which is inserted into the sample. The reheating treatments with longer holding times (such as 2 hours and 3 hours) were carried out at selected soaking temperature, as seen in the Table 3-2 summarising the reheating treatments (e.g. temperatures and times) for the investigated steels under different conditions. In order to investigate if any non-uniform austenite grain growth occurred at initial reheating condition, the starting austenite grain size for each condition was characterised by using the reheating treatment at 920 ºC (above A_{c3}) for a short holding time of 10 minutes.

3.3.3 Tempering heat treatment

Reheated and quenched samples were subsequently tempered at 550 ºC for 6 hours (except for homogenised samples), to reveal the prior-austenite grain boundaries when etching in hot saturated picric acid solution. The tempering treatment allows elements, such as phosphorus, to segregate to the prior-austenite boundaries, which are attacked by the picric acid etchant, thereby delineating the boundaries and revealing a distinct prior austenite microstructure.

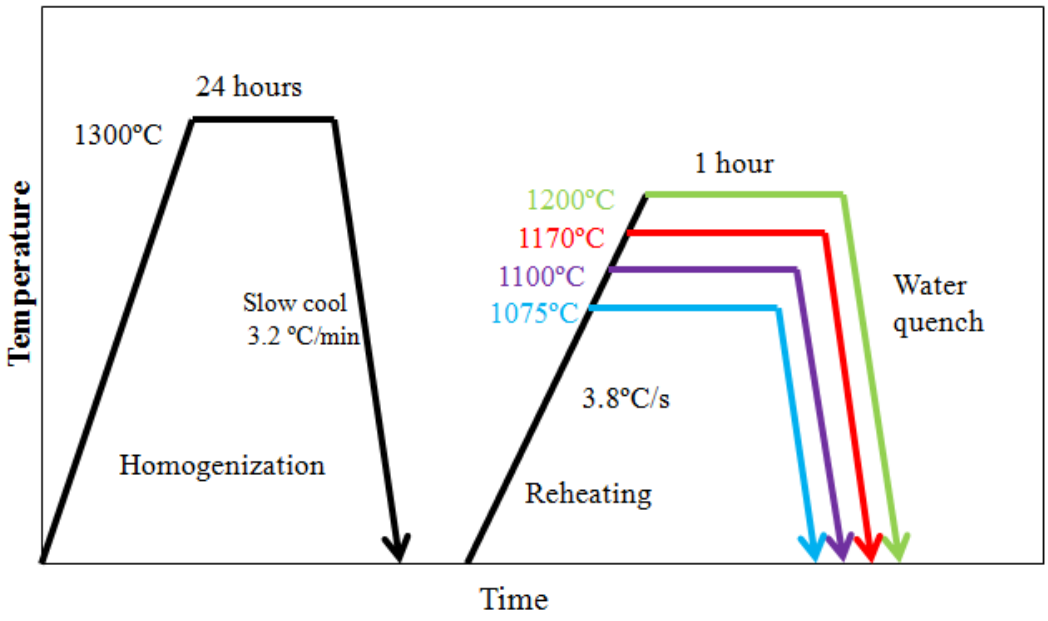

Figure 3-4 Schedule of homogenisation treatment and reheating treatment in the as-cast ingot Al-Nb steel (samples were taken from quarter thickness location).

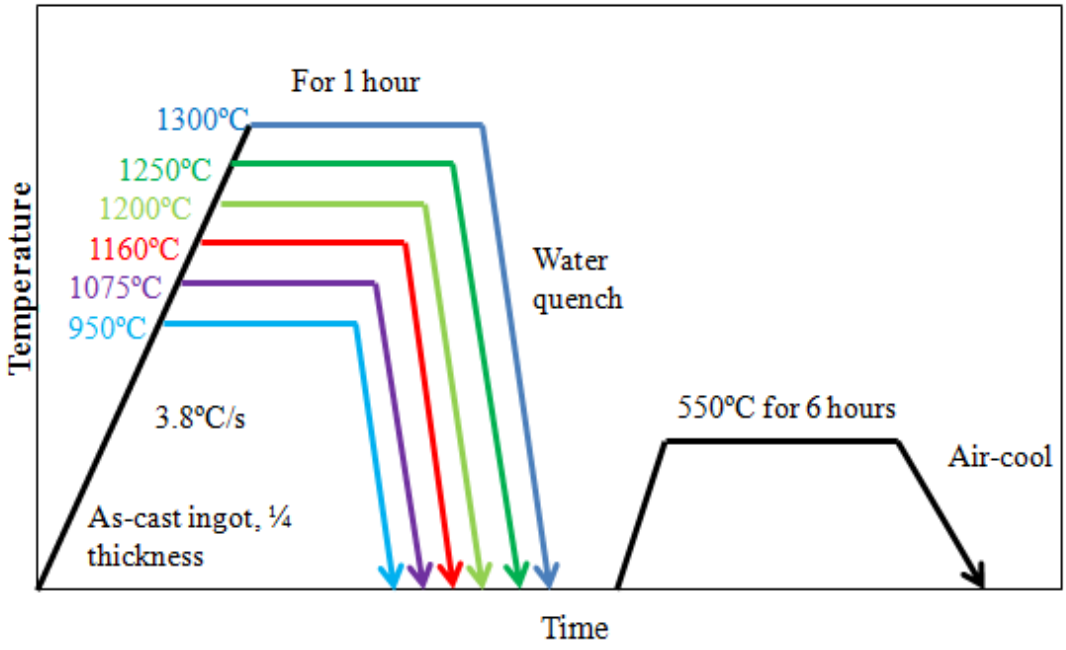

Figure 3-5 Reheating schedule of as-cast Al-Nb ingot samples (taken from 1/4 thickness location).

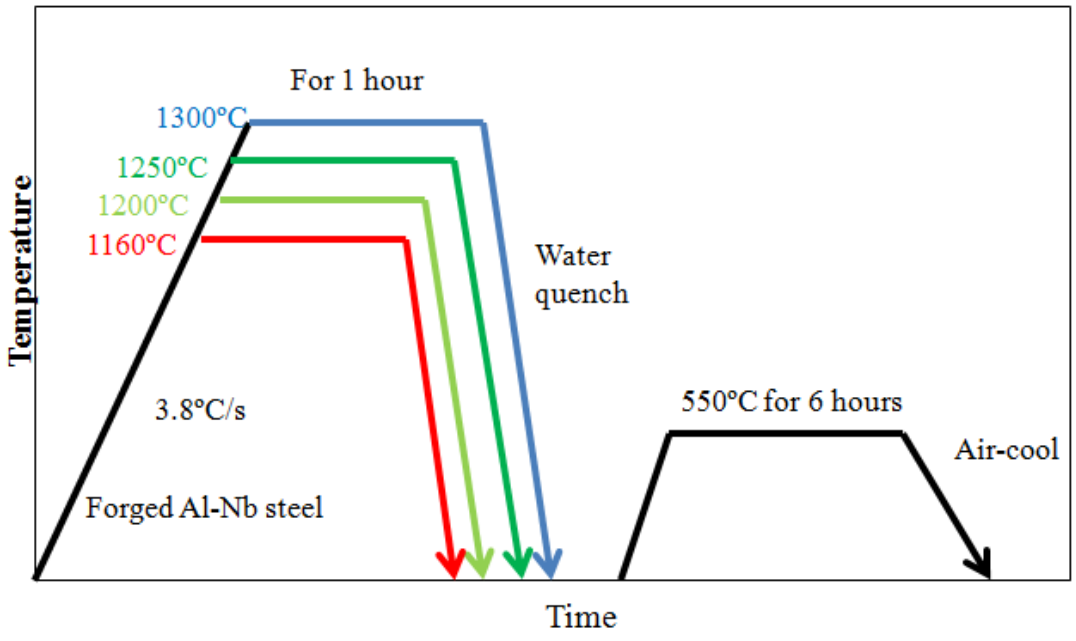

Figure 3-6 Reheating treatments for the forged Al-Nb steel.

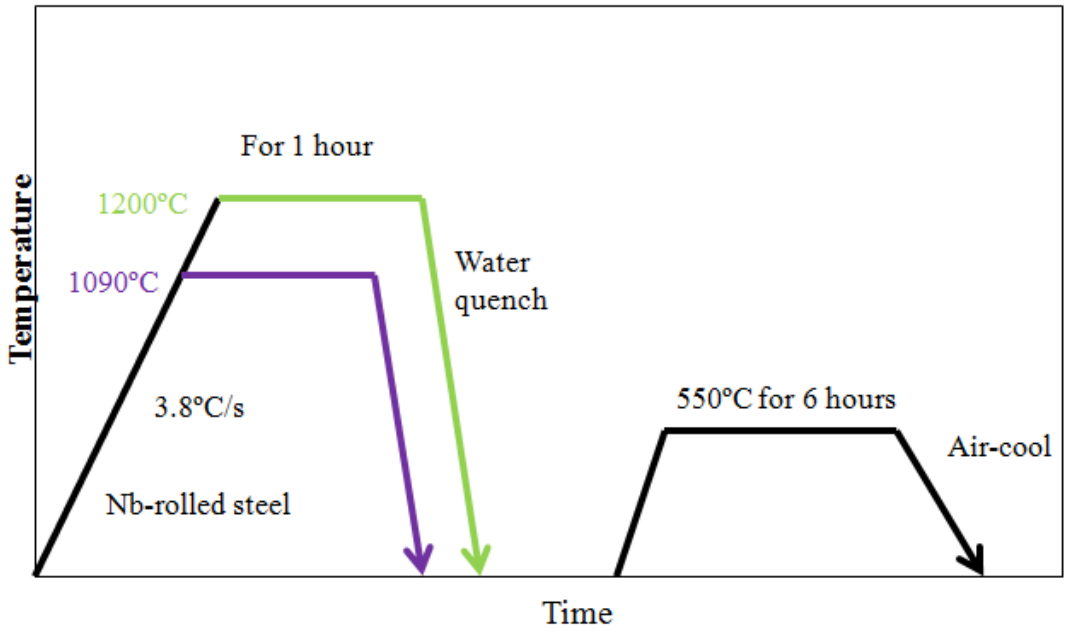

Figure 3-7 Reheating schedule of rolled Nb-containing steel.

Table 3-2 Reheating treatments (temperatures and times) for different steels.

Steels	1 hour	2 hours	3 hours
Homogenised Al-Nb	1075, 1100,1130, 1150,1170, 1200	1170	1170
As-cast Al-Nb	950, 1050, 1075, 1100,1130, 1150, 1160, 1185, 1200, 1230, 1250, 1280,1300	1160, 1200	1160,1200
Forged Al-Nb	1160, 1200, 1250, 1300	-	1160, 1200
Rolled Nb-containing	1090, 1200	1090	1090

3.4 Microstructure characterisation

3.4.1 Sample preparation

The heat treated samples were sectioned along the primary dendrite growth direction for the as-cast steel, the forging direction for the forged Al-Nb steel and the rolling direction for the as-rolled Nb-containing steel. The mounted samples (in Bakelite)

were ground and polished to a 1 µm MD-Nap diamond finish. To reveal the ferrite and pearlite microstructure, the polished samples were etched in 2%-nital (2 ml HNO_3 in 98 ml ethanol). The quenched and tempered specimens were also etched in hot (60 ºC) saturated aqueous picric acid (20g picric acid, 1000 ml H_2O, 14 drops HCl and 5 ml TEEPOL) with magnetic stirring, to reveal the prior austenite grain structure. If required, further light polishing (1 µm finish) was carried out to improve the clarity of the boundaries in contrast to the matrix. Thermal-etching (polished sample was encapsulated in silica glass) and oxidation-etching (polished sample) methods were also carried out at a temperature of 950 ºC for 10-15 minutes to reveal prior austenite grain boundaries, but the size determined was inaccurate (a lot of ghost boundaries were present) for those reheated samples.

3.4.2 Optical microscopy and image analysis

The as-cast, homogenised and heat treated samples were characterised in the Zeiss Akioskop-2 optical microscope equipped with AxioVison image capture software to provide images of microstructure consisting of ferrite and pearlite, secondary dendrite arm spacing (SDAS) and martensitic structures.

ImageJ software (Windows version) was used to measure and analyse the proportion of ferrite, in the ferrite + pearlite microstructure, and the prior-austenite grain size (measured manually) in the martensitic structure, in terms of equivalent circle diameter (ECD) method [24], the equation as shown below:

$$ECD = 2\sqrt{\frac{\bar{A}}{\pi}} \qquad 3\text{-}1$$

Where, $\bar{A}$ is average area value of measured grain. About 1000-2000 grains were measured by ECD methods for each microstructure, the grain size distribution (area-fraction) was established following the approach of individual grain size classes[166], where normal grain growth is shown with a uniform distribution, abnormal grain growth with a large grain size range distribution, Figure 2-37(f), and/ or bimodal grain size distribution, Figure 2-39(b).

The SDAS was charactersied by more than 100 measurements of the centre to centre distance between two adjacent secondary interdendrite spacing, perpendicular to the arms. The area fraction of pearlite was also measured in the ferrite + pearlite microstructure.

3.4.3 Scanning Electron Microscopy

The precipitates were characterised in the as-cast, homogenised and re-heated samples using JEOL 7000 scanning electron microscope (SEM) operating at 20 kV with field emission gun (FEG). The chemical composition of particles was determined using JEOL 7000 SEM equipped with an Oxford INCA energy dispersive X-ray spectroscopy (EDS) system, conducted at 10 mm working distance with 20 kV operating voltage. INCA software was used to provide the elemental concentration by point analysis. To achieve an accurate elemental analysis of particles, a comparison EDS spectrum was also obtained on the adjacent matrix. EDS mapping was also used. The area fraction and number density of Nb-rich and Al-rich precipitates were measured for around 20 continuous fields of view, each field of view covered around 430 μm^2 area. Moreover, secondary-electron (SE) for morphology analysis; and back-scattered electron (BSE) for compositional contrast (due to different atomic numbers),

were used to identify the particles of Al-rich (generally dark) and Nb-rich (normally bright).

chapter 4 Initial microstructure and modelling prediction for the as-cast and homogenised Al-Nb steel

Characterisation of the initial condition of the as-cast ingot of the Al-Nb steel, such as the microstructure, micro-segregation, and precipitate distribution is required for design of the experimental reheat treatment schedules. The microstructure of the homogenised specimens was also characterised to verify the grain structure and precipitates distribution, after removal of segregation, before the reheat treatments.

4.1 Microstructure for as-cast Al-Nb material

The initial microstructure of as-cast steel is shown in Figure 4-1, which consists of dark pearlite and bright ferrite where pearlite forms in the interdendritic regions allowing the original as-cast dendritic morphology to be revealed; this agrees with the literature reports in Figure 2-5. Some idiomorphic α-ferrite phases particles have been found in the pearlite region, which is consistent with literature reports discussed in section 2.3.3 [38]. The measured area fraction of pearlite for Al-Nb steel is around 18±0.5%, which is close to the results of Slab-1 steel (19 ± 0.06% pearlite area fraction with 0.1 wt% C, 1.42 wt% Mn, 0.045 wt% Nb and 0.046 wt% Al, Table 2-1) [18] and the Slab-2 steel (18.14 ± 0.5% of pearlite area fraction with 0.1 wt% C, 1.41 wt% Mn, 0.027 wt% Nb and 0.029 wt% Al, Table 2-1) [38], Table 2-8.

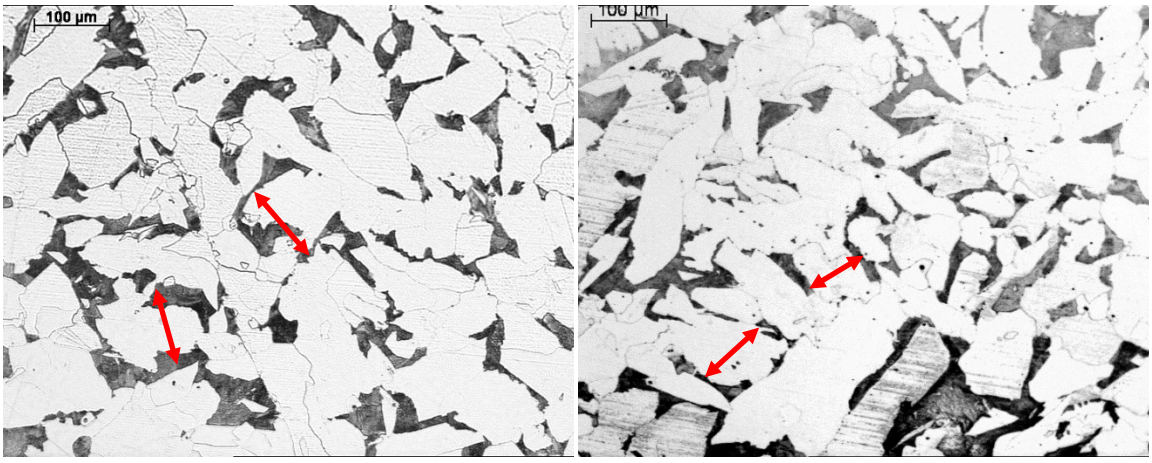

(a) (b)

Figure 4-1 Initial microstructure (a) and (b) of as-cast Al-Nb ingot at the 1/4 position, consisting of bright ferrite and dark pearlite, with SDAS arrowed in the red line.

4.1.1 Microsegregation characterisation in Secondary Dendrite Arm Spacing (SDAS)

The average secondary dendrite arm spacing, which corresponds to the mean interdendritic pearlite spacing, was measured at 150 ± 50 µm for the 1/4 thickness position of the as-cast Al-Nb ingot, and the solidification rate estimated for this SDAS of as-cast Al-Nb steel was 0.4 ºC/s according to equation 2-1, which was used in the modelling prediction by DICTRA.

To obtain a general trend of dendritic segregation for Mn contents, the measurements from line-scans were analysed for the as-cast specimens (in 2D section) across several dendritic (ferrite) and interdendritic (pearlite) regions. An example is shown in Figure 4-2 (a), EDS analysis was carried out across pearlite and ferrite regions (as indicated by red line).

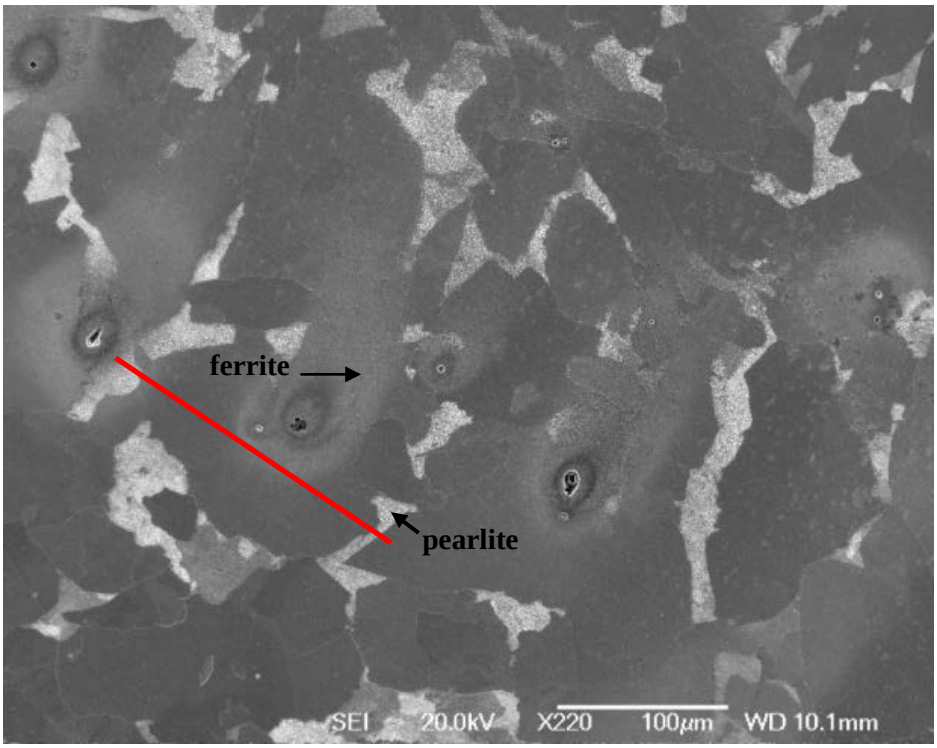

(a)

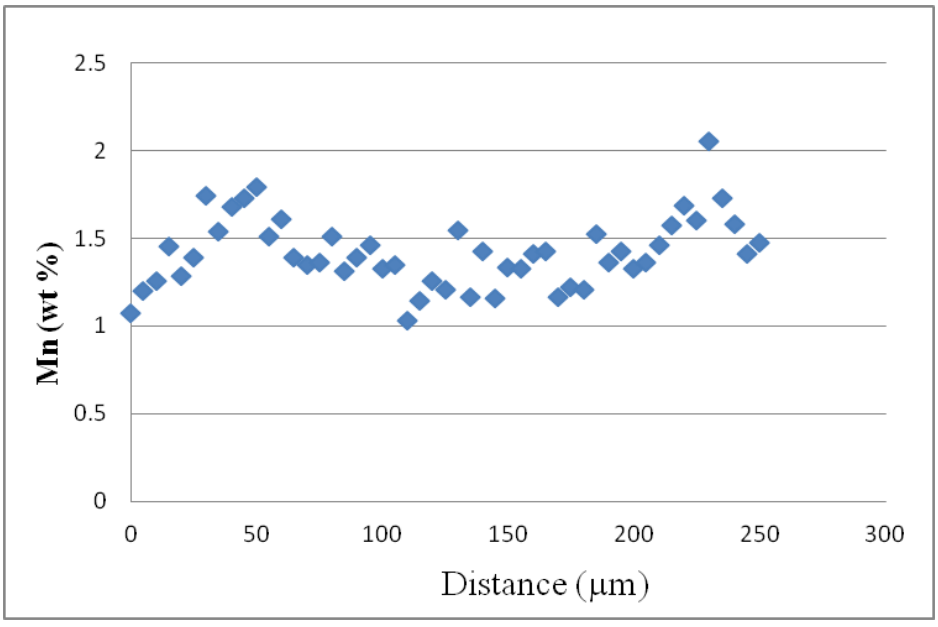

(b)

Figure 4-2 (a) SEM image showing EDS scan line measurement of Mn content across dendrites (dark) and interdendritic regions (grey); (b) Mn content along the selected line.

Figure 4-2(b) shows the variation in [Mn] determined by EDS along the selected line in Figure 4-2(a), which indicates an increase of Mn content on the crossing from

dendritic ferrite (around 1.3-1.4 wt%) to the interdendritic pearlite (around 1.7-1.9 wt%). The two peaks of Mn content correspond to the interdendritic pearlite with enriched solute content which confirms the interdendritic segregation. However, the centre regions of the dendritic and interdendritic structure might not be fully characterised from the line-scans in 2D section, as the EDS analysis samples a volume approximately 1 μm in diameter below the surface. It cannot be ensured that the depth of the EDS can go through the centre regions of dendrite and interdendritic in a 3D structure. The line-scans can be used to describe the general segregation trend, but it is not possible to obtain a quantitative segregation profile just by the line scan due to the significant scatter in the results. The cumulative profile based on ranking data from EDS grid-mapping was used to describe the segregation level in 3D structure, as discussed in section 2.2.2

EDS grid-mapping was applied by EDS analysis of around 300 points in total, arranged in a square pattern with a spacing greater than half the SDAS value (75 μm), as shown in Figure 4-3(a). The EDS detected values were calibrated with a systematic error of around +8%, due to the contamination of the detector which results in the inaccuracy of the EDS data [37]. The results demonstrate that the general Mn content in the pearlite regions (indicated by the black arrows with the Mn content around 1.6-1.8 wt%) is larger than that in the ferrite region (indicated by the green arrow with approximate 1-1.4 wt% of Mn). The concentration profile was generated by reordering cumulative results against the half secondary dendrite arm spacing of 75 μm (approximately 300 ranking grid results correspond to the length scale from 0 μm (assumed to be dendrite centre) to 75 μm (assumed to be interdendritic centre) at a

spacing of 0.25μm, then they were finally plotted as 1μm interval, as shown in Figure 4-3(b)). It indicates that the minimum Mn content is around 1 wt% and the maximum value is approximately 1.7 wt%. These values can be used to compare the modelling prediction by Thermo-Calc and DICTRA, as will be fully discussed in section 4.3.2.2.

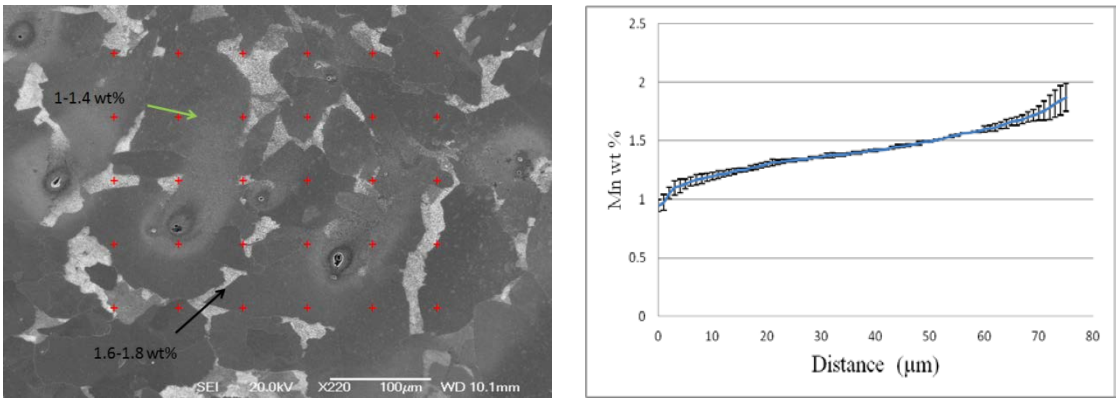

(a) (b)

Figure 4-3 (a) Grid analysis points located over both dendritic (dark region) and interdendritic (grey region) areas in as-cast microstructure; (b) Mn content against the distance of half SDAS.

4.1.2 Initial grain size distribution and precipitate characterisation

The initial ferrite grain size distribution was determined by measuring 1000 ferrite grains, and plotting them as grain size classes, as indicated in Figure 4-4, which shows a uniform distribution of ferrite grains with a mode grain size (peak grain size of distribution) about 90 μm. Non-uniform ferrite grain growth (abnormal large ferrite grains and the bimodal ferrite grain distribution) was not observed in the initial microstructure.

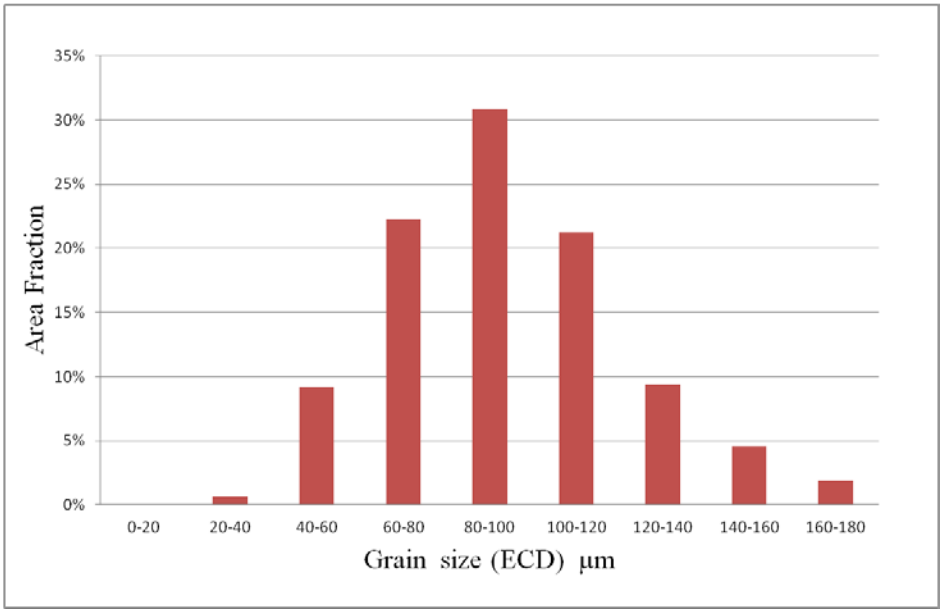

Figure 4-4 Initial α-ferrite grain size distribution for the as-cast microstructure.

Precipitates were characterised using SEM analysis, to determine the size and number density of Al-rich particles and Nb-rich particles within the dendritic and interdendritic regions. SE (secondary-electron) and BSE (back-scattered electron) imaging were both used to characterise the precipitates in terms of morphology analysis and compositional contrast.

Al-rich particles, expected to be AlN, with irregular shape (or facet and rounded shape, as discussed in section 2.3.2) have been mainly observed in the dendritic ferrite regions, shown in Figure 4-5(a). The BSE image in Figure 4-5 (b) is consistent with this being an Al-rich particle as it has darker contrast than the matrix. Regions with a lower average atomic weight compared to the matrix, such as Al-rich particles, are known to appear darker under BSE imaging [18]. An EDS trace analysis shows the Al peak in Figure 4-5(c), confirming that the precipitate is based on Al compared to in the matrix (Figure 4-5 (d)).

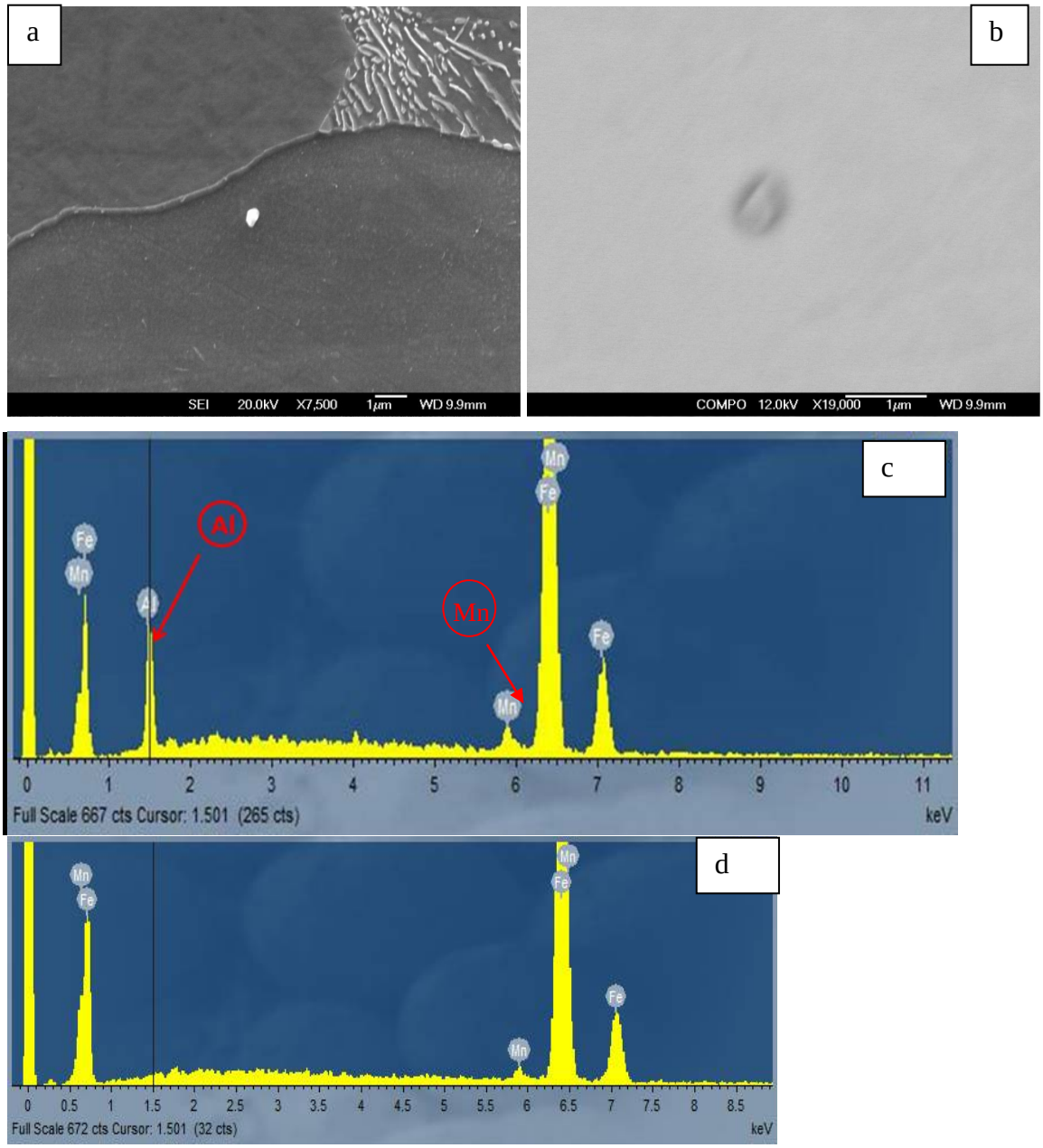

Figure 4-5 Al-rich particle was shown in (a) SE image; (b) BSE image; EDS trace indicating the (c) Al peak and (d) in the matrix.

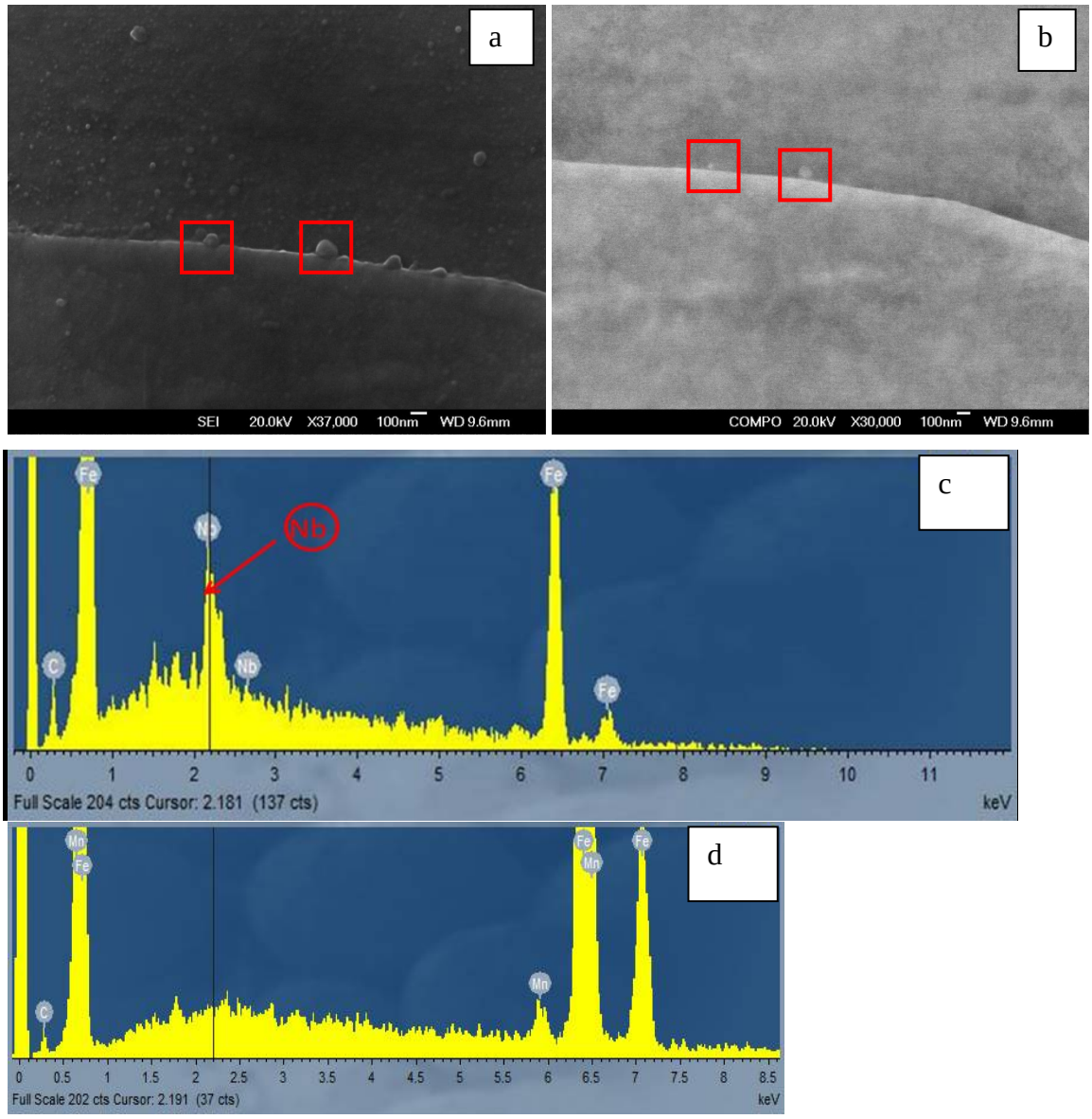

Figure 4-6 Nb-rich particle, expected to be Nb(C,N) indicated with red rectangle frame, shown in (a) SE image; (b) BSE image; EDS trace indicating the (c) Nb peak and (d) in the matrix.

Figure 4-6(a) shows spherical Nb-rich particles, probably Nb(C,N), decorating a boundary of ferrite in the as-cast structure. The brighter appearance of the particles in the BSE image, Figure 4-6(b), is consistent with the heavier atom of Nb than Fe, which has been verified by the EDS spectrum shown in Figure 4-6(c), indicating an Nb peak.

Particles in solute-depleted region were characterised in the ferrite phase, and precipitates in the interdendritic particles were investigated in the pearlite phase. However, some of the particles in the pearlite phase were difficult to identify due to the visual impact caused by the pearlite structures. Hence, some idiomorphic ferrite islands (surrounded by pearlite as discussed in section 2.3.3) in the pearlite region, shown in Figure 4-7 (a), were investigated to characterise the particles distribution for the solute-enriched region, as was reported by Zheng [38]. Figure 4-7(b) shows a cluster of Nb-rich particles appearing inside the idiomorphic ferrite island, which was confirmed by EDS analysis in Figure 4-7(c), indicated by the Nb peak in the spectrum.

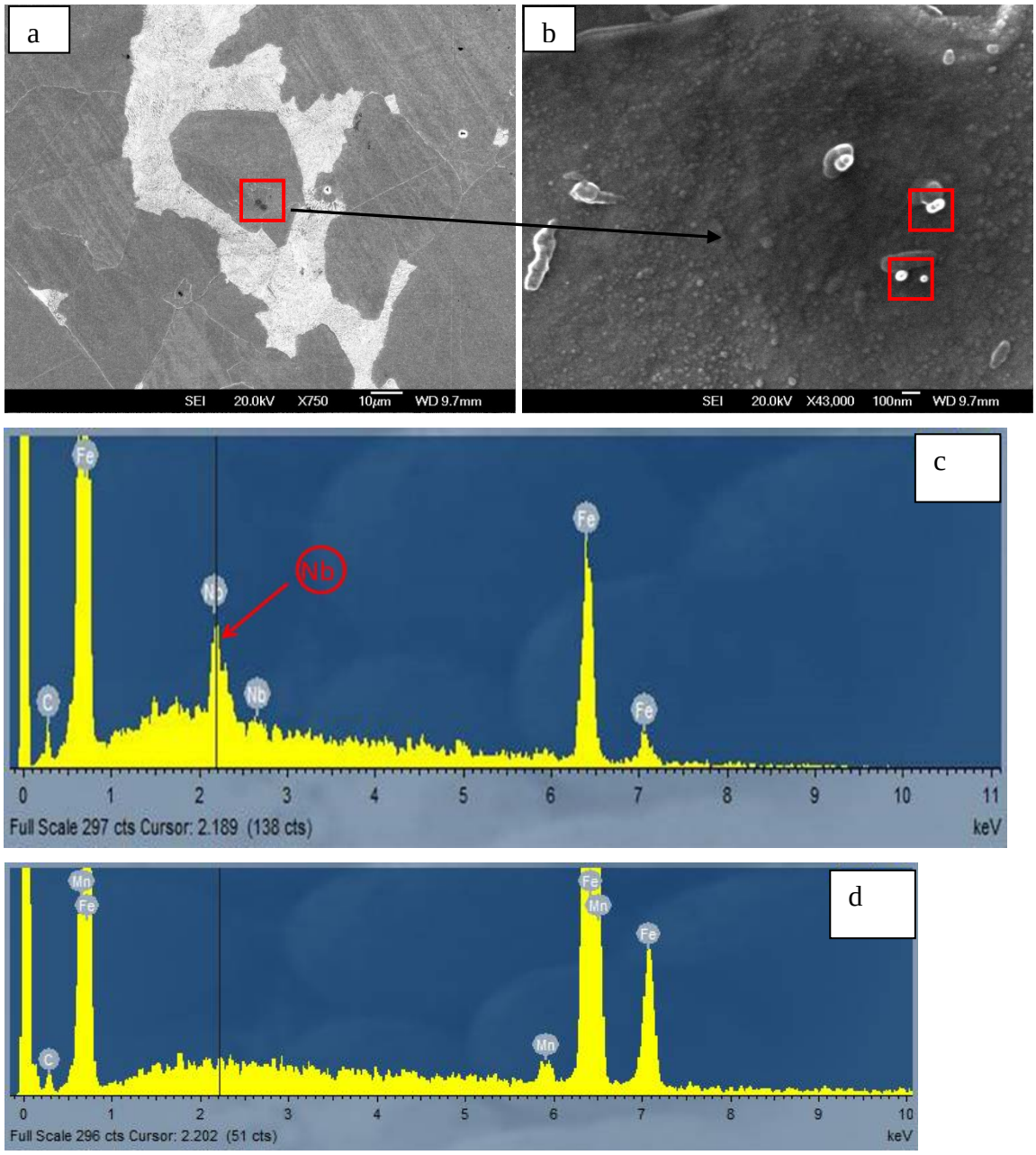

Figure 4-7 (a) Isolated ferrite located in a pearlite region; (b) Nb-rich particles distributed within this region; EDS trace indicating the (c) Nb peak and (d) in the matrix.

Due to the limited segregation tendency of Al compared to Nb (as discussed in section 2.2.1), the Al-rich particles are expected to be randomly distributed throughout the matrix, whereas a slightly larger number of precipitates are presented in dendritic ferrite (Al slightly enriched in the solid phase during solidification according to

Thermo-Calc prediction reported by Chakrabarti, Figure 2-22 [25]). The stronger segregation of Nb in the interdendritic region has resulted in a larger number of Nb-rich precipitates in the solute-enriched pearlite region. Kundu [18] has reported the distribution of investigated precipitates (AlN and Nb(C,N)) which was obtained by quantitative measurements for the same as-cast Al-Nb steel, as shown in Figure 4-8. The area fraction measurement of precipitates is assumed to be equal to the volume fraction of phase. The particles spatial distribution agrees with the general segregation behaviour of Al and Nb reported previously [18, 25, 38] , indicating a lower volume fraction and number density of Nb-rich precipitates in the dendritic solute-depleted region, compared to Al-rich particles in the same region, Table 4-1. The dendritic AlN particles supply additional pinning force in the absence of Nb(C,N) particles or on their dissolution in the dendritic region, therefore potentially combating the development of the bimodal grain growth structures seen due to Nb segregation [22, 23, 25, 26]. The particle size ranges of Nb(C, N) and AlN do not show a significant difference separately in the dendritic solute-depleted region (Nb(C,N): 100-150 nm; AlN: 150-200 nm) and interdendritic solute-enriched region (Nb(C,N): 100-150 nm; AlN: 150-200 nm) in terms of the mode size, Table 4-1.

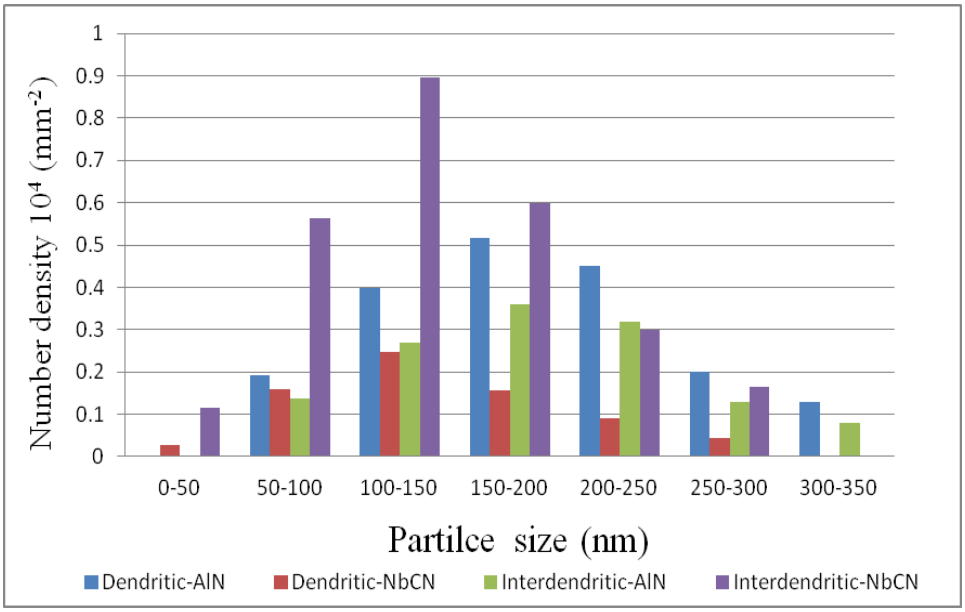

(a)

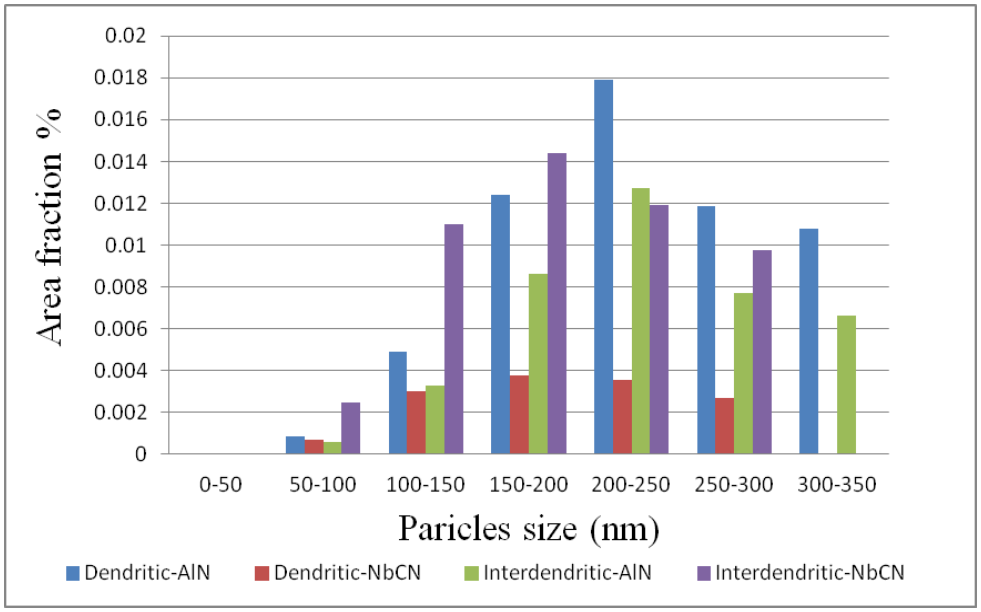

(b)

Figure 4-8 Distribution of precipitates size with (a) number density and (b) area fraction, in the dendritic and interdendritic region reported by Kundu [18].

Table 4-1 Precipitate characteristics (mode size based on the number density distribution (Figure 4-8(a)), number density and volume fraction in total) of AlN and Nb(C, N) in the regions of dendritic region and interdendritic region.

	Dendritic-AlN	Dendritic-NbCN	Interdendritic-AlN	Interdendritic-NbCN
Average (mode size) precipitate size, nm	150-200	100-150	150-200	100-150
Precipitate number density, $\times 10^4$ /mm^2	1.89	0.73	1.29	2.64
Volume fraction (area fraction), %	0.059	0.014	0.04	0.05

4.2 Microstructure for homogenised Al-Nb steel

To investigate abnormal large grain growth in the Al-Nb steel, the specimens with a uniform composition were required, which were provided by homogenisation treatment at 1300 ºC for 24 hours.

4.2.1 Microstructure characterisation for homogenised specimens

The microstructure of the homogenised specimen is present in Figure 4-9, consisting of randomly distributed α-ferrite and pearlite. The dendritic structures, observed in the as-cast ingot microstructure (as seen in Figure 4-1), were removed by the homogenisation treatment, thereby providing the microstructure without solute-enriched and solute-depleted region. EDS-line scans for Mn were used to verify the segregation-free nature of the matrix, Figure 4-10 (a). The Mn level, determined by EDS along the line shown, is given in Figure 4-10 (b), with scatter being seen around the average concentration of 1.4 wt% (indicated as red dotted line), although some higher contents (of around 1.5-1.65 wt%) have been observed at pearlite. This may arise during diffusional formation of ferrite and pearlite forms when Mn (an austenite stabiliser) is rejected into the

remaining austenite during transformation [37]. The removal of segregation has, however, resulted in re-distribution of pearlite to a non-interdendritic arrangement. The pearlite fraction in homogenised condition has been reduced to be approximately 10 ± 0.6%, which is less than that in the as-cast condition, as shown in Figure 4-1. Generally, the relatively uniform content of Mn can be expected after homogenised treatment at 1300 ºC for 24 hours. Whilst the results of EDS line scan for microalloying elements (e.g Nb, Al, V) were not available because of the low content of alloying element (< 0.05 wt %) present in the matrix. However, the distribution of Nb after the homogenisation treatment was presumably uniform, as the homogenisation treatment of 1300 ºC for 24 hours was designed based on the calculated diffusion behaviour of Nb across a distance of 75 μm (half distance of SDAS), as discussed in section 2.2.1 and section 3.3.1.

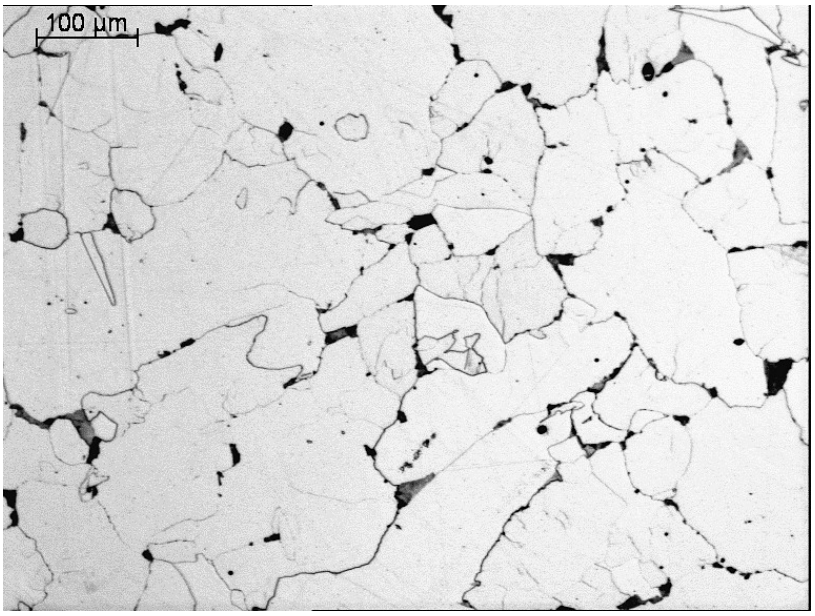

Figure 4-9 Initial microstructure of the homogenised Al-Nb steel.

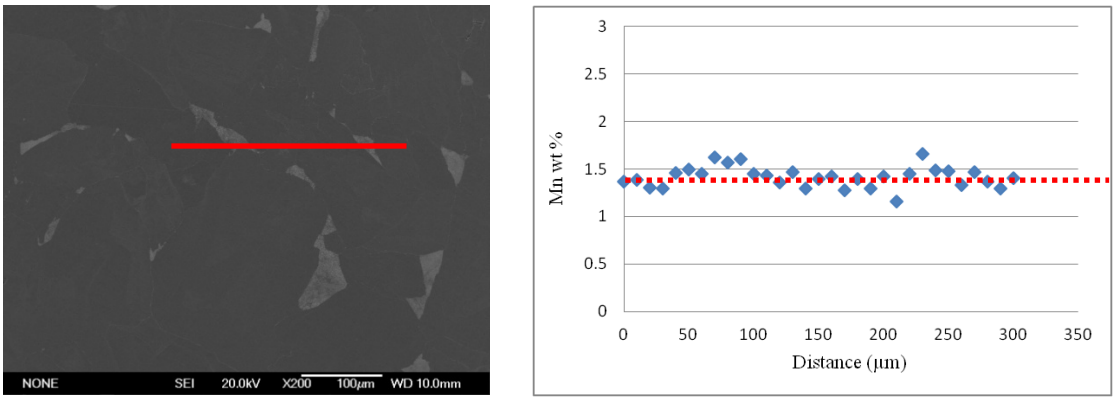

(a) (b)

Figure 4-10 (a) Line-scan EDS analysis in the homogenised sample along the selected line (red line); (b) contents of Mn against distance (average Mn content is indicated as red dotted line).

The ferrite grain size distribution for the homogenised specimens is shown in Figure 4-11, from measurement of around 1000 ferrite grains. The mode grain size is around 90 μm, similar to that of the as-cast material, but the grain size distribution is slightly more skewed to larger sizes, with the maximum size observed being 200-220 μm whilst in the as-cast material this was 160-180 μm.

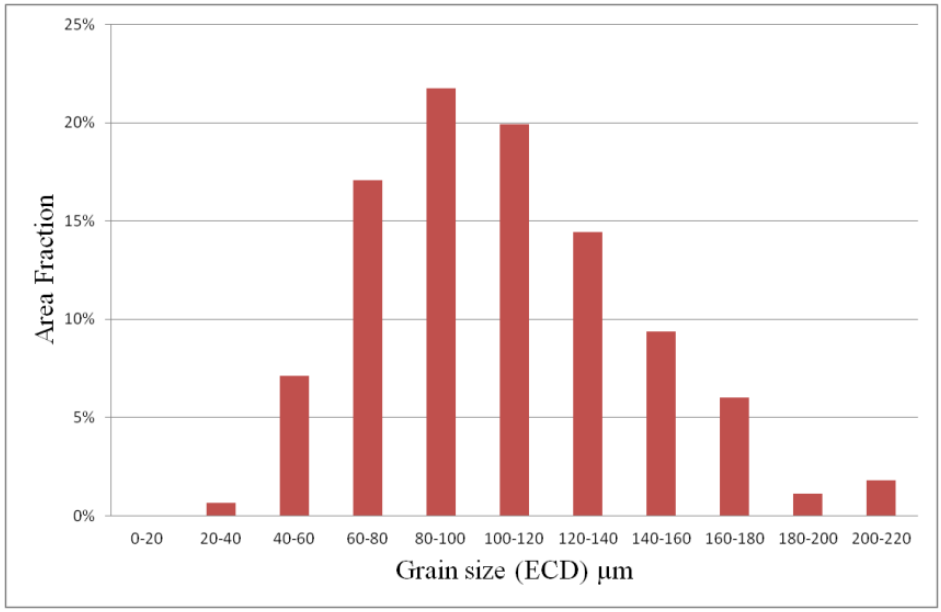

Figure 4-11 Initial ferrite grain size distribution in the homogenised Al-Nb steel.

4.2.2 Precipitates in homogenised condition

Particle characterisation in the homogenised sample was carried out using SEM, with SE imaging (Figure 4-12(a)), and BSE imaging was used to analyse the particles type since the Al-rich particles appear dark and Nb-rich particles appear bright, as indicated in Figure 4-12(b). Further confirmation of particles types was carried out by EDS analysis of selected particles showing the peaks of Al and Nb, as seen in Figure 4-12 (c) and (d) separately.

From analysis of the SEM images, the particles of Nb(C,N) and AlN formed above A_3 temperature are expected to be distributed uniformly in the homogenised sample, as they are mostly formed and developed before the redistribution of solute during transformation from austenite to ferrite. Figure 4-13 (a) shows that a larger number of Nb-rich particle in the size range of 150-200 nm is present than that of Al-rich particles. Whereas, a larger area fraction of Al-rich particle in size range 200-300 nm has been observed in Figure 4-13 (b) due to the observation of larger number of coarser particles (200-300 nm) compared to Nb-rich precipitates. In Table 4-2, there is no significant difference between AlN and Nb(C,N) particles in terms of size, number density and volume fraction. However, it indicates that a lower volume fraction of particle has been achieved in the homogenised sample than in the as-cast sample (Table 4-1), which may be due to a uniform distribution of microalloying elements (meaning less supersaturation is expected at a high temperature) resulting in well-redistributed particles (with a low number density per unit area) formed at a lower temperature (will be discussed in section 4.3), which is consistent with the literature reports discussed in section 2.3.3.

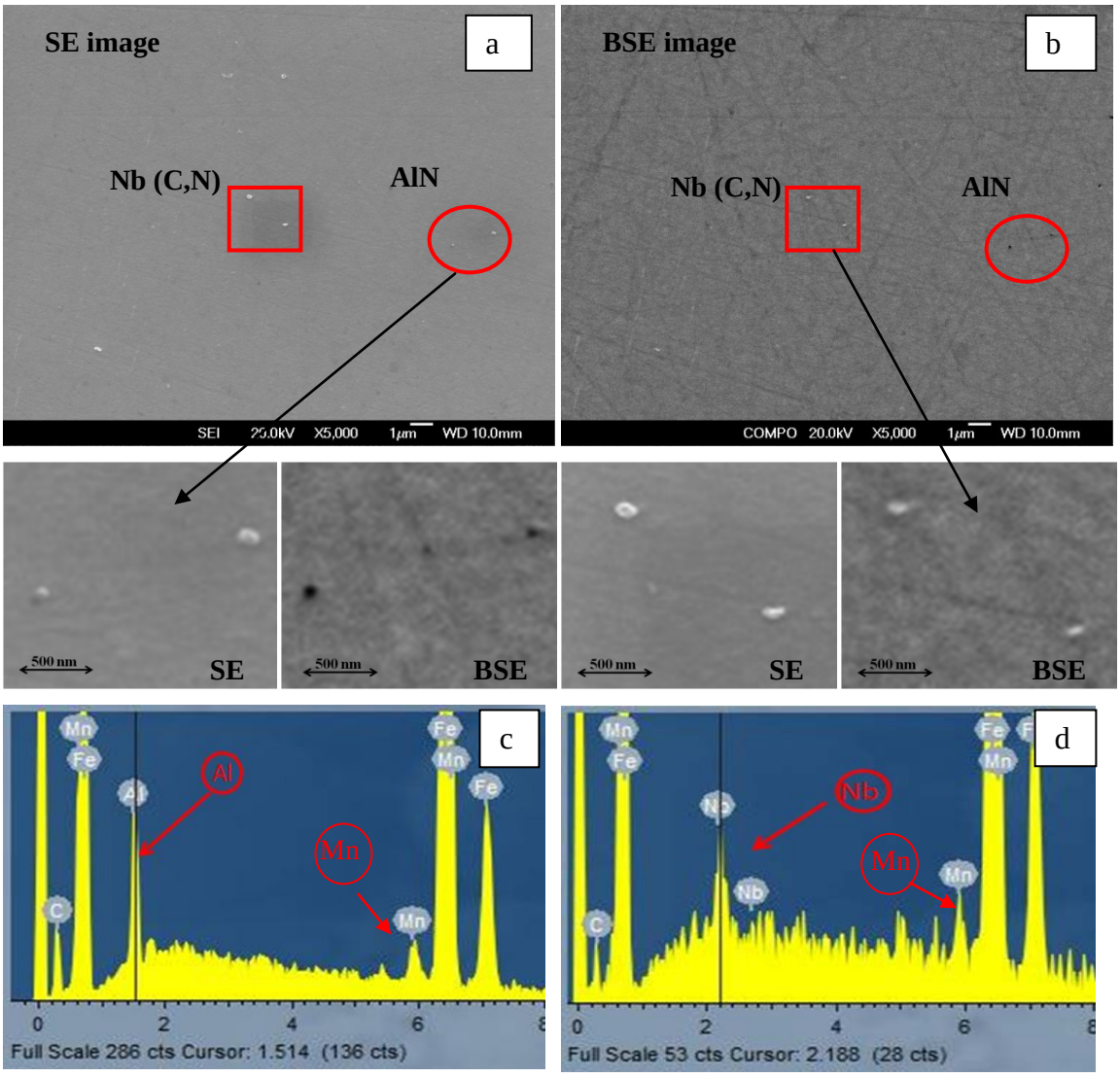

Figure 4-12 (a) Morphology analysis under SE image; (b) BSE image shows the Al-rich particles (indicated in red circle) and Nb-rich particles (indicated in red rectangle); (c) and (d) EDS trace indicating the Al and Nb peak in the spectrum taken from the investigated particles separately.

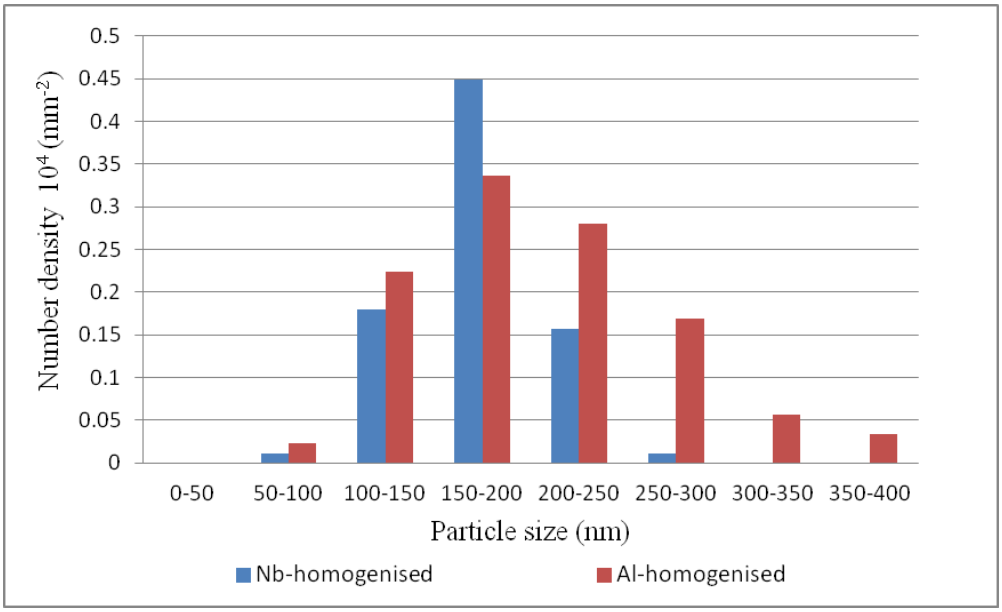

(a)

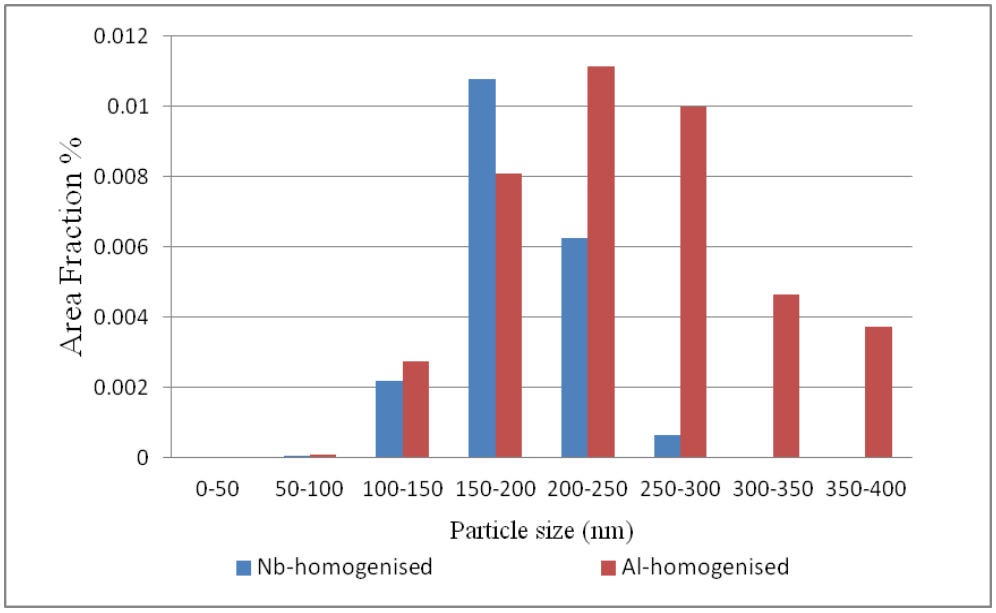

(b)

Figure 4-13 Particle size distribution with (a) number density and (b) area fraction, for Al-rich and Nb-rich particles in the homogenised condition.

Table 4-2 Precipitation behaviours of AlN and Nb(C,N) in homogenised Al-Nb steel.

	AlN	Nb(C,N)
Average (mode size) precipitate size, nm	150-200	150-200
Precipitate number density, $\times 10^4$ /mm^2	1.12	0.81
Volume fraction (area fraction), %	0.04	0.02

4.3 Predicted composition distribution and precipitate stabilities for homogenised and segregated conditions

Thermo-Calc modelling was used to predict the equilibrium phase transformation temperatures, precipitate dissolution temperatures and volume fractions in the homogenised composition. DICTRA was used to predict the elemental profiles due to segregation, therefore, giving the composition distributions over the half secondary dendrite arm spacing distance (i.e. from solute-depleted region to solute-enriched region), which can be used to predict the particle dissolution temperatures and volume fractions at key locations (e.g. dendritic and interdendritic region) in the as-cast condition with heterogeneous composition.

4.3.1 Solidification sequence predicted by Thermo-Calc in Al-Nb steel

The solidification sequence during casting in Al-Nb steel was predicted by Thermo-Calc based on the as-received chemical composition. The diagram of phase transformation from 1600 ºC to 1400 ºC is shown in Figure 4-14, which indicates that the Al-Nb steel undergoes a peritectic reaction during solidification.

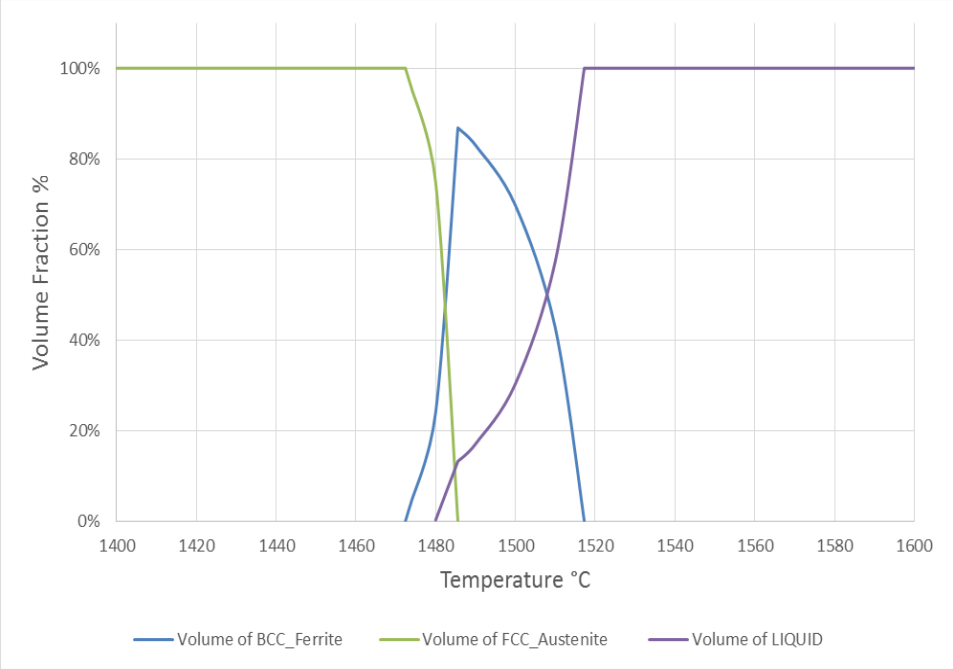

Figure 4-14 Phase transformation was predicted by Thermo-Calc during solidification for Al-Nb steel with as-received chemical composition.

The solidification sequence and temperatures (liquidus, peritectic and solidus) are shown in Figure 4-15; equilibrium solidification starts from 1517 ºC as δ-ferrite. The first solidified δ-ferrite develops as a solute-depleted dendrite region with alloying elements being partitioned into the liquid region. The peritectic reaction occurs at 1485 ºC, where γ-austenite first forms at the interface between the liquid and δ-ferrite solid.

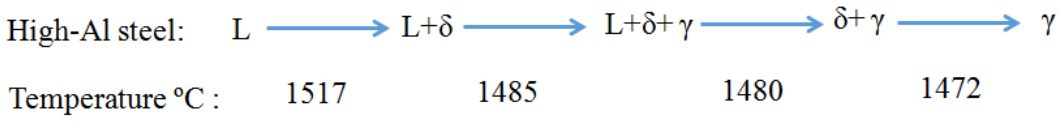

Figure 4-15 Solidification sequence for the high-Al steel (Al-Nb steel), with the temperatures predicted by Thermo-Calc with liquidus, peritectic, solidus temperatures

As assumed in section 2.2.4, the newly formed austenite can act as a barrier layer [37, 79] having a lower diffusivity of alloying elements than that in the δ-ferrite, Table 2-4,

which retains the segregation that has occurred down to the peritectic temperature. The partition coefficients (content in solid compared to liquid) of microalloying elements (e.g. Al and Nb) in the austenite are lower than those in ferrite (Table 2-3) resulting in a lower content of microalloying elements in the austenite layer than that in the pre-formed δ-ferrite, as shown in Figure 2-22 [25]. A larger partition coefficient has been observed for Mn in the austenite than in the ferrite phase, meaning that the austenite stabiliser element of Mn is expected to be enriched in the austenite layer through peritectic reaction, as seen in Figure 4-16. Austenite first forms when there is about 15% solute-enriched interdendritic liquid (Figure 4-14), which is close to the experimentally determined amount of pearlite present, i.e. an area fraction 18%, as shown in Table 4-3, and is consistent with the similar results reported in the literature, i.e. 12.5% for Thermo-Calc prediction to 19% of the pearlite in the cast Slab-1 (by Kundu, Table 2-1) [18], and 13% (Thermo-Calc prediction) to 18% (experimental) in Slab-2 (by Zheng, Table 2-1) [38], as seen in Table 2-8. There is around 3%-6.5% difference given, with more measured pearlite being observed than the predicted amount of solute-enriched area, which is probably due to the non-equilibrium cooling for the cast ingot during solid state [38]. The results suggest that the final pearlite originates from the same place as being associated with the interdendritic liquid from the peritectic reaction.

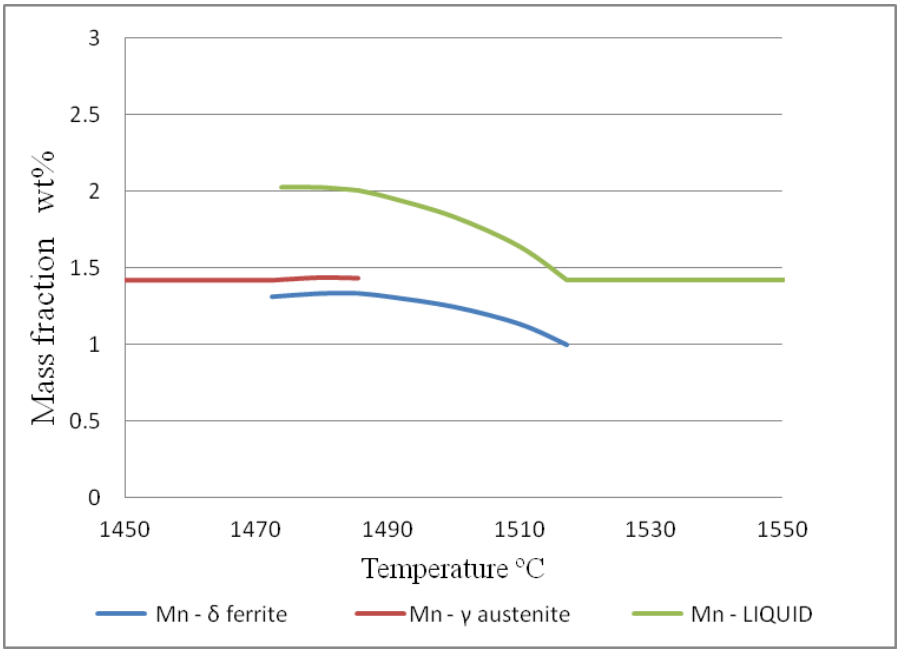

Figure 4-16 Mass fraction of Mn in liquid, δ-ferrite, and γ-austenite during solidification predicted by Thermo-Calc for Al-Nb steel with received chemical composition in Table 3-1.

Table 4-3 Fractions of solute-enriched (liquid region) and solute-depleted (solid region) predicted by Thermo-Calc at the peritectic temperature.

As-cast Al-Nb	Solute-enriched	Solute-depleted
Thermo-Calc	15%	85%
Experiment	18%	82%

4.3.2 Prediction of precipitates dissolution temperature

Due to the pinning force provided by microalloying precipitates, grain growth during reheating is strongly controlled by the stability of the particles, i.e. determined by precipitates dissolution temperature, which can be predicted by Thermo-Calc.

4.3.2.1 Homogenised condition

The chemical compositions were used in the Thermo-Calc software to calculate the precipitation behaviour. The investigated precipitates of AlN and Nb(C,N) are expected to be stable at temperatures as shown in Figure 4-17, i.e. AlN and Nb(C,N) precipitates form at around 1170 ºC and 1090 ºC respectively. During the cooling process, AlN forms and the volume fraction increases from 0.0005 vol. % at 1170 ºC to 0.035 vol. % at 1070 ºC, whilst the slope of curve is gradually changed to be flat from 1070 ºC to 850 ºC, as seen in Figure 4-17, probably due to the maximum amount of AlN having been reached with temperatures decrease. The volume fraction of Nb(C,N) increases to 0.023 wt% as temperature is reduced to 850 ºC, where the formation curve flattens and less further precipitation is predicted. During reheating, precipitate dissolution is expected to follow a similar route but in reverse such that the volume fractions of precipitates decrease gradually as the temperature increases, as shown in Figure 4-17, the amounts of AlN and Nb(C,N) are gradually reduced from 850 ºC to 1100 ºC. Once the temperature is higher than 1100 ºC, Nb(C,N) particles are fully dissolved, and only AlN particles remain in the solid, assuming equilibrium conditions are reached. However, the AlN particles undergo a dramatic drop in volume fraction when the temperature is close to the precipitate dissolution temperature, from 1100 ºC to 1170 ºC. This prediction indicates that abnormal grain growth might occur in this temperature range (1100 ºC - 1170 ºC) due to the local rapid dissolution of AlN during reheating treatment. Above 1170 ºC, due to dissolution of all the main precipitates, normal grain growth can be expected to happen again without further pinning effect.

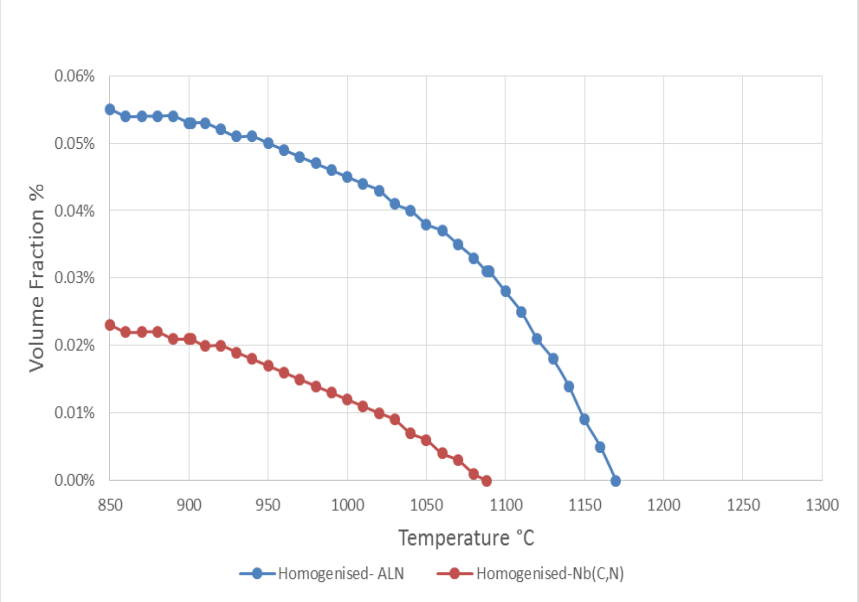

Figure 4-17 Volume fraction and stability of AlN and Nb(C, N) were predicted by Thermo-Calc, for the homogenised Al-Nb steel.

According to Figure 4-17, AlN particles are probably more significant in controlling grain growth in the homogenised condition compared to Nb(C, N), due to the larger volume fraction (0.055 %) of particles presented, combined with their similar size (150-200 nm) to the Nb(C,N) – determined experimentally, as seen in Table 4-2. AlN has a higher predicted thermodynamic stability (1170 ºC) than Nb(C, N) in homogenised condition, and may have a pinning effect in the absence of Nb(C,N) above 1100 ºC.

4.3.2.2 Segregated condition

The microalloying elements in the as-cast steel are expected to be distributed heterogeneously over the distance between solute-enriched (interdendritic) and solute-depleted (dendritic) regions. Therefore, a composition profile (composition as a

function of distance) is required to describe the elemental spatial distribution, which can be used to predict different precipitate dissolution temperatures in different regions.

As discussed previously in section 4.3.1, the amount of solute-enriched and solute-depleted regions can be predicted as being the interdendritic liquid and solid at the peritectic temperature. The contents of Mn in the dendritic solid (predicted 85% solid as seen in Table 4-3, presumably corresponding to the distance of 0 μm – 64 μm across half the SDAS) and interdendritic liquid regions (predicted 15% liquid presumably corresponding to 64 μm – 75 μm of the half SDAS) were predicted by Thermo-Calc at the peritectic temperature of 1485 ºC, and then compared to the experimental Mn concentration profile (Figure 4-3 (b)), as shown in Figure 4-18. It indicates that the simulated concentration of Mn has a poor agreement to the experimental composition profile, which means that Thermo-Calc at the peritectic temperature cannot predict a composition profile that is consistent with final measured experimental results.

DICTRA was used to predict the microsegregation development of Mn during phase transformation. The cooling process at quarter position was assumed to be divided into water cooling and air cooling stages. During water cooling process, the cooling rate was assumed to be same as the solidification rate of 0.4 ºC/s (as discussed in section 4.1.1) predicted by equation 2-1. The air cooling process was assumed to start from 1250 ºC, and the average cooling rate of 0.1 ºC/s was taken as input for DICTRA calculation [37]. It has been found that the predicted concentration profiles of Mn had no changes observed at temperatures below proeutectoid temperatures. The simulated profile of Mn at 780 ºC was plotted to compare with the experimental composition profile, as seen in Figure 4-19 below. It indicates that the predicted profile is generally

consistent with the final experimental results, while the initial part of Mn profile (an obvious slope on the left hand side) has been observed because of the partition of Mn occurred during the transformation from austenite to α-ferrite. Therefore, the concentration profile predicted by DICTRA can be used reasonably to describe the microsegregation behaviour of Mn, and it also can be expected to be used for other elements in the Al-Nb steel.

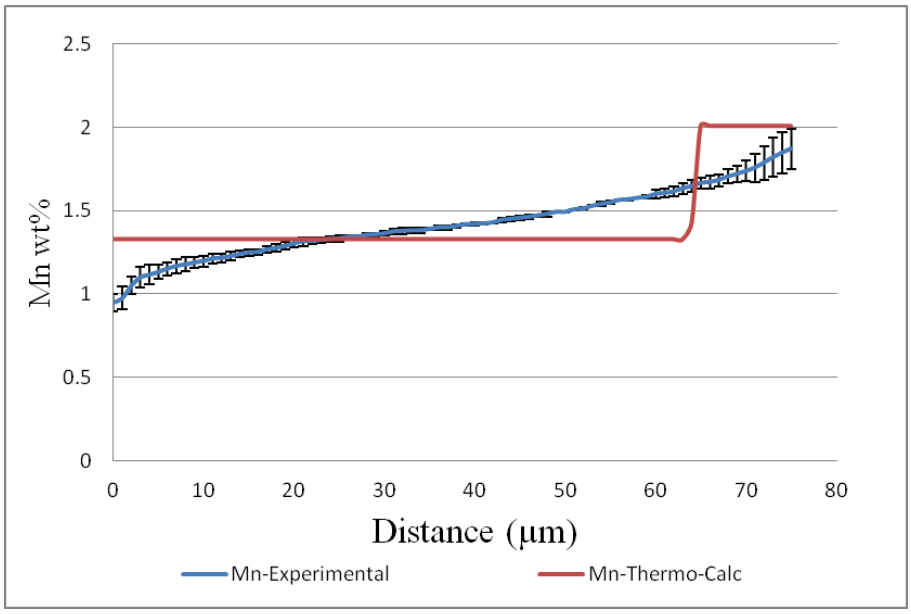

Figure 4-18 Comparison between the Mn contents predicted by Thermo-Calc at the peritectic temperature of 1485 ºC and experimental Mn concentration profiles (as seen in Figure 4-3).

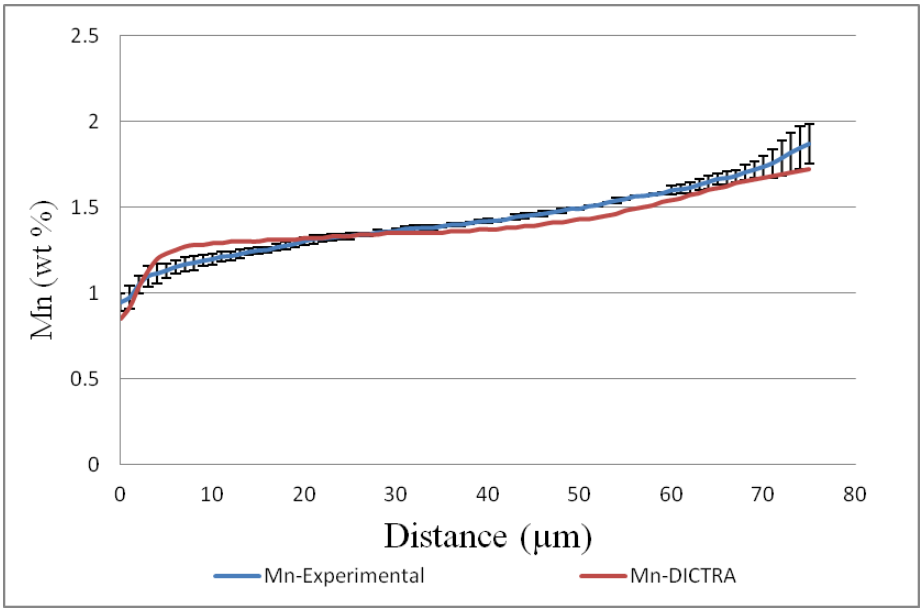

Figure 4-19 Comparison between the DICTRA prediction of Mn composition profile during proeutectoid reaction at 780 ºC and measured Mn concentration profile (as seen in Figure 4-3).

Microalloying elements, such as Al and Nb, form the precipitates at temperatures higher than the proeutectoid reaction, and the precipitation is also strongly related to the segregated composition which is uncertain (especially for the Nb). The concentration profiles of Al and Nb were predicted by DICTRA at a high temperature close to the solidus temperature. However, it has been found that the predicted composition of Mn at the interdendritic centre region was extremely high when simulated at the solidus temperature of 1480 ºC (equals to the last liquid temperature, as discussed in 2.2.4). The temperatures at the complete solid stage (for example 1476 ºC close to 1480 ºC), which have taken into the consideration of the complete redistribution of elements during phase transformation between liquid and solid, can be used to predicted concentration profile of Al and Nb.

The composition profiles of Nb and Al were predicted by DICTRA at a temperature 1476 ºC, Figure 4-20, which shows that the Nb content increases markedly at a distance of around 60 μm from the dendrite centre, and the maximum composition ratio of 3.3 (interdendritic [Nb] of 0.062 wt% compared with a bulk value of 0.019 wt%) can be expected. Al still shows the slight segregation in the dendritic region with a nearly uniform distribution predicted by DICTRA, a partition ratio 0.86 (0.049 wt% at interdendritic centre to 0.057 wt% in average composition) is observed lower than '1' which is consistent with the partition ratio reported from literature (Table 2-6, as discussed in section 2.2.4). Concentration steps have been observed in Nb and Al profiles at a distance of around 15 μm from the left hand side (Figure 4-20), which is due to the lower partition behaviour between liquid and austenite than between liquid and ferrite, as seen in Table 2-3. These steps may not be observed after complete phase transformation from δ-ferrite to austenite, as the elements have already been redistributed during phase transformation at the moving ferrite-austenite interface.

Therefore, the DICTRA predicted contents of Al and Nb (Table 4-4) were used as input in Thermo-Calc software, along with the average C and N values (due to the higher diffusivities of these elements in austenite, assuming that they are uniformly distributed [38]), and the bulk compositions (Table 3-1) of the other alloying elements (as they do not influence the precipitation behaviour of AlN and Nb(C, N) significantly, as discussed in section 3.2.2), to calculate the precipitation behaviour as a function of temperatures, as shown in Figure 4-21.

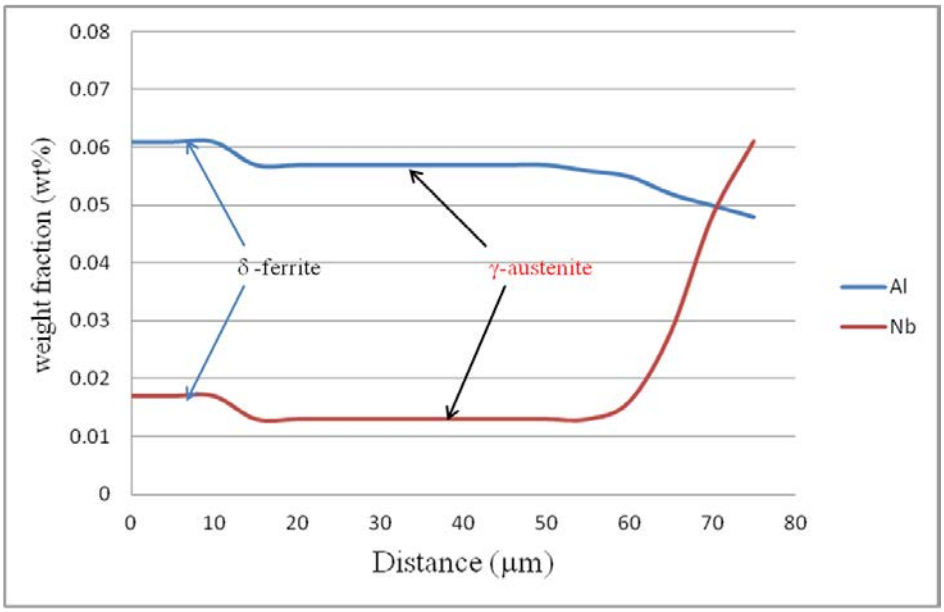

Figure 4-20 DICTRA predicted composition profile of Nb and Al at complete solid temperature 1476 ºC (close to solidus temperature of 1480 ºC) over the distance of half SDAS around 75μm.

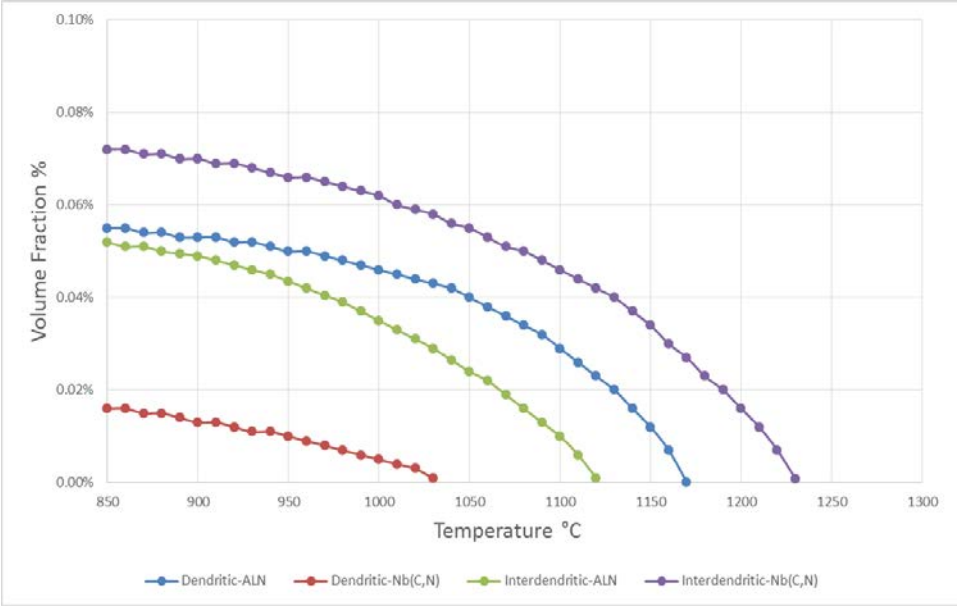

Figure 4-21 Volume fractions of AlN and Nb(C, N) were predicted by Thermo-Calc, in the dendritic region and interdendritic region.

During reheating, it is expected that the dendritic Nb(C,N) particles dissolve first at 1030 ºC, followed by the interdendritic AlN precipitates (1120 ºC). These two precipitate dissolution temperatures may not be significant for grain growth in these regions, since more stable (with higher volume fraction) precipitates are still present: AlN precipitates for the dendritic region and Nb(C, N) particles for the interdendritic region, have the dissolution temperatures of around 1160 ºC and 1230 ºC respectively. The predicted precipitate dissolution temperatures are summarised in Table 4-4. Experimental reheating temperatures were determined as the different precipitate dissolution temperatures and around ± 30 ºC, to investigate grain growth at these critical temperatures.

Table 4-4 Precipitates dissolution temperatures of AlN and Nb(C,N) for homogenised and as-cast (segregated) conditions.

	Al / wt%	AlN / ºC	Nb / wt%	Nb(C,N) / ºC
Average (homogenised)	0.057	1170	0.019	1090
As-cast dendritic-centre	0.059	1160	0.014	1030
As-cast interdendritic-centre	0.049	1120	0.062	1230

4.4 Summary and discussion

The microstructures of the as-cast ingot (with segregated composition) and homogenised samples (with uniform composition) were characterised in terms of microsegregation level, ferrite grain size, and microalloying precipitate size and distribution at the initial condition before reheating. Thermo-Calc and DICTRA software were used to predict the particle thermal stability and composition segregation

profile respectively. The simulated segregation profile predicted by DICTRA at the 1476 ºC (at the complete solid temperature) was assumed to be the composition profile, which was used to predict the precipitation behaviour (precipitate stability and particle volume fraction) by Thermo-Calc in the segregated sample. This is based on the compositions determined from the regions of dendritic centre (left hand side on the profile) and interdendrite-centre (on the right of the concentration profile).

After the homogenisation treatment, the ferrite grain size is similar to that in the as-received cast ingot condition. Nb-rich particles (expected to be Nb(C, N)) were found in as-cast segregated steel (Figure 4-8) and homogenised steel (Figure 4-13), with a large number density but small size (100-200 nm). Table 4-5 shows a similar particle size (200-250 nm, based on the particle size distribution with area fraction) of AlN in homogenised and as-cast segregated steel with a narrow range of formation temperatures predicted by Thermo-Calc (1120 ºC -1170 ºC, as seen in Table 4-5). However, it has found that Thermo-Calc predicted formation temperature of 1090 ºC for Nb(C,N) in homogenised steel, is lower than that in the interdendritic region (1230 ºC), but it is higher than the dendritic Nb(C,N) formation temperature at 1030 ºC. It means that the strong segregation of Nb has occurred in the as-cast steel which results in a significantly difference in the formation temperatures of Nb(C,N) in the dendritic and interdendritic regions. The mode size of Nb(C, N) in homogenised steel is 150-200 nm which is similar to that in as-cast steel, which means that the segregation behaviour of Nb does not affect the particle mode size of Nb(C, N) significantly, but can influence the overall number density, volume fraction, and the particle's thermal stability. The dominant particles (greatest number density and largest volume fraction)

in the as-cast steel are the dendritic Al-rich particles (number density: 1.89×10^4 /mm^2; volume fraction: 0.059 %) and interdendritic Nb-rich particles (number density: 2.64×10^4 /mm^2; volume fraction: 0.05%), as seen in Table 4-1, which agree with published literature reports [18, 38].

Table 4-5 Summarised information of AlN and Nb(C,N) with precipitate mode size (which is based on the particle size distribution with volume fraction (Figure 4-8(b) and Figure 4-13(b)) and formation/dissolution temperatures predicted by Thermo-Calc, for the homogenised and as-cast segregated condition.

	Particle mode size/ nm	Predicted T/ ^{o}C
Average (homogenised)- AlN	200-250	1170
As-cast interdendritic- AlN	200-250	1120
As-cast dendritic- AlN	200-250	1160
Average (homogenised)-Nb(C,N)	150-200	1090
As-cast interdendritic- Nb(C,N)	150-200	1230
As-cast dendritic- Nb(C,N)	150-200	1030

The volume fraction of microalloying precipitates (Al-rich and Nb-rich particles) in different conditions predicted by Thermo-Calc have been used to compare the experimental values measured by SEM analysis, as shown in Table 4-6. It indicates that the overall particle volume fraction in homogenised condition (SEM: 0.06 % and Thermo-Calc: 0.078 %) is notably lower than they are in as-cast segregated steel (SEM: 0.163 % and Thermo-Calc: 0.195 %). The results indicate the modelling predictions fit the experimental results well but with a maximum discrepancy of 0.022 % being observed in the interdendritic segregation of Nb. This overestimation is probably due to an inaccurately predicted composition of Nb in the solute-enriched region, or because of some Nb(C,N) particles that have been missed during SEM analysis.

However, the interdendritic Nb-rich particle shows a small size of 150-200 nm in a large volume fraction of 0.05%, which can provide pinning force in the interdendritic region based on the equation 2-9 (discussed in section 2.4.2) to restrain the grain growth. An overestimation of 0.015 % (SEM 0.04% < Prediction 0.055%) has been seen for AlN in the homogenised steel, and it is probably due to some AlN particles that have been missed in the SEM characterisation. Reheating treatments are discussed in the next chapter based on the predicted particle dissolution temperatures to investigate grain growth at critical temperatures.

Table 4-6 Comparison between the measured particle volume fractions of Al-rich and Nb-rich and the modeling predictions.

	SEM result. %	Modeling prediction. %
Homogenised-Nb(C,N)	0.02	0.023
Homogenised-AlN	0.04	0.055
As-cast dendritic-Nb(C,N)	0.014	0.016
As-cast dendritic-AlN	0.059	0.055
As-cast interdendritic-Nb(C,N)	0.05	0.072
As-cast interdendritic-AlN	0.04	0.052

chapter 5 Grain growth behaviour during reheating treatment for homogenised condition of Al-Nb steel

The homogenised Al-Nb specimens were reheated to investigate the grain growth behaviour in a condition with a uniform distribution of AlN and Nb(C,N). The predicted nature of grain growth was examined by comparing with the experimental grain growth in the homogenised Al-Nb steel, linking to the thermal stability of microalloying precipitate during reheating treatments.

5.1 Grain growth prediction

The limiting grain sizes were predicted by using equation 2-11 to describe the critical grain sizes (when driving force for grain growth = pinning force from particles, discussed in section 2.4.2) for different reheating temperatures.

The particle radius (cm) for a given temperature can be calculated by equation 2-8 (in section 2.3.4) using the parameters of: σ is the interfacial energy (equal to the grain boundary energy of $800 \cdot 10^{-7}$ J/cm^2 [136, 137]). V is the molar volume of pinning particles which can be predicted by Thermo-Calc calculation: AlN has a molar volume approximately 6.4 cm^3/mol; Nb(C,N) particles show a molar volume of around 6.8 cm^3/mol which is close to the result (6.72 cm^3/mol) that has reported in the literature [138, 139]. C^s is the concentration of the saturated solution in austenite that is predicted by Thermo-Calc (in mass fraction), Figure 5-1. The parameter of t is the particle growth time (3600s for 1 hour), while R is the universal gas constant (=8.31 J/mol·K)

and *T* is absolute temperature (K). *D* is the diffusivity of the microalloying element (Al and Nb) in the matrix, which can be described by equation 2-3, as given as [66]:

$$D_{Nb} = 0.83 \cdot \exp\left(-\frac{266479}{RT}\right) cm^2/s;$$

$$D_{Al} = 5.9 \cdot \exp\left(-\frac{241417}{RT}\right) cm^2/s\ .$$

The diffusivity of Al and Nb in austenite are shown in Figure 5-2, which indicates that the diffusion of Al is faster than Nb when the temperature is above 1000 ºC (as a larger D_0 and smaller activation energy exists for Al than Nb, as seen above), which agrees to the results reported by Priadi [139]. The initial radius of Al-rich ($112 \cdot 10^{-7}$ cm) and Nb-rich ($87 \cdot 10^{-7}$ cm) measured in section 4.2.2 have been used in the equation 2-8, to calculate the growth of AlN and Nb(C,N) up to the precipitate dissolution temperatures of Nb(C,N) at 1090 ºC and AlN at 1170 ºC, as indicated in Figure 5-3.

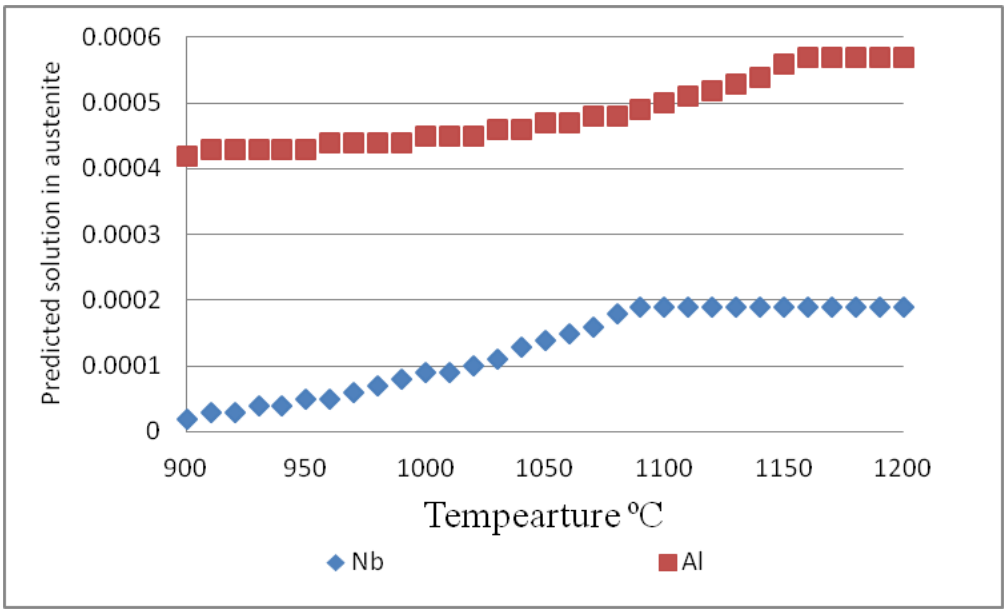

Figure 5-1 Solution of Al and Nb in austenite was predicted by Thermo-Calc (in mass fraction) against temperatures.

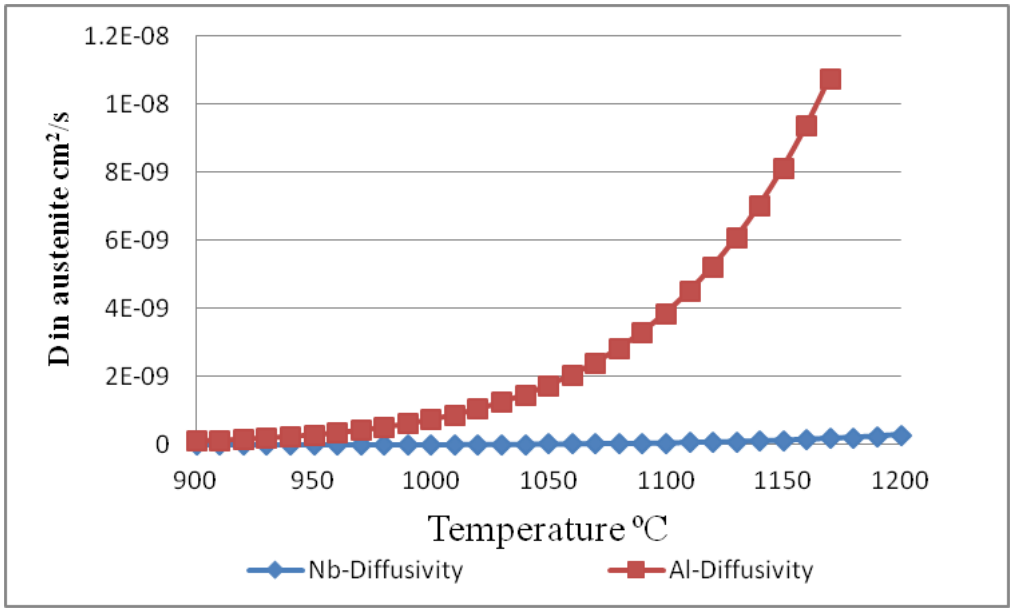

Figure 5-2 Diffusivity of Al and Nb in austenite against the temperature.

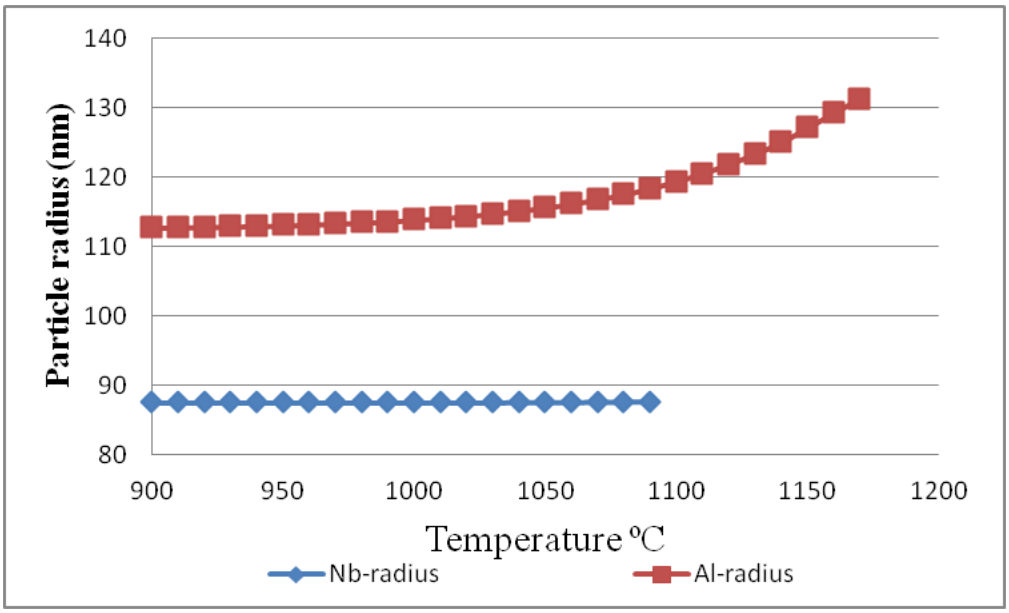

Figure 5-3 Predicted particle growth as a function of temperature for *t*=3600s.

The parameters of Z and m shown in Table 5-1 (as discussed in section 2.4) were used to predict the limiting grain size by equation 2-11. Due to the fact that the Al-rich and Nb-rich particles co-exist during reheating treatment, the values of particle radius are

simplified to be the average particles size of AlN and Nb(C,N), whilst the total volume fraction of these two particle types have been taken as input for the equation 2-11.

Table 5-1 Parameters of *Z* and *m* were used to predict the limiting grain size

Z	1.9 [160-162]	1.7 [150]
m	1 [25]	0.9 [151-153]

The predicted critical grain sizes as a function of temperature (before Al-rich particles dissolve at 1170 ºC) in the homogenised steel can be seen in Figure 5-4. A steep increase of limiting grain size is observed at around 1090 ºC, when Nb(C,N) particles dissolve (as predicted in Figure 4-17) and AlN starts to coarsen (as seen in Figure 5-3), which results in a reduction in the particle pinning force which is based on equation 2-9 in section 2.4.2. When the temperatures are close to 1170 ºC, the large predicted limiting grain sizes have been observed, which means that the grain coarsening can be expected to occur from local dissolution of AlN. Figure 5-4 shows that using a low value of *m* (for example, $m = 0.9$ rather than $m = 1$) can be expected to reduce the limiting grain size, and they were examined by experimental results, as will be fully discussed in section 5.2.3.

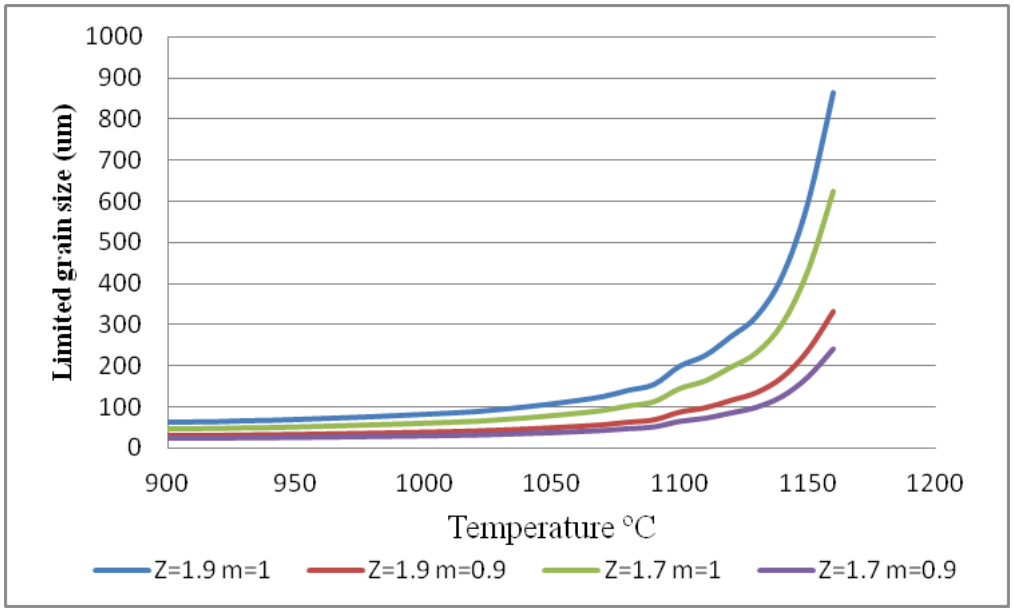

Figure 5-4 Predictions of limiting grain size in various parameters of *Z* and *m*.

5.2 Grain growth during reheating treatment

The samples of homogenised Al-Nb steel were reheated at temperatures in the range from 1075 ºC to 1200 ºC for 1 hour, to determine the grain growth behaviour at temperatures around the dissolution temperatures of the Nb(C,N) and AlN.

5.2.1 Microstructure at reheated temperatures

The starting prior austenite grain size in the homogenised Al-Nb steel was characterised when reheated at 920 ºC (above the A_{c3} temperature) for 10 minutes then quenched; the obtained mode grain size is approximately 27.5 µm, as shown in Figure 5-5, which indicates a uniform grain growth has occurred.

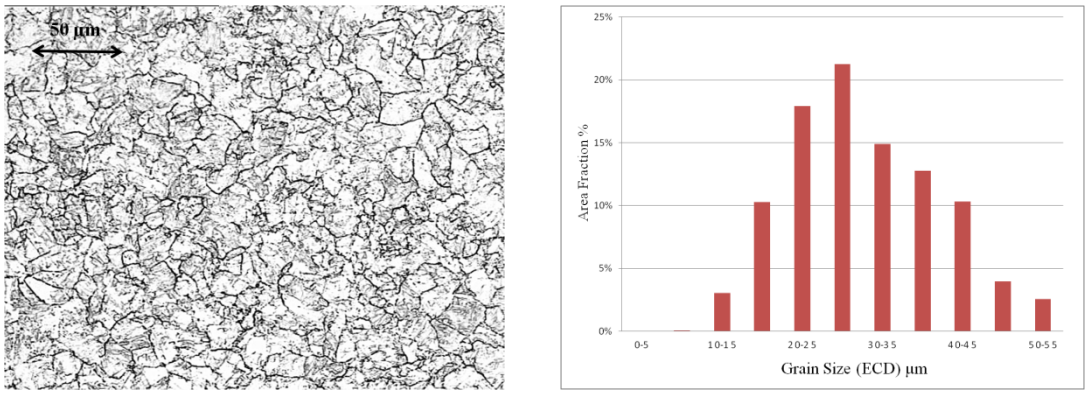

(a) (b)

Figure 5-5 Starting austenite grain grow at 920 ºC for 10 minutes: (a) prior austenite microstructure and (b) grain size distribution.

A fine and uniform grain size distribution with a mode size of 27.5 µm, was observed after one hour reheating at 1100 ºC, as shown in Figure 5-6 (a, b). At this temperature, the Nb-rich precipitates are expected to have dissolved, based on the Thermo-Calc predicted stability temperature of 1090 ºC. The result indicates that the grain boundaries are still pinned by the more stable Al-rich particles even after the Nb-rich precipitates have dissolved, since the grain size is similar to the starting prior austenite grain size (27.5 µm) based on the pinning effect from Al-rich particles and Nb-rich particles. It indicates that there is no grain growth occurring at temperatures below 1100 ºC, which means that the particle pinning force is effective at these temperatures.

On reheating at 1170 ºC (the predicted dissolution temperature of the Al-rich precipitate) for one hour, abnormally large grain was formed, which was surrounded by uniform fine grains, as shown in Figure 5-6 (c). Abnormally large grains have formed on reheating to the temperature at which the most stable pinning microalloying precipitates (AlN in the homogenised Al-Nb steel) start to dissolve, resulting in the local pinning force being reduced such that grains grow readily; and this agrees to the

literature reports as discussed in section 2.4.3.1 and the abnormal grain growth prediction as discussed above in section 5.1. Figure 5-6(d) shows that the grain size distribution is divided into NGG (normal grain growth) and AGG (abnormal grain growth) regions based on the criteria of abnormal grains which have been reported in the literature [160], as discussed in section 2.4.3.1. The mode grain size of 35 μm has been observed as normal grain size whilst the abnormal grains are identified when the grain size is above around 70 μm (discussed in section 2.4.3.1, RD≥0.9), with a low area fraction in an extensive size range (from 70 μm to 290 μm) being observed. It is also found that the abnormally large grains occur randomly either individually or in low number clusters because grain growth in most regions is expected to be prevented by un-dissolved Al-rich particles, as will be discussed in section 5.2.2.

Normal grain growth happened again for reheating at temperatures above 1200 ºC, Figure 5-6(e), where all particles were expected to have dissolved according to the modelling prediction. Figure 5-6 (f) shows a uniform coarse grain size distribution with a mode grain size of 110 μm, which is significantly larger than mode grain size of 35 μm that has been observed at 1170 ºC. It means that the obvious grain growth can be expected in homogenised Al-Nb steel at the temperatures above the dissolution temperature of AlN at 1170 ºC. However, the abnormally large grains have not been observed at this temperature, and this is probably because the precipitate pinning force has been reduced uniformly which allows most grains to coarsen.

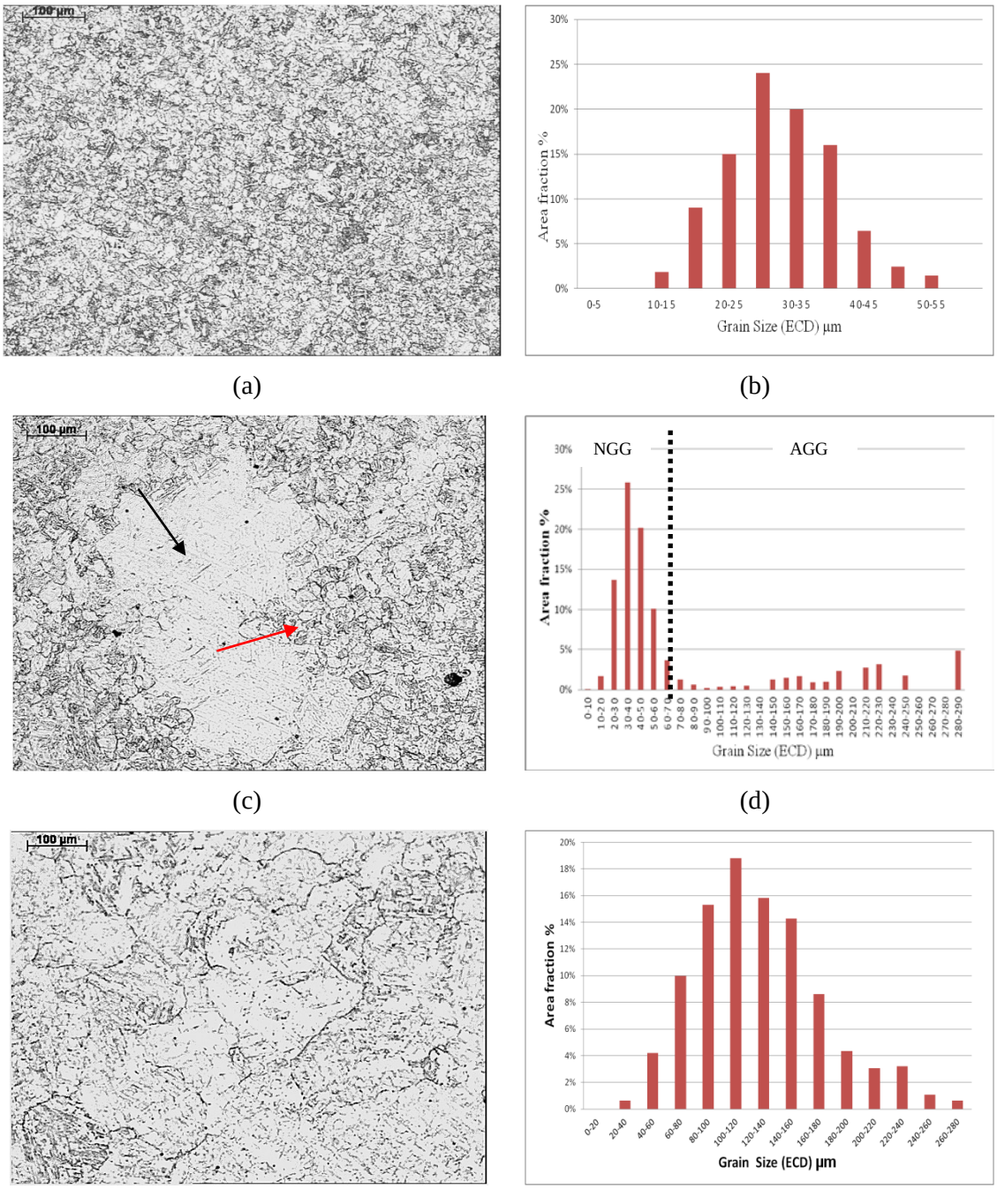

Figure 5-6 Prior austenite grain structure and grain size distributions for the homogenised steel after reheating for one hour at: (a, b) 1100 ºC, above to the dissolution temperature of Nb (C,N) at 1090 ºC; (c, d) 1170 ºC, corresponding to the dissolution temperature of AlN; abnormal large grain is indicated by black arrow and the adjacent small grains are arrowed with red line; (e, f) 1200 ºC, at the temperature where all precipitates are expected to be dissolved. NGG: Normal Grain Growth; AGG: Abnormal Grain Growth.

On reheating the homogenised Al-Nb steel, abnormal grain growth has been observed at 1170 ºC with an isolated nature (surrounded by small grains), as seen in Figure 5-6 (c), which is similar to reports in the literature of grains growing abnormally in a homogenised Al-containing steel (Al: 0.04 wt%, composition in Table 2-1) at 1050 ºC [30] (Figure 2-37 (a)), and at a reheating temperature of 1200 ºC in a homogenised Nb-V steel (composition in Table 2-1) [40], Figure 2-37 (b). Abnormal grain growth has been confirmed to occur at/ or close to the predicted AlN dissolution temperature (1170 ºC in the homogenised Al-Nb steel, rather than 40-70 ºC below this temperature as reported in the literature [163]), which agrees to reports in the literature, where abnormal grain growth has occurred at the temperature on reheating the homogenised steel to the dissolution temperature of pinning precipitates, e.g. 1200 ºC of Nb(C,N) in the Nb-V steel (Nb: 0.05 wt%, Table 2-1), shown in Table 5-2.

A large grain size to average grain size ratio of around 7 has been found during abnormal grain growth in the Al-Nb steel, which is significantly greater than the abnormal grain growth criterion of '2' [160], as discussed in section 2.4.3.1. This result agrees with the abnormal grain growth reported in an Al-containing steel and Nb-V steel, which had a ratios of 8.6 and 6.3 separately (Table 5-2), with similar abnormal grain sizes (250-260 μm) and average grain sizes (30-40 μm) observed in these steels.

Table 5-2 Comparison of abnormal grain growth in the homogenised steel, for Al-Nb steel, Al-steel [30] and Nb-V steel [40].

	Al-Nb steel	Al-steel	Nb-V steel
Composition: wt%	C:0.1; Al: 0.057; Nb:0.019; V:0.052	C: 0.2; Al:0.04	C: 0.09; Al: 0.03; Nb:0.05; V: 0.06
Initial condition	Homogenised	Homogenised	Homogenised
Predicted T_{diss} / ºC	1170	1020	1200
Reheated temperature/ ºC	1170	1050	1200
Average grain size, µm	35	30	40
Largest grain size, µm	250	260	250
Ratio: L/A	7.1	8.6	6.3

5.2.2 Precipitates characterization

SEM results (EDS mapping) in Figure 5-7 (a, b and c) indicate that after reheating at 1100 ºC (above the predicted dissolution temperature of Nb(C,N) at 1090 ºC) for 1 hour there are very few Nb-rich particles present, which suggests that the Nb-rich particle has dissolved at this temperature. The grain boundaries of the finer prior-austenite grains are decorated by the more stable Al-rich precipitates (higher dissolution temperature than Nb-rich particles in the homogenised Al-Nb steel), which can be expected to provide a pinning force against grain growth (indicated by red arrows in Figure 5-7 (d, e and f).

Figure 5-8 (a) shows a SEM image from the specimen that was reheated at 1170 ºC for 1 hour, indicating a typical abnormally large grain surrounded by small grains. EDS mapping was carried out and identified Al-rich particles on the boundaries of the large abnormal grains and the adjacent small grains. No Nb-rich particles have been observed, which confirms the complete dissolution of Nb-rich particles at this higher

temperature (1170 ºC); higher than the predicted dissolution temperature of Nb(C,N) at 1090ºC. The abnormal large grain growth can be attributed to the local dissolution of Al-rich particles at/ close to their dissolution temperature of 1170 ºC. Figure 5-8 (b, c) shows that Al-rich particles decorate on the boundary of the abnormally large grain, with the number ratio (numbers of precipitate on the boundary compared to overall numbers of precipitates from abnormally large grain area) of 0.34 which is lower than that in the small grained regions (numbers ratio of 0.61), as shown in Figure 5-8 (d, e), meaning that the amount of precipitate in abnormal largely grain boundaries has been reduced. It indicates that abnormal grain growth can be expected to occur when the local particles have dissolved (as reduction in number density results in local unpinning). Grain growth is prevented in the finer grains (size of 30 - 40 µm, as seen in Figure 5-6 (d)) with large number densities of precipitate pinning their boundaries (e.g. a cluster of Al-rich particles have been seen on the boundary of small grains in Figure 5-8(f, g)), which is nearly three times higher than that on the boundaries of abnormally large grains. This result suggests that the partial dissolution of microalloying precipitates can be expected to result in the occurrence of abnormal grain growth in the homogenised Al-Nb steel.

The SEM results agree and support the grain growth behaviour expected during reheating treatments (in section 5.2.1), which is based on the thermal stability of the microalloying particles predicted by Thermo-Calc (in section 4.3.2.1). It indicates that abnormal grain growth occurs on reheating close to the dissolution temperature of the pinning particles which results in the local unpinning effect due to a reduced number

density of AlN on the boundary, and this agrees to the literature reports [30, 40] in section 2.4.3.1.

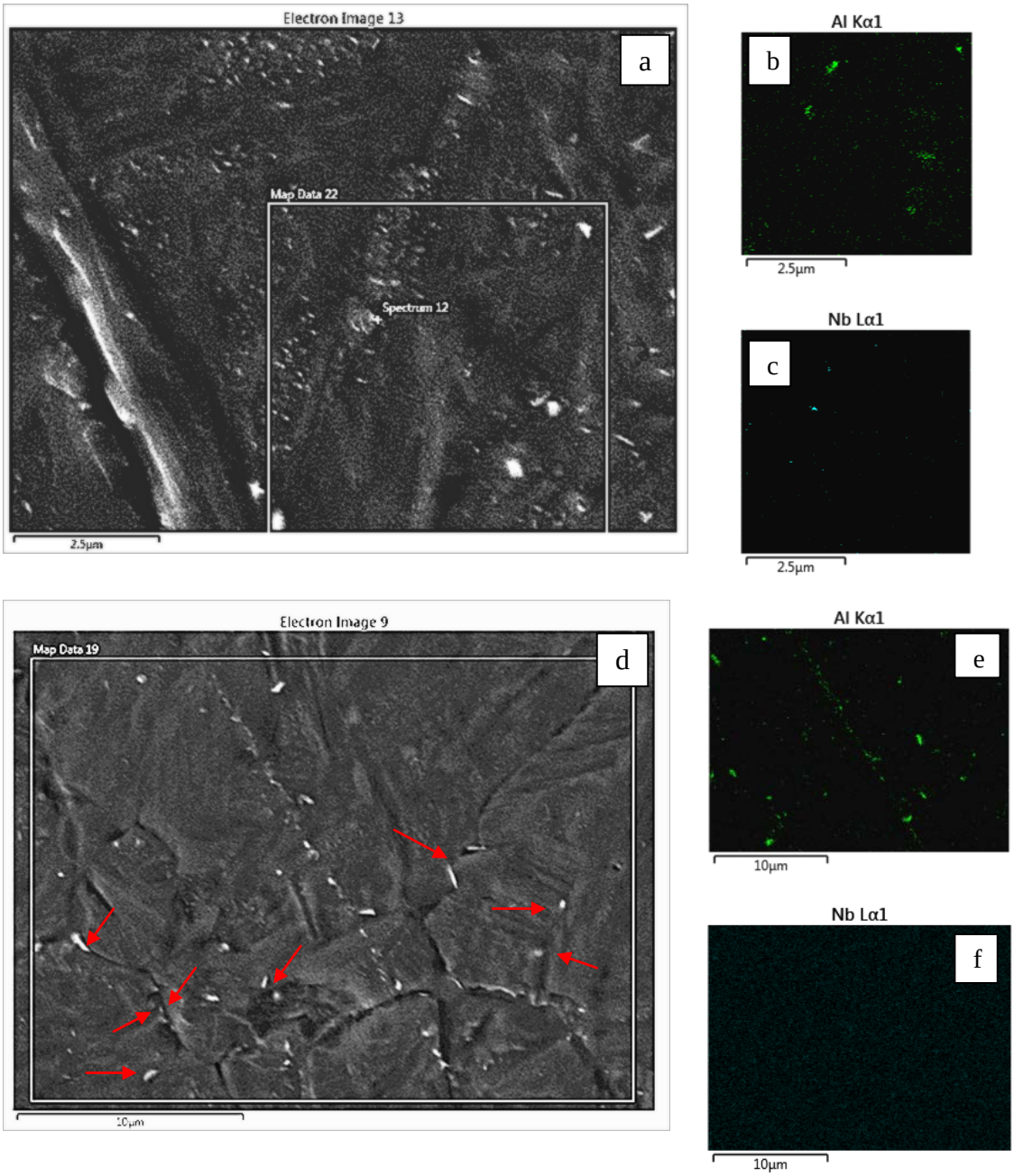

Figure 5-7 SEM images and EDS mapping analysis for Al-rich and Nb-rich precipitate distributions after reheating at 1100 ºC for one hour. Red arrows indicate the presence of AlN on grain boundaries to pin the grain growth.

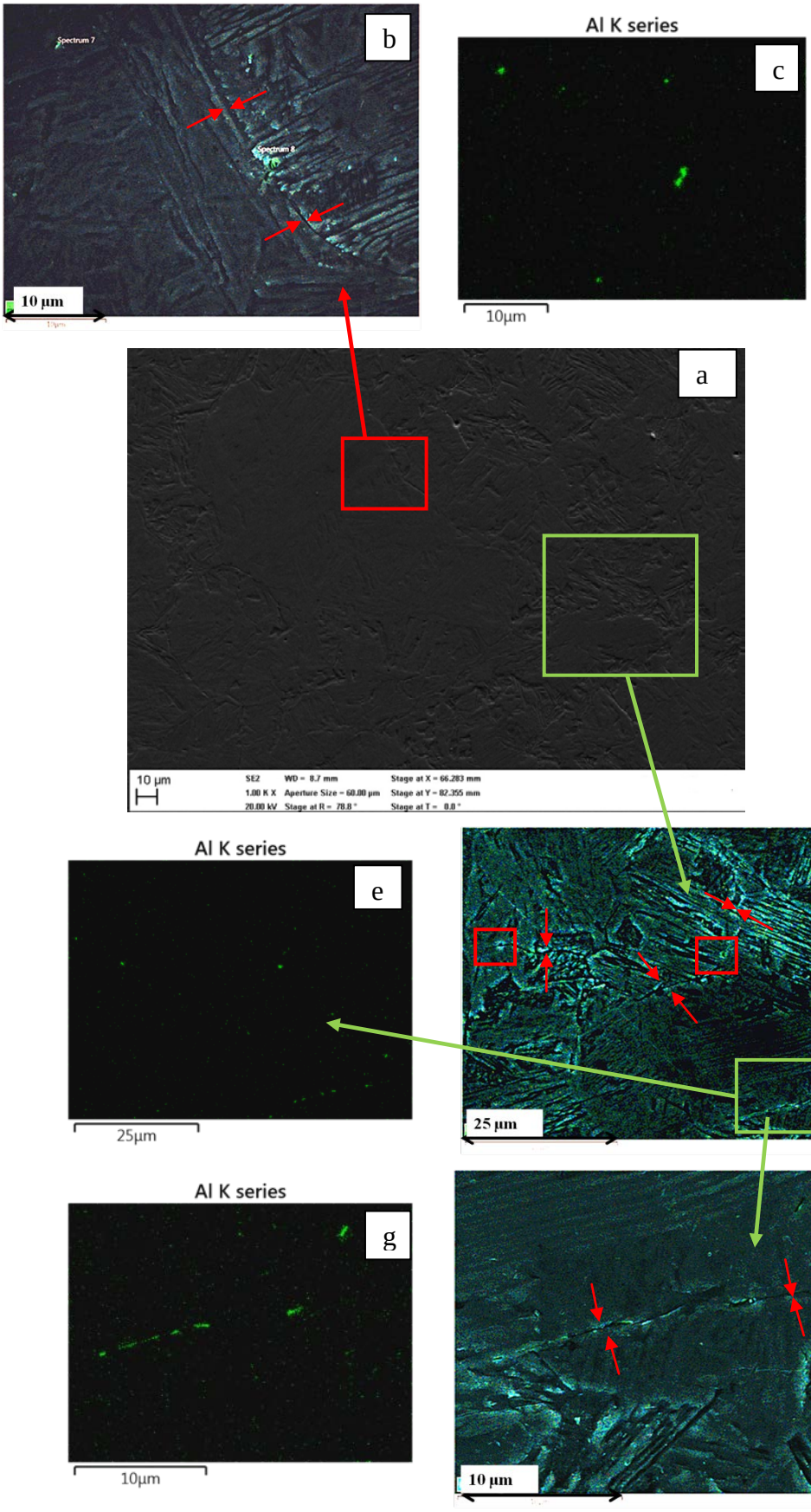
b
Spectrum 7
Spectrum 8
10 µm
Al K series
c
10µm
a
10 µm
SE2 WD = 8.7 mm Stage at X = 66.283 mm
1.00 K X Aperture Size = 60.00 µm Stage at Y = 82.355 mm
20.00 kV Stage at R = 78.8 ° Stage at T = 0.0 °
Al K series
e
25µm
d
25 µm
Al K series
g
10µm
f
10 µm

Figure 5-8 SEM images and EDS mapping analysis for the precipitates in homogenised Al-Nb steel reheated at 1170 ºC for one hour; (b, c) Al-rich particles at the boundary of abnormally large grains; and (d, e, f, g) Al-rich particles on the boundaries of small grains. Grain boundaries are indicated by red arrows.

5.2.3 Grain growth behaviour with temperature

Further reheating treatments were carried out to determine the grain growth behaviour as a function of temperature, the results are summarised in Figure 5-9, which shows that grain growth has been prevented at temperatures lower than 1170 ºC (predicted dissolution temperature of AlN). The results indicate that Nb-rich particles do not appear to have any significant role on grain boundary pinning, compared to the AlN particles, on reheating in this steel at temperatures above 1100 ºC and their dissolution does not result in any noticeable grain growth. Abnormal grain growth has been observed when reheating the homogenised steel to the AlN precipitate dissolution temperature (1170 ºC) with an abnormal grain size to mode grain size ratio of 7.1, but not at reheating temperatures 30 ºC below and 30 ºC above the dissolution temperature, where a uniform fine (mode grain size of 35 μm) grain size has been seen at the low temperature (1140 ºC) and a uniform coarse grain size (mode grain size of 110 μm) has been observed at the high temperature (1200 ºC). Consequently, abnormal grain growth occurs at a specific critical temperature (for example 1170 ºC in homogenised Al-Nb steel) or in a narrow temperature range, which can be avoided by controlling the reheating temperature.

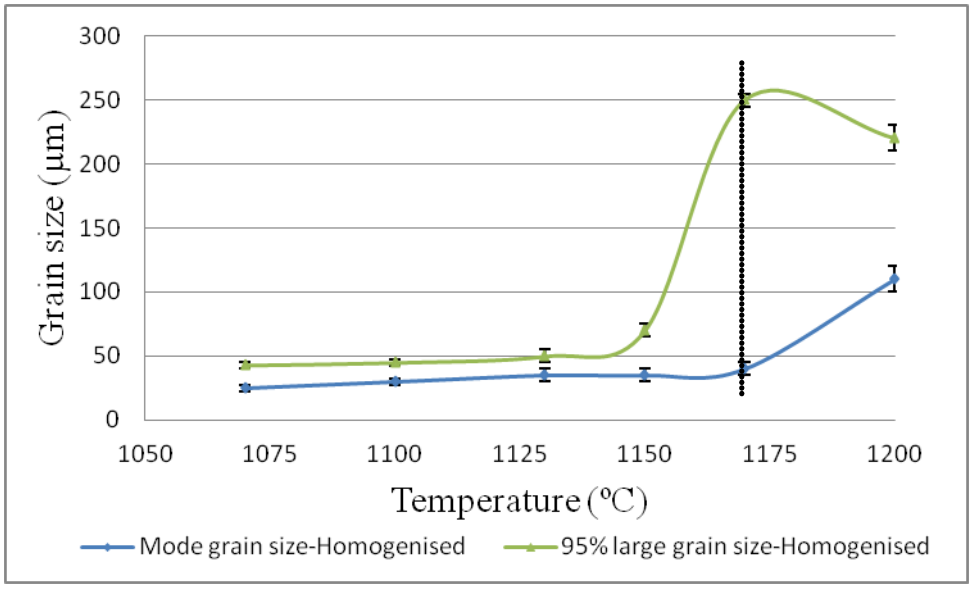

Figure 5-9 Grain size development as function of reheating temperatures is shown in the homogenised steel. Dashed line shows the temperature where abnormally large grain growth happened; (Mode GS: mode grain size from area fraction distribution; 95%-large GS: largest grain size corresponding to the accumulated area fraction of 95%).

The comparison between experimental austenite grain growth in homogenised Al-Nb steel (as seen in Figure 5-9) and the average austenite grain size development in literature reports [40, 143, 155] (as shown in Figure 2-31 and Figure 2-35, in section 2.4) can be seen in Figure 5-10, to help elucidate the pinning effect of Al-rich particle in the Al-Nb steel.

As shown in Figure 5-10 (a), there is little grain growth in homogenised Al-Nb steel at the temperatures lower than 1200 ºC, which indicates a similar mode grain size compared to the average grain size in microalloyed steels from literature reports (mainly using mixed precipitates of Nb(C,N) and TiN) [40, 155]. It indicates that the pinning effect of AlN and Nb (C,N) in homogenised Al-Nb steel is likely to be similar to the pinning effect of those microalloying precipitates of Nb(C,N) and TiN in the

EQ70 steel [155] and Slab-A steel [40]. However, on reheating at 1200 ºC, the mode grain size in Al-Nb steel is approximately 110 µm which is significantly larger than the small size of around 60 µm in the microallying steels from literature reports. This result means that coarse grains can be expected in homogenised Al-Nb steel when AlN has dissolved at reheating temperatures higher than its predicted dissolution temperature of 1170 ºC. Therefore, the AlN in homogensied Al-Nb steel can be expected to prevent grain growth at low temperature (< 1170 ºC) which is dependent on the thermal stability of Al-rich particles correlating to the given content of Al.

The grain growth in C-Mn steel reported in the open literature [143] can be assumed as the grain growth behaviour when no pinning force is present on their boundaries, and it can be used to compare to the abnormally large grain size which has been observed in homogenised Al-Nb steel, as seen in Figure 5-9. Figure 5-10 (b) indicates the comparison between the measured large austenite grain size (95% accumulated area fraction) in homogenised Al-Nb steel and the austenite grain size in C-Mn steel from the open literature [143]. It suggests that the large grain growth in homogenised Al-Nb steel shows a stable small size of around 50 µm at reheating temperatures lower than 1150 ºC, compared to the C-Mn steel which has an obvious grain size increasing from 130 µm to 180 µm. This result means that the large grain growth in homogenised Al-Nb steel is prevented by the precipitates at a temperature lower than 1150 ºC, including at the dissolution temperature of Nb(C,N) at 1090 ºC, which means AlN particles are effective enough to fully prevent large grain boundary movement on their own (Figure 5-7).

On reheating to a temperature that is above 1150 ºC, an obvious largest grain size (95% area fraction) of 250 µm has been observed at 1170 ºC as the local dissolution of AlN results in abnormal grain growth, which is close to the grain size of 270 µm in C-Mn steel. This indicates that the abnormal grain growth is associated with local unpinning from homogenised Al-Nb steel, which presumably grows to a similar grain size as that in the C-Mn steel which has no precipitate pinning effect.

Figure 5-11, shows that the experimental grain size (mode grain size and 95% large grain size) at reheating temperatures below 1170 ºC (AlN dissolution temperature) are less than all the predictions using the parameters Z = 1.7 - 1.9 and m = 0.9 - 1 (discussed in section 5.1). The experimental mode grain size (30 - 40 µm) shows a significant difference to the predicted limiting grain size (50 - 250 µm). On reheating at 1170 ºC, there is no limiting grain size predicted as there is no particle volume fraction at this temperature (f = 0, as complete dissolution of AlN is predicted in Thermo-Calc at this temperature). Therefore, the limiting grain size cannot be used to predict the abnormally large grain size (250 µm) when it occurs at 1170 ºC.

However, the curves with a lower value of the exponent m (=0.9) (equation 2-11) are closer to the experimental results than those with a higher growth exponent (m = 1), as seen in Figure 5-11, due to the lower particle volume fraction present (discussed in section 2.4.2). Therefore, a lower exponent, e.g. m = 0.8, was used in equation 2-11 which shows that the predicted limiting grain size is generally close to measured large grain size (95% area fraction) at temperature range of 1100 ºC-1150 ºC, as shown in Figure 5-12. This may be due to the limiting grain size being fitted with a lower value of m to deal with a markedly low particle volume fraction of 0.0007 measured in

homgenised Al-Nb steel. There is no significant difference in the predictions if a Zener value of 1.7 or 1.9 is used. However, the value of Z = 1.9 was used to investigate the abnormally large grain growth behaviour, which was determined by the criterion of abnormal grains (RD = 0.9, discussed in section 2.4.3.1) reported in literature [160], as discussed in section 2.4.3.1.

Consequently, as seen in Figure 5-13, the predicted limiting grain size using parameter of Z=1.9 and m=0.8 would be expected to describe the largest grain size (in 95% area fraction) which have been prevented from pinning effect of AlN and Nb(C,N) in the homogenised Al-Nb steel, and the limiting grain size is generally less than the average grain size in C-Mn steel from literature reports [143] (assumed to be microalloying element free steel). Therefore, the likelihood of abnormal grain growth may be estimated from the size difference between these two predicted grain sizes, i.e. the gradually expanded spacing of size difference (e.g. from 1000 ºC to 1150 ºC, Figure 5-13) may result in likelihood of abnormal grain growth as locally unpinned grains are able to grow to much larger size. On reheating the homogenised Al-Nb steel at temperatures of 1075 ºC -1150 ºC, the largest grains have been restricted to a size below 75 μm which is generally close to the limiting grain size (< 90 μm), but less than the grain size in C-Mn steel (<180 μm). The size difference is expanded from 70 μm (at 1075 ºC) to 140 μm (at 1150 ºC) which means that the grains can be expected to grow to be larger (in absence of pinning effect) with increase of reheating temperatures. Some of them are expected to grow abnormally by consuming the adjacent small grains at 1170 ºC, where local unpinning is expected due to the partial dissolution of AlN.

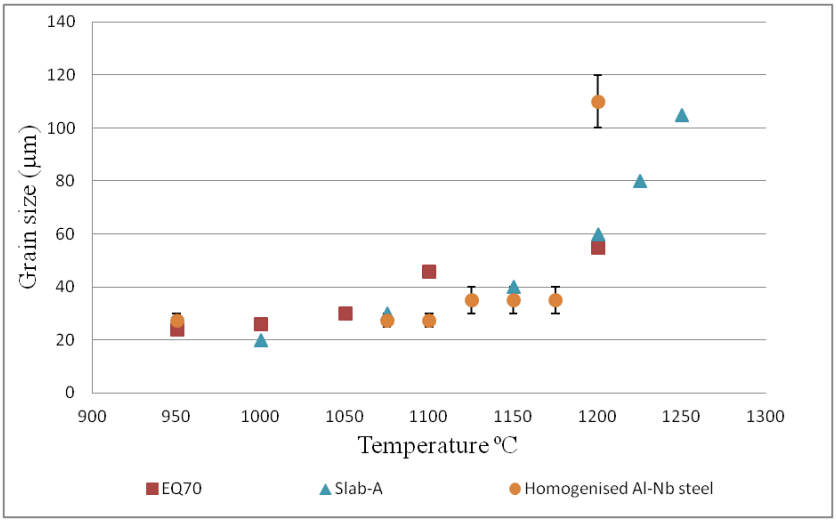

(a)

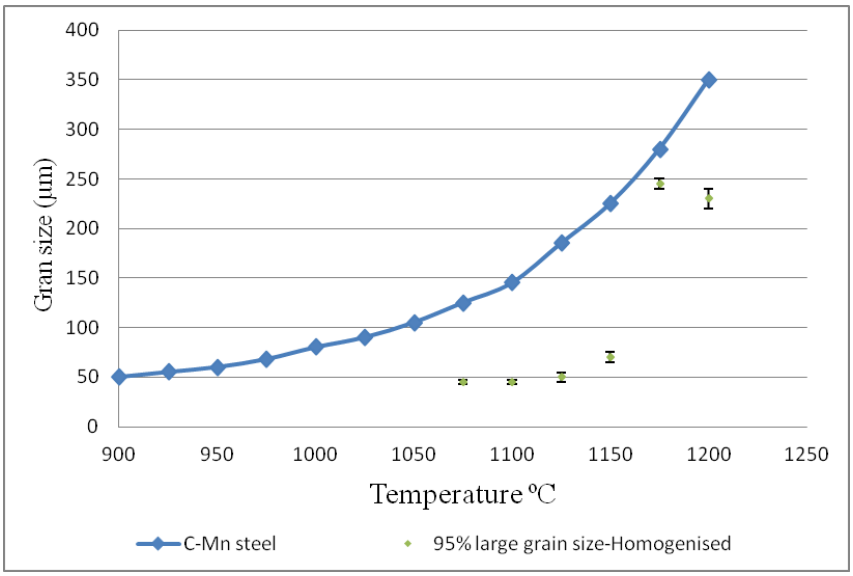

(b)

Figure 5-10 (a) Comparison between the experimental mode grain size of Al-Nb steel and average grain size of microalloyed steel (as shown in Figure 2-35); (b) the 95% area fraction large grain size compared to average grain size of C-Mn steel (as seen in Figure 2-31).

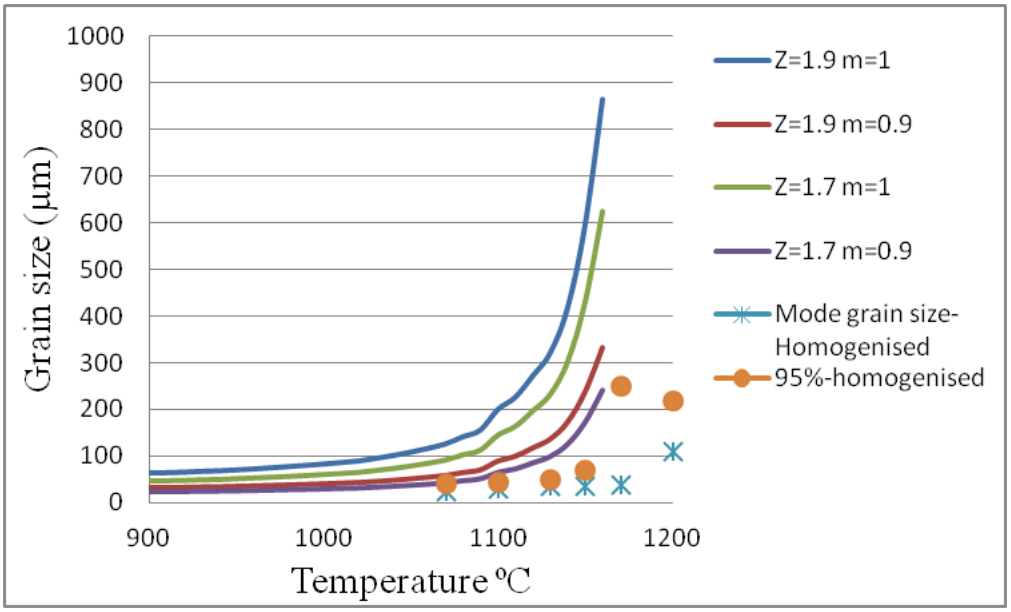

Figure 5-11 Predicted limiting austenite grain size and the measured size for different reheating temperatures.

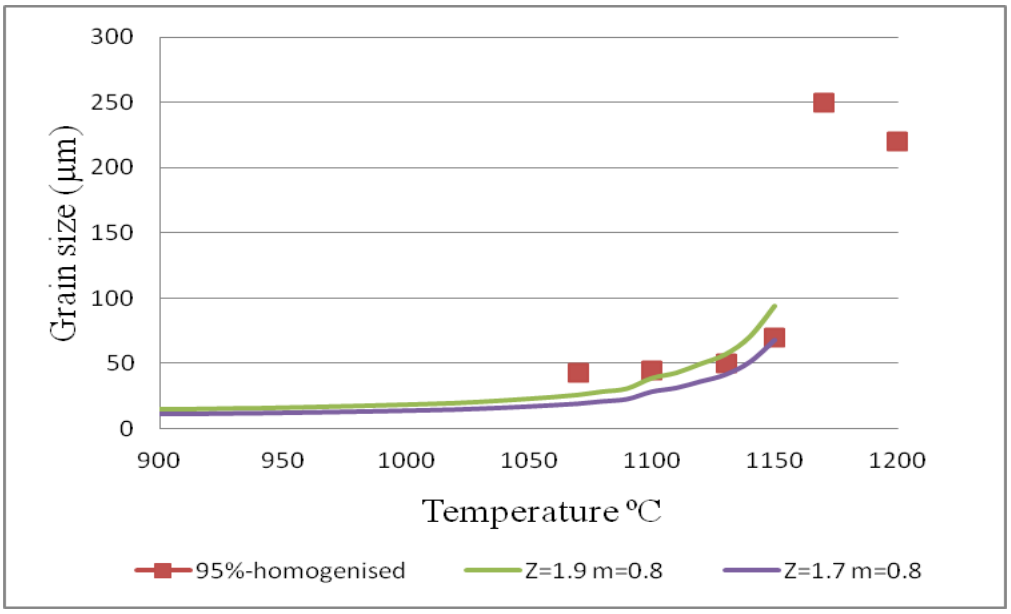

Figure 5-12 Limiting austenite grain size is compared to the measured largest grain size (grain size at 95% accumulated area fraction).

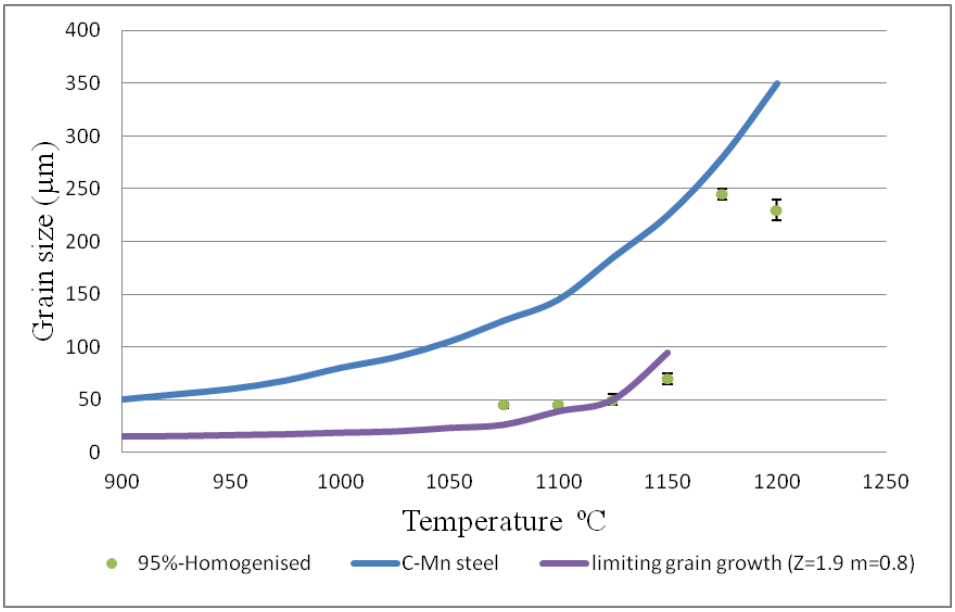

Figure 5-13 Measured largest grain size (95% area fraction) compared to the predicted limiting grain size (using Z=1.9, m=0.8) and the reported general grain size in C-Mn steel.

5.2.4 Effect of reheating time on abnormal grain growth for homogenised condition

Abnormal grain growth was observed at the dissolution temperature (1170 ºC) of Al-rich particles. Several further reheating treatments (with longer soaking times) were carried out to investigate the development of the abnormally large grains.

Reheating to 1170 ºC for two and three hours was used to examine the effect of reheating times on abnormal grain growth behaviour. Micrographs, as shown in Figure 5-14(a, b), indicate the obvious growth of the abnormal grains (as indicated by black arrows) which are surrounded by small grains (arrowed by the red arrows). The grain size distributions in Figure 5-14(c) demonstrate the continued growth of the large grains in terms of their maximum size and also increasing area fraction occupied compared to the finer grains, for example the area fraction corresponding to the fine

mode grain size decreases from 40% (1 hour) to 28% (2 hour), and 14% (3 hours). Moreover, the grain growth behaviour in Figure 5-15 shows that the size of the abnormally largest grains continues to increase with longer reheating times; the largest grain size for the abnormal grains has changed from around 250μm (1 hour), to 270μm (2 hours) and 320 μm (3 hours), whilst the mode grain size is stable at around 40-60 μm. This result suggests that the further local AlN dissolution can be expected at the longer reheating time, which results in the initial abnormal grains continuing to grow to be a coarser size.

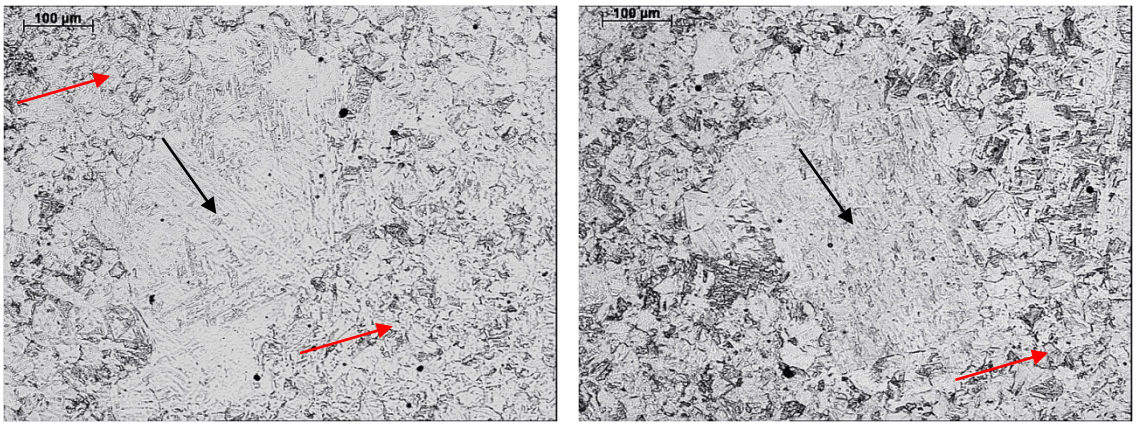

(a) (b)

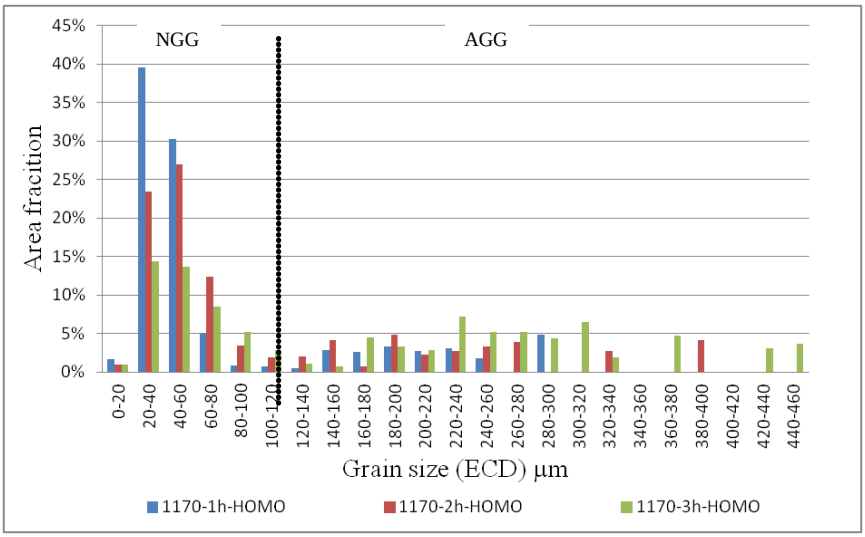

(c)

Figure 5-14 Microstructure of abnormal grain growth for Al-Nb containing steel at 1170 ºC for: (a) two hours; and (b) three hours; Grain size distribution at 1170 ºC for one, two and three hours.

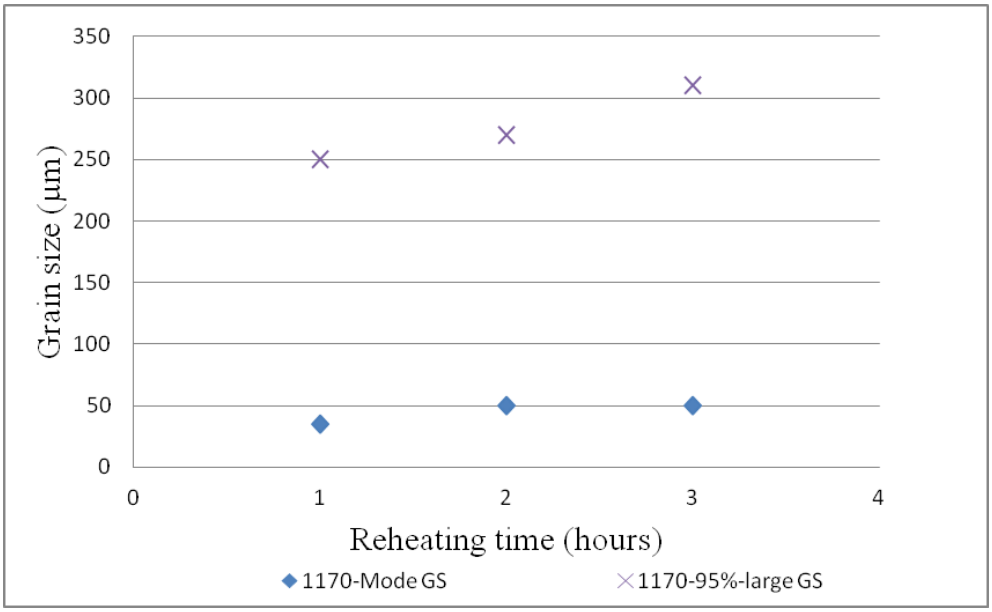

Figure 5-15 Grain size development of homogenised specimens after reheating at 1170 ºC for one, two and three hours: Mode grain size from area fraction distribution (Mode GS); and large grain size represented by the accumulated area fraction 95% (95%-large GS).

5.3 Summary

Abnormal grain growth occurred in the homogenised Al-Nb steel on reheating to 1170 ºC for one hour when the most stable microalloying precipitates (AlN in the Al-Nb steel) started to dissolve. The Al-rich particles are expected to be distributed uniformly in the sample initially and provide pinning force after the Nb-rich precipitates have dissolved at 1100 ºC, to inhibit grain growth and maintain the initial small austenite grain size. Partial dissolution of Al-rich particle has occurred at the reheating temperature of 1170 ºC, resulting in the local unpinning which allows growth of abnormally large grains. Particle distribution in the regions of large grain and small grain area were examined using SEM, and few AlN particles have been observed on the boundaries of the abnormally large grains, which have a lower number density than that in the small grain regions. Longer reheating times (two and three hours) have

shown that the abnormal grains can continue to grow, and this suggests that the pinning particles observed in the large grain boundaries (reheating for one hour) are either not sufficient in number to effectively pin the boundaries, or are not stable enough such that with further reheating time more particles have dissolved allowing the abnormally large grains to grow coarser.

It has been found that the grain growth and particle dissolution behaviour can be predicted based on modelling calculations using Thermo-Calc software for the thermal stabilities of precipitate. The predictions fit well with the experimental results suggesting that Thermo-Calc can be used to predict the precipitate dissolution temperature when grain growth, especially abnormal grain growth, occurs during reheating for the steel in the homogenised condition. The size difference between the grain size using grain growth in C-Mn steel (assumed as no particle pinning effect) and limiting grain size can be expected to characterise the occurrence or the severity of probable abnormal grain growth, e.g. an expanded size difference may result in the occurrence of abnormally large grains in absence of the precipitate pinning effect.

Consideration of the role of non-uniform microalloying precipitate distributions, due to segregation, on grain size development on reheating, and how well this can be predicted, will be considered in the next chapter.

chapter 6 Grain growth behaviour during reheating treatment for segregated condition in Al-Nb steel

In Chapter 5 it was shown that abnormal grain growth has occurred during reheat treatment in the homogenised Al-Nb steel. In this Chapter, the as-cast Al-Nb steel, with dendritic solute segregation was further investigated to understand if any grains grew abnormally during reheating taking into account the influence of the heterogeneous distributions of particles, i.e. the enriched interdendritic Nb-rich particle and dendritic Al-rich particle.

6.1 Predictions for grain growth in segregated condition

The grain size development for C-Mn steel (as seen in Figure 2-31, in section 2.3.1 which has also been used to analyse the grain growth behaviour in homogenised Al-Nb steel) can be used to compare with the grain growth behaviour in as-cast Al-Nb steel. After AlN is dissolved at temperatures above 1160 ºC (predicted dissolution temperature of dendritic AlN by Thermo-Calc), presumably the grain growth in the solute-depleted region for the as-cast Al-Nb steel can be expected to be similar that in the C-Mn steel (in absence of microalloying particle pinning effect). The grain size in the solute-enriched region is likely to be smaller than that in the solute-depleted region for 1 hour reheating treatment (discussed in 2.4.3.2[22-25]).

The limiting grain size was predicted and examined for the homogenised condition (discussed in section 5.1), which indicated that the parameters of Z = 1.9 and m = 0.8 gave good fits for the largest grain size observed at temperatures before precipitates

were dissolved at 1170 ºC (dissolution temperature of AlN). In the as-cast material, segregation means that there are different compositions in the dendritic and interdendritic regions (segregated composition of Nb and Al can be seen in Table 4-4), therefore calculations for limiting grain size were carried out separately for the two regions assuming each region had a separate but uniform composition. The parameters for the dendritic solute-depleted region and interdendritic solute-enriched region were predicted by Thermo-Calc: (1) molar volume of Nb(C,N) (around 6.8 cm^3/mol) and AlN particles (around 6.4 cm^3/mol) were predicted for both the dendritic and interdendritic regions, which was close to the predictions in section 5.1; (2) the equilibrium contents of the [Al] and [Nb] in the matrix austenite were predicted by Thermo-Calc (the same predicted method also has been used for homogenised condition, discussed in section 5.1).

Particle growth was predicted using equation 2-8 (in section 2.3.4) assuming: initial mode particle radii of Al-rich (112 nm) and Nb-rich (87 nm), as seen in Table 4-5, were same in both areas of dendritic and interdendritic regions; the particle growth time t=3600s (1 hour) was taken as input in equation 2-8. The predicted particle radii are shown in Figure 6-1, indicating a slight growth of AlN (e.g. radius from 112 nm to 130 nm in the dendritic region) and a stable radius of Nb(C, N) (approximately 87 nm) with increasing temperature, which gives a similar growth behaviour compared to that in the homogenised steel, as seen in Figure 5-3 (in section 5.1). For the growth of AlN or Nb(C, N) during reheating in the dendritic region and interdendritic region respectively, it does not show any differences in terms of precipitate mode size from the different solute regions in the as-cast Al-Nb steel, as shown in Figure 6-1. This

agrees with the experimental results reported by Kundu [18], for example the mode sizes of dendritic Nb(C,N) and interdendritic Nb(C,N) were the same (approximately 150-200 nm) on reheating at 1125 ºC.

The predicted limiting grain sizes are plotted in Figure 6-2 by taking the following parameters as the input into equation 2-11, in section 2.4.2 (Z = 1.9; m = 0.8; r = average radius of predicted size of Al-rich and Nb-rich particles; and f = total volume fraction of Al-rich and Nb-rich particles for separate solute-level regions). The curves show that the limiting grain size development in separate regions, where for the dendritic region, the limiting grain size increases at temperatures above 1030 ºC (Nb(C,N) dissolution temperature) and then a maximum size of around 130 µm can be expected at 1150 ºC (close to the AlN dissolution temperature 1160 ºC, as indicated by blue dashed line in Figure 6-2); whilst in the interdendritic region, a maximum grain size (140 µm) is predicted at 1220 ºC (close to the Nb(C,N) dissolution temperature 1230 ºC, as indicated by red dashed line in Figure 6-2).

Figure 6-3 shows the size difference (proposed in section 5.2.3, Figure 5-13) between limiting grain size and the grain size in C-Mn steel (discussed above). The size difference is expanded as temperature increased (for example in the dendritic region, the size difference is increased from 60 µm at 1000 ºC to 130 µm at 1130 ºC; in the interdendritic region, the size difference is from 65 µm at 1000 ºC to 310 µm at 1200 ºC) until the pinning force starts to be reduced, allowing limiting grain size closer to the grain size in C-Mn steel (e.g. dendritic region: > 1130 ºC; interdendritic region: >1200 ºC). Therefore, the prediction of grain growth behaviour in as-cast steel is for: (1) Large grains may grow in dendritic region when the reheating temperature is

over 1160 ºC (AlN particles dissolution temperature), however these grains may not become very large (abnormal) grains if they are prevented by the pinning effect from the interdendritic regions (large number density of Nb(C, N)) to limit their size to less than segregation band separation, (e.g. $< 150 \pm 50$ µm). (2) Abnormal grain growth may occur at the dissolution temperature of Nb-rich particles in the interdendritic region (approximately 1230 ºC) when their pinning force is removed.

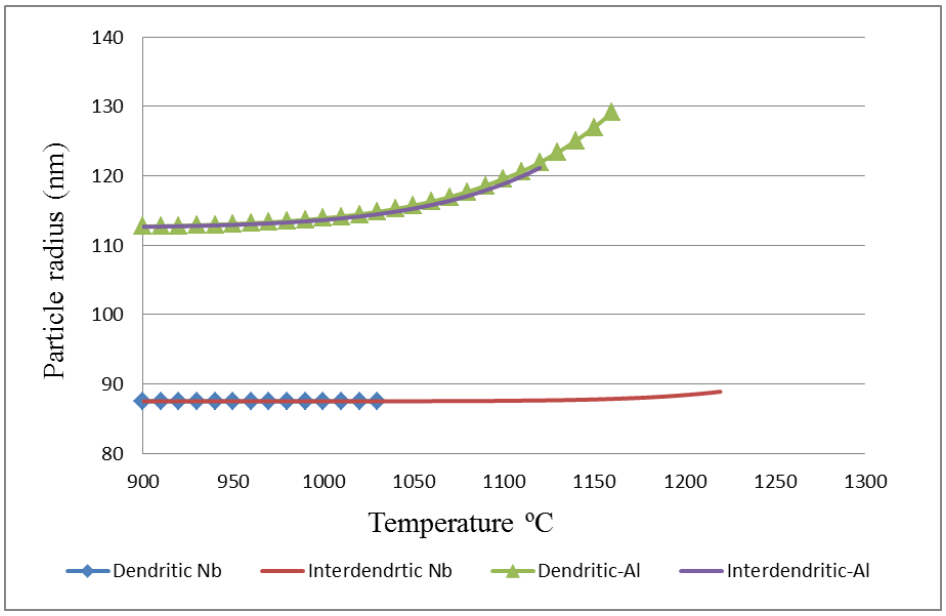

Figure 6-1 Predicted particle radius as a function of temperature for holding times of *t*=3600s.

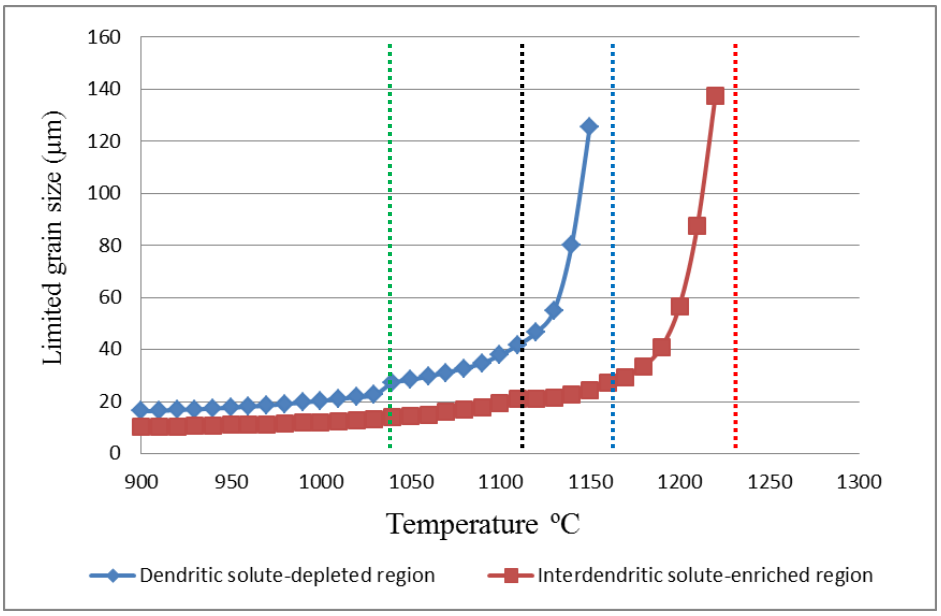

Figure 6-2 Predicted limiting grain sizes as function of temperatures (for 1 hour) in the dendritic and interdendritic regions, with parameters of Z = 1.9 and m = 0.8; the dashed line indicates the predicted dissolution temperature of precipitate in different regions for: dendritic Nb(C,N) at 1030 °C (green); interdendritic AlN at 1120 °C (black); dendritic AlN at 1160 °C (blue); and interdendritic Nb(C,N) at 1230 °C (red).

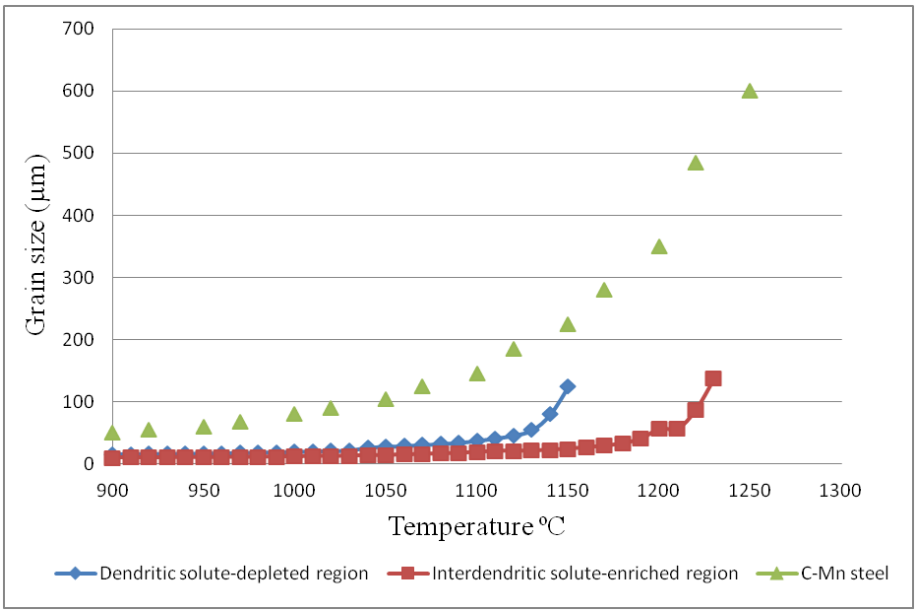

Figure 6-3 Comparison between the grain size development in C-Mn steel and predicted limiting grain size in the dendritic and interdendritic region.

6.2 Grain growth behaviour as a function of reheating temperature

As-cast Al-Nb specimens were reheated for 1 hour in the temperature range from 950 ºC to 1300 ºC, measuring prior austenite grain sizes across the critical dissolution temperatures for the particles present in different (solute-enriched and solute-depleted) regions.

6.2.1 Reheated microstructure at critical temperatures

The as-cast material was reheated at 920 ºC for 10 minutes then quenched and tempered, to determine the starting austenite grain size prior to any grain growth during reheating. Figure 6-4(a) shows the microstructure which consists of the darker etched areas corresponding to the solute-enriched regions (due to the more phosphorus segregated in this region at the grain boundaries, therefore, the boundaries being deeply attacked by the picric acid etchant), and the lighter areas associated with the solute-depleted regions. The differing contrasts of etched areas have not been observed in the homogenised Al-Nb steel. The distance between the darker etched segregated bands is equal to the secondary dendrite arm spacing of around 150 ± 50 µm, which means that the segregation spacing can also be identified in the heated microstructure, and this is in agreement with the report from the literature [30]. The different grain sizes in the solute-enriched and solute-depleted regions have been observed from heated grain structure, as indicated in Figure 6-4(b), where there is a smaller mode grain size (22.5 µm) in the solute-enriched region than in the solute-depleted region (27.5 µm). Therefore, the segregation of microalloying elements does not show any significant effect on the starting austenite grain size distributions, which indicates a uniform overall grain size distribution with a mode grain size of around 27.5 µm.

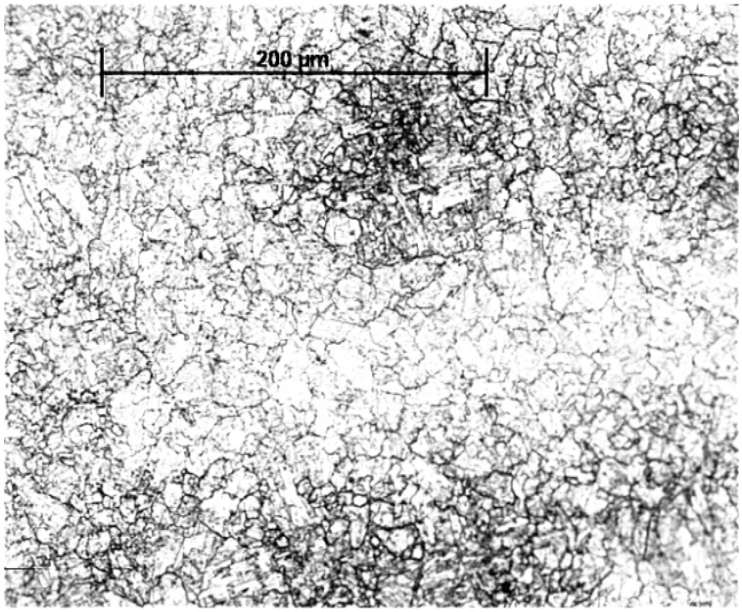

(a)

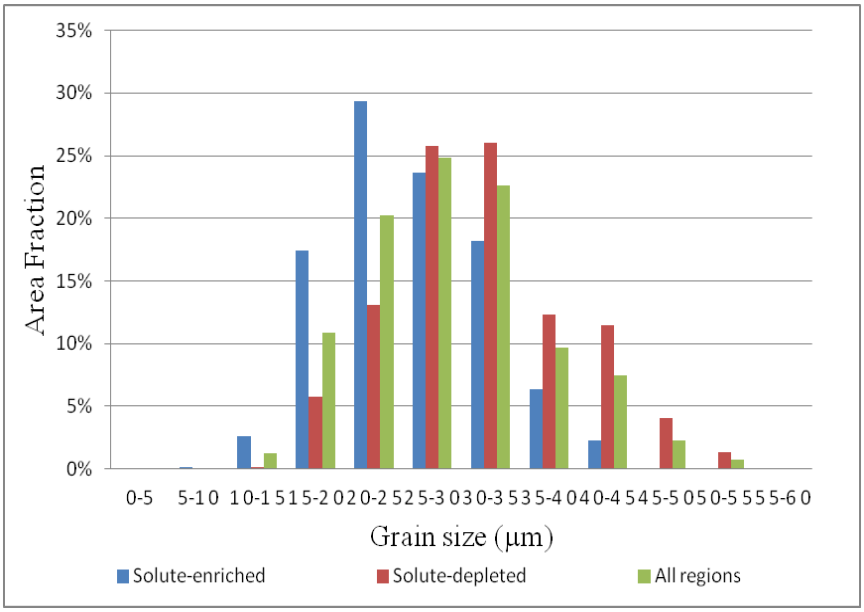

(b)

Figure 6-4 Austenite grain size at 920 ºC for 10 minutes: (a) prior austenite microstructure and (b) overall grain size distribution and distributions in solute-enriched and solute-depleted regions separately.

a. 1050 ºC and 1130 ºC

As-cast specimens were reheated for one hour at temperatures of 1050 ºC and 1130 ºC, higher than the dissolution temperatures of dendritic Nb(C,N) (1030 ºC) and interdendritic AlN (1120 ºC) respectively, as indicated in Figure 4-21, to investigate the grain growth behaviour after these particles were completely dissolved. Micrographs in Figure 6-5 (a, c) demonstrate the similar microstructures consisting of uniform small grains, which are verified by the grain size distributions in Figure 6-5 (b, d). No obvious abnormal or bimodal grain size distributions have been observed at these reheating temperatures. Therefore, it can be considered that the pinning effect provided by the stable dendritic Al-rich particles, which can be used to prevent the grain growth in solute-depleted region (when reheating temperature above the dendritic Nb(C,N) dissolution temperature of 1030 ºC), and the stable interdendritic Nb-rich particles which have restricted the grain growth from the solute-enriched region (above the interdendritic AlN dissolution temperature 1120 ºC). On reheating at 1050 ºC and 1130 ºC, the mode grain size is same with approximately 32.5 μm, as seen in Figure 6-5 (b, d), which is close to the initial austenite grain size (27.5 μm) obtained at 920 ºC, indicating that there is little grain growth at temperatures below 1130 ºC, due to the stable pinning force provided by the particles in the solute-depleted region (Al-rich) and in the solute-enriched region (Nb-rich).

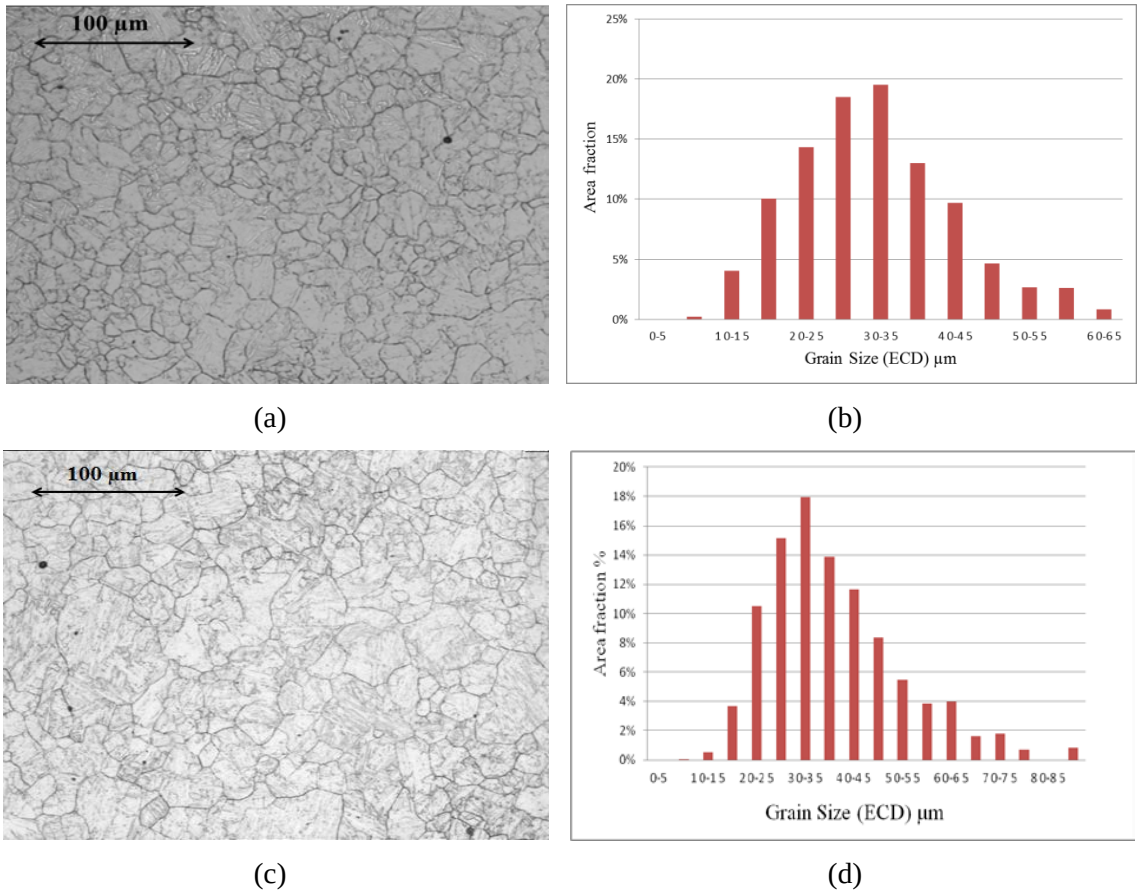

Figure 6-5 Prior austenite grain structures and grain size distributions for the as-cast segregated specimens were reheated for 1 hour at: (a, b) 1050 ºC, above the dissolution temperature of Nb-rich particle in dendritic region; (c, d) 1130 ºC, above to the dissolution temperature of Al-rich particles for the interdendritic region.

b. 1160 ºC and 1200 ºC

Reheating at 1160 ºC (predicted dissolution of AlN in dendritic region) for 1 hour resulted in obvious grain growth as indicated in Figure 6-6 (a). The micrograph shows that the grain structure consists of regions of small grain and large grain. The bands of small grains are more deeply etched by the picric acid etchant, Figure 6-6, corresponding to the original solute-enriched regions, which is similar to the dark etched regions observed in initial prior austenite grain structure reheating at 920 ºC for 10 minutes, as seen in Figure 6-4. This indicates that the grains in the solute-enriched

regions have stayed small due to the strong pinning force supplied by the Nb-rich particles. On this assumption, the large grains formed in the dendritic solute-depleted regions are consistent with the dissolution of the dendritic Al-rich particles. Consequently, the bimodal grain size distribution has been observed with two obvious 'mode' grain sizes (75 μm and 135 μm arrowed in Figure 6-6 (b)), which correspond to the bands of small grains and large grains separately, showing PGSR (peak grain size range, as discussed in section 2.4.3.2) of around 60 μm. Bimodal grain growth is different to abnormal grain growth, for which a few individual very large grains encircled by the small grains are expected. For the bimodal grain structure shown in Figure 6-6 (b) the large grain size (195μm in 95% area fraction) to mode grain size (75 μm) ratio is around 2.6, whilst for the abnormal grain structure seen in the homogenised material (Figure 5-6 (d) for reheating at 1170 ºC) the ratio is approximately 7.1 (mode grain size: 35 μm; large grain size: 250 μm, Figure 5-9). The large grains observed in the segregated material, forming in the solute-depleted regions, are likely to be restricted from further growth when their boundaries reach the solute-enriched region, where the stronger pinning force due to the Nb-rich particles remaining at this temperature is experienced. Therefore, the largest 95% area fraction grain size (195μm) is observed in the dendritic region, which is close to the segregation band separation (approximately 150 ± 50 μm). A typical bimodal grain growth is observed (mentioned above) which is similar to the result reported by Chakrabarti [24] [103] (large grain growth in the dendritic region with no Nb-rich particles, but it is limited by solute-enriched band structure with a large population of Nb-rich particles present, discussed in section 2.4.3.2).

When the reheating temperature was increased to 1200 ºC for one hour, the bands of small and large grains were still observed, as indicated in Figure 6-6(c). The bimodal grain size distribution in Figure 6-6 (d) demonstrates two distinct mode grain sizes of 75 µm and 185 µm (PGSR=110µm). It does not show grain growth in terms of smaller mode grain size (75 µm) compared to that at the lower temperature of 1160 ºC (75 µm), indicating that the interdendritic particles (Nb(C,N)) have prevented the grain growth from the interdendritic region on reheating at 1200 ºC. However, a significant growth in terms of large mode grain size (185 µm) is observed, which is greater than that at 1160 ºC (135 µm), suggesting that the further reduced pinning effect can be expected in the dendritic region (more AlN has dissolved in the dendritic region), and the mobility in the dendritic region at the temperature of 1200 ºC is likely greater than that at 1160 ºC. However, a nearly stable large grain size (95% area fraction) is observed at 1160 ºC (195 µm) and 1200 ºC (205 µm), which means that boundary pinning at the solute-enriched band (provided by interdendritic Nb-rich particles) is still stable to limit dendritic large grain size within the distance of SDAS.

In summary, the typical abnormally large grains (isolated in the smaller grains) have not been seen in the as-cast Al-Nb steel when the Al-rich particles have dissolved over the temperatures range from 1160 ºC to 1200 ºC. However, the ratio of 2.6 (95% area fraction large grains size to mode grain size) in bimodal grain size distribution is greater than the abnormal grains criterion of 1.9 reported from literature [160-162] (as discussed in section 2.4.3.1). The observed large ratio in the bimodal grain size distribution is likely due to the bands of large grains appeared in dendritic regions (bimodal grain growth), which is different to the nature of abnormal grain growth

(isolated by small grains) found in the homogenised Al-Nb steel and literature. The pinning force provided by precipitates from the solute-enriched bands is expected to be the critical factor to influence the grain growth behaviour, which results in a bimodal grain size distribution rather than abnormal grain growth in the as-cast Al-Nb steel.

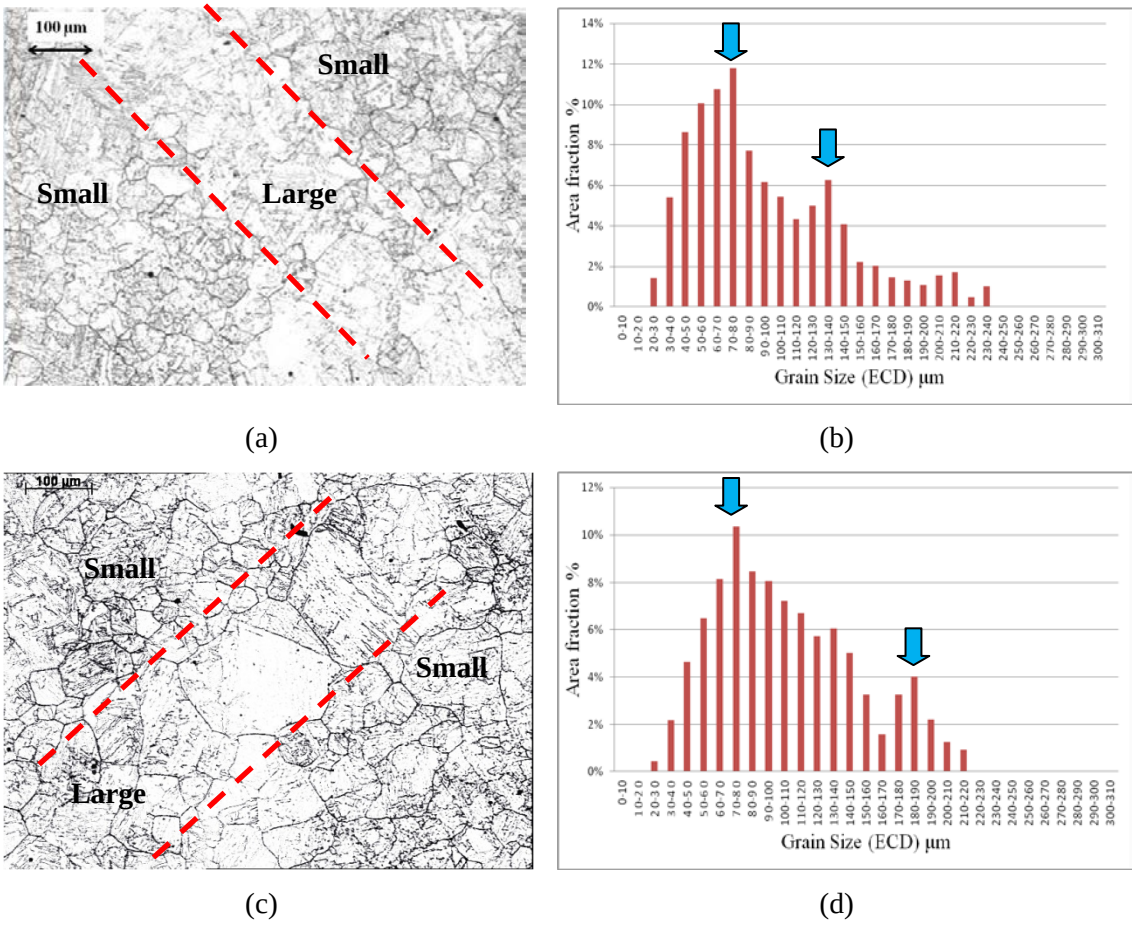

Figure 6-6 Prior austenite grain structures and grain size distributions for the as-cast segregated specimens after reheating for 1 hour at: (a, b) 1160 ºC, corresponding to the Al-rich particles dissolution temperature in the dendritic region; (c, d) 1200 ºC. Blue arrows indicate the mode grain sizes in a bimodal grains size distribution.

c. 1230 ºC , 1280 ºC and 1300 ºC

1230 ºC is the temperature for predicted dissolution of the Nb-rich particles in the interdendritic regions: obvious grain growth has been observed in mode grain size (90

μm) and largest grain size (250 μm: 95% area fraction) compared to that at the low temperature of 1200 ºC (mode grain size of 75 μm and largest grain size of 205 μm), as seen in Figure 6-7 (a, b), which is consistent with the reduced pinning from Nb-rich precipitates in the interdendritic region.

After reheating at 1280 ºC and 1300 ºC most precipitates are expected to be dissolved according to the Thermo-Calc prediction. However, the experimental results show that the weak bimodal grain structure has been observed at high temperature (> 1280 ºC, Figure 6-7 (d, f)), which suggests that some grain growth is likely to be prevented by the undissolved Nb(C, N). On reheating to 1280 ºC for 1 hour, significant grain growth has occurred compared to that at lower temperatures, as shown in Figure 6-7 (c), where the mode grain size has increased to 225 μm and the ratio between the largest and mode grain size is approximately 2.1, Figure 6-7 (d). The results suggest that the large grains in the dendritic region are no longer pinned and can grow at the expense of smaller grains in the interdendritic region, when the interdendritic Nb(C, N) has dissolved.

On reheating to 1300 ºC, the micrograph in Figure 6-7 (e) indicates that the grain structure shows a weak bimodal grain size distribution, Figure 6-7 (f), with two mode grain sizes of 325 μm and 525 μm. This suggests that during reheating of the as-cast (segregated) sample, bimodal distributions may develop and these can then persist through the interdendritic particle dissolution. It is also possible that the DICTRA prediction of the segregation level of Nb is not accurate, i.e. some of Nb-rich particles might not be completely dissolved at the temperatures above 1230 ºC for 1 hour.

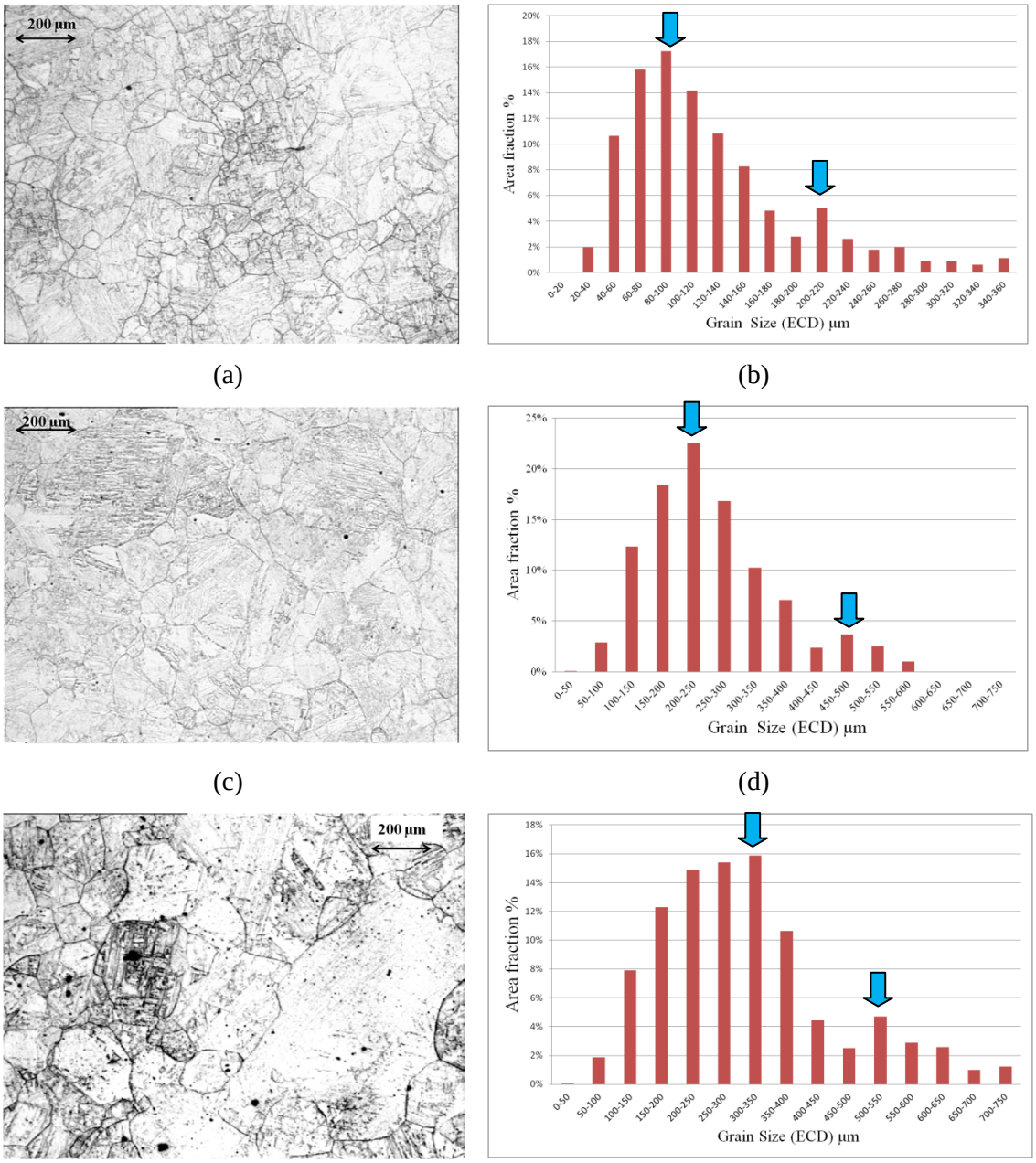

Figure 6-7 Prior austenite grain microstructures and grain size distributions for the as-cast segregated steel after reheating for 1 hour at: (a, b) 1230 ºC, corresponding to the dissolution temperature of interdendritic Nb-rich particles; (c, d) 1280 ºC and (e. f) 1300 ºC at the temperatures where all the particles are expected to be dissolved. Mode grain sizes are indicated by the arrows.

Table 6-1 shows a comparison of bimodal grain growth between Al-Nb cast steel and Slab-1 cast steel [24]. Due to the segregation of Nb, a larger number density of Nb(C,N) particles is expected in the interdendritic region both for Al-Nb steel (2.64×10^4 /mm^2, Table 4-1) and Slab-1 (60×10^4 /mm^2, Table 2-10), compared to the dendritic solute-depleted region (Nb(C,N) in Al-Nb steel: 0.73×10^4 /mm^2 and Slab-1 steel: 12×10^4 /mm^2) respectively. A significantly larger number density of Nb(C,N) has been observed in Slab-1 steel due to its higher Nb content (0.045 wt%) compared to the Al-Nb steel (0.019 wt%). Relatively well distributed AlN has been observed in both Al-Nb steel and Slab-1 steel with a slightly higher number density of particles observed in the Al-Nb steel due to its higher Al content.

On reheating the Al-Nb steel, bimodal grain growth has been observed during reheating at temperatures between 1160 ºC and 1200 ºC (Figure 6-6), which has large mode grain sizes of 135 μm and 185μm separately, but generally less than the secondary dendrite arm spacing (150 ± 50 μm). This result indicates that the precipitates in the interdendritic band provide sufficient pinning force to prevent the large grains growing beyond the dendritic region. This is similar to the observation of bimodal grain growth in Slab-1 steel: on reheating to Slab-1 steel at 1150 ºC, an obvious band of small grains and large grains have been observed (Figure 2-39 (a)), which has a large grain size of 220μm, again less than the measured SDAS (211±36μm) [24]. A large mode grain size to small grain size ratio of 5.5 has been seen in Slab-1 steel, which is significantly greater than the ratio (1.8) observed in the Al-Nb steel (Table 6-1) and a larger PGSR (peak grain size range, as discussed in section 2.4.3.2) has also been observed in Slab-1 steel (180 μm) than that in the cast Al-Nb steel (60-

110 μm), meaning more severe bimodal grain growth has occurred in Slab-1 steel. This may be due to the larger segregation spacing observed in Slab-1 (211 ± 36 μm) than Al-Nb steel (150 ± 50 μm) meaning the grains in the dendritic region (solute-depleted) can grow larger. In addition a smaller mode grain size of 40 μm in the interdendritic area has been seen in Slab-1 steel compared to Al-Nb steel (75 μm), which may indicate a stronger pinning force operating in Slab-1 (due to the larger Nb(C,N) number density being observed), which restrains the grain growth at this region.

Therefore, to minimise the severity of bimodal grain size development, a small SDAS is desired with sufficient pinning particles in the interdendritic region to prevent large grain growth from the dendritic region.

For Al-Nb steel, it has been found that bimodal grain growth occurred at 1160 ºC-1200 ºC, which is at/or higher than the AlN predicted dissolution temperature 1160 ºC, agreeing with the result reported for Slab-1 steel [24] where bimodal grain growth was seen on reheating at 1150 ºC, which is higher than the dendritic-AlN predicted dissolution temperature of 1125ºC in that steel. It indicates that large grain growth in the dendritic region is strongly correlated with the AlN dissolution behaviour. The higher predicted dissolution temperature of AlN in the Al-Nb steel results in a higher reheat temperature required to result in bimodal grain growth. This indicates that a higher content of Al is beneficial in increasing the reheat temperature at which bimodal grain growth occurs and reducing the temperature range over which a bimodal grain structure is seen (e.g. bimodal grain growth occurs at 1160 ºC in Al-Nb steel (0.057 wt% Al) which is higher than 1125 ºC in Slab-1 steel (0.046 wt% Al)).

There is no obvious bimodal grain growth when reheating at the higher temperatures, e.g. the relatively uniform coarse grain structure occurs at reheating temperatures above 1250 ºC in Al-Nb steel and a high reheating temperature at 1225 ºC for Slab-1 steel [24, 25]. This is likely to be due to the decrease of pinning force from interdendritic Nb(C,N) which has dissolved at the predicted dissolution temperature, e.g. predicted Nb(C,N) dissolution temperatures of 1230 ºC in Al-Nb steel and 1225 ºC in Slab-1.

Table 6-1 Comparison of bimodal grain growth between the Al-Nb steel and Slab-1steel [24].

	Al-Nb steel	Slab-1steel [24]
Composition/ wt%	Al: 0.057; Nb:0.019	Al: 0.046; Nb:0.045
SDAS/ μm	150±50	211±36
Solute-enriched Nb(C,N): number/mm^2	2.64× 10^4	60 × 10^4
Solute-depleted Nb(C,N): number/mm^2	0.73× 10^4	12× 10^4
Dendritic AlN dissolution temperature / ºC	1160	1125
Reheated temperature/ ºC	1160-1200	1150
Grain size ratio: large GS/ small GS (μm)	135/75: 1.8	220/40: 5.5
PGSR	60-110	180
PHR	0.4-0.5	0.4

6.2.2 Precipitates characterization in reheated samples

Bands of large and small grains were found in the as-cast steel, after reheating at the critical temperatures range from 1160 ºC to 1200 ºC. SEM analysis was used to investigate the precipitate distribution and any correlation to the occurrence of bimodal grain size development. SEM images in Figure 6-8 (a, b) show the typical bands of large and small grains in the sample reheated to 1160 ºC, where the band separation distance (between two adjacent small grains bands) is similar to the secondary dendrite

arm spacing (150 ± 50 μm) measured in the as-cast microstructure. The coarse Al-rich particles (of around 250-300 nm size) found in the large grain regions, Figure 6-8 (c), have been confirmed by the Al peak indicated in the EDS spectrum (in Figure 6-8 (d)). The presence of Al-rich particles in the dendritic regions indicates that complete dissolution of AlN particle based on Thermo-Calc prediction, has not occurred at the predicted dissolution temperature of 1160 ºC.

Spherical Nb-rich particles were discovered in the fine-grained bands and were often present in clusters with a higher number density than that of Al-rich particles, as indicated in Figure 6-8 (f). The EDS analysis in Figure 6-8 (g) shows a peak of Nb present in the spectrum taken from the investigated particles. There were no Nb-rich particles observed in the coarse-grained bands (expected as the reheating temperature was higher than the dissolution temperature for Nb-rich particles in the solute-depleted regions). A few Al-rich precipitates present in the large-grained region appeared to be insufficient to restrict grain growth resulting in the large grains developing from the dendritic solute-depleted regions. The results suggest that the high number density of Nb-rich particles found in the fine-grained bands provides effective pinning (large number density) in the solute-enriched region to prevent the large grains formed in the dendritic regions.

When the as-cast steel was reheated at 1200 ºC for 1 hour, the bimodal structures were still observed in SEM images, Figure 6-9 (a), showing bands of large and small grains. Similar to the sample reheated at 1160 ºC, Nb-rich particles were also observed in the fine-grained region of the 1200 ºC reheated sample, providing the pinning force limiting grain growth not only in the solute-enriched region (resulting in bands of small

grains) but also for the dendritic large grains. No Al-rich particle was found in the reheated sample which was consistent with that more grain growth occurred in the solute-depleted region but limited by the solute-enriched bands (i.e. when reaching the segregation band separation of 150 ± 50 μm), as evidenced by the larger mode grain size (185 μm) at 1200 ºC, Figure 6-6 (d), than that at 1160 ºC (135 μm), Figure 6-6 (b).

Therefore, it can be seen that the development of bimodal grain structure in Al-Nb containing steel is consistent with the particle distributions and local dissolution temperatures in the dendritic structures, i.e. the large grain growth in the solute-depleted dendritic region is caused by the dissolution of Al-rich particle, whilst the remaining Nb-rich particles in the solute-enriched (interdendritic) region maintain the smaller grain size in this area.

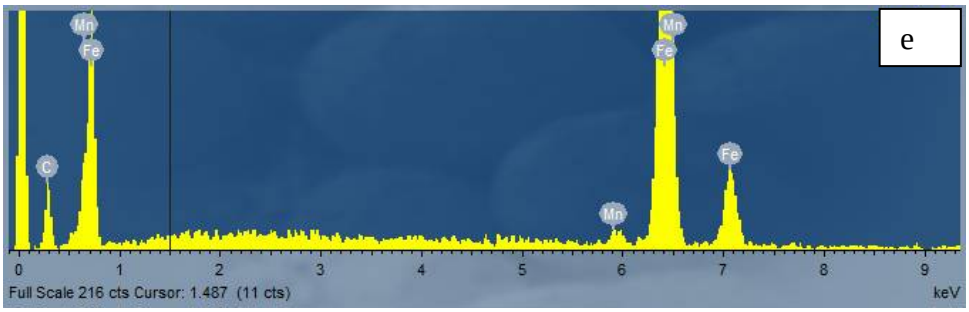
e
Mn
Fe
C
Mn
Fe
Fe
Mn
0 1 2 3 4 5 6 7 8 9
Full Scale 216 cts Cursor: 1.487 (11 cts)
keV

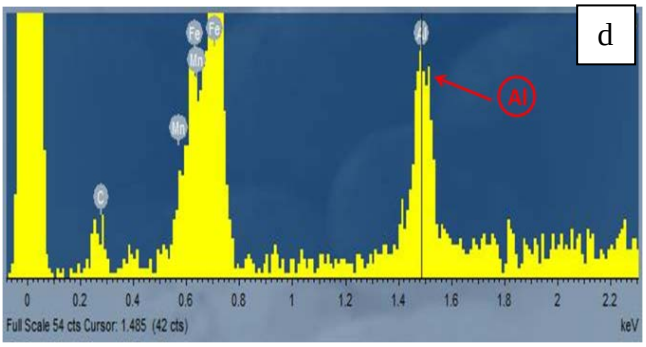
d
Fe
Fe
Mn
Mn
C
Al
0 0.2 0.4 0.6 0.8 1 1.2 1.4 1.6 1.8 2 2.2
Full Scale 54 cts Cursor: 1.485 (42 cts)
keV

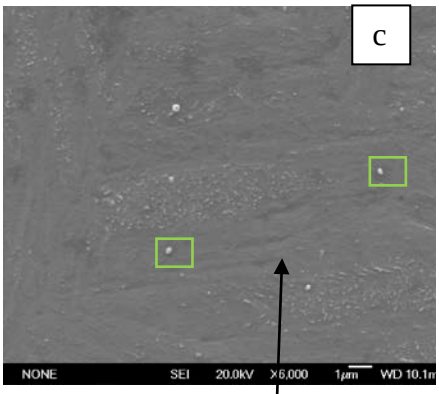
c
NONE SEI 20.0kV X6,000 1μm WD 10.1m

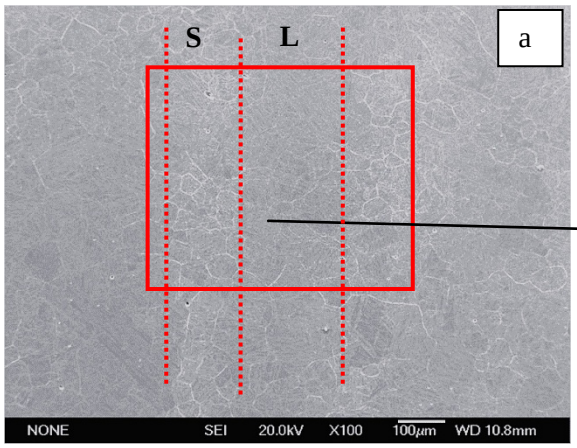
a
S
L
NONE SEI 20.0kV X100 100μm WD 10.8mm

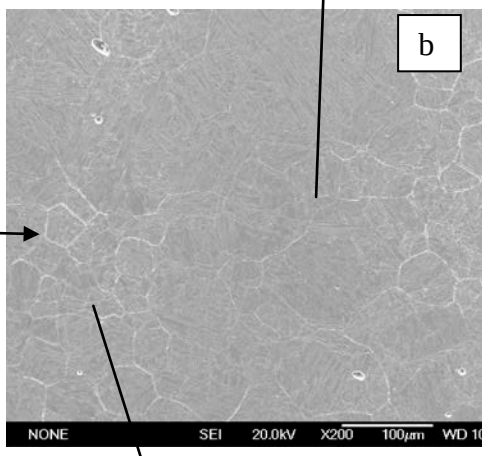
b
NONE SEI 20.0kV X200 100μm WD 1

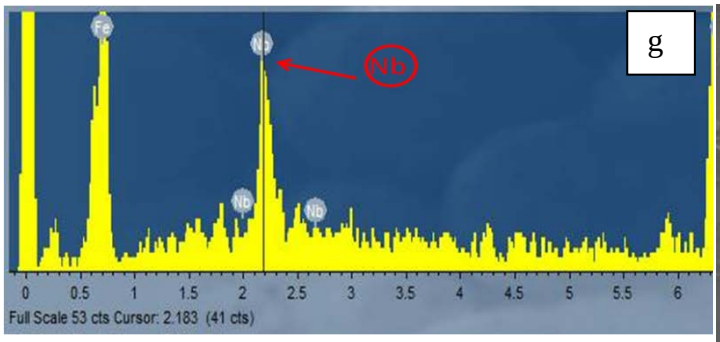
g
Fe
Nb
Nb
Nb
Nb
0 0.5 1 1.5 2 2.5 3 3.5 4 4.5 5 5.5 6
Full Scale 53 cts Cursor: 2.183 (41 cts)

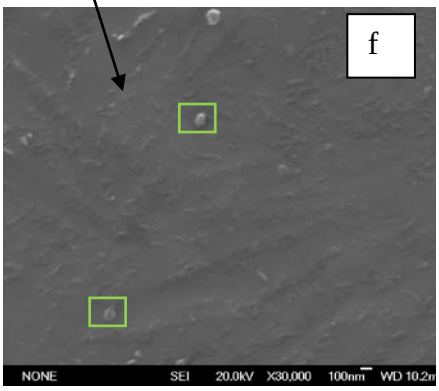
f
NONE SEI 20.0kV X30,000 100nm WD 10.2m

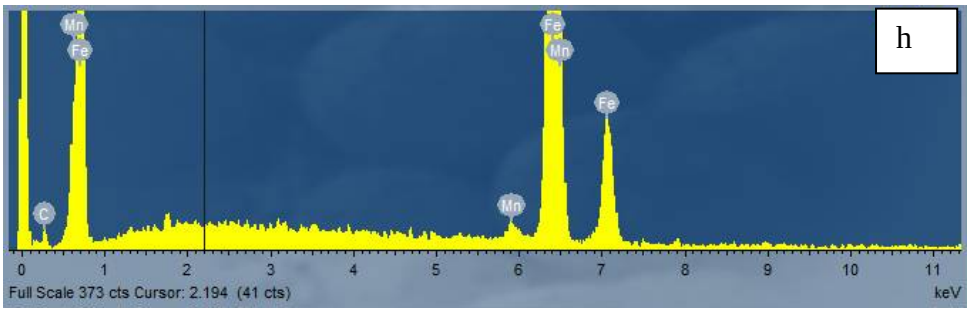

Figure 6-8 Precipitates distributed in segregated specimens after reheating at 1160 ºC for 1 hour: (a, b) bands of large and small grains under SEM images (S: small grain area; L: large grain area); (c) Al-rich particles, expected to be AlN present in the large grain region and (d) EDS trace indicating the Al peak; (f) Nb-rich precipitates, expected to be Nb(C,N) present in small grains region and (g) EDS trace indicating the Nb peak; (e, h) EDS analysis in matrix.

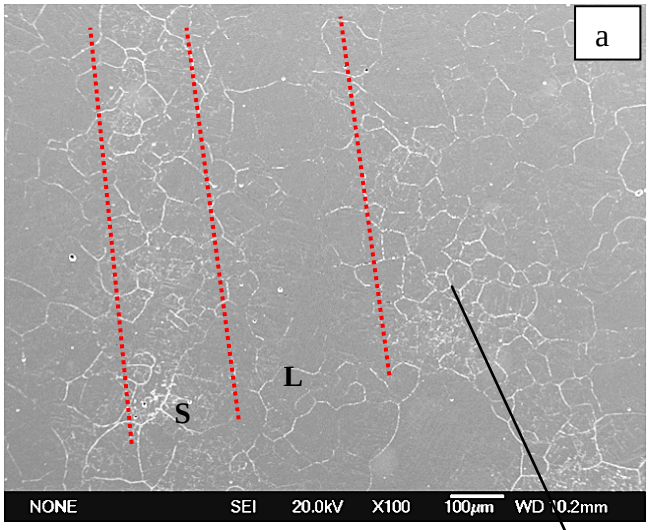
a
L
S
NONE SEI 20.0kV X100 100µm WD 10.2mm

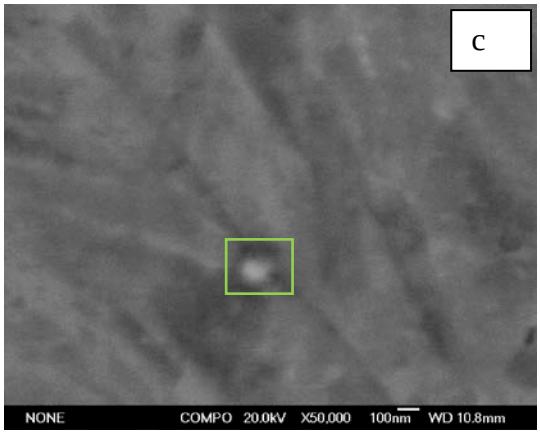
c
NONE COMPO 20.0kV X50,000 100nm WD 10.8mm

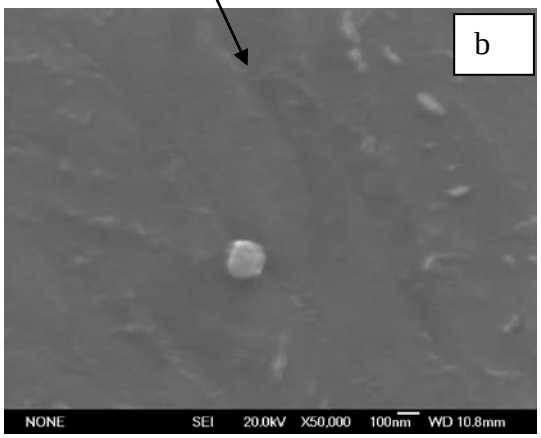
b
NONE SEI 20.0kV X50,000 100nm WD 10.8mm

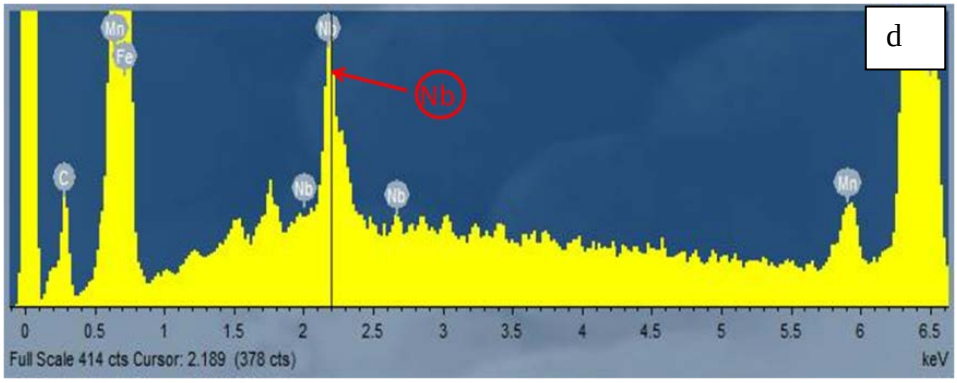
d
Mn
Fe
Mn
Nb
C
Nb
Nb
Mn
0 0.5 1 1.5 2 2.5 3 3.5 4 4.5 5 5.5 6 6.5
Full Scale 414 cts Cursor: 2.189 (378 cts)
keV

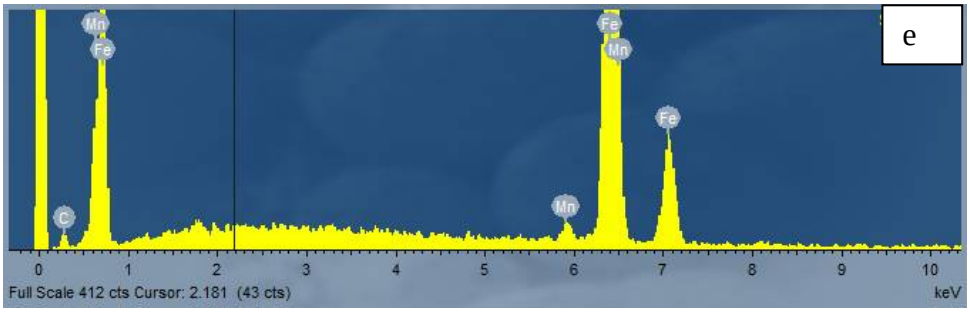
e
Mn
Fe
Fe
Mn
Fe
C
Mn
0 1 2 3 4 5 6 7 8 9 10
Full Scale 412 cts Cursor: 2.181 (43 cts)
keV

Figure 6-9 Particles distribution in as-cast steel, after reheating at 1200 ºC for 1 hour: (a) banded microstructure showing obvious large grains (indicated as 'L') and small grains (indicated as 'S') under SEM image; Nb-rich precipitates present in the small grain bands in SE image (b) and BSE image (c); and (d) EDS trace indicates the Nb peak; (e) EDS analysis in matrix.

6.2.3 Grain growth behaviour over full reheating temperature range

Grain size development was further examined for more reheating temperatures in the range from 950 ºC to 1300 ºC, as shown in Figure 6-10. The grain growth curve of the as-cast sample was plotted by using the smaller mode grain size if the bimodal grain growth occurred. The grain growth behaviour is discussed in each of the different temperature ranges as follows.

When reheating for one hour in the temperature range of 950 ºC - 1130 ºC, there was no grain growth observed which indicated the stable grain size approximately of 30 µm, as shown in Figure 6-10. Reheating at 1150 ºC and 1160 ºC for one hour resulted in obvious grain growth with the mode grain size increasing from around 30-35 µm for reheated temperatures <1150 ºC to approximately 75 µm at 1160 ºC. The large grain size for the 95% area fraction also increased significantly from approximately 45-65 µm for reheating temperatures below 1150 ºC to around 195 µm at 1160 ºC. A further increase in reheating temperature to 1185 ºC and 1200 ºC resulted in similar grain growth compared to 1160 ºC, as seen in Figure 6-10, which indicated the similar grain size at 1200 ºC with a stable mode grain size of 75 µm being observed and the 95% area fraction grain size increasing slightly to be approximately 205 µm. It indicated that the development of bimodal grain growth was stable for the temperature range of 1160 ºC -1200 ºC resulting in a flat curve with a stable size development in Figure

6-10. Reheating for one hour in the temperature range of 1230 ºC-1300 ºC resulted in the significantly grain growth with the steep curves (> 1230 ºC), as shown in Figure 6-10, which indicated that the pinning force in the interdendritic solute-enriched region was ineffective (presumably due to the dissolution of interdendritic Nb(C,N) at 1230 ºC) at these high temperatures.

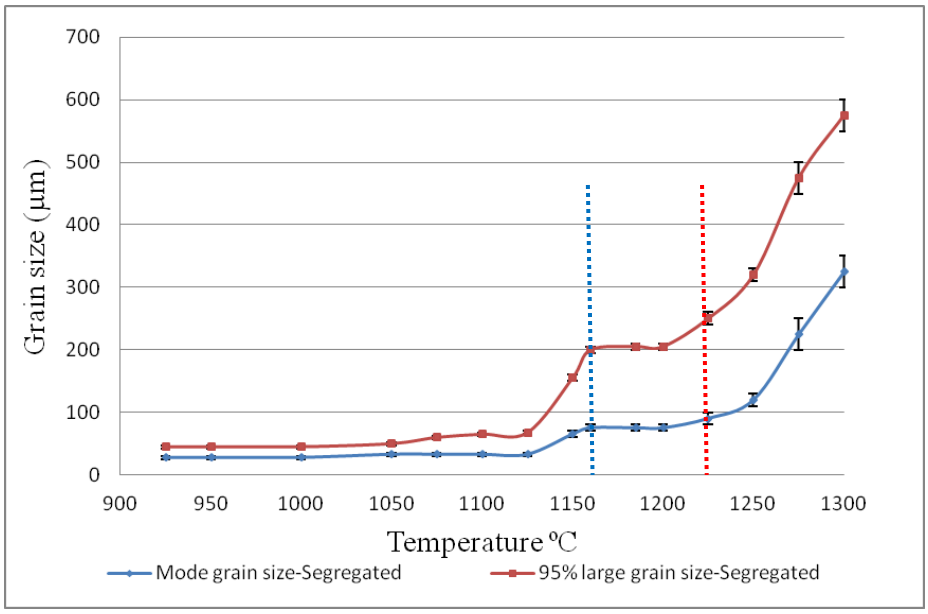

Figure 6-10 Grain size development with reheat temperatures from 950 ºC - 1300 ºC for the as-cast, segregated steel in terms of mode grain size and 95% large grain size. The blue dashed line indicates the predicted dissolution temperature of the pinning dendritic AlN; and the red one indicates the predicted dissolution temperature of the interdendritic Nb(C,N).

Reported grain size development in C-Mn steel was used to compare to the measured 95% area fraction large grain size, as shown in Figure 6-11. On reheating at low temperatures (<1150 ºC), a flat growth trend (a stable size is approximately 50-60 µm) can be observed for the measured grains due to there being little grain growth expected in the as-cast Al-Nb steel, which is generally less than the grain sizes of C-Mn steel. This indicates that the pinning effect is expected (pinned by AlN and Nb(C,N)) to

prevent the grain growth at this temperature. On reheating at 1150 ºC, the largest grain size (in 95% area fraction) shows a markedly growth in size of around 150 μm which is less than the grain size in C-Mn steel (220 μm), but significantly larger than the grain size of 50-60 μm in Al-Nb steel at low temperature (<1150 ºC). This result means that some large grain growth has occurred from the dendritic region, which is due to the dendritic AlN starting to dissolve when close to its predicted dissolution temperature at 1160 ºC. From 1160 ºC to 1200 ºC, the stable size of around 200 μm has been observed for the large grains due to the pinning effect from the interdendritic precipitate, and this results in a flat curve differing from the grain size curves in C-Mn steel. It means that the pinning effect from the interdendritic band in the as-cast steel can be expected to prevent the large grains growth from dendritic region when dendritic AlN has dissolved.

The limiting grain size proposed previously (Figure 6-2 in section 6.1) was used to examine the grain growth in the as-cast (segregated) material with increase of reheating temperature. According to the criterion of abnormal grain growth (Z=1.9), the curves of limiting grain sizes are given in solute-enriched and solute-depleted regions respectively, Figure 6-12, which shows that the experimentally measured large grain sizes (95% area fraction) are close to the limiting grain sizes predicted in the dendritic region. A larger grain size (150 μm) has been observed at 1150 ºC than the limiting grain size (125 μm), which means that abnormal grain growth can take place but is limited by the segregation bands (Nb-enriched region) during growth. Abnormal grain growth would be expected at temperatures of around 1230 ºC (when interdendritic Nb(C,N) particles have dissolved), but as the microstructure at this point

is bimodal, rather than uniform, then no abnormal grain growth (with nature of isolated large grains) has been observed. Therefore, the prediction of limiting grain growth for as-cast (segregated) condition is not consistent with the experimental grain growth as assumed in section 6.1.

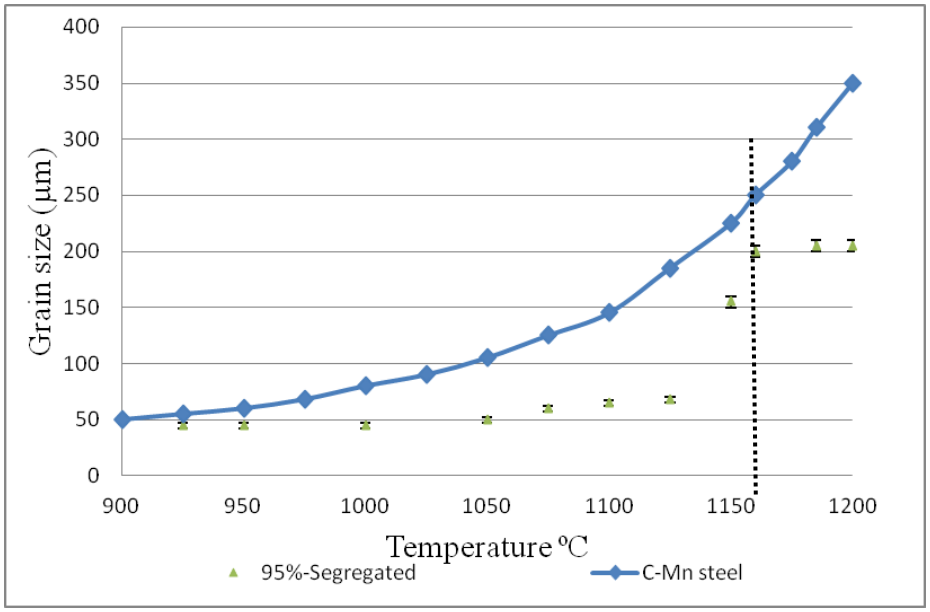

Figure 6-11 Comparison between the largest 95% area fraction grain size and the grain size development from C-M steel (Figure 2-31). Dashed line represents the dissolution temperature of dendritic AlN.

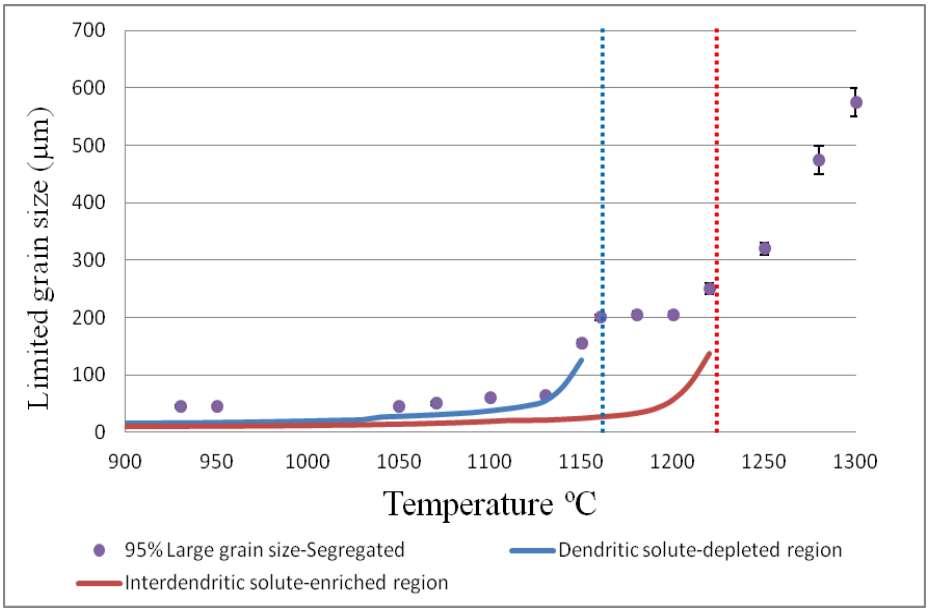

Figure 6-12 Limiting grain size compare to the measured large grain size at 95% accumulated area fraction. The blue dashed line indicates the dissolution temperature of AlN in the dendritic region; and the red dashed line indicates the dissolution temperature of Nb(C, N) in the interdendritic region.

6.2.4 Grain growth with the increased holding time

It was found that bimodal grain growth occurred in the temperatures range of 1160 ºC-1200 ºC for one hour, which is related to the pinning force supplied by solute-enriched bands. Reheating trials for two and three hours were carried out at the temperatures of 1160 ºC, 1185 ºC and 1200 ºC, to investigate if abnormal grain growth occurred with prolonged reheating time or whether the bimodal grain structure seen after one hour reheating was retained.

Figure 6-13 (a, b) shows the grain structures obtained after reheating at 1160 ºC for 2 and 3 hours, where the obvious bimodal structure of coarse and fine grains remains. It does not show any formation of abnormal large grains, which indicates that the segregation bands (Nb-enriched regions) are still effective in restricting any grain

growth from the dendritic region. The grain size distribution is given in Figure 6-13 (c), where the grain size class shifts from left (smaller grain size) to right (coarser grain size) slightly after 3 hours. However, the mode grain size does not show any obvious growth from 1 hour (75 μm), to 2 hours (75 μm) to 3 hours (90 μm). There is no obvious expansion of the grain size range observed which corresponds to the fact that these large grains are still limited by the spacing of segregated bands.

At 1200 ºC, when the reheating time was increased from one to three hours, the micrographs in Figure 6-14 (a, b) show that growth occurred for the large grains whilst some smaller grains still remained. The mode grain size is shifted in the grain size distribution, as shown in Figure 6-14 (c): reheating time of 1 hour (75 μm), to 2 hours (110 μm) and 3 hours (150 μm). This suggests that there is less stable pinning in the segregated band region for the large grain growth when the reheating times have increased at 1200 ºC.

Further reheating treatments were examined at 1185 ºC, increasing the reheating time from 1 to 2 and 3 hours. The grain growth behaviour for all three temperatures with increasing reheating time is summarised in Figure 6-15. At 1200 ºC the grain sizes are similar to those at 1160 ºC and 1185 ºC after one hour reheating but increase further on longer reheating times, showing more obvious growth compared to the relatively stable grain sizes at 1160 ºC. These results suggest that there is a sufficient driving force to overcome the interdendritic pinning force with increasing reheating time, when there is some localised dissolution of the interdendritic precipitates and/ or coarsening of these precipitates such that the pinning force is reduced.

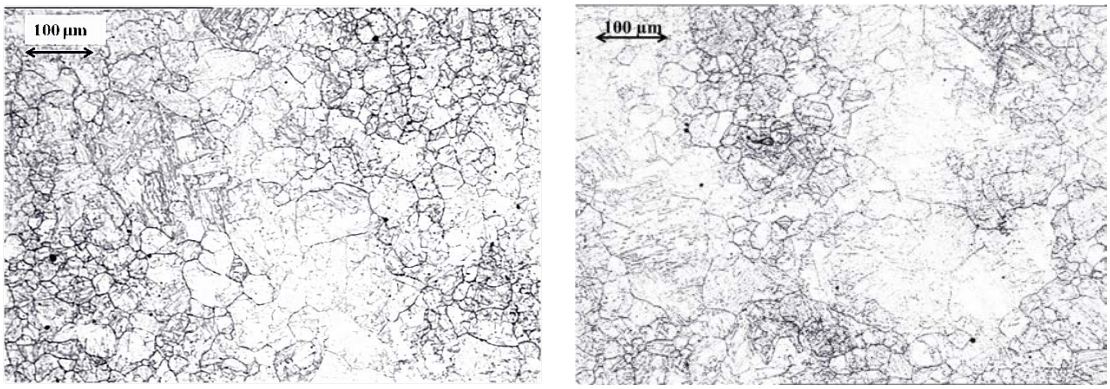

(a) (b)

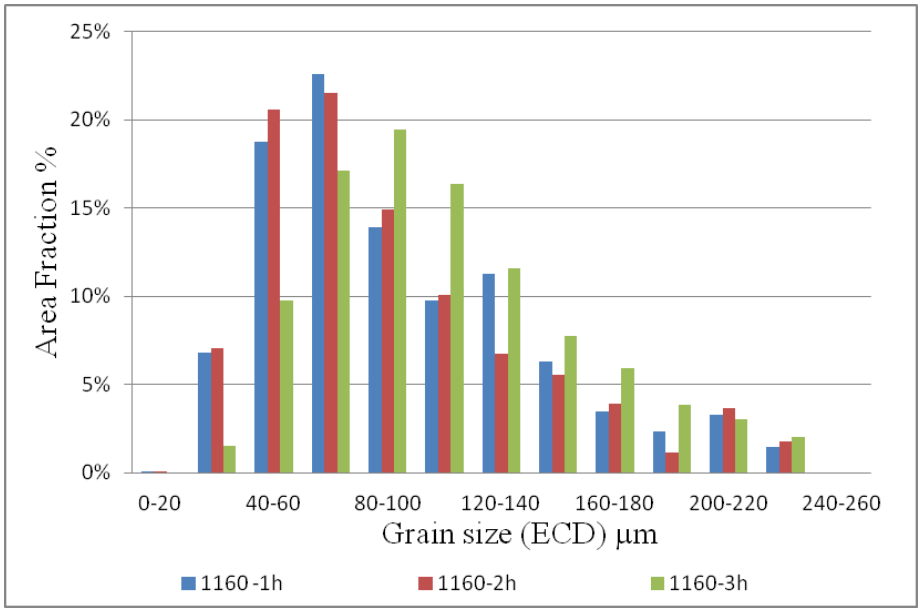

(c)

Figure 6-13 Prior austenite microstructure of bimodal grain growth (bands of large grains and small grains) at 1160ºC for: (a) 2 hours; (b) 3 hours; (c) grain size distribution at 1160 ºC for 1, 2 and 3 hours.

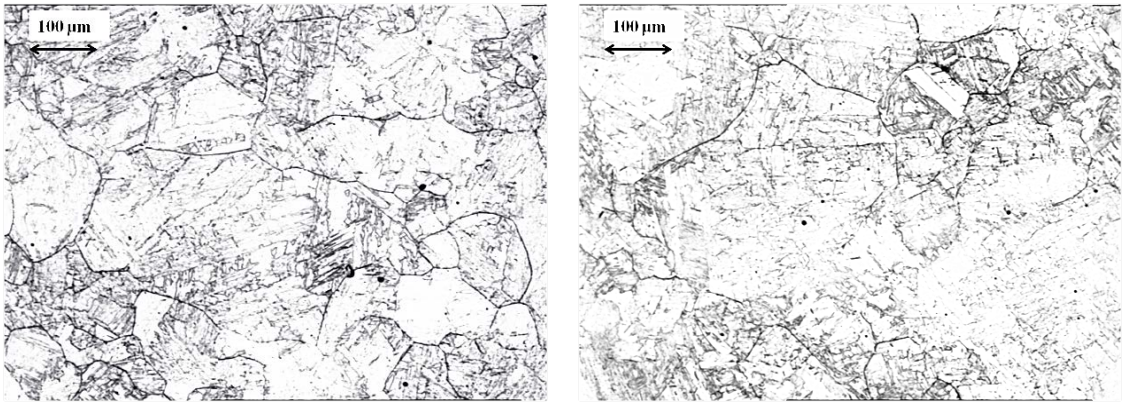

(a) (b)

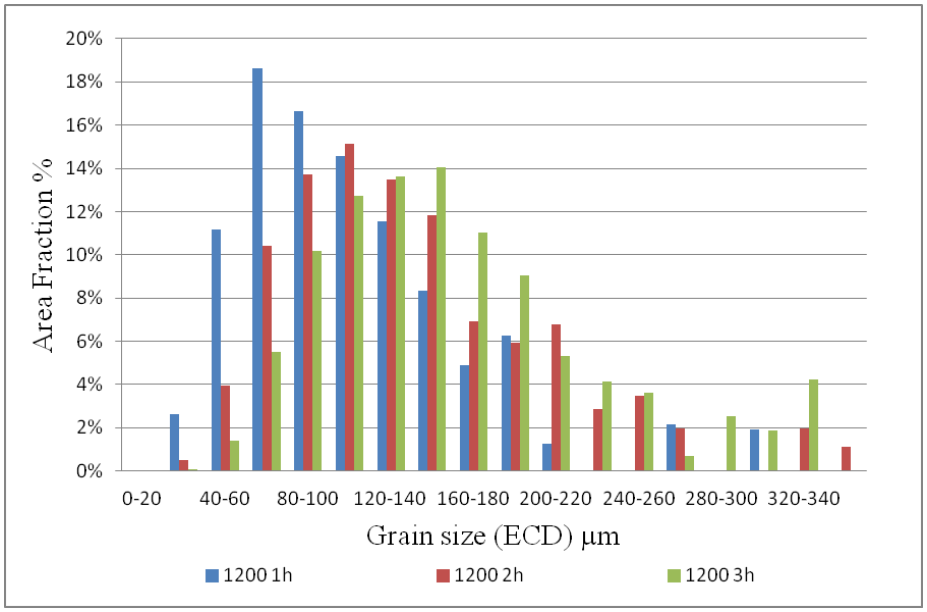

(c)

Figure 6-14 Prior austenite microstructure of bimodal grain growth at 1200 ºC for: (a) 2 hours; (b) 3 hours; (c) grain size distribution of 1200 ºC for 1, 2 and 3 hours.

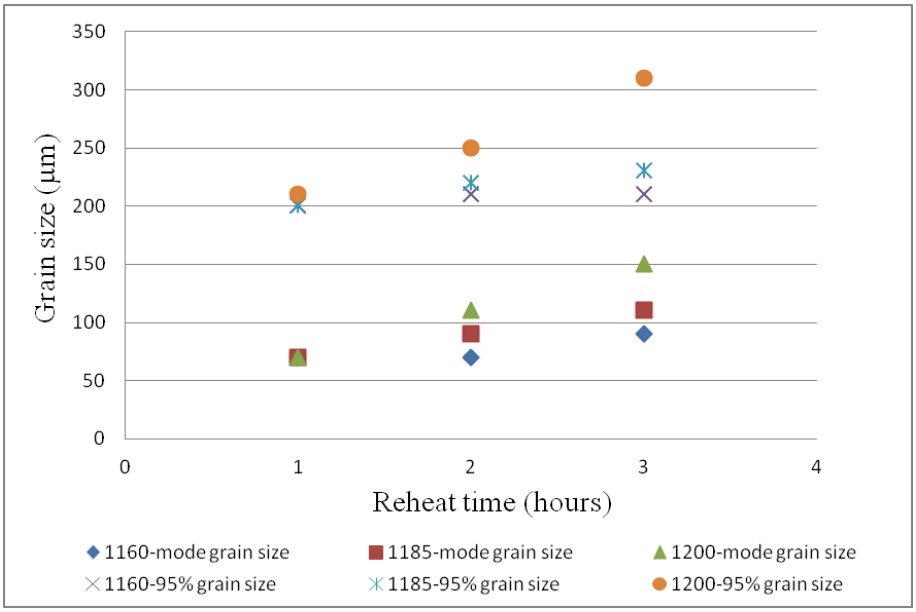

Figure 6-15 Grain growth development in mode grain size and 95% large grain size for 1160 ºC, 1185 ºC and 1200 ºC, reheating times for 1 hour, 2 hours and 3 hours.

6.3 Summary and discussion

Based on grain growth from the reheating trials for the as-cast (segregated condition) specimens, the addition of Al in Nb-containing steel can result in a uniform grain size, with AlN particles preventing grain growth in the dendritic region after the dendritic Nb-rich particles have dissolved, but before the dissolution of Al-rich particles (at 1160 ºC for the present steel).

The grain growth behaviours for the homogenised and segregated conditions are compared in Figure 6-16, and show little/ no grain growth in both conditions before the dissolution temperatures of Al-rich particle have been reached (1170 ºC in homogenised condition and 1160 ºC in segregated condition). This indicates that a uniform structure can be achieved in Nb-containing steel when Al-rich particles are present (before the dissolution of Al-rich particles), independent of the initial element

distribution. After reaching the critical temperatures (Al-rich particle dissolution temperature in each condition), abnormal large grains have occurred in the homogenised condition whilst most grains have a stable fine size; bimodal grains have developed in the segregated condition with bands of small and large grains. There is no obvious abnormally large grain growth in the as-cast Al-Nb steel due to the pinning force supplied in the segregated bands (containing Nb-rich particles), meaning large grain growth in the dendritic region is limited to the spacing of the interdendritic regions, which is equal to the SDAS of around 150 ± 50 μm. The bands of coarse grains and fine grains with a ratio between the largest (95% area fraction grain size) and mode grain size of 2.6 has achieved at 1160 ºC in the as-cast Al-Nb steel, which is significantly less than the ratio of 7.1 for the typical abnormal large grain growth observed at 1170 ºC in the homogenised Al-Nb steel. It is found that the abnormal grain growth has taken place over a certain temperature (1170 ºC) which is narrower than the temperatures range (1160 ºC -1200 ºC) for bimodal grain growth in the as-cast segregated condition.

Figure 6-17 shows the different grain growth behaviour under conditions when pinning Al-rich precipitates have dissolved for the homogenised and as-cast material. With increase of the reheating times, similar grain growth behaviour has been observed in terms of the mode grain size in both conditions. Obvious grain growth can be seen for the large grains in the homogenised samples, which differs from the limited grain growth in the as-cast steel, due to the effective pinning from the precipitates in the segregated bands. Further investigation indicates that the pinning force from the segregated bands is still effective on reheating at the temperature range from 1160 ºC

to 1200 ºC for 1 hour. However, the pinning force is reduced at 1200 ºC with longer reheating times.

The experimental results suggest that the dissolution temperatures predicted by Thermo-Calc for the as-cast material are reasonably accurate for determining the temperature range when different grain growth behaviours are expected, either resulting in bimodal grain structures (when dendritic pinning precipitates have dissolved) or coarse grain structures (when the more stable interdendritic precipitates have dissolved). The limiting grain size predicted in the dendritic region agrees with the measured large grains, until reheating at 1150 ºC (close to the AlN dissolution temperature of 1160 ºC), when a measured large grain size of 150 μm has been observed which is greater than the limiting grain size of 125 μm. No abnormal grains were observed when reheated above interdendritic Nb(C,N) dissolution temperature (>1230 ºC), as the bands of coarse grains have developed in segregated steel instead of an abnormally large grain isolated from smaller grains.

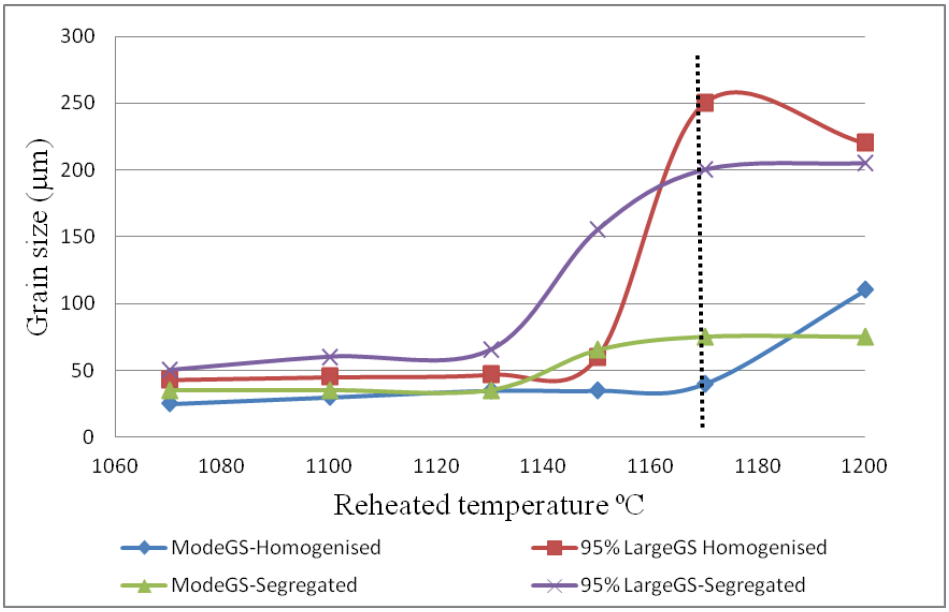

Figure 6-16 Grain growth behaviour in homogenised and segregated Al-Nb steels, after reheating in the temperature range from 1070 ºC to 1200 ºC. Approximate predicted dissolution temperature of Al-rich particles is indicated as dark dotted line.

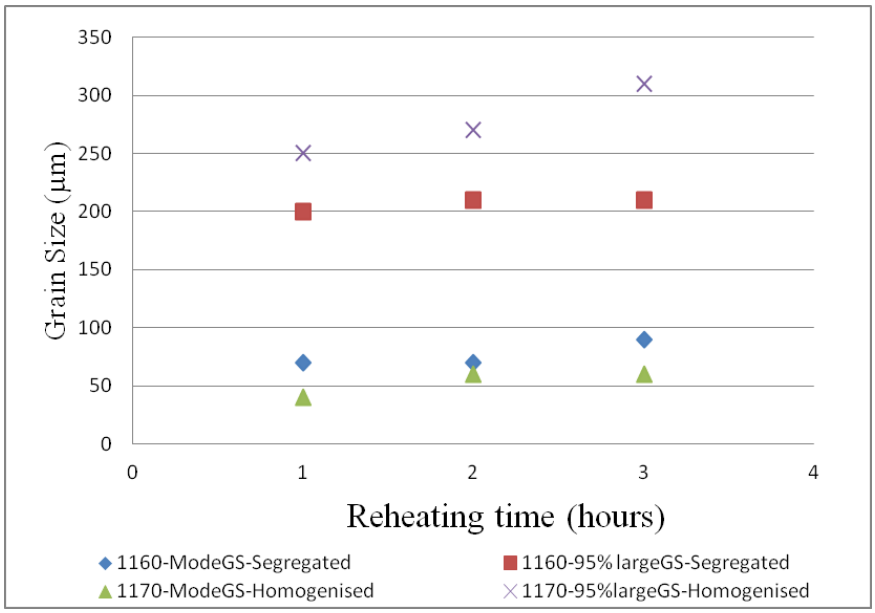

Figure 6-17 Grain growth behaviour with increased reheating times at: 1160 ºC for as-cast (segregated) condition; and 1170 ºC for homogenised condition. (GS: grain size).

chapter 7 Grain growth in forged Al-Nb steel and rolled Nb-containing steel

It has been found that the segregated bands in the as-cast steel can restrict grain growth from the dendritic regions (solute-depleted regions) during reheating, and prevent the occurrence of abnormal grains, although a bimodal grain structure can be formed, as discussed in Chapter 6. In order to investigate whether the distance between the segregation bands has any effect on grain size development, several reheating trials were carried out on the Al-Nb containing steel after it had been forged to reduce the segregation band separation distance. The forged sample was subjected to the same reheating trials as the as-cast steel and the grain sizes examined.

7.1 Initial microstructure for the forged Al-Nb sample

7.1.1 Microstructure and segregation bands

Figure 7-1 shows a structure with distinct dark bands (pearlite phase) separated by ferrite with a spacing of around 65 ± 10 μm, which is significantly smaller than the secondary dendrite arm spacing observed in the as-cast condition (150 ± 50 μm), where the ratio of the two spacing is around 0.4. This indicates that the deformation of 70% (0.7 strain applied), i.e. 40 mm height to 12 mm height (ratio of 0.3) has reduced the spacing of the segregation bands approximately as expected (some barrelling of the sample occurred meaning the reduction is less than theoretically predicted). Most of the pearlite bands observed in the forged Al-Nb steel are continuous.

Figure 7-2(a) shows the starting prior austenite microstructure in the forged sample reheated at 920 ºC for 10 minutes, indicating that the microstructure consists of more

deeply etched segregation bands separated by lighter grey areas, which is similar to the as-cast condition, Figure 6-4, due to solute enrichment. A fine and uniform grain structure has been developed at this temperature, with a slightly smaller mode grain size (12.5 μm) in the solute-enriched region compared to that in the solute-depleted region (17.5 μm), whilst a similar mode size of 17.5 μm has been found overall.

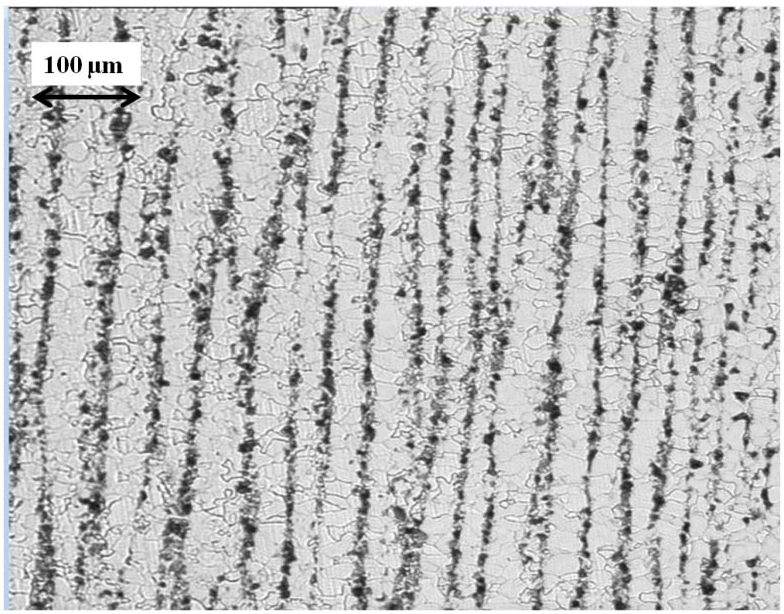

Figure 7-1 Initial microstructures of ferrite and pearlite in the forged Al-Nb sample.

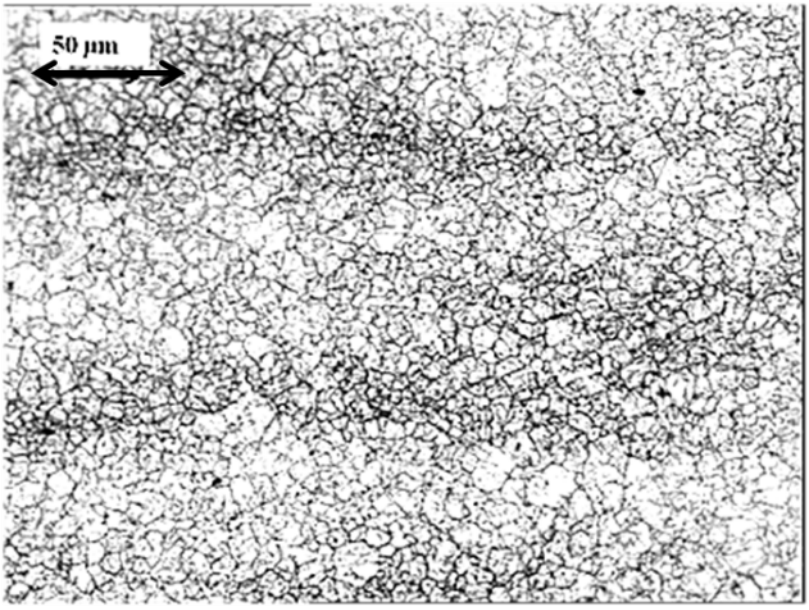

(a)

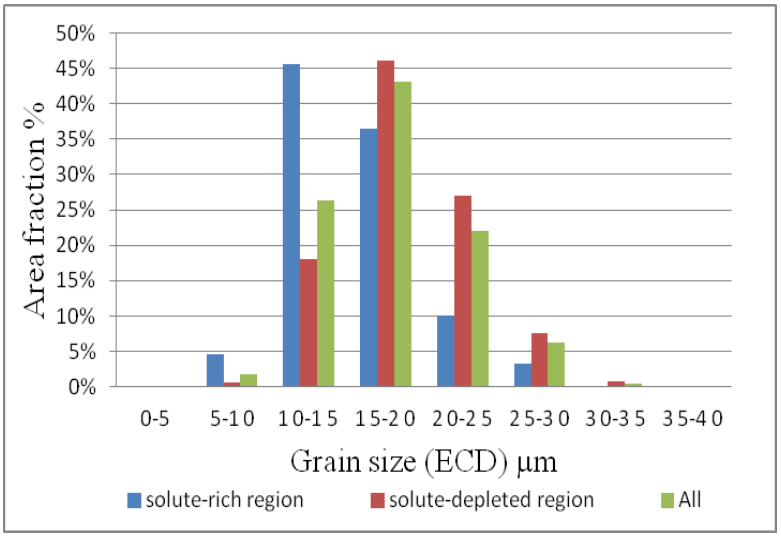

(b)

Figure 7-2 Starting grain size at 920 ºC for 10 minutes: (a) prior austenite microstructure and (b) grain size distribution in regions of solute-enriched and solute-depleted, and for the overall regions.

7.1.2 Precipitate characterization in initial forged sample

The precipitates were characterised in the slow cooled (ferrite and pearlite) forged sample by SEM analysis in the solute-depleted (ferrite) and solute-enriched (pearlite) regions. The micrographs in Figure 7-3 (a, b) show the distribution of Al-rich and Nb-

rich precipitates in the pearlite region characterised by SE (Secondary-Electron) and BSE (Back-Scattered Electron) images, with EDS analysis for Al and Nb identification. The solute-enriched region is not entirely comprised of pearlite, as some ferrite regions, wholly within pearlite, can also be in the solute-enriched region [38], as discussed in section 2.3.3. Precipitates from solute-enriched regions were therefore characterised and identified in regions of pearlite and isolated ferrite. A large number of Nb-rich particles, expected to be Nb(C, N), were observed in the solute-enriched bands appearing bright, in the BSE image in Figure 7-3 (b). The EDS spectrum from a spherical Nb-rich particle in Figure 7-3 (c) indicates an Nb peak as shown in Figure 7-3 (d). Al-rich particles, expected to be AlN, were also observed in the solute-enriched regions as dark spots, as shown in Figure 7-3 (b). The Al peak was identified in the EDS spectrum analysis in Figure 7-3 (f), confirming the particle in Figure 7-3 (e) to be Al-rich. It has been found that the precipitates could be characterised by SE and BSE image analysis based on their morphology (appropriate shape and size) and contrast. Figure 7-4 (a) shows many Al-rich particles present in the ferrite solute-depleted region, corresponding to the dark spots observed in Figure 7-4 (b). The Nb-rich particles were observed to coexist with the Al-rich particles, shown in Figure 7-4(c), i.e. the bright spot indicated close to the dark Al-rich particles in Figure 7-4 (d). The cluster of particles in Figure 7-4 (e, f), were determined to be Al-rich precipitates.

The size distribution, presented as number density in Figure 7-5 (a), and area fraction in Figure 7-5 (b) of the particles was measured. The particle distributions in the forged condition are similar to those presented in the as-cast samples (Figure 4-8), i.e. a lower number density and area fraction (or volume fraction) of Nb-rich particles in the

solute-depleted region (ferrite) compared to the solute-enriched regions, as expected from the predicted segregated composition. There are more Al-rich particles in the ferrite regions, compared to those in pearlitic regions, which agrees with the distribution of AlN particles found in the as-cast Al-Nb steel. A large numbers of Nb-rich particles, with a size of around 100-150 nm are present in the solute-enriched pearlite region which is similar to the as-cast condition. A larger number density of Al-rich particles is present in the solute-depleted region compared to the dendritic Nb-rich particles, and the reheating work on the as-cast material suggests that they can control grain growth in this region before the critical temperature for their dissolution has been reached (predicted as 1160 ºC).

In summary, the precipitate distributions in the forged sample (Al-rich and Nb-rich particles in the solute-enriched and solute-depleted regions) are generally similar to that in the as-cast condition.

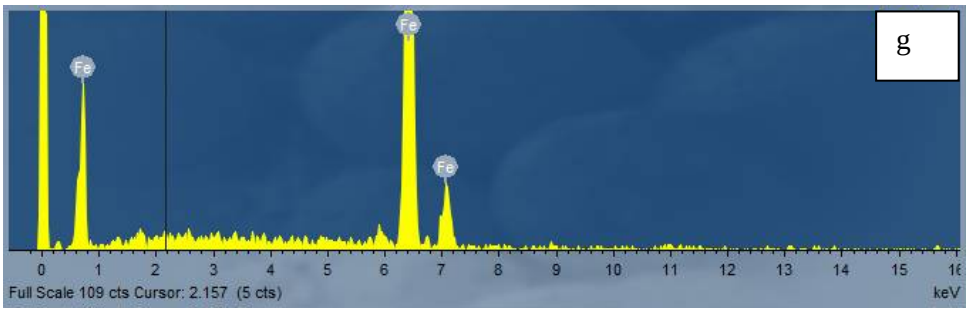
g
Fe
Fe
Fe
0 1 2 3 4 5 6 7 8 9 10 11 12 13 14 15
Full Scale 109 cts Cursor: 2.157 (5 cts)
keV

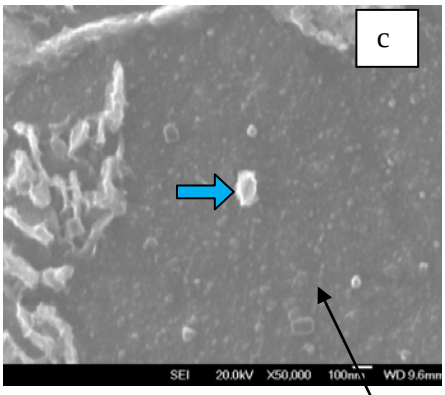
c
SEI 20.0kV X50,000 100nm WD 9.6mm

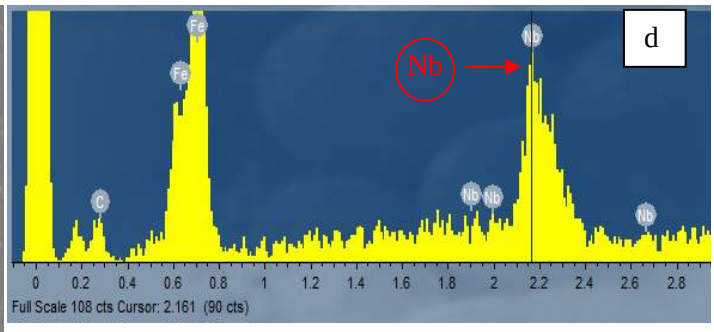
d
Fe
Fe
Nb
Nb
C
Nb Nb
Nb
0 0.2 0.4 0.6 0.8 1 1.2 1.4 1.6 1.8 2 2.2 2.4 2.6 2.8
Full Scale 108 cts Cursor: 2.161 (90 cts)

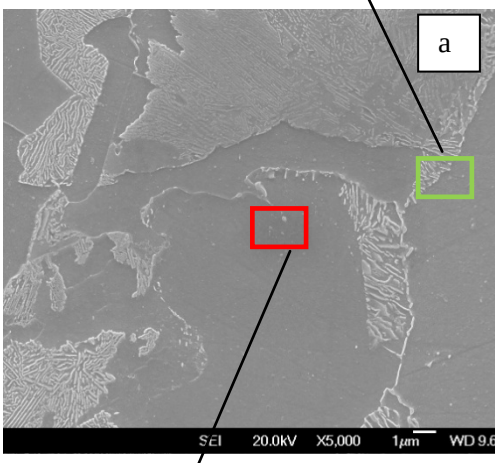
a
SEI 20.0kV X5,000 1μm WD 9.6

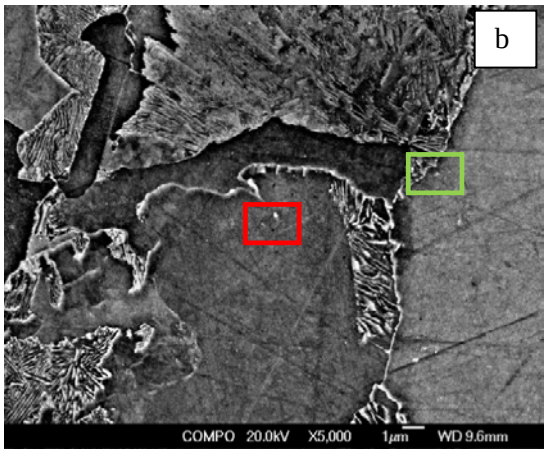
b
COMPO 20.0kV X5,000 1μm WD 9.6mm

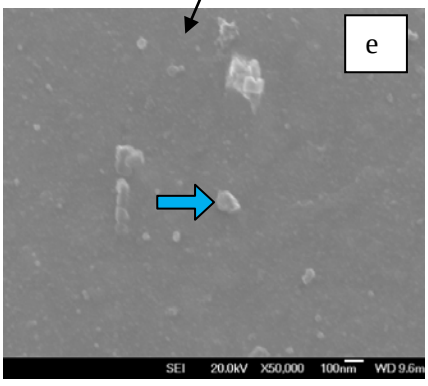
e
SEI 20.0kV X50,000 100nm WD 9.6m

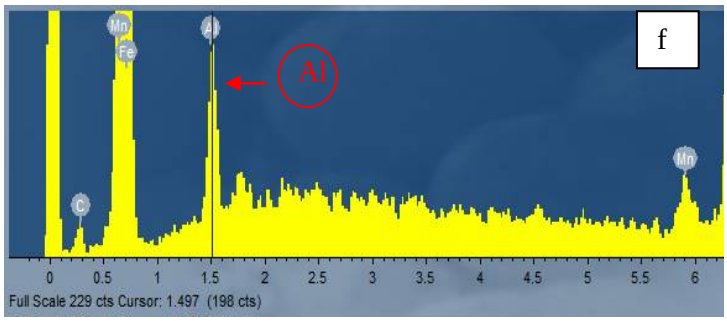
f
Mn
Fe
Al
Al
Mn
C
0 0.5 1 1.5 2 2.5 3 3.5 4 4.5 5 5.5 6
Full Scale 229 cts Cursor: 1.497 (198 cts)

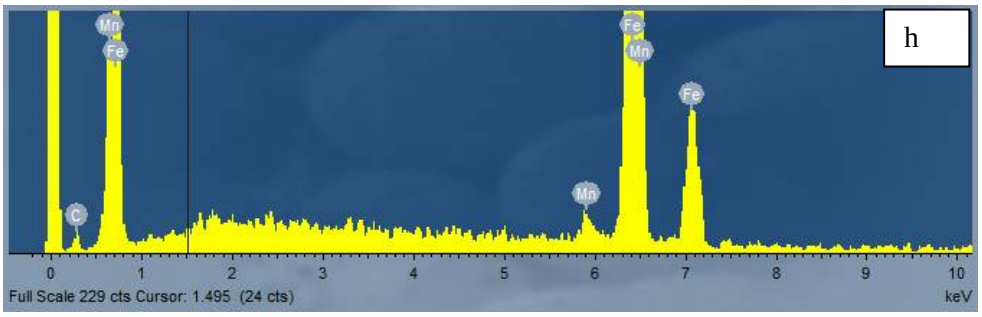

Figure 7-3 Precipitates in pearlite regions in the forged condition: (a) SE micrograph; (b) BSE image for composition analysis; (c) SE image of Nb-rich particles, probably Nb(C,N); (d) EDS trace indicating a Nb peak; (e) SE image of Al-rich particles, probably AlN; (f) EDS trace indicating an Al peak; (g, h) EDS spectra from the matrix.

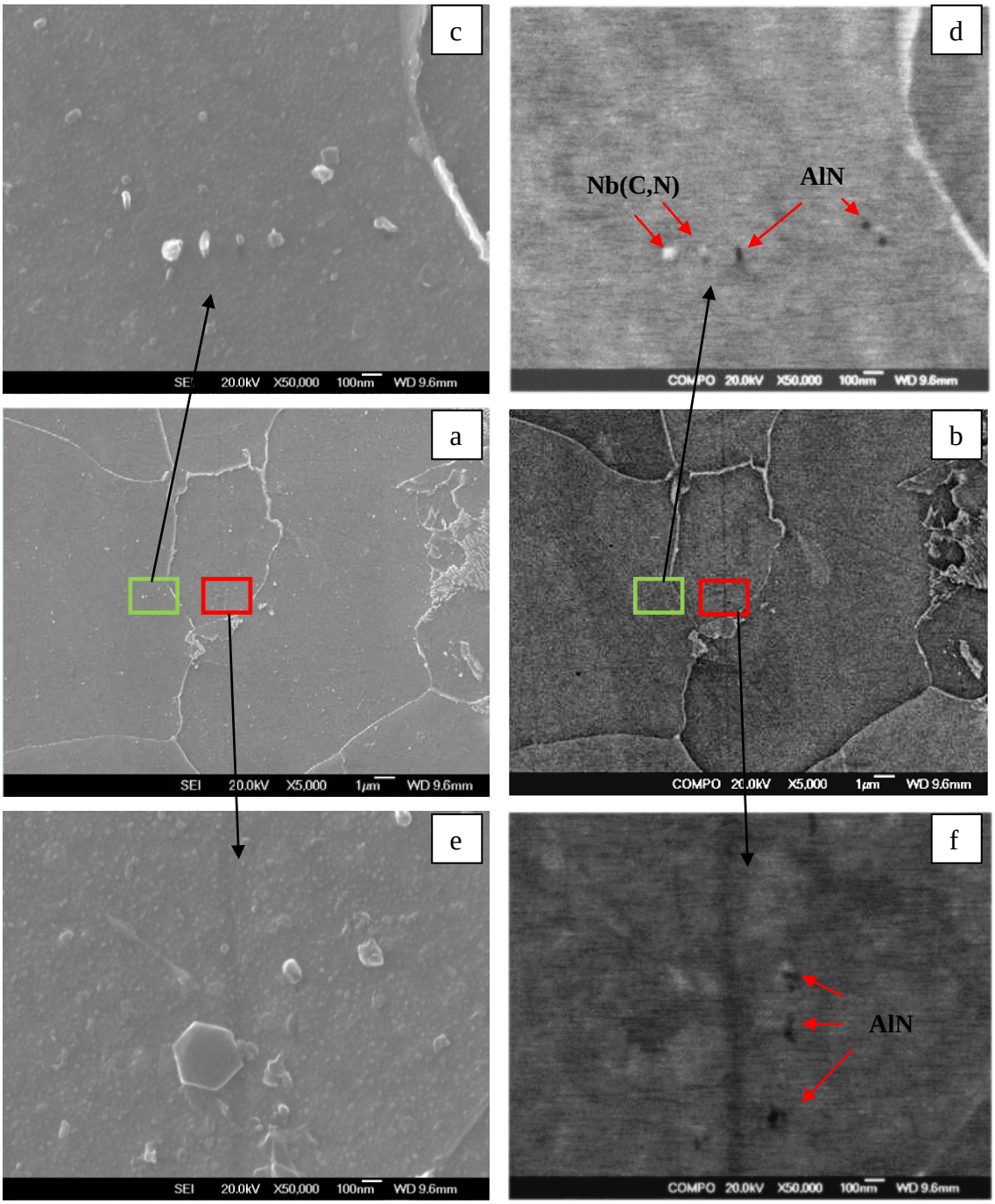

Figure 7-4 Micrographs show the precipitates in ferrite regions in the forged condition: (a) SE image; (b) BSE image; and (c) Nb-rich particles coexisting with Al-rich precipitates in SE image, and under (d) BSE imaging; a cluster of Al-rich particles in (e) SE image and (f) BSE image.

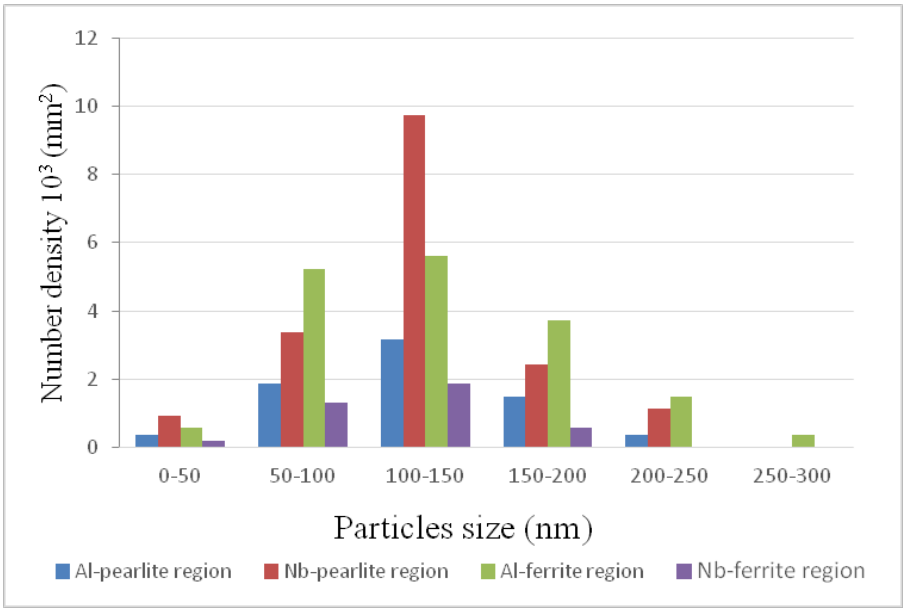

(a)

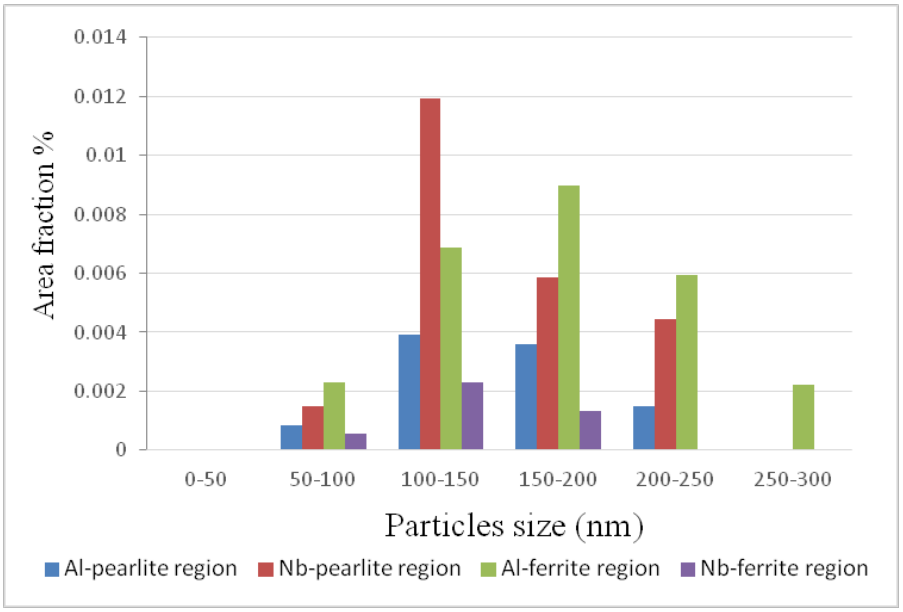

(b)

Figure 7-5 Particles size distributions expressed as (a) number density and (b) area fraction, for the Al-rich and Nb-rich precipitates in the dendritic and interdendritic regions separately.

7.2 Grain growth behaviour in forged Al-Nb steel

In the as-cast sample, it was found that a stable bimodal grain size was observed in the reheating temperatures range from 1160 ºC to 1200 ºC for one hour reheating treatment,

which corresponded to the dissolution of Al-rich particles in the dendritic region resulting in grain growth in this region, and the pinning effect of Nb(C, N) in the segregation bands retaining fine grains in this region. The forged specimens with reduced segregation band spacing, was also examined after reheating in this temperature range to investigate if bimodal structures or abnormal grains occurred.

7.2.1 Microstructure and grain size distribution

When the forged steel was reheated at 1160 ºC for one hour, the microstructure did not show a pronounced bimodal grain distribution, Figure 7-6 (a), i.e. there were no obvious bands of small and large grains observed which indicated a uniform fine grain size. The microstructure after reheating at 1200 ºC also shows relatively uniform grain growth (in Figure 7-6 (b)). The grain size distributions are shown in Figure 7-6 (c) and indicate a similar mode grain size of 65 µm for 1160 ºC and 1200 ºC samples. It is clear that significant grain growth has occurred (compared to the initial mode grain size of 17.5 µm) and most grains have a similar size to the segregation distance (65 ± 10 µm). This suggests that on reheating at 1160 ºC, the grains in the solute-enriched regions can be expected to grow but have been limited to the band distance of segregation spacing when the AlN particles in the dendritic regions have been dissolved. However, the band thickness (25 ± 5 µm) in forged Al-Nb steel is very close to the initial austenite grain size (17.5 µm), meaning the pinning effect from this banded structure might not be sufficient to prevent the grain growth. This means that some starting austenite grains can be expected to span the segregation spacing and sweep into the next solute-enriched banded structure, for example large initial grains 27.5 µm in size originated from pearlitic region may be spanning the solute-enriched

regions. This is different from the large band thickness (75 ± 10 μm) and the small initial grain size (27.5μm) conditions that were operating in the as-cast steel (as seen in Figure 6-4), where a number of fine grains have been formed within the pearlite regions but the grain growth has been prevented with pinning particles on their boundaries.

The grain growth at 1200 ºC in forged steel, as shown in Figure 7-6, has indicated that there is no significant development in terms of mode and largest grain size compared to 1160 ºC. It is consistent with the stable grain size observed in as-cast steel in the temperature range of 1160 ºC - 1200 ºC. It means that the band pinning is still effective when the band distance has been reduced after the forging process.

When reheated at 1250 ºC (higher than the predicted interdendritic Nb(C,N) dissolution temperature of 1230 ºC), the grain structure was coarser than that at 1200 ºC but reasonably uniform, as shown in Figure 7-7 (a). The grain size distribution in Figure 7-7 (b) demonstrates a uniform distribution with a larger mode grain size of around 90 μm. The ratio of largest 95% area fraction grain size (210 μm) to the mode grain size (90 μm) is 2.3 at temperature 1250 ºC. However, on reheating at 1300 ºC, the microstructure in Figure 7-8 (a) indicates pronounced grain growth compared to the lower reheated temperatures (1160 ºC - 1250 ºC) where only a few very large grains have appeared. The grain size distribution shows a mode grain size of around 225 μm, which is significantly larger than their size (65-90 μm) at lower temperatures from 1160 ºC-1250 ºC. The largest grain size (95% area fraction) of 425 μm is significantly coarser than that at 1250 ºC (210 μm). It has been found that there were no typical isolated abnormal grains observed in the forged condition for any reheating conditions.

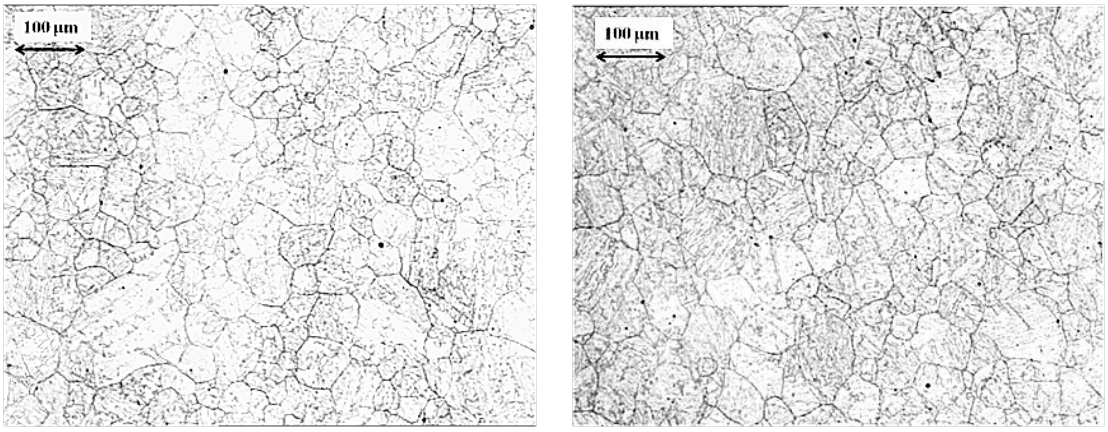

(a) (b)

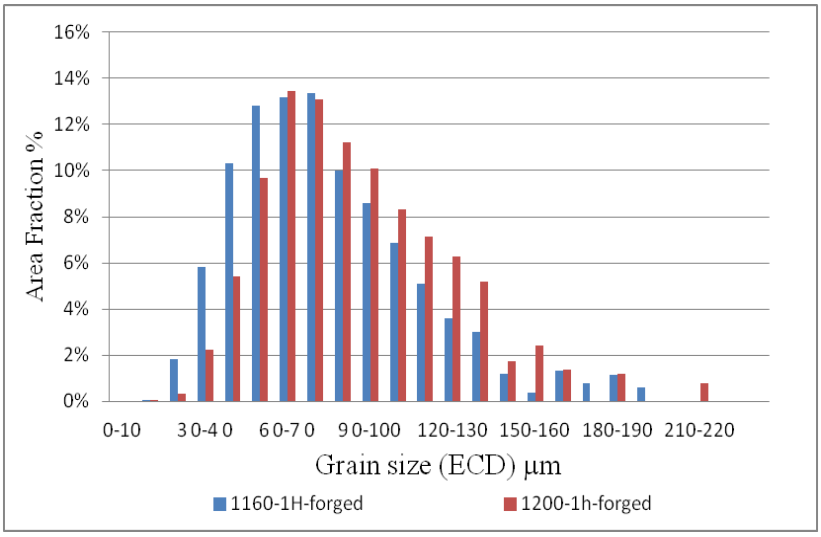

(c)

Figure 7-6 Prior austenite microstructure in forged steel, after reheating at (a) 1160 ºC, corresponding to dissolution temperature of dendritic Al-rich particles; (b) 1200 ºC; (c) grain size distribution, after reheating at 1160 ºC and 1200 ºC.

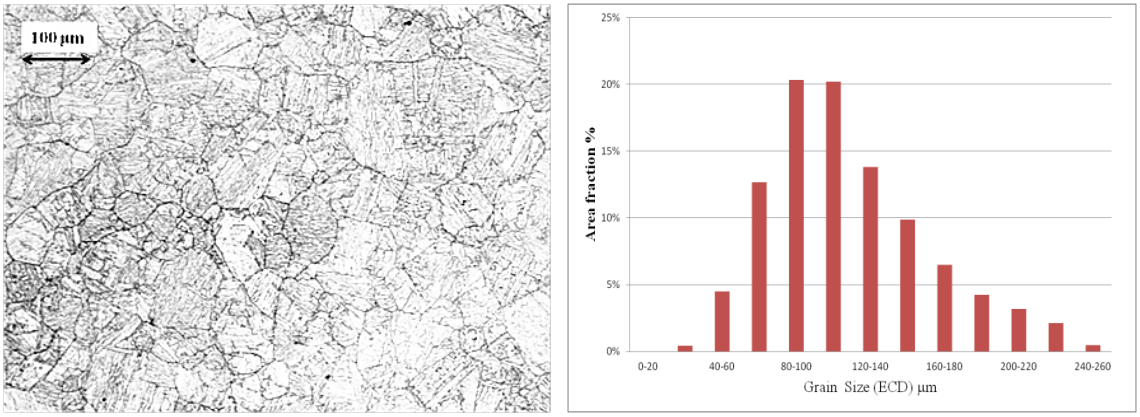

(a) (b)

Figure 7-7 (a) Prior austenite microstructure; and (b) grain size distribution, after reheating at 1250 ºC in forged steel.

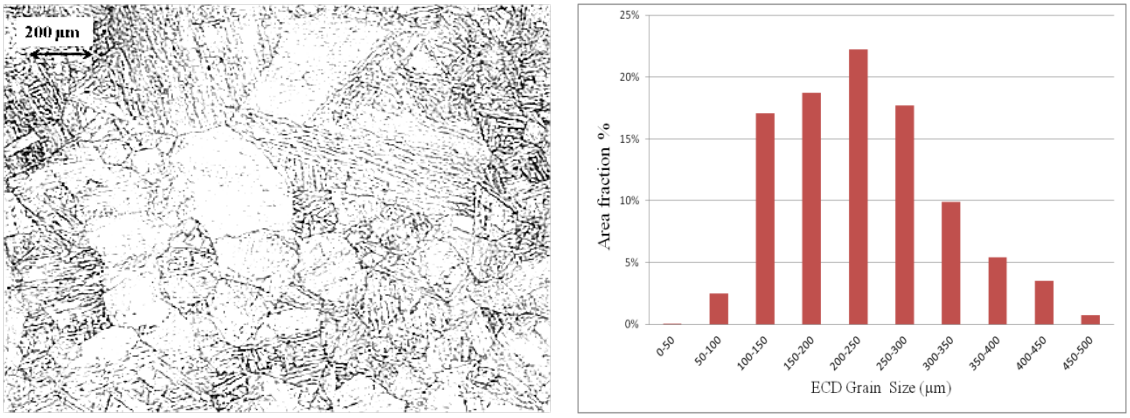

(a) (b)

Figure 7-8 (a) Prior austenite microstructure; and (b) grain size distribution, after reheating at 1300 ºC in forged specimens.

7.2.2 Precipitate characterization

The forged specimen reheated at 1160 ºC for 1 hour does not show obvious bands of large and small grains which were observed in the as-cast material when reheated to the same temperature, instead a relatively uniform microstructure has been found in the SEM image, as shown in Figure 7-9 (a). However, some regions with relatively large grains can still be identified (indicated in the black rectangle in Figure 7-9 (a)), where a few Al-rich particles have been observed, which is similar to the as-cast condition, as

discussed in section 6.2.2. The Al-rich particles found in the large grained regions are shown in Figure 7-9 (b) and exhibit an irregular shape. EDS analysis in Figure 7-9 (c) has confirmed the particles to be Al-rich. Analysis of the smaller grained regions, indicated by the red rectangle frame, in Figure 7-9 (a), shows spherical Nb-rich particles distribute as a cluster (Figure 7-9 (d)), and have confirmed as Nb-rich by EDS analysis in Figure 7-9 (e) which is consistent with previous characterisation of solute-enriched areas, in section 6.2.2. Therefore, the particle distributions in the forged sample are consistent with the behaviour observed in the as-cast condition, when reheating at 1160 ºC.

After reheating at 1200 ºC for 1 hour the microstructures are shown in Figure 7-10 (a), which still do not show any pronounced bimodal grain growth, giving a similar uniform distribution to that of the specimens reheated at 1160 ºC, with relatively small grain area (indicated by red rectangle) and relatively large grain region (indicated by black rectangle). Irregular Nb-rich particles have been observed in small grain area, as shown in Figure 7-10 (b, c). EDS analyses indicated the Nb peaks (Figure 7-10 (d)) in the spectra taken from the investigated particles separately compared to in the matrix (Figure 7-10 (e)). No Al-rich particles have been found in the large grained regions on reheating at 1200 ºC, meaning that complete dissolution of Al-rich precipitates has occurred at this temperature. It has found that the particle distribution in forged steel is similar to that in the segregated condition (as discussed in section 6.2.2) at 1200 ºC.

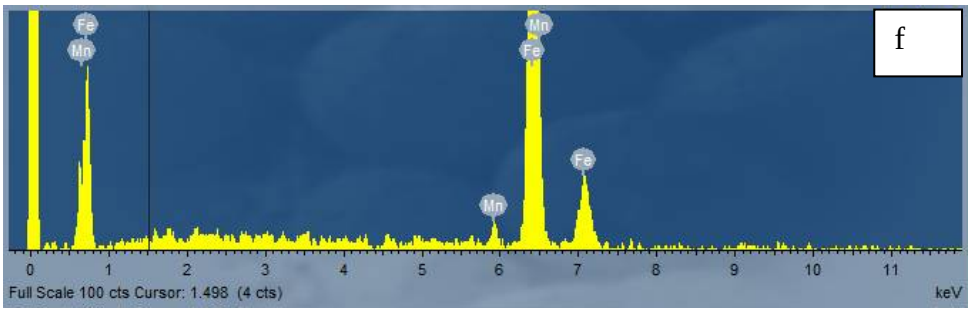
f
Fe
Mn
Mn
Fe
Fe
Mn
0 1 2 3 4 5 6 7 8 9 10 11
Full Scale 100 cts Cursor: 1.498 (4 cts)
keV

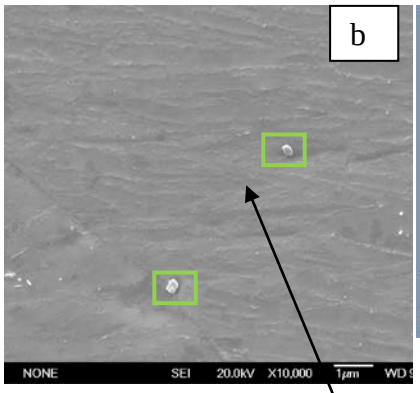
b
NONE SEI 20.0kV X10,000 1μm

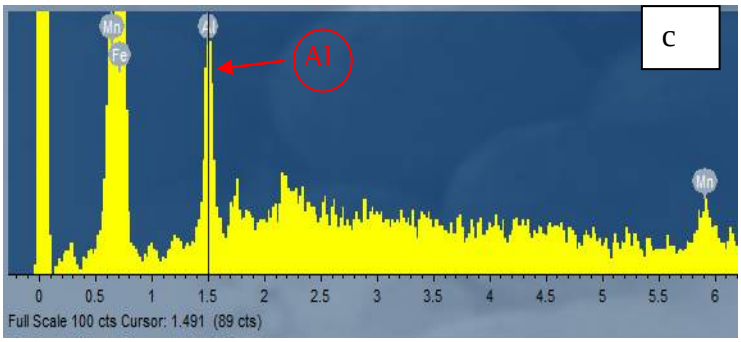
c
Mn
Fe
Al
Mn
0 0.5 1 1.5 2 2.5 3 3.5 4 4.5 5 5.5 6
Full Scale 100 cts Cursor: 1.491 (89 cts)

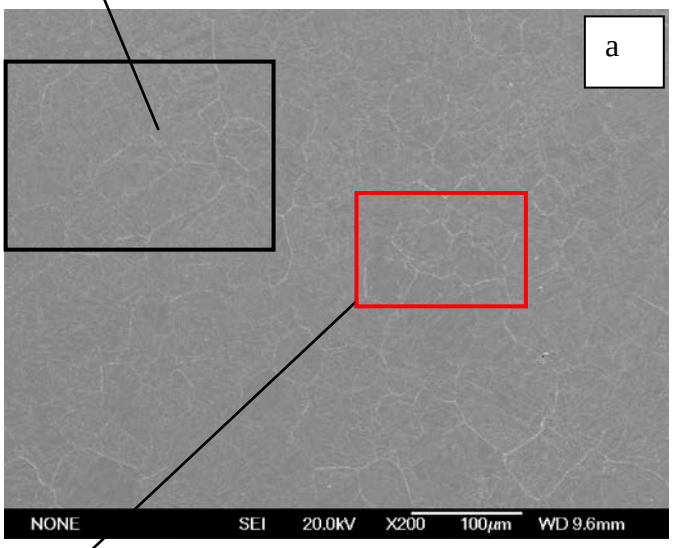
a
NONE SEI 20.0kV X200 100μm WD 9.6mm

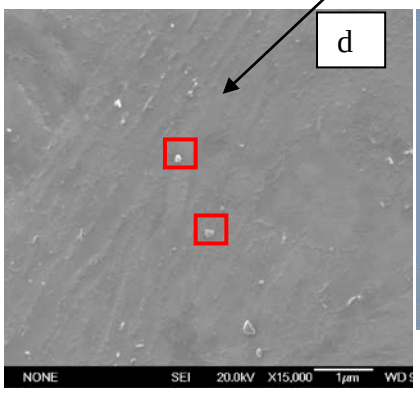
d
NONE SEI 20.0kV X15,000 1μm

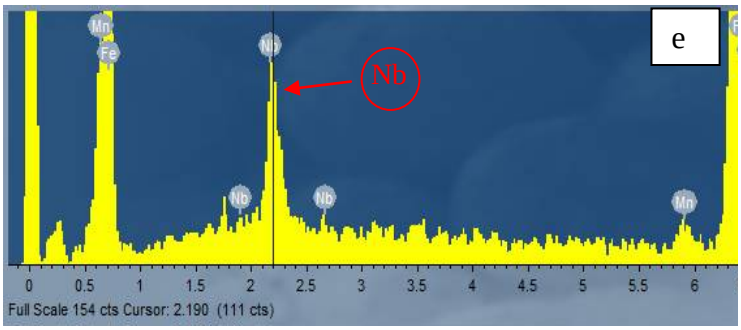
e
Mn
Fe
Nb
Nb
Nb
Nb
Mn
0 0.5 1 1.5 2 2.5 3 3.5 4 4.5 5 5.5 6
Full Scale 154 cts Cursor: 2.190 (111 cts)

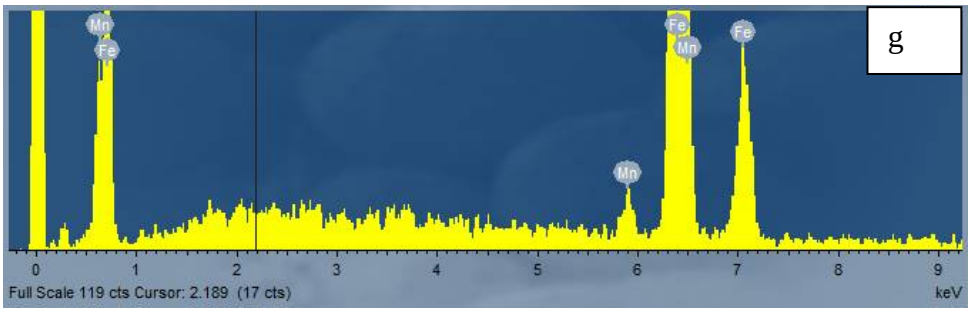

Figure 7-9 Precipitates distributed in forged specimens after reheating at 1160 ºC for 1 hour: (a) SEM image shows the microstructure with no bands of large and small grains; (b) Al-rich precipitates present in relatively large grains; (c) EDS trace indicating the Al peak; (d) Nb-rich particles found in the relatively small grains and (e) Nb peak in EDS spectrums taken from the investigated particles; (f, g) EDS spectra from the matrix.

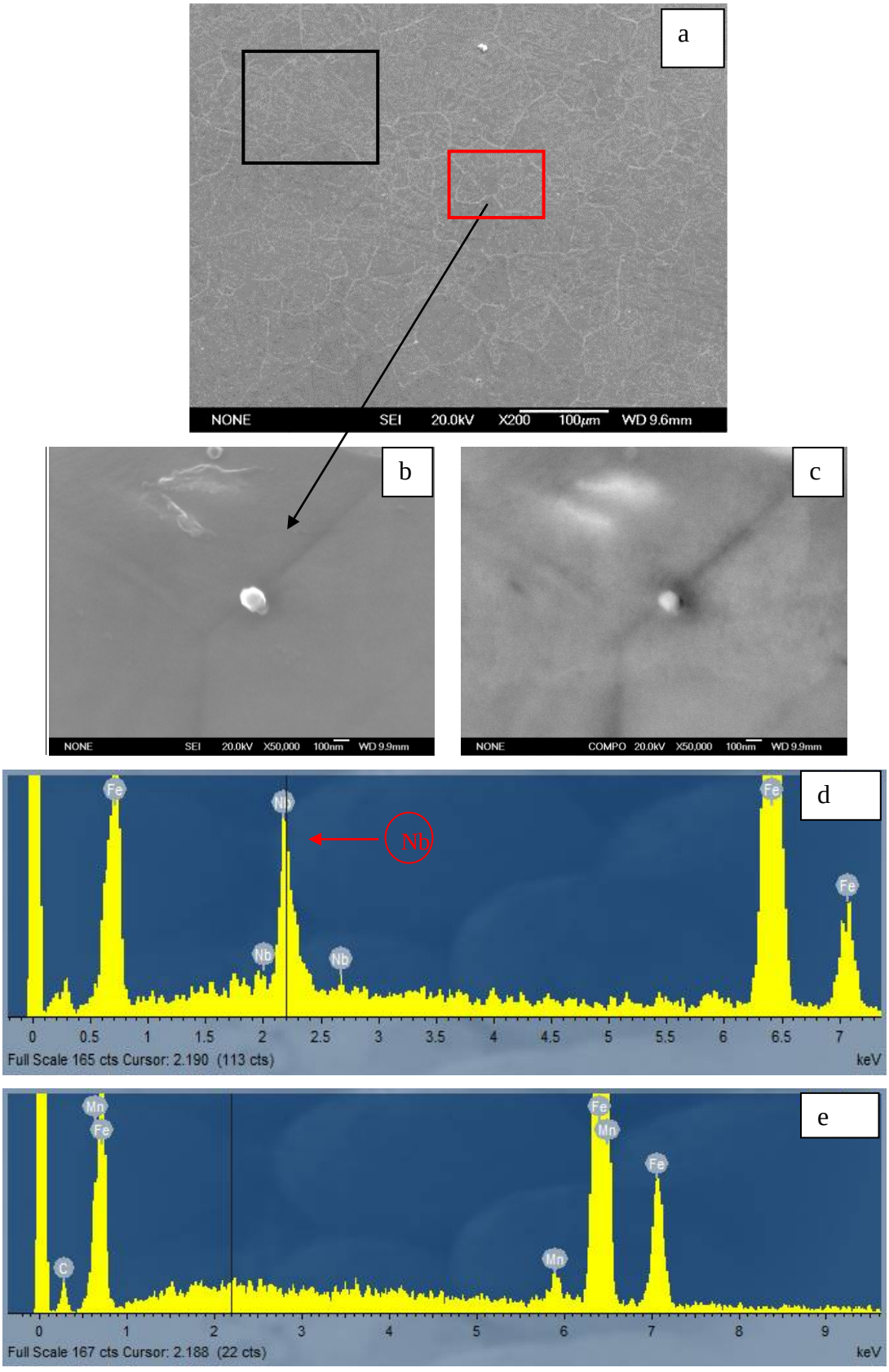
a
NONE SEI 20.0kV X200 100µm WD 9.6mm
b
NONE SEI 20.0kV X50,000 100nm WD 9.9mm
c
NONE COMPO 20.0kV X50,000 100nm WD 9.9mm
d
Fe
Nb
Nb
Nb
Fe
Fe
0 0.5 1 1.5 2 2.5 3 3.5 4 4.5 5 5.5 6 6.5 7
Full Scale 165 cts Cursor: 2.190 (113 cts)
keV
e
Mn
Fe
C
Fe
Mn
Mn
Fe
0 1 2 3 4 5 6 7 8 9
Full Scale 167 cts Cursor: 2.188 (22 cts)
keV

Figure 7-10 Particles distribution in forged steel, after reheating at 1200 ºC for 1 hour: (a) grain structures present in SEM images; Nb-rich particles remaining in relatively small grain regions, with imaging of SEI (b) and BSE (c); (d) EDS shows the Nb peak; (e) EDS spectra from the matrix.

7.2.3 Grain growth with increased holding time at critical temperatures

Further reheating trails were carried out to investigate whether a bimodal grain size distribution can be developed with increasing holding time.

At 1160 ºC when the reheating times were increased from 1 hour to 3 hours, the prior austenite grains still gave uniform distributions (i.e. no evidence of bimodal grain growth), as indicated in Figure 7-11 (a) and the grain size distribution in Figure 7-11 (b), where the mode grain size was around 65 μm, which was similar to the samples reheated for 1 hour. The results indicate that the bimodal grain growth observed in the segregated as-cast condition might not occur if the segregation spacing is reduced. Therefore, an increased solidification rate, which can be expected to reduce the secondary dendrite arm spacing (Figure 2-6, discussed in section 2.1.3), could lead to a more uniform grain structures if sufficient pinning force is provided in the segregated structure.

When the forged specimens were reheated at 1200 ºC for 3 hours, coarser grain structures were observed, compared to reheating for one hour, but no obvious isolated abnormally large grains occurred, shown in Figure 7-11 (c). A mode grain size of 90 μm can be seen from the grain size distribution in Figure 7-11 (d), which is coarser than after reheating at 1200 ºC for 1 hour (65 μm). The grain growth may be due to greater precipitate dissolution with increased holding times, which agrees with the

grain growth behaviour observed in the as-cast steel under the same reheated conditions.

The change in mode and large grain sizes (95% accumulated area fraction) with reheat temperature and time is shown in Figure 7-12. A stable grain size at 1160 ºC has been observed from 1 hour to 3 hours, having a constant mode grain size of 65 µm and large grain size of around 140 µm. When the forged sample was reheated at 1200 ºC for 1 hour, there was no significant difference in prior austenite grain size compared to the size at 1160 ºC for 1 hour. However, the mode grain size increased from 65 µm at 1 hour, to 90 µm at 3 hours, and the large grains jumped from 140 µm to 210 µm after holding for longer times. This means that the band pinning is not effective when holding for a longer reheating time at 1200 ºC, which is due to the fact that the Nb(C, N) in the solute-enriched band region has been gradually dissolved at this high temperature.

The results indicate that grain growth behaviour in the forged condition followed the same general development which was found in the as-cast condition with unpinning taking place in the dendritic regions at the reheating temperatures of 1160 ºC-1200 ºC, corresponding to the dissolution of AlN. However, the bimodal grain size distribution observed in the as-cast steel was not seen when the segregation spacing was decreased in the forged sample. This indicates that the band pinning is still effective when band distance has been reduced, and the segregation distance is small enough to limit the grain growth from dendritic solute-depleted region (after AlN particles have dissolved) to be a small size of around 65 µm.

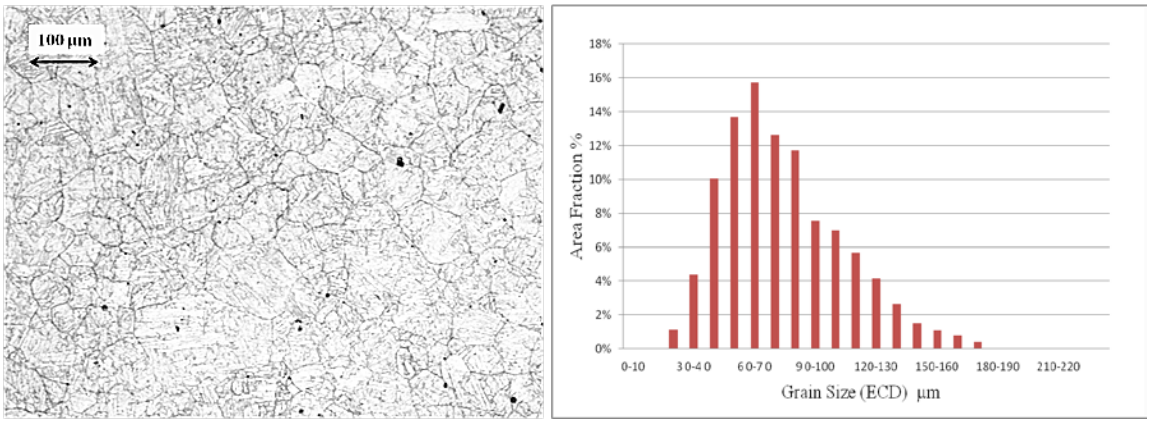

(a) (b)

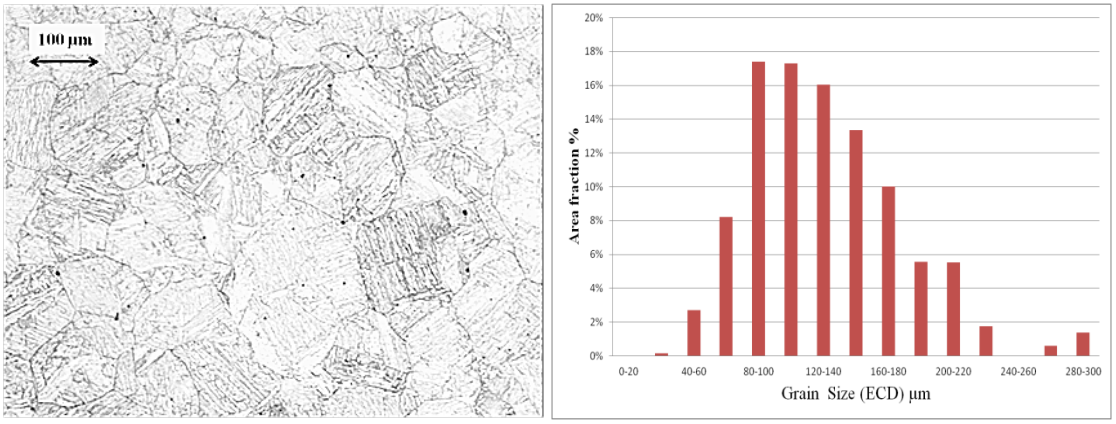

(c) (d)

Figure 7-11 Prior austenite grain structures, after reheating at (a) 1160 ºC for 3 hours; and (b) grain size distribution; microstructures when reheated at (c) 1200 ºC for 3 hours; and (d) grain size distribution.

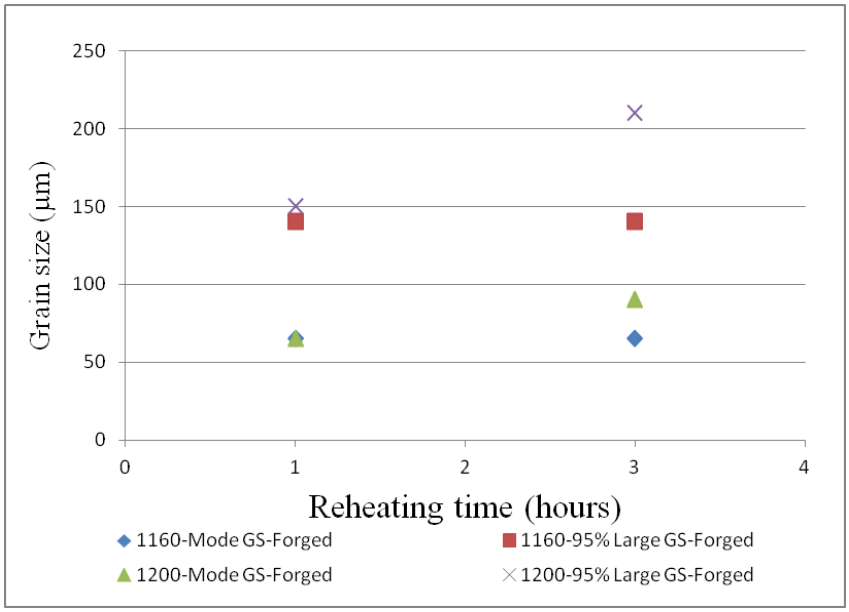

Figure 7-12 Grain size of forged specimens after reheating at 1160 ºC and 1200 ºC, for 1 hour and 3 hours: mode grain size from area fraction distribution (Mode GS); and large grain size represented by the accumulated area fraction of 95% (95%-large GS).

7.3 Initial microstructures and modelling in rolled Nb-containing steel

In the as-cast Al-Nb containing steel, it has been found that the segregation bands can limit the growth of large grains from the solute-depleted regions during reheating in the temperature range of 1160-1200 ºC resulting in a bimodal grain structure. In the homogenised material isolated abnormally larger grains have developed in this temperature range (at 1170 ºC). In the forged specimens the segregation banding is reduced to the separation distance of approximately 65 µm (greater than the starting prior austenite grain size 17.5 µm). During reheating in the temperature range of 1160-1200 ºC uniform grain growth has occurred resulting in a uniform coarse grain structure. In this section the effect of reheating on a commercial rolled Nb-containing steel, with a higher content of Nb (0.028 wt%) and lower amount of Al (0.031 wt%)

than in the Al-Nb containing steel (0.019 wt% Nb and 0.057 wt% Al), and a significantly reduced segregation band spacing has been investigated.

7.3.1 Initial microstructure of rolled Nb-containing steel

The as-received Nb-containing steel had been hot rolled (80% reduction) and air cooled and the resulting microstructure with a banded ferrite and pearlite structure is shown in Figure 7-13 (a). The ferrite grain size distribution in Figure 7-13(b) shows a mode grain size of 32.5 μm in the rolled Nb-containing steel (larger than the initial ferrite grain size of 22.5 μm in the forged Al-Nb steel), which is close to the measured spacing of the segregation bands, of around 35 ± 10 μm. It is found that the band thickness is approximately 10 ± 5 μm, and it is smaller than that of 25 ± 5 μm in the forged Al-Nb steel. Unlike the mostly continuous band structure exhibited in the forged Al-Nb containing steel (Figure 7-1), non-continuous segregation bands (presumably with less continuous pearlite) are present in the rolled Nb-containing steel. Some of the ferrite grains have been observed to stretch into the banded structure (pearlite regions), Figure 7-13 (a). The Nb-rich precipitates are mainly distributed at/ or near the pearlite regions (solute-enriched region), as discussed in the work on the Al-Nb steel, which is consistent with literature report [17]. Due to the small thickness of the banded structure in rolled Nb-containing steel (even smaller than that in the forged Al-Nb steel), some grains may span the banded structure under the greater driving force associated with the austenite-ferrite transformation and so they are likely to break free from the pinning effect of the solute-enriched regions (banded structure).

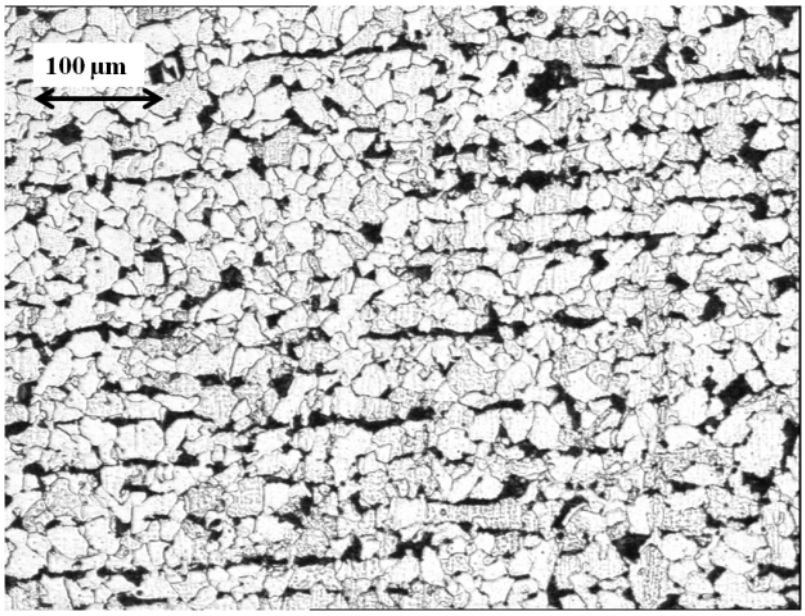

(a)

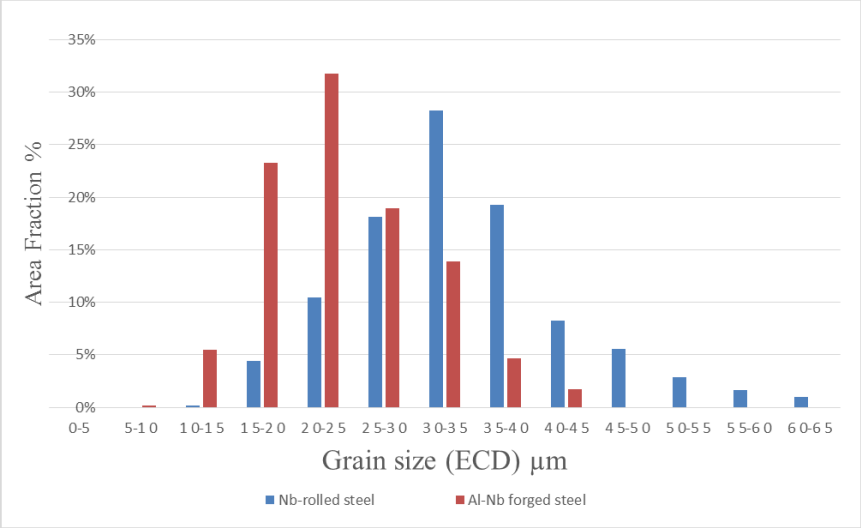

(b)

Figure 7-13 (a) Initial microstructures consist of segregation bands of rolled Nb-containing steel; (b) ferrite grain size distribution in forged Al-Nb steel and rolled Nb-containing steel.

7.3.2 Segregation predictions for rolled Nb-containing steel

The segregation band spacing of 35 µm and rolling reduction of 80% to 25 mm means that the secondary dendrite arm spacing (SDAS) can be assumed to be around 175 µm. Using equation 2-1 and taking 0.15 wt% C as input, the predicted cooling rate during

solidification is approximately 0.3 ºC/s. Similar to the predictions for the as-cast Al-Nb steel (as discussed in section 4.3.2), the composition profiles of Al and Nb over the half distance of SDAS (87μm) were predicted by DICTRA at the fully solid stage (at temperature of around 1476 ºC), shown in Figure 7-14 (a). The steps observed in the predicted composition profiles at the distance of around 15 μm are due to the appearance of austenite on cooling with lower solubility of Al and Nb in that phase than in ferrite, which is similar to the predicted composition step that have been observed in cast Al-Nb steel (Figure 4-20). The Nb profile shows a low content around 0.022 wt% in the solute-depleted regions and a high content of around 0.081 wt% in the solute-enriched region; and it shows that Al has a relatively stable concentration from the profile, which is 0.031 wt% in the dendritic region and 0.027 wt% in the interdendritic centre region.

The thermal stabilities of the microalloying element-rich particles were predicted by Thermo-Calc, using the segregated Al and Nb contents predicted from DICTRA (Figure 7-14(a)) and taking the average contents of other elements as input (as discussed in section 3.2.2). It can be seen from Figure 7-14 (b) that the Nb(C, N) particles in the solute-enriched region are predicted to be dissolved at approximately 1250 ºC, whilst the Al-rich (predicted to be AlN) precipitates in the same region have a significant lower dissolution temperature at around 1030 ºC. In the solute-depleted dendritic region, the dissolution temperature for AlN (1090 ºC) is higher compared to the Nb-rich ones (970 ºC). The volume fraction of Nb-rich precipitates in the solute-enriched region is predicted to be around 0.094 %, which is greater than for the Nb-

rich particles in the solute-depleted region or the Al-rich particles in either region, this means there should be high number density of Nb-rich particles.

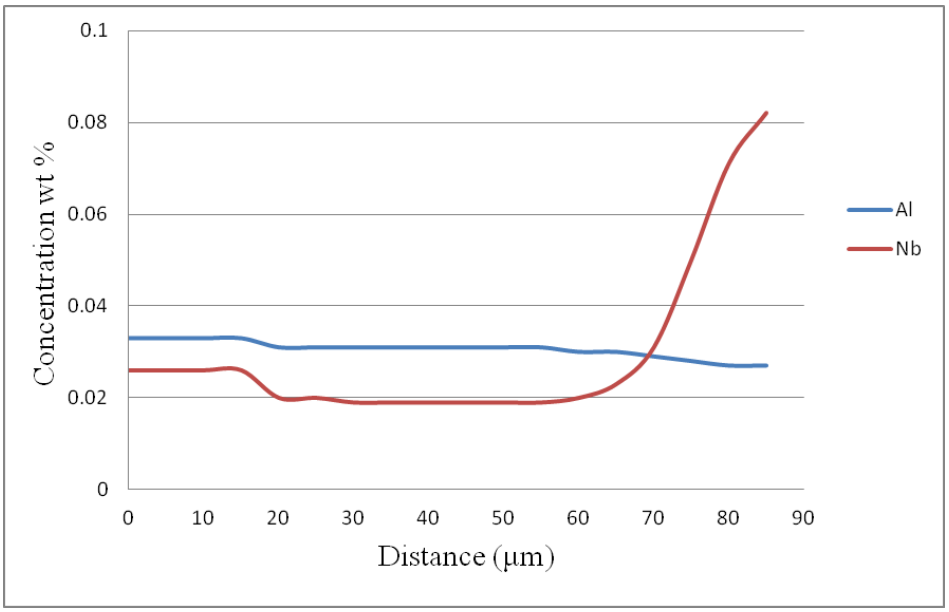

(a)

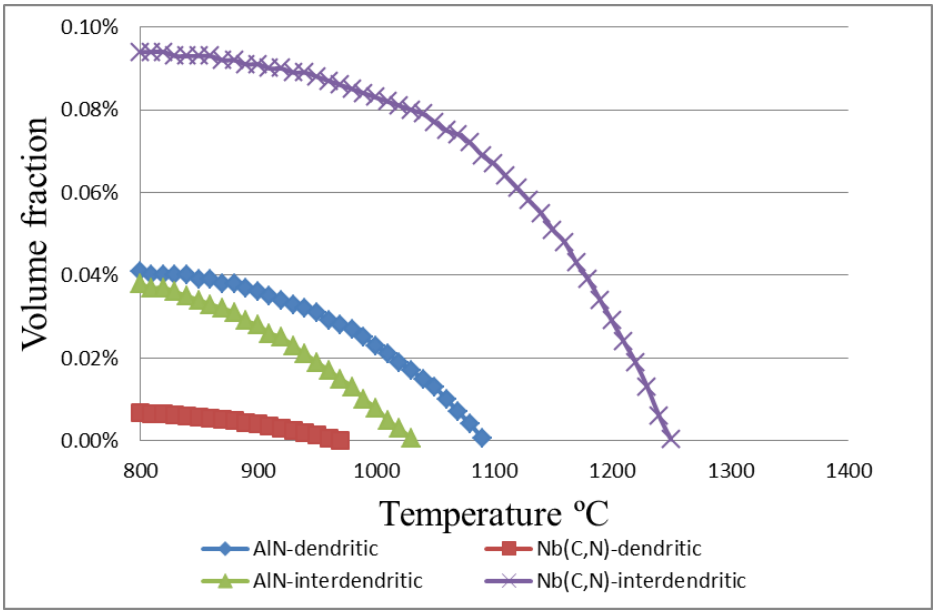

(b)

Figure 7-14 Modelling prediction in rolled Nb-containing steel for: (a) segregation profile over a distance of half SDAS of around 87 μm, predicted by DICTRA; (b) volume fraction and dissolution temperatures of microalloying precipitates of AlN and Nb(C,N) in solute-enriched and solute-depleted regions.

7.3.3 Precipitates characterisation in rolled Nb-containing steel

The initial microstructures contain bands of ferrite and pearlite, which were examined separately to characterise the particle distributions. Figure 7-15 (a) shows the typical banded structure. Very few Al-rich particles have been found in the ferrite regions; one example can be seen in Figure 7-15 (c, d). This is different to the relatively high number of Al-rich particles (of around 1.7×10^4 /mm^2 in total) observed in the Al-Nb steel (Figure 7-5). A higher number of Nb-rich particles have been observed in Figure 7-15 (e, f). It indicates that the Nb content (0.028 wt%) in rolled Nb-containing steel is higher than that in cast Al-Nb steel, resulting that much of the N is used to form Nb(C, N) therefore there is very little N left to form AlN, hence the low number density of particles present. The predicted Nb(C, N) volume fraction of 0.094 % in Thermo-Calc, Figure 7-14 (b), is larger than that in Al-Nb steel (Figure 4-21) with 0.072 % being seen. It is therefore possible that little AlN can be formed in rolled Nb-containing steel, due to the content of N (0.006 wt%) and Al (0.031 wt%) which is lower than that in the Al-Nb steel (N: 0.008 wt%; Al: 0.057 wt%).

The precipitates in the solute-enriched segregation bands were investigated by examining the pearlite regions (or the isolated ferrite within the pearlite areas), where a very high number of Nb-rich particles were seen, shown in Figure 7-16 (a, b). A typical area (as indicated by the red rectangular frame) has a cluster of Nb-rich precipitates in the solute-enriched region (pearlitic regions), as shown in Figure 7-16 (c, d). The particle size distributions in Figure 7-17 (a) indicate a large number density of Nb-rich particles, whilst Al-rich precipitates are difficult to observe resulting in a significantly lower amount compared to the Al-Nb steel. For the rolled Nb-containing

steel, a larger number density of 3.5×10^4 /mm^2 of Nb-rich particles of size 100-150 nm has been seen in the solute-enriched region, Figure 7-17 (a), which is higher than in the forged Al-Nb steel (with a number density of 0.9×10^4 /mm^2 in same size of 100-150 nm, Figure 7-5).

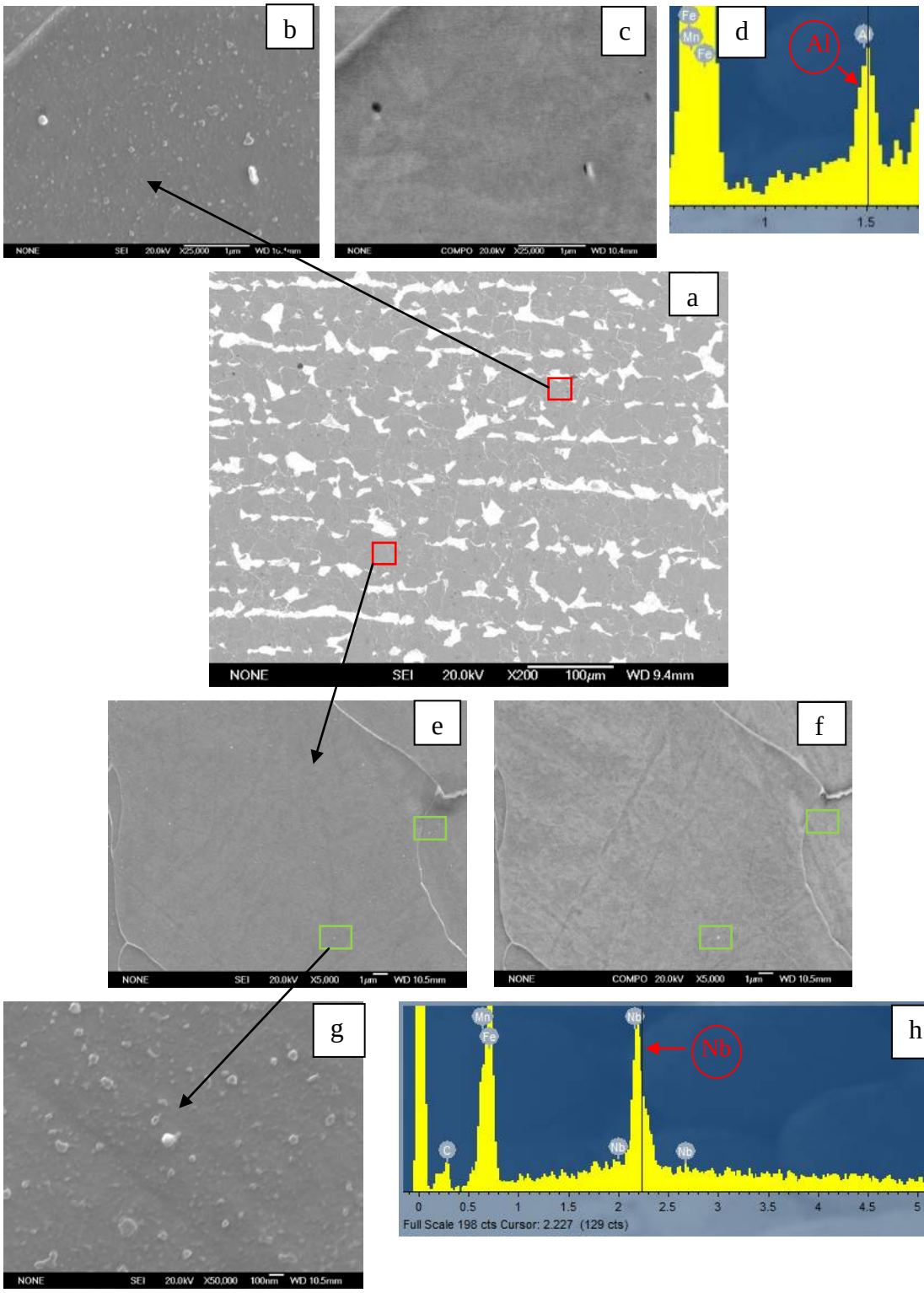
b
c
d
Fe
Mn
Fe
Al
Al
1
1.5
a
NONE SEI 20.0kV X200 100µm WD 9.4mm
e
f
NONE SEI 20.0kV X5,000 1µm WD 10.5mm
NONE COMPO 20.0kV X5,000 1µm WD 10.5mm
g
h
Mn
Fe
Nb
Nb
C
Nb
Nb
0 0.5 1 1.5 2 2.5 3 3.5 4 4.5 5
Full Scale 198 cts Cursor: 2.227 (129 cts)
NONE SEI 20.0kV X50,000 100nm WD 10.5mm

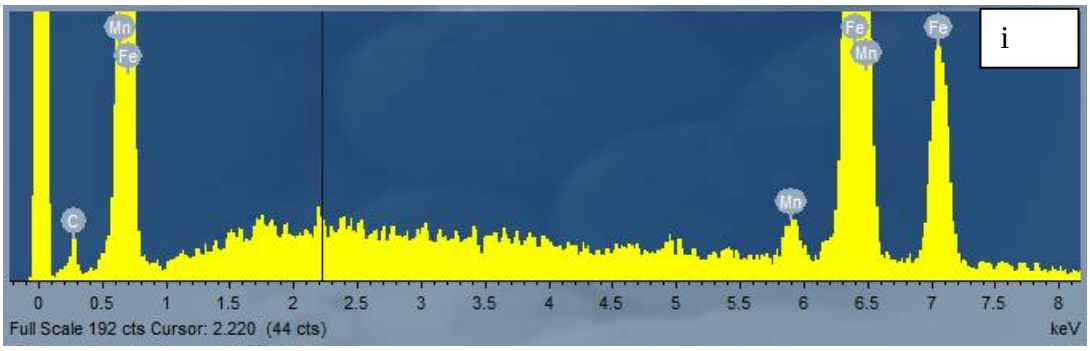

Figure 7-15 Precipitates distributed in ferrite grains regions of rolled Nb-containing steel: (a) bands of ferrite and pearlite structures in SEM micrograph; Al-rich particles present in ferrite region in (b) SE image and (c) BSE image; (d) EDS trace analysis indicating an Al peak; Nb-rich particles distributed in ferrite structures in (e) SE image and (f) BSE image; typical Nb-rich particle with spherical shape in SE image (g); EDS trace shows the (h) Nb peak in the particle and (i) matrix.

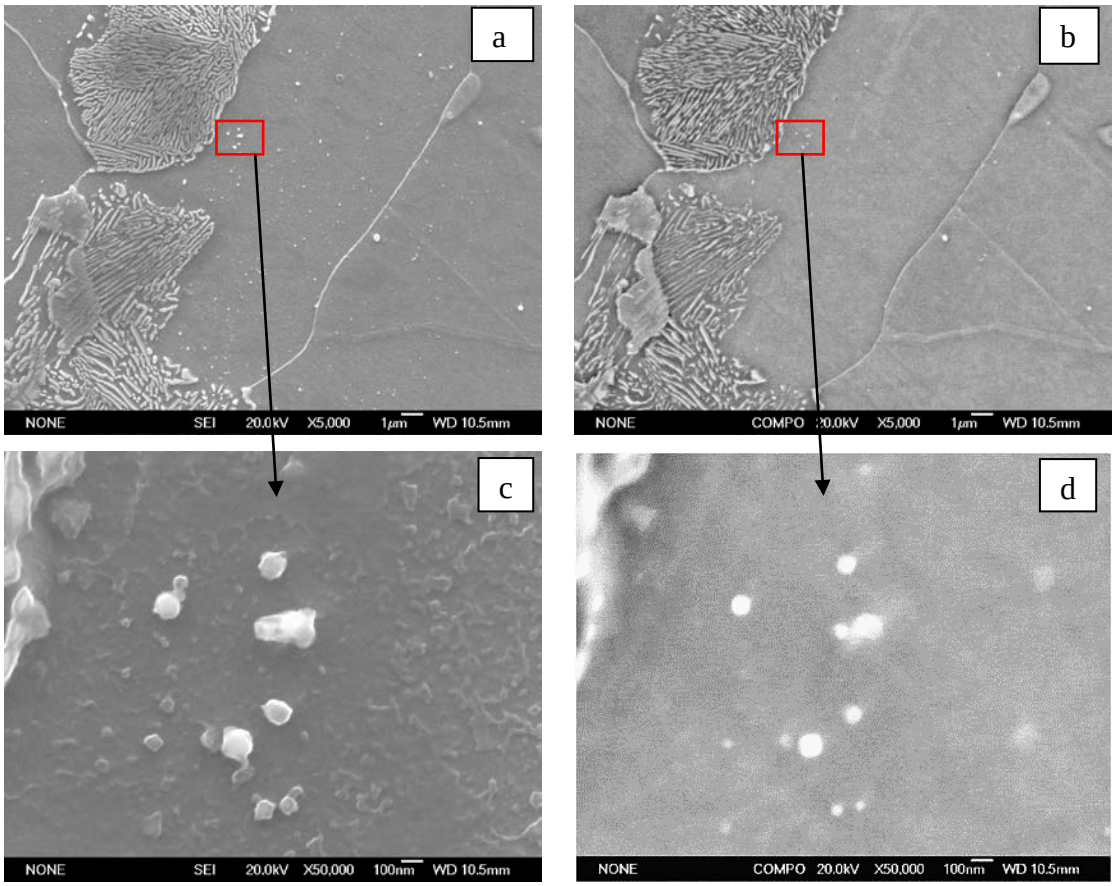

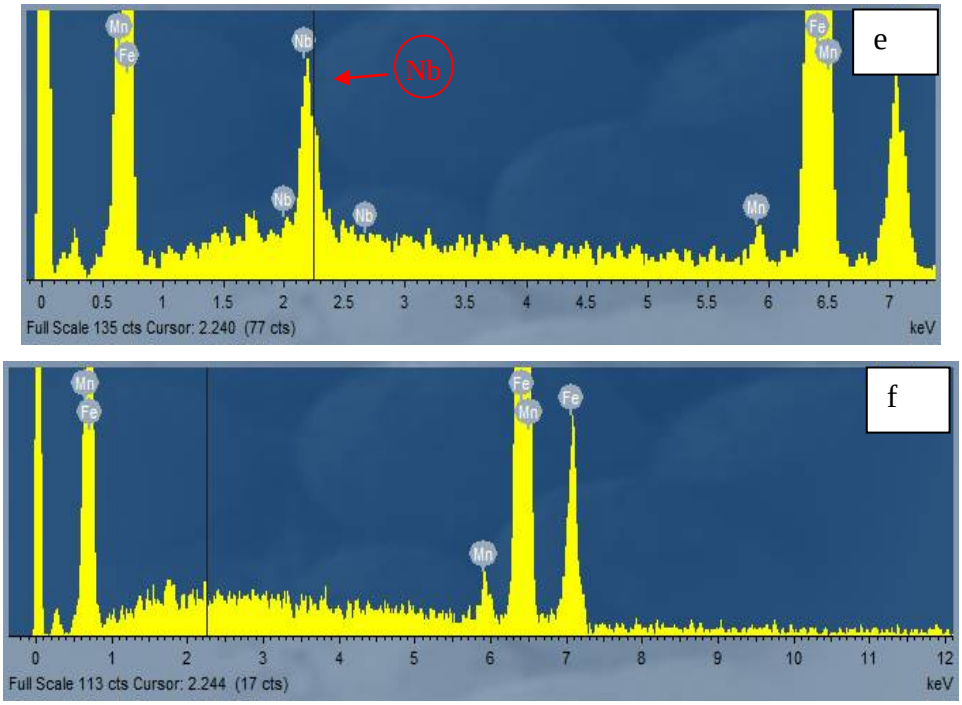

Figure 7-16 Particles in pearlite regions in rolled Nb-containing steel: high number of Nb-rich particles present in (a) SE image and (b) BSE image; the cluster of Nb-rich particles present near pearlite region by (c) SE imaging and (d) BSE imaging; (e) EDS trace analysis showing a Nb peak; (f) EDS trace from matrix.

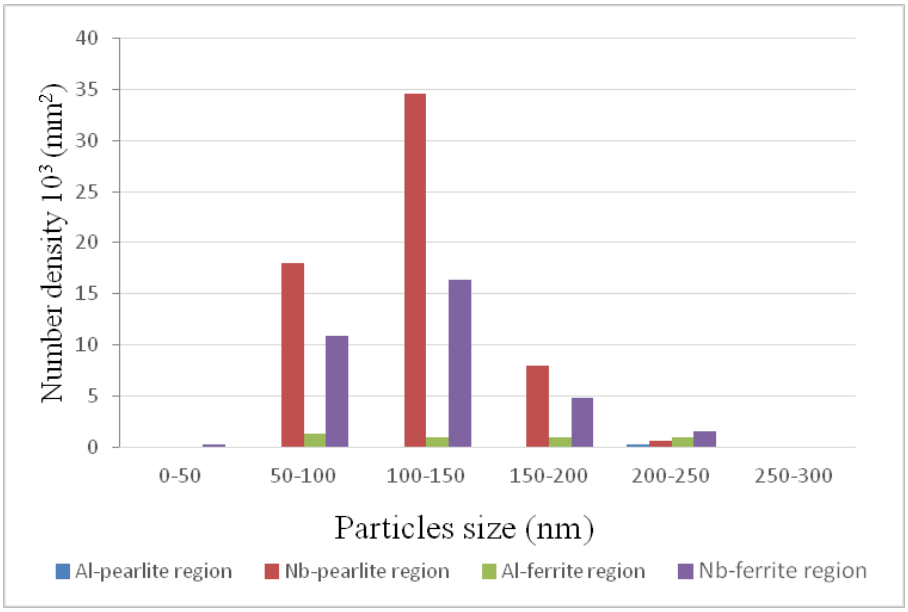

Figure 7-17 Particle size distribution and number density for Al-rich and Nb-rich precipitates were characterised in ferrite and pearlite regions.

In the rolled Nb-containing steel, with a higher Nb content (0.028 wt%) than in the cast Al-Nb steel (Nb: 0.019 wt%), the predicted Nb segregation (from the composition profile simulated by DICTRA) to the interdendritic region (0.082 wt%) is larger than for the cast Al-Nb steel (0.062 wt%). This results in the larger numbers of Nb-rich particles (expected to be Nb(C,N)) observed in the interdendritic regions for the rolled Nb-containing steel, of around 5.9×10^4 /mm^2 (Figure 7-17), than that in the Al-Nb cast steel (Nb-rich particles: 2.6×10^4 /mm^2 Figure 4-8 and Table 4-1). This result indicates that the segregation severity of Nb depends on the bulk content, consistent with previous results reported in the literature (Table 2-10), where a larger number density of Nb(C, N) (in the interdendritic region) has been observed for the Slab-1 with a higher Nb content (0.045 wt%) than in the Slab-3 steel (Nb: 0.02 wt%).

Al shows a similar segregation behaviour in as-cast Al-Nb steel (Al: 0.057 wt%) and rolled Nb-containing steel (Al: 0.031 wt%), with partition ratios (contents in the interdendritic region to the bulk composition) of around 0.84 and 0.83 respectively, which agrees with the literature, where the same partition ratio for Al (0.98) was predicted in Slab-1 (Al: 0.046), Slab-2 (Al: 0.029) and Slab-3 (Al: 0.036), as seen in Table 2-6 [25]. A higher content of Al in the dendritic region is predicted in Al-Nb steel (0.059 wt%) than that in rolled Nb-containing steel (0.032 wt%), resulting in a larger amount of Al-rich particles found in the dendritic region for the Al-Nb steel compared to the rolled Nb-containing steel. It is found that a larger number density of 1.89×10^4 /mm^2 has been observed for dendritic AlN in the Al-Nb steel (Al: 0.057 wt%) (Figure 4-8), than that in the rolled Nb-containing steel (0.4×10^4 /mm^2, Figure 7-17) with a lower Al content (0.031 wt%).

7.4 Grain growth at critical temperatures

In as-cast and forged Al-Nb steel, it was found that the large grains originated in the solute-depleted region on reheating to temperatures when the Al-rich particles had dissolved, but they were pinned by particles in the segregation band limiting their size. For the rolled Nb-containing steel, a bimodal grain structure might be expected based on the predicted particle dissolution temperatures (i.e. Al-rich particles dissolving in the solute-depleted region (1090 ºC) and Nb-rich particles remaining in the solute-enriched region), or a uniform fine grain structure can be expected if the segregation band pinning is effective in preventing grain growth as the segregation spacing is small. Therefore, reheating trials were carried out at the Al-rich particles dissolution temperature of 1090 ºC, to see whether abnormal grain growth occurred, and at 1200 ºC to investigate whether bimodal grain growth happened.

The starting prior austenite grain structure in the rolled Nb-containing steel, shown in Figure 7-18, is similar to the initial microstructure in forged Al-Nb steel, Figure 7-2, indicating that it consists of more deeply etched segregation bands separated by lighter grey areas. The average grain size is approximately 27.5 μm, larger than the starting austenite grain size (17.5 μm) in the forged Al-Nb steel (Figure 7-2). This may be due to the formation of large austenite grains from the pearlitic banded regions which are not continuous in the rolled Nb-containing steel compared to forged Al-Nb steel (as discussed in section 7.3.1), or some grains have spanned the banded the structure (thickness of 10 ± 5 μm) as assumed in section 7.3.1. A narrower spacing of the segregation bands is seen in rolled Nb-containing steel (of around 35 ± 10 μm), compared to that in forged Al-Nb steel (65 ± 10 μm), Figure 7-2.

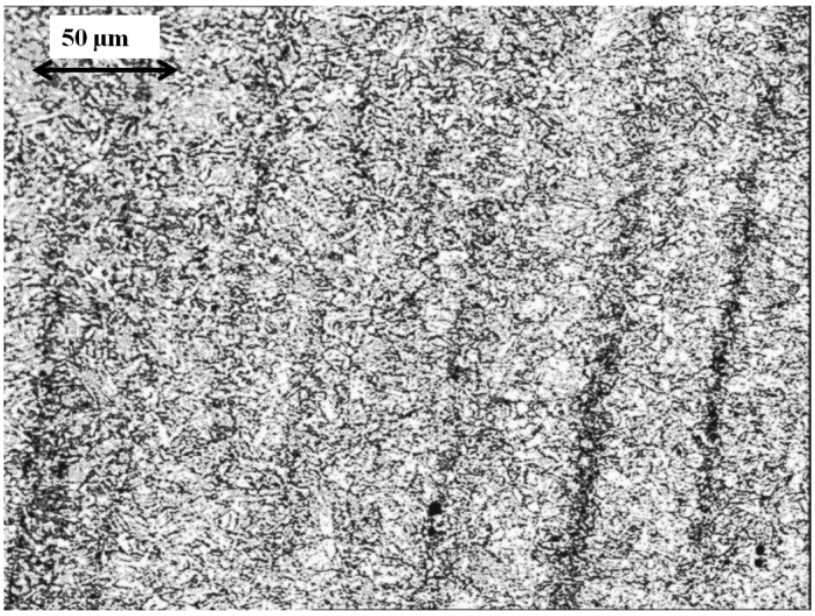

Figure 7-18 Prior austenite grain structure is shown in rolled Nb-containing steel when reheating to 920 ºC for 10 minutes.

7.4.1 Microstructure and grain size distribution

The prior austenite grain structure after reheating at 1090 ºC for 1 hour is shown in Figure 7-19 (a and b) where an isolated large grain surrounded by fine grains can be observed. The ratio of large grain size to average grain size (mode grain size) taken from the grain size distribution in Figure 7-19 (c) is ≈ 3: mode grain size 70 µm and large grain size 200 µm (at 95% accumulated area fraction). The isolated nature and large size ratio (> 2, based on the criterion reported in literature, in section 2.4.3.1) is identified for the large grains to be abnormal. There are no obvious bands of large grains observed, meaning that bimodal grain structures have not developed in the rolled Nb-containing steel, as shown in Figure 7-19 (c), with a coarser grain size range 200-300 µm being observed. The mode grain size of 70 µm is larger than the segregation distance of 35 ± 10 µm, due to the fact that the thickness of the band is small (10 ± 5 µm) and the segregation band is not continuous (as discussed in section

7.3.1), so most of the grains originating from pearlitic regions can be large enough to sweep through the next solute-enriched band when it is encountered, which is equal to the distance of two segregation bands, of around 70 μm.

The formation of abnormal grains indicates that the AlN particles in the solute-depleted regions must have some pinning effect, so that local unpinning can be expected at the AlN dissolution temperature (1090 ºC), which results in some grains (which have already spanned the narrow segregation band) growing abnormally.

However, the random and isolated abnormal grains observed in the rolled Nb-containing steel do not show the same growth behaviour as those in the homogenised Al-Nb steel, as the large to mode grain size ratio is only 3, which is significantly smaller than the ratio of 7.1 for the homogenised Al-Nb steel. This is possibly due to there being very little growth (35 μm) of the normal grains which are mostly pinned by the non-dissolved AlN in the homogenised Al-Nb steel at 1170 ºC, as shown in Figure 5-8, whilst the mode grains in the rolled Nb-containing steel show significant grain growth, spanning the solute-enriched regions after being reheated at 1090 ºC (mode grain size = 70 μm, as was discussed above). In addition, the abnormal grains growth from the rolled Nb-containing steel can be expected to be prevented when an effective pinning force has been further encountered from a solute-enriched band with Nb(C,N) present. However, in homogenised Al-Nb steel, the abnormal grains can be expected to grow further in absence of any band pinning force. Therefore, it indicates that the existence of a solute-enriched band in the microalloyed steel can be used to limit the abnormal grain growth during the reheating treatment.

There are no abnormal grains observed when reheating the rolled Nb-containing steel at 1200 ºC which indicates that a uniform coarse grain structure has occurred, as shown in Figure 7-20 (a). A mode grain size of 130 µm and large grain size of 190 µm have been observed in rolled Nb-containing steel, and they are larger than that in the forged Al-Nb steel at 1200 ºC, as seen in Figure 7-6, which indicates a uniform grain structure with mode grain size of 70 µm and largest grain size of 150 µm.

The ratio of larger grain to mode grain size is decreased from 2.9 (mode grain size 70 µm and large grain size 200 µm) at 1090 ºC, to 1.5 (mode grain size 130 µm and large grain size 190 µm) at 1200 ºC. This indicates that austenite grain growth has occurred (especially for the normal grains) at a reheat temperature of 1200 ºC, even though the interdendritic Nb(C,N) dissolution temperature (of around 1250 ºC) has not been approached. It means that the segregation banded structures are possibly not very effective when they have a feature of discontinuous and their thickness is not large enough, resulting in more grains can be expected to grow largely by spanning several solute-enriched regions.

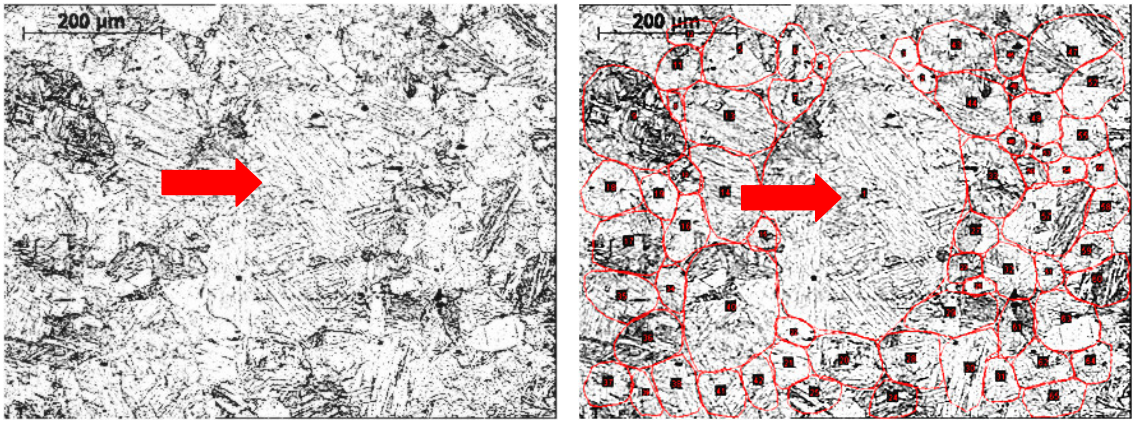

(a) (b)

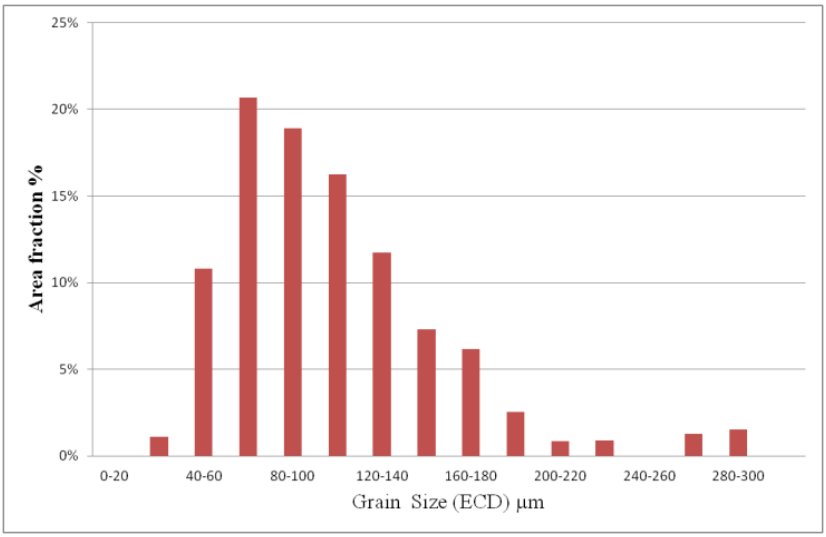

(c)

Figure 7-19 Rolled Nb-containing steel after reheating at 1090 ºC: (a, b) prior austenite microstructure with abnormal large grains as arrowed (grain boundaries highlighted in (b)); (c) grain size distribution with area fraction.

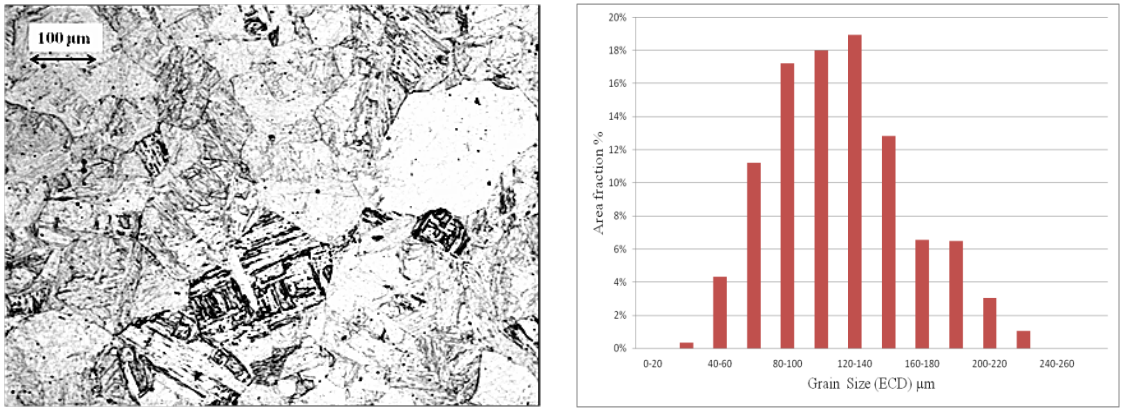

(a) (b)

Figure 7-20 (a) Prior austenite microstructure and (b) grain size distribution after reheating at 1200 ºC in rolled Nb-containing steel.

7.4.2 Precipitate characterization

Precipitates were characterised in the rolled Nb-containing steel after reheating at 1090 ºC for 1 hour, to see the particles distribution behaviour in the area where abnormal large grains were observed. Figure 7-21 (a) shows an SEM micrograph, where an isolated large grain (as indicated by red arrow) surrounded by fine grains can be observed. The particular area with boundaries of the abnormally large grain and smaller grains (indicated by green rectangular frame in Figure 7-21(a)), was further investigated under BSE analysis and a few bright particles (expected to be Nb-rich particles) were observed on the boundaries, shown in Figure 7-21(b). SEM analysis indicates spherical and irregular particles at the boundary (in Figure 7-21(c)), which are brighter than the matrix in the BSE image and hence are Nb-rich, shown in Figure 7-21(d). No AlN is observed on the abnormal grain boundaries, which is as expected due to dissolution of AlN at this temperature. A large number of Nb-rich particles appear in the smaller grain regions, which can be expected to have the pinning effect

which prevents grain growth. Therefore, an isolated abnormal grain surrounded by small grains is observed in rolled Nb-containing steel.

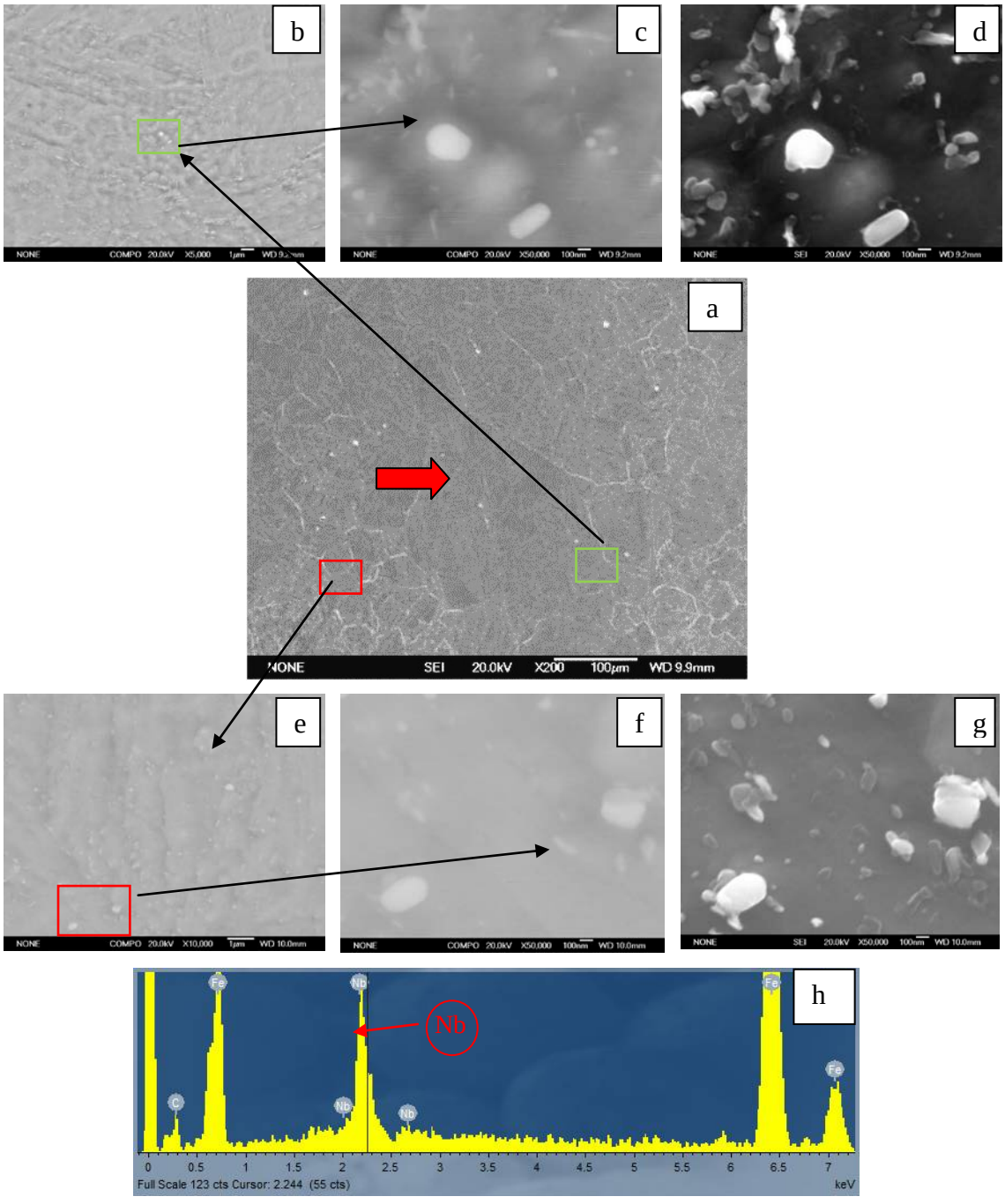

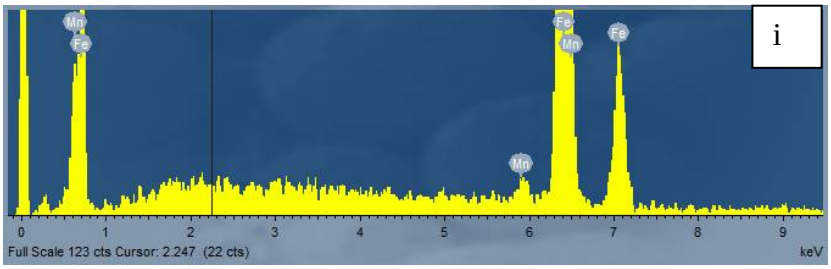

Figure 7-21 Precipitate characterisation under SEM analysis in the rolled Nb-containing steel reheated at 1090 ºC: (a) SE image indicates the microstructure consists of abnormal large grains as indicated by the red arrow, surrounded by smaller grains; (b) precipitates present in the boundary of large grains close to smaller grains; (c) Nb-rich particles in BSE images and (d) shows the morphology of Nb-rich particles in SE image; (e) Nb-rich particles located in the smaller grains region with (f) BSE image and (g) SE images; (h) EDS trace show an example of a Nb peak in the particle and (i) in the matrix.

7.4.3 Grain growth behaviour for longer reheating times

It has been found that the segregation bands were mostly ineffective for grain boundary pinning when reheating the rolled Nb-containing steel to 1090 ºC, as the large grains can be expected to span the areas of both solute-depleted regions and solute-enriched regions. Further reheating trials were investigated for rolled Nb-containing steel at 1090 ºC with longer times to see grain growth at 1, 2 and 3 hours. Figure 7-22(a) shows the grain size distributions at 1090 ºC, which indicate growth for the mode grain size (from 70 µm at one hour to 110 µm at three hours) and with more grains observed in a large size range when the reheating times are prolonged. The mode grain size of 110 µm observed for reheating to 1090 ºC for three hours, was close to the mode grain size of 130 µm when the rolled Nb-containing steel was reheated at 1200 ºC for 1 hour. This result suggests that the precipitates in the solute-enriched segregation bands are ineffective for grain boundary pinning (may be due to the dissolution of Nb(C,N)) when the rolled Nb-containing specimens are subjected to the higher temperatures or

longer holding times. It is similar to the grain growth that has been seen in the homogenised Al-Nb steel, when reheating at 1170 ºC for 1, 2 and 3 hours (Figure 5-15).

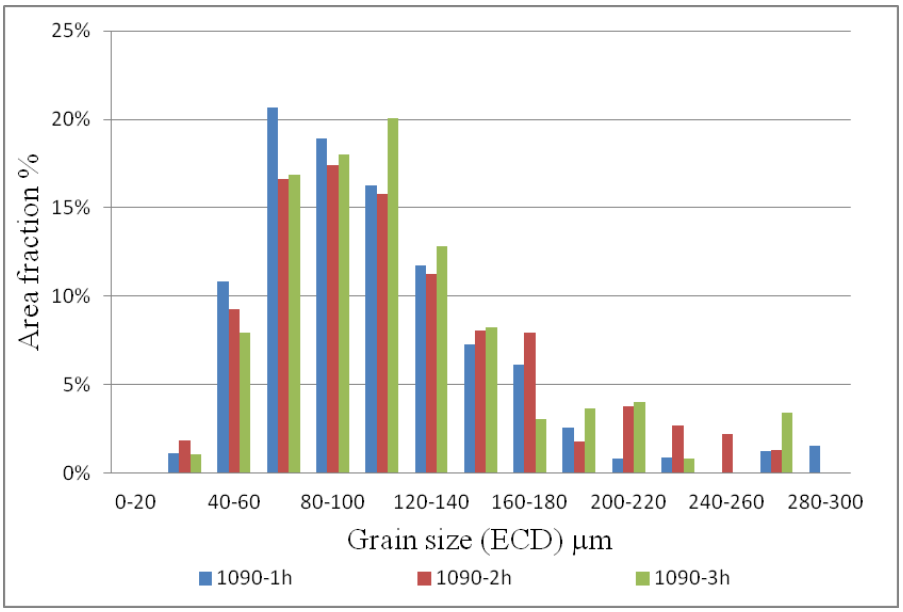

(a)

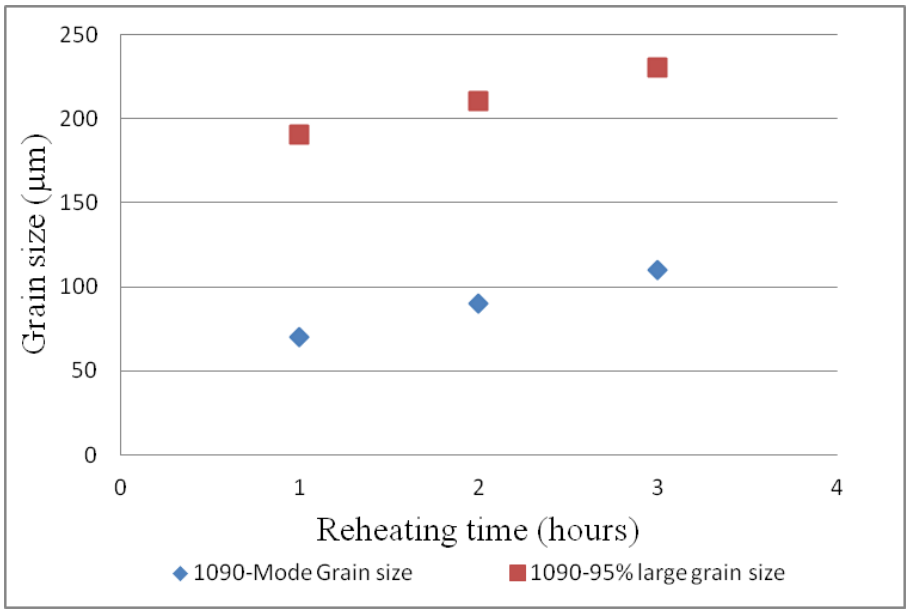

(b)

Figure 7-22 Austenite grain growth characteristics in rolled Nb-containing steel after reheating at 1090 ºC for 1, 2 and 3 hours: (a) grain size distributions and (b) grain size development with longer reheating time in mode grain size and large grain size (represented by the accumulated area fraction 95%).

7.5 Summary

On reheating in forged Al-Nb steel, no grains grow abnormally but a uniform microstructure has been observed over the temperature range from 1160 ºC to 1200 ºC, which differs from the obvious bands of small and coarse grains (bimodal grain growth) seen in as-cast Al-Nb steel, as shown in Figure 7-23. Significant grain growth is observed in both forged and as-cast Al-Nb steel when interdendritic Nb(C,N) starts to dissolve above 1250 ºC. With a longer reheating times (up to three hours) for the forged steel, a stable grain size has been observed at 1160 ºC, Figure 7-24(a), whilst obvious grain growth has been seen at reheating temperature of 1200 ºC, Figure 7-24 (b). It is similar to grain size development in the as-cast Al-Nb steel with longer holding times. These results indicate that the continuous band structure present in forged Al-Nb steel can be expected to have a boundary pinning effect to prevent the grain growth to be a small size in narrow segregation spacing.

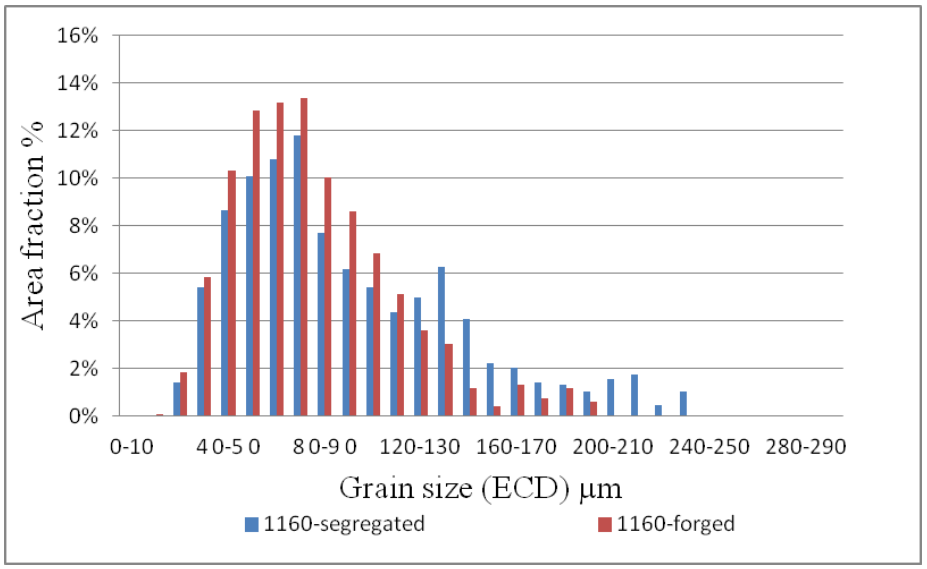

Figure 7-23 Grain size distribution for the segregated and forged conditions after reheating at 1160 ºC for 1 hour.

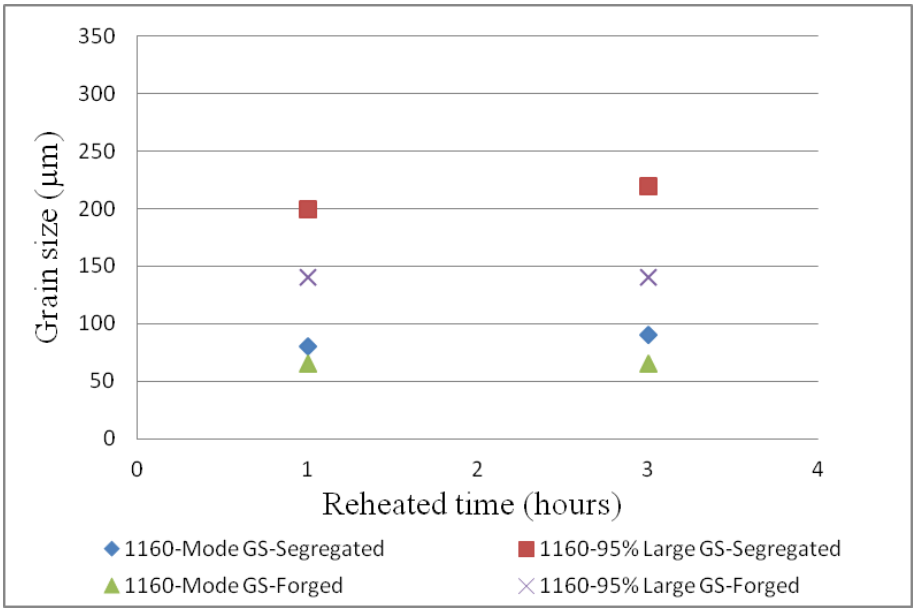

(a)

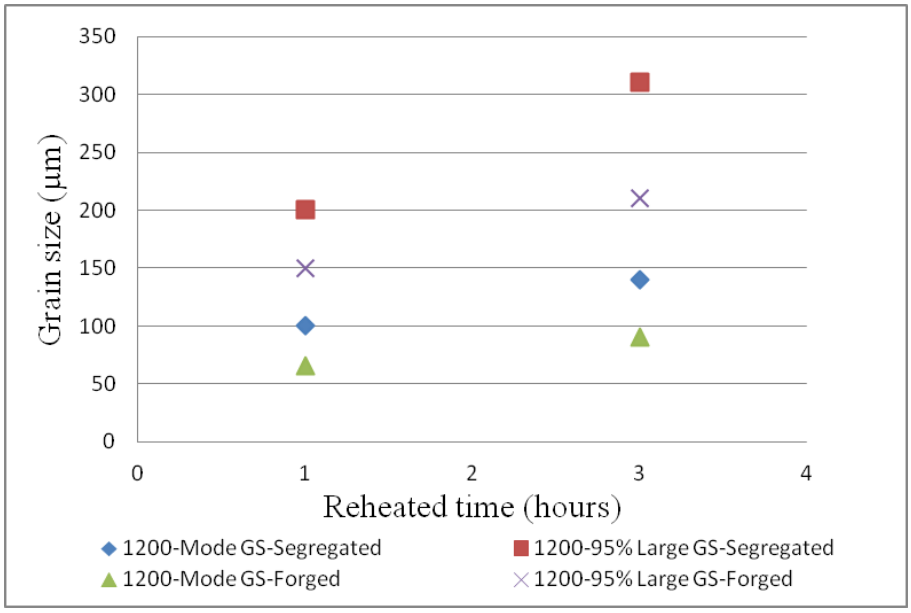

(b)

Figure 7-24 Grain growth behaviour in mode grain size and 95% accumulated large grain size for increasing reheating times at: (a) 1160 ºC; and (b) 1200 ºC for forged and as-cast condition; (GS: grain size).

However, isolated abnormal grain growth (ratio ≈ 3) was seen on reheating in rolled Nb-containing steel, at the AlN predicted dissolution temperature of 1090 ºC. It is different to the abnormal grains that observed in the homogenised Al-Nb steel (ratio ≈ 7) with a distinct skewed size distribution, as seen in Figure 7-25 (a), which indicates that small grains in size of 20-40 μm have taken a large volume fraction, approximately 70% in the grain size distribution, whilst the same volume fraction of around 70% have been found to be occupied by a wide size range (40-120 μm) from the grain size distribution of rolled Nb-containing steel, as seen in Figure 7-19.

This result indicates different mechanisms for abnormal grains growth: on reheating in homogenised Al-Nb steel, the large grains grow abnormally at the expense of the adjacent small ones when local unpinning occurs (AlN particles are partially dissolved), whilst on reheating in rolled Nb-containing steel, some of the abnormal grains may originate from those large grains which have spanned several segregation spacing when the AlN precipitates have been fully dissolved. The further growth of the abnormal grains can be expected in both the homogenised Al-Nb steel and rolled Nb-containing steel for a longer reheating time, as seen in Figure 7-25 (b).

A uniform fine grain structure can be expected for narrow segregation spacing, starting with a smaller initial size (< bands separation and band thickness), for example in forged Al-Nb steel. However, the pinning effect from the solute-enriched bands might be insufficient for those austenite grains that formed in pearlitic regions with the features of discontinuity and small thickness, resulting in some large initial grains observed (>= segregation bands distance) which can be expected to span several

segregation regions that become abnormal, for example reheating in rolled Nb-containing steel.

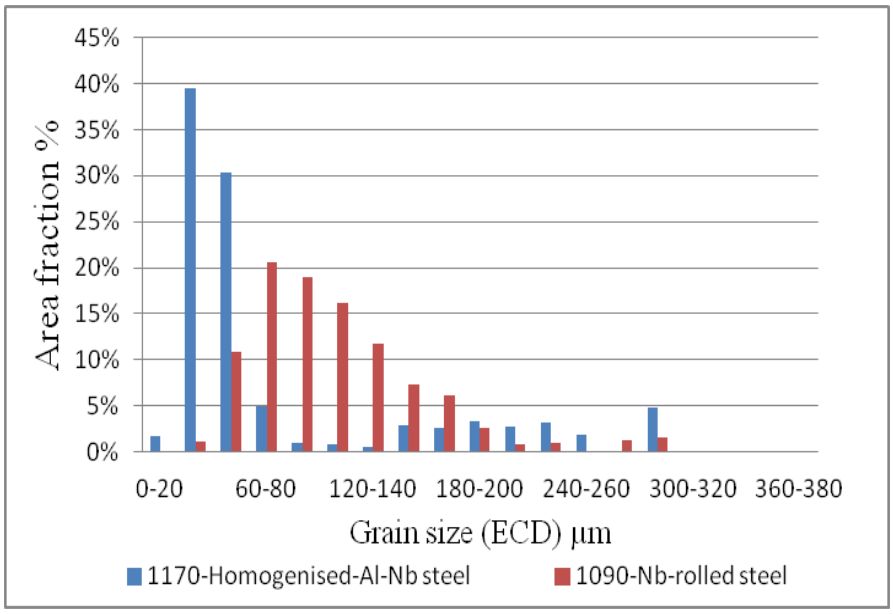

(a)

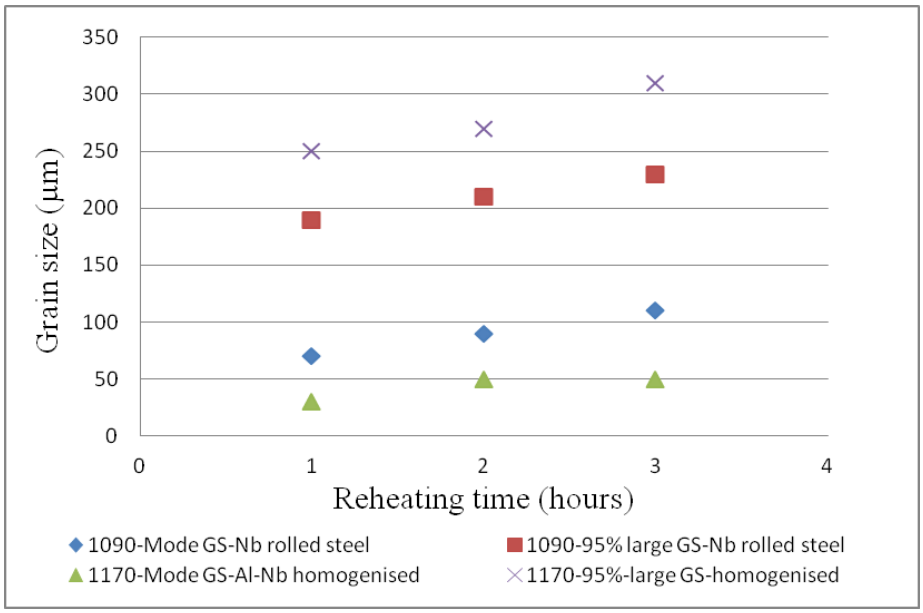

(b)

Figure 7-25 After homogenised Al-Nb steel reheated to 1170 ºC, and rolled Nb-containing steel reheated at 1090 ºC; (a) comparison of grain size distribution for abnormal grains occurred in these two steels; and (b) grain growth development with longer reheating times in mode grain size and large grain size (represented by the accumulated area fraction 95%).

The austenite grain growth behaviour in banded structure can be depicted by a simple schematic diagram, as shown in Figure 7-26 (in forged Al-Nb steel), and Figure 7-27 (in rolled Nb-containing steel). The austenite forms mostly at the positions of pearlitic region, interface of pearlite and ferrite phases, and in some boundaries of ferrite-ferrite grains. When dendritic AlN particles are dissolved at 1160 ºC in forged Al-Nb steel, the growth of austenite grains formed from boundaries of ferrites (indicated as 'B') and at the interface of pearlite and ferrite phases (indicated as 'C' in Figure 7-26), are prevented by the segregated band pinning effect and limited to a size close to the band separation distance of around 65 ± 10 μm, consistent with the mode grain size of 65 μm, as seen in Figure 7-6 (c). The austenite formed from pearlitic region can be restricted to be a small size within the banded structure (indicated as 'A', is approximately 25 μm) with a large thickness (>= 25 μm). This is due to a number of fine austenite grains that can be expected to have rapid nucleation within the solute-enriched banded structure (with the large thickness), which results in dissipation of the driving force and leaves these fine austenite grains with pinning particles (Nb-rich particles) on their boundaries. However, some austenite grains from pearlitic regions can break through the band pinning effect due to large driving force of the boundaries of austenite-ferrite during the transformation and insufficient pinning effect from some fine banded structure (for example thickness of band is small), resulting in the a few large grains (indicated as 'D' in Figure 7-26) that have spanned the banded structure.

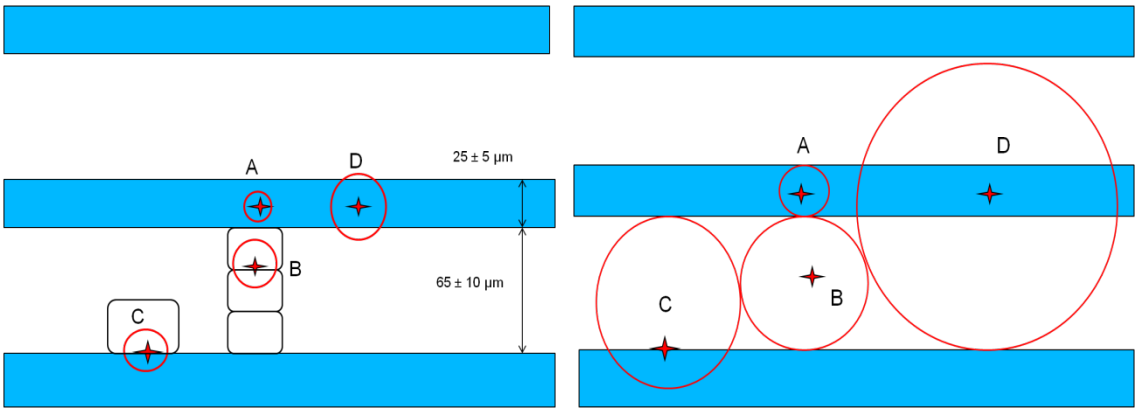

(a) (b)

Figure 7-26 Schematic of grain growth in forged Al-Nb steel indicating (a) nucleation of austenite from initial ferrite and pearlite structure; (b) austenite grain growth at 1160 ºC when AlN has been dissolved. The diagrams include the initial ferrite (represented by black rectangle), nucleated position of austenite (red star), austenite grain (red circular), and banded structure (blue bar). Band distance is around 65 ± 10 µm, and band thickness is approximately 25 ± 5 µm.

In rolled Nb-containing steel at the reheating temperature of 1090 ºC, austenite grains formed from the pearlitic region (indicated as 'H' in Figure 7-27) and interface of ferrite and pearlite phases (indicated as 'G') can mostly span the banded structure which has a small thickness of around 10 ± 5 µm. So the grain size is approximately 75 µm which is approximately double the band separation of 35 ± 10 µm, and it is consistent with a mode grain size of around 75µm observed in Figure 7-19 (c). A few grains formed from ferrite regions (solute-depleted region) are expected to be limited to be a small size (indicated as 'F' in Figure 7-27). The austenite grains formed at the positions of discontinuous banded structure (interface of ferrite and pearlite phase in banded regions, indicated as 'E' in Figure 7-27) can be expected to grow abnormally (when the pinning effect of AlN is lost) by spanning several solute-enriched and solute-depleted regions, whilst the shape of these grains is probably squeezed when it

crosses the gaps in the banded structure (with pinned Nb-rich present), which is consistent of the abnormal grains observed in Figure 7-19.

This indicates that reduced segregation spacing and greater continuity are beneficial to limit growth of the grains from solute-depleted region to be smaller, resulting in a relatively uniform size distribution taking into account the pinning effects from the solute-enriched region.

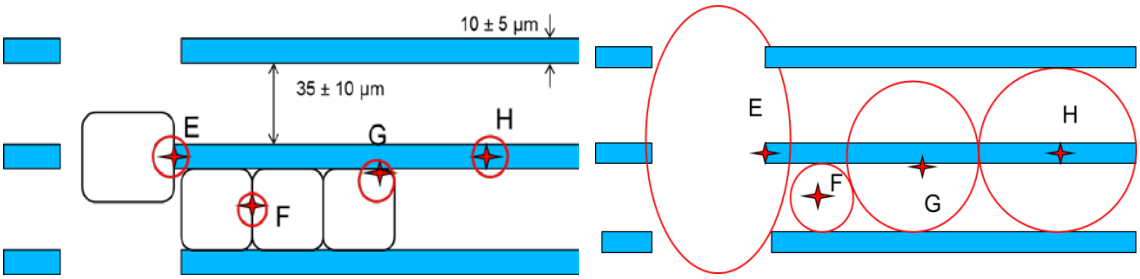

(a) (b)

Figure 7-27 Schematic of grain growth in rolled Nb-containing steel showing (a) nucleation of austenite from initial ferrite and pearlite phase; (b) austenite grain growth at temperature of 1090 ºC when AlN has been dissolved. Band separation distance is around 35 ± 10 µm; band thickness is approximately 10 ± 5 µm

In summary, the non-uniform grain growth behaviour, including bimodal and abnormal grain growth, gives an inhomogeneity in the final microstructure containing large and small grains, and is mainly due to dissolution of particles resulting in local unpinning.

The fact that a large grain size ratio of 2.6 is seen from bimodal grain growth (Table 7-1), which is close to that observed for the abnormal grains occurring in the rolled Nb-containing steel (2.8), means that a large grain size to average grain size ratio may not be the only criterion needed to define abnormal grain growth, as the morphology and grain size distribution are also important. Abnormal grain growth: a localised

phenomenon with large grains having an isolated nature, being indicated by a largely skewed grain size distribution (i.e. a wide and flat distribution discussed in section 2.4.3.1); and bimodal grain growth: microstructures with bands of large grains and bands of small grains in a double mode grain size distribution (discussed in section 2.4.3.2).

Table 7-1 Grain growth behaviour for Al-Nb steel at homogenised, segregated and forged condition and rolled Nb-containing steel correlating to: dissolution temperature, segregation spacing, band thickness, initial grain size, and grain size after heat treatment (mode grain size and large grain size at 95% accumulated area fraction).

μm	Homogenised	Segregated	Forged	rolled Nb
T_{diss} / ºC	1170	1160	1160	1090
Segregation spacing	-	150±50	65±10	35±10
Band thickness	-	75±10	25±5	10±5
Initial GS	27.5	27.5	17.5	27.5
Mode GS	35	75/135	65	70
Large GS	250	195	140	200
Ratios	7.1	2.6/1.4	2.1	2.8

Consequently, a range of grain growth behaviour, including ‘normal grain growth-abnormal (bimodal) grain growth-normal grain growth’, has been observed in the Al-Nb steel and rolled Nb-containing steel corresponding to the particles’ dissolution behaviour, as seen in Table 7-2, which agrees with the typical grain growth behaviour in HSLA steel reported in the literature [30, 31, 40, 154], as discussed in section 2.4.3. Abnormal grain growth has not occurred in the as-cast (segregated) Al-Nb steel, and no bimodal grain growth is observed in the homogenised condition. Uniform grain

growth is observed at all temperatures on reheating of the forged Al-Nb steel (Table 7-2), which is different to the other typical grain growth behaviours seen in HSLA steel, due to the reduced band segregation spacing.

Table 7-2 Grain growth behaviour at critical temperatures for Al-Nb steel, in homogenised, as-cast (segregated) and forged condition and rolled Nb-containing steel with: UGG-F: uniform grain size distribution with fine grain size; UGG-C: uniform grain size distribution with coarse grain size; AGG: abnormal grain growth; BGG: Bimodal grain growth.

T/ ºC	Homogenised	Segregated	Forged	Rolled Nb
<1090	UGG-F	UGG-F	UGG-F	UGG-F
1090	UGG-F	UGG-F	UGG-F	AGG
1160 (1170)	AGG	BGG	UGG-F	-
1200	UGG-C	BGG	UGG-F	UGG-C
1200-1300	-	BGG	UGG-C	-
1300	-	UGG-C	UGG-C	-

chapter 8 Conclusions

The grain growth behaviour during reheating between 950 ºC - 1300 ºC of as-cast Al-Nb steel (containing 0.019 wt% Nb and 0.057 wt% Al) and rolled Nb-containing steel (containing 0.028 wt% Nb and 0.031 wt% Al) has been investigated. In particular the role of microalloying element segregation during casting, and hence the spatial distribution of microalloying precipitates, on grain boundary pinning during reheating has been considered. The main conclusions from the work are:

Characterise segregation and precipitation distribution

1. The as-cast Al-Nb steel showed a secondary dendrite arm spacing (SDAS) of 150 $\pm$ 50 μm. After forging the segregation band spacing was 65 $\pm$ 10 μm. The segregation band spacing in the rolled Nb-containing steel was 35 $\pm$ 10 μm.

2. The segregation levels of Mn in the as-cast Al-Nb steel were determined by measuring the Mn content using SEM-EDS. A maximum content of around 1.7 wt% and minimum content of around 1 wt% were seen in the interdendritic-centre and dendritic-centre regions separately. The Mn segregation level was predicted using DICTRA modelling and agreed with the experimental values. DICTRA modelling was then used to predict the segregated microalloy contents.

3. For the as-cast Al-Nb steel, more Nb(C, N) particles were seen in the interdendritic region (2.64×10^4 /mm^2) than in the dendritic region (0.73×10^4 /mm^2). Al shows segregation into the dendritic regions, hence a larger number density of AlN

particles (1.89×10^4 /mm^2) was seen in this area than in the interdendritic region (1.29×10^4 /mm^2).

Grain growth during reheating treatment

1. Bimodal grain growth occurred in the as-cast Al-Nb steel when reheating above the dendritic AlN dissolution temperature (most stable dendritic particles) in the range from 1160 ºC to 1200 ºC, with the stable interdendritic pinning force from Nb(C,N) particles limiting the size of the large grains in the dendritic region.

2. AlN particles are able to restrict grain growth during reheating and can be used to reduce the temperature range over which bimodal grain growth occurs (compared to an Nb-only containing steel).

3. Bimodal severity (ratio between the coarse and fine mode grain size) is greater for a larger segregation distance, i.e. a more severe bimodal structure was seen in cast Slab-1 steel (ratio: 5.5; SDAS: 211 $\pm$ 36 μm) reported in the literature than the as-cast Al-Nb steel (ratio: 1.8; SDAS: 150 $\pm$ 50 μm). Uniform grain growth was observed in a forged Al-Nb steel with segregation spacing reduced to 65 $\pm$ 10 μm.

4. Abnormal grain growth (AGG) was seen in the homogenised Al-Nb steel and the rolled Nb-containing steel at reheating temperatures that correlate the AlN dissolution temperature. The abnormal grain growth mechanism is slightly different in the two steel: random local unpinning in the homogenised condition from AlN dissolution, and compared to precipitate dissolution in the solute-depleted bands in the rolled steel (where the bands containing the high precipitate

number density are too narrow/ discontinuous and the spacing between bands too small to effectively pin a large growing grain). The abnormal grain size to mode grain size ratio is larger in the homogenised Al-Nb steel (6-8) than in the rolled Nb-containing sample (3).

5. Abnormal grain growth in homogenised Al-Nb steel occurred at 1170 ºC close to the dissolution temperature of the AlN particles; there were no abnormal grains when the reheating temperature was below or more than 30 ºC above the particle dissolution temperature.

6. The difference between abnormal grain growth and bimodal grain growth has been identified: abnormal grain growth occurs over a narrow temperature range and has an isolated nature of individual large grains surrounded by small grains; whilst bimodal grain growth is seen over a wide temperature range and has a band structure containing coarse grains and small grains.

chapter 9 Future work

From this investigation, a banded structure with segregated Nb (which is desired with narrow segregation separation and great continuity resulting in the band pinning effect) can be expected to avoid abnormal and bimodal grain growth, while the addition of Al in Nb-containing steel is beneficial to reduce the temperature range over which the bimodal grain growth is seen (due to the extra pinning effect of AlN in the Nb-depleted region). For further research on grain growth behaviour in HSLA steel, the following suggestions can be made:

1. Further particles characterision in the Al-Nb steel. Particle dissolution behaviour leading to bimodal grain growth has been identified when reheating at temperatures above the predicted dissolution temperature for dendritic particles but below that for interdendritic particles, however, a more quantitative analysis of number density and particle size should be carried out to give better data to determine the critical pinning force required for bimodal grain growth restriction.

2. Thermo-mechanically controlled rolled (TMCR) testing on the Al-Nb steel. The Al-Nb steel, with uniform and fine grain structures, can be subjected to hot deformation (e.g. Gleeble testing) to see if the Al-rich particles have an effect on the recrystallisation process or the recrystallised grain size. Testing of the Al-Nb steel with a bimodal grain structure (after reheating at 1160 ^{o}C to dissolve AlN in the matrix) can be carried out to determine if strain induced Al-rich particles form and affect the recrystallisation kinetics.

3. Examining the role of Al and Nb content in HSLA steel. Segregation and precipitation predictions for Al-Nb steels with different Al and Nb contents can be carried out to determine the reheating temperature range for uniform structures in particular to determine if increases in Al levels can be used to minimise (or eliminate) the formation of bimodal grain structures. Different levels of Nb in HSLA steels could be investigated to determine the level of pinning for limitation of grain growth.

4. Different segregation spacing. Only three segregation spacings (as-cast, forged and rolled) have been investigated in this work. The segregation spacing can be controlled by changing the cooling rate during casting and further spacings (relative to the initial austenite grain structure) should be considered during reheating trials, particularly for different Nb content steels, to determine its role on bimodal/ abnormal grain growth.

5. Further verification of the modelling predictions. Thermo-Calc and DICTRA can be used to give modelling predictions based on the methods that have been applied in this project. The results achieved in future should be verified to see whether the modelling prediction is accurate enough to predict the critical temperatures for grain growth for the different initial conditions. Thereby it can be used in future to design reheating treatment schedules for the HSLA steels with different compositions.

List of References

[1] Bleck W, Phiu-On K. Microalloying of cold-formable multi phase steel grades. Materials Science Forum: Trans Tech Publ; 2005. p. 97-114.
[2] Cuddy L. Microstructures developed during thermomechanical treatment of HSLA steels. Metallurgical Transactions A. 1981;12:1313-1320.
[3] Davis C. The effect of microalloy precipitates on final product mechanical properties. Transactions of the Indian Institute of Metals. 2006;59:695-710.
[4] KONSTRUKCIJSKA VMH. High-strength low-alloy (HSLA) steels. Materiali in tehnologije. 2011;45:295-301.
[5] Korchynsky M. Advanced metallic structural materials and a new role for microalloyed steels. Materials Science Forum: Trans Tech Publ; 2005. p. 471-480.
[6] Little E. The physical metallurgy of microalloyed steels. Materials Science and Technology. 2000;16:941.
[7] Rashid M. High-strength, low-alloy steels. Science. 1980;208:862-869.
[8] Talbot D. The effects of plate processing parameters on the microstructure, mechanical properties and precipitation characteristics of niobium-containing high strength low alloy steels: University of Birmingham; 2002.
[9] Vervynckt S, Verbeken K, Lopez B, Jonas J. Modern HSLA steels and role of non-recrystallisation temperature. International Materials Reviews. 2012;57:187-207.
[10] Gray R, Irving W, Baker R. Steelmaking, Casting and Rolling of Pipeline Steels in B. S. C. Manufacture, Fabrication and Operation of Pipelines. 1982:3.
[11] Chakraborti N, Kumar R, Jain D. A study of the continuous casting mold using a pareto-converging genetic algorithm. Applied Mathematical Modelling. 2001;25:287-297.
[12] Reed-Hill RE, Abbaschian R. Physical metallurgy principles. 1973.
[13] Porter DA, Easterling KE, Sherif M. Phase Transformations in Metals and Alloys, (Revised Reprint): CRC press; 2009.
[14] Flemings MC. Solidification processing. Metallurgical transactions. 1974;5:2121-2134.
[15] Bower TF, Flemings MC. Formation of the chill zone in ingot solidification. AIME MET SOC TRANS. 1967;239:216-219.
[16] Davis CL, Strangwood M. Segregation behaviour in Nb microalloyed steels. Materials Science and Technology. 2009;25:1126-1133.
[17] Davis CL, Strangwood M. Preliminary study of the inhomogeneous precipitate distributions in Nb-microalloyed plate steels. J Mater Sci. 2002;37:1083-1090.
[18] Kundu A. Grain structure development during casting, reheating and deformation of Nb-microalloyed steel: University of Birmingham; 2011.
[19] Reed R, Akbay T, Shen Z, Robinson J, Root J. Determination of reaustenitisation kinetics in a Fe–0.4 C steel using using dilatometry and neutron diffraction. Materials Science and Engineering: A. 1998;256:152-165.
[20] Oliveira FLG, Andrade MS, Cota AB. Kinetics of austenite formation during continuous heating in a low carbon steel. Materials Characterization. 2007;58:256-261.
[21] Caballero F, Capdevila C, Andrés CGD. Modelling of kinetics of austenite formation in steels with different initial microstructures. ISIJ international. 2001;41:1093-1102.

[22] Chakrabarti D, Davis CL, Strangwood M. Characterisation of bimodal grain structures and their dependence on inhomogeneous precipitate distribution during casting. Materials Science Forum: Trans Tech Publ; 2005. p. 613-622.
[23] Chakrabarti D, Davis C, Strangwood M. Characterisation of bimodal grain structures in HSLA steels. Materials Characterization. 2007;58:423-438.
[24] Chakrabarti D. Development of bimodal grain structures and their effect on toughness in HSLA steel: University of Birmingham; 2007.
[25] Chakrabarti D, Davis C, Strangwood M. Development of bimodal grain structures in Nb-containing high-strength low-alloy steels during slab reheating. Metallurgical and Materials Transactions A: Physical Metallurgy and Materials Science. 2008;39:1963-1977.
[26] Chakrabarti D, Strangwood M, Davis C. Effect of bimodal grain size distribution on scatter in toughness. Metallurgical and Materials Transactions A: Physical Metallurgy and Materials Science. 2009;40:780-795.
[27] Zhou TH, Zurob HS. Abnormal and post-abnormal austenite grain growth kinetics in Nb-Ti microalloyed steels. Canadian Metallurgical Quarterly. 2011;50:389-395.
[28] Zhou TH, Zurob HS. Abnormal and post-abnormal austenite grain growth kinetics in Nb–Ti microalloyed steels. Canadian Metallurgical Quarterly. 2011;50:389-395.
[29] Rios PR. Abnormal grain growth development from uniform grain size distributions. Acta Materialia. 1997;45:1785-1789.
[30] Zhang X, Matsuura K, Ohno M. Abnormal Grain Growth in Austenite Structure Reversely Transformed from Ferrite/Pearlite-Banded Structure. Metallurgical and Materials Transactions A. 2014;45:4623-4634.
[31] Flores O, Martinez L. Abnormal grain growth of austenite in a V–Nb microalloyed steel. J Mater Sci. 1997;32:5985-5991.
[32] Chun YB, Hwang SK, Kwun SI, Kim MH. ABNORMAL GRAIN GROWTH OF Zr-1wt .% Nb ALLOY AND THE EFFECT OF Mo ADDITION. Acta Metallurgica. 1999;40:1165-1170.
[33] Yu Q, Sun Y. Abnormal growth of austenite grain of low-carbon steel. Materials Science and Engineering: A. 2006;420:34-38.
[34] Kundu A, Davis C, Strangwood M. Grain size distributions after single hit deformation of a segregated, commercial Nb-containing steel: prediction and experiment. Metallurgical and Materials Transactions A. 2011;42:2794-2806.
[35] Tanaka T. Controlled rolling of steel plate and strip. International metals reviews. 1981;26:185-212.
[36] Bhattacharjee D, Davis C, Knott J. Predictability of Charpy impact toughness in thermomechanically control rolled (TMCR) microalloyed steels. Ironmaking & steelmaking. 2003;30:249-255.
[37] Zhang D. Characterisation and modelling of segregation in continuously cast steel slab: University of Birmingham; 2015.
[38] Zheng S, Davis C, Strangwood M. Elemental segregation and subsequent precipitation during solidification of continuous cast Nb–V–Ti high-strength low-alloy steels. Materials Characterization. 2014;95:94-104.
[39] Roy S, Patra S, Neogy S, Laik A, Choudhary S, Chakrabarti D. Prediction of inhomogeneous distribution of microalloy precipitates in continuous-cast high-strength, low-alloy steel slab. Metallurgical and Materials Transactions A. 2012;43:1845-1860.
[40] Roy S. Effect of microalloy precipitates on austenite grain growth during reheating treatment of HSLA steel: Indian Institute of Technology; 2013.
[41] Trivedi R, Kurz W. Dendritic growth. International Materials Reviews. 1994;39:49-74.

[42] Tiaden J. Phase field simulations of the peritectic solidification of Fe–C. Journal of crystal Growth. 1999;198:1275-1280.
[43] Ohno M, Matsuura K. Diffusion-controlled peritectic reaction process in carbon steel analyzed by quantitative phase-field simulation. Acta Materialia. 2010;58:6134-6141.
[44] Fredriksson H, Nylen T. Mechanism of peritectic reactions and transformations. Metal Science. 1982;16:283-294.
[45] Fredriksson H, Stjerndahl J. Solidification of iron-base alloys. Metal Science. 1982;16:575-586.
[46] Kagawa A, Okamoto T. Influence of alloying elements on temperature and composition for peritectic reaction in plain carbon steels. Materials science and technology. 1986;2:997-1008.
[47] Fredriksson H. The mechanism of the peritectic reaction in iron-base alloys. Metal Science. 1976;10:77-86.
[48] Cahn JW. The kinetics of grain boundary nucleated reactions. Acta Metallurgica. 1956;4:449-459.
[49] Bhadeshia H, Honeycombe R. Steels: microstructure and properties: microstructure and properties: Butterworth-Heinemann; 2011.
[50] Zhang M-X, Kelly P. The morphology and formation mechanism of pearlite in steels. Materials Characterization. 2009;60:545-554.
[51] Mehl RF, Hagel WC. The austenite: pearlite reaction. Progress in Metal Physics. 1956;6:74-134.
[52] Benedicks C. A new form of pearlite. Metallurgie. 1909;6:567-568.
[53] Suzuki A, Suzuki T, Nagaoka Y, Iwata Y. On secondary dendrite arm spacing in commercial steels having different carbon contents. Nippon Kinzoku Gakkai-Si. 1968;32:1301-1305.
[54] Cramb A. Secondary Dendrite Arm Spacings in Continuous Cast, Thin Steel Sections. Casting of Near Net Shape Products. 1988:673-682.
[55] El-Bealy M, Thomas B. Prediction of dendrite arm spacing for low alloy steel casting processes. Metallurgical and materials transactions B. 1996;27:689-693.
[56] Essadiqi E, Collins L, Shehata M, Chiang L. 2nd Canada–Japan Symp. on Modern Steelmaking and Casting Techniques. Canadian Institute of Mining, Metallurgy, and Petroleum, Montreal; 1994.
[57] Irving WR. Continuous casting of steel. The Institute of Materials(UK), 1993. 1993:216.
[58] Krauss G. Solidification, segregation, and banding in carbon and alloy steels. Metallurgical and Materials Transactions B. 2003;34:781-792.
[59] Won Y-M, Thomas BG. Simple model of microsegregation during solidification of steels. Metallurgical and Materials Transactions A. 2001;32:1755-1767.
[60] Pickering EJ. Macrosegregation in steel ingots: the applicability of modelling and characterisation techniques. ISIJ international. 2013;53:935-949.
[61] Flemings M. Principles of control of soundness and homogeneity of large ingots. JOURNAL OF METALS: MINERALS METALS MATERIALS SOC 420 COMMONWEALTH DR, WARRENDALE, PA 15086; 1979. p. F47-F47.
[62] Takahashi T, Kudo M, Ichikawa K. Solidification of Iron and Steel: A Data Book on the Solidification Phenomena of Iron and Steel. ISIJ, Tokyo. 1977.
[63] Priestner R, Li P, Zhou C, Ibraheem A. Microalloy precipitation in HSLA steel austenite. Thirty First Annual Technical Meeting of the International Metallographic Society1998. p. 447-454.

[64] Ghosh A. Segregation in cast products. Sadhana. 2001;26:5-24.
[65] Fisher R, Speich G, Cuddy L, Hu H. Phase Transformations During Steel Production. Physical Chemistry in Metallurgy U S Steel Research Lab, Monroeville, Pa 1976, 463-488. 1976.
[66] Choudhary S, Ghosh A. Mathematical model for prediction of composition of inclusions formed during solidification of liquid steel. ISIJ international. 2009;49:1819-1827.
[67] Battle TP, Pehlke RD. Equilibrium partition coefficients in iron-based alloys. Metallurgical and Materials Transactions B. 1989;20:149-160.
[68] Luo S, Zhu M, Louhenkilpi S. Numerical simulation of solidification structure of high carbon steel in continuous casting using cellular automaton method. ISIJ international. 2012;52:823-830.
[69] Shewmon P. Diffusion in solids. The Minerals, Metals & Materials Society, Diffusion in Solids Second Edition(Retroactive Coverage)(United States), 1989. 1989:246.
[70] Yamada W, Matsumiya T, Ito A. Development of simulation model for composition change of nonmetallic inclusions during solidification of steels. IISC The Sixth International Iron and Steel Congress1990. p. 618-625.
[71] Ueshima Y, Mizoguchi S, Matsumiya T, Kajioka H. Analysis of solute distribution in dendrites of carbon steel with δ/γ transformation during solidification. Metallurgical Transactions B. 1986;17:845-859.
[72] Flemings MC, Nereo G. MACROSEGREGATION. PT. 1. AIME Met Soc Trans. 1967;239:1449-1461.
[73] Pottore N, Garcia C, DeArdo A. Interrupted and isothermal solidification studies of low and medium carbon steels. Metallurgical Transactions A. 1991;22:1871-1880.
[74] Black J. Modeling the effects of chemical segregation on phase transformations in medium carbon bar steels1998.
[75] Flemings M, Poirier D, Barone R, Brody H. Microsegregation in iron-base alloys. J Iron Steel Inst. 1970;208:371-381.
[76] Sung P, Poirier DR. Liquid-solid partition ratios in nickel-base alloys. Metallurgical and Materials Transactions A. 1999;30:2173-2181.
[77] Sawada Y, Foley R, Thompson S, Krauss G. Microstructure-Property Relationships in Plain-Carbon, and Vanadium and V+ Nb Microalloyed Medium Carbon Steels. 35 th Mechanical Working and Steel Processing Conference1993. p. 263-286.
[78] Zhang X. Research on abnormal grain growth in reversely transformed austenite structure [an abstract of dissertation and a summary of dissertation review]. 2014.
[79] Zhang D, Strangwood M. Characterisation and modelling of microsegregation in low carbon continuously cast steel slab. Proceedings of the 2013 International Symposium on Liquid Metal Processing & Casting2013. p. 321-327.
[80] Clyne T, Kurz W. Solute redistribution during solidification with rapid solid state diffusion. Metallurgical Transactions A. 1981;12:965-971.
[81] Ohnaka I. Mathematical analysis of solute redistribution during solidification with diffusion in solid phase. Transactions of the Iron and Steel Institute of Japan. 1986;26:1045-1051.
[82] Kobayashi S. Solute redistribution during solidification with diffusion in solid phase: a theoretical analysis. Journal of crystal growth. 1988;88:87-96.
[83] Voller V, Beckermann C. A unified model of microsegregation and coarsening. Metallurgical and Materials Transactions A. 1999;30:2183-2189.

[84] Miettinen J. Mathematical simulation of interdendritic solidification of low-alloyed and stainless steels. Metallurgical Transactions A. 1992;23:1155-1170.
[85] Miettinen J. Calculation of solidification-related thermophysical properties for steels. Metallurgical and Materials Transactions B. 1997;28:281-297.
[86] Sarreal J, Abbaschian G. The effect of solidification rate on microsegregation. Metallurgical Transactions A. 1986;17:2063-2073.
[87] Ganesan S, Poirier D. Solute redistribution in dendritic solidification with diffusion in the solid. Journal of crystal growth. 1989;97:851-859.
[88] Brody HD. Solute redistribution in dendritic solidification: Massachusetts Institute of Technology; 1965.
[89] MATSUMIYA T, KAJIOKA H, MIZOGUCHI S, UESHIMA Y, ESAKA H. Mathematical analysis of segregations in continuously-cast slabs. Transactions of the Iron and Steel Institute of Japan. 1984;24:873-882.
[90] Clyne T. Numerical modelling of directional solidification of metallic alloys. Metal Science. 1982;16:441-450.
[91] Yamashita T, Okuda K, Obara T. Application of thermo-calc to the developments of high-performance steels. Journal of phase equilibria. 1999;20:231-237.
[92] Lippard H, Campbell C, Dravid V, Olson G, Björklind T, Borggren U, et al. Microsegregation behavior during solidification and homogenization of AerMet100 steel. Metallurgical and Materials Transactions B. 1998;29:205-210.
[93] Kuehmann C, Olson G. Computational materials design and engineering. Materials Science and Technology. 2009;25:472-478.
[94] Hakan Atapek Ş, Erişir E, Gümüş S. Modeling and thermal analysis of solidification in a low alloy steel. Journal of thermal analysis and calorimetry. 2013;114:179-183.
[95] Ågren J. Computer simulations of diffusional reactions in complex steels. ISIJ International. 1992;32:291-296.
[96] P. Shi BS. Thermo-Calc software user's guide. 2008.
[97] Jansson B, Jönsson B, Sundman B, Ågren J. The thermo calc project. Thermochimica acta. 1993;214:93-96.
[98] Andersson J-O, Helander T, Höglund L, Shi P, Sundman B. Thermo-Calc & DICTRA, computational tools for materials science. Calphad. 2002;26:273-312.
[99] Shi P-F, Engström A, Höglund L, Qing C, Sundman B, Ågren J, et al. Computational thermodynamics and kinetics in materials modelling and simulations. Journal of Iron and Steel Research, International. 2007;14:210-215.
[100] Borgenstam A, Höglund L, Ågren J, Engström A. DICTRA, a tool for simulation of diffusional transformations in alloys. Journal of phase equilibria. 2000;21:269-280.
[101] Tither G. The development and applications of niobium-containing HSLA steels. HSLA Steels: Processing, Properties and Applications. 1990:61-80.
[102] Willms R. High strength steel for steel constructions. Nordic Steel. 2009.
[103] Chakrabarti D, Davis C, Strangwood M. The effect of precipitate distributions on HSLA grain structures. International Symposium of Research Students on Material Science and Engineering December2004. p. 20-22.
[104] DeArdo A. Niobium in modern steels. International Materials Reviews. 2003;48:371-402.
[105] Rios P. Expression for solubility product of niobium carbonitride in austenite. Materials science and technology. 1988;4:324-327.

[106] Palmiere E, Garcia C, De Ardo A. Compositional and microstructural changes which attend reheating and grain coarsening in steels containing niobium. Metallurgical and Materials Transactions A. 1994;25:277-286.
[107] Lakshmanan V, Kirkaldy J. Solubility product for niobium carbide in austenite. Metallurgical Transactions A. 1984;15:541-544.
[108] Inoue K, Ohnuma I, Ohtani H, Ishida K, Nishizawa T. Solubility Product of TiN in Austenite. ISIJ international. 1998;38:991-997.
[109] Taylor K. Solubility products for titanium-, vanadium-, and niobium-carbide in ferrite. Scripta metallurgica et materialia. 1995;32:7-12.
[110] Speer J, Michael J, Hansen S. Carbonitride precipitation in niobium/vanadium microalloyed steels. Metallurgical Transactions A. 1987;18:211-222.
[111] Wilson F, Gladman T. Aluminium nitride in steel. International Materials Reviews. 1988;33:221-286.
[112] Houghton D. Equilibrium solubility and composition of mixed carbonitrides in microalloyed austenite. Acta metallurgica et materialia. 1993;41:2993-3006.
[113] Charleux M, Poole W, Militzer M, Deschamps A. Precipitation behavior and its effect on strengthening of an HSLA-Nb/Ti steel. Metallurgical and Materials Transactions A. 2001;32:1635-1647.
[114] Yuan S, Liang G. Dissolving behaviour of second phase particles in Nb–Ti microalloyed steel. Materials Letters. 2009;63:2324-2326.
[115] Du J, Strangwood M, Davis C. Effect of TiN particles and grain size on the charpy impact transition temperature in steels. Journal of Materials Science & Technology. 2012;28:878-888.
[116] Du J. Examination of the effect of tin particles and grain size on the charpy impact transition temperature in steels: University of Birmingham; 2012.
[117] Zhang L, Davis C, Strangwood M. Effect of TiN particles and microstructure on fracture toughness in simulated heat-affected zones of a structural steel. Metallurgical and Materials Transactions A. 1999;30:2089-2096.
[118] Zhang L, Davis C, Strangwood M. Dependency of fracture toughness on the inhomogeneity of coarse TiN particle distribution in a low alloy steel. Metallurgical and Materials Transactions A. 2001;32:1147-1155.
[119] El-Faramawy HS, Ghali SN, Eissa MM. Effect of titanium addition on behavior of medium carbon steel. Journal of Minerals and Materials Characterization and Engineering. 2012;11:1108.
[120] Mao X, Huo X, Sun X, Chai Y. Strengthening mechanisms of a new 700MPa hot rolled Ti-microalloyed steel produced by compact strip production. Journal of Materials Processing Technology. 2010;210:1660-1666.
[121] Cuddy L. The effect of microalloy concentration on the recrystallization of austenite during hot deformation. The Metallurgical Society/AIME. 1982:129-140.
[122] Cuddy L. Thermomechanical Processing of Microalloyed Austenite, ed. by AJ DeArdo. GH Ratz and PJ Wray, TMS-AIME, Warrendale, PA. 1982;129.
[123] Baker T. Processes, microstructure and properties of vanadium microalloyed steels. Materials Science and Technology. 2009;25:1083-1107.
[124] Li Y, Wilson J, Craven A, Mitchell P, Crowther D, Baker T. Dispersion strengthening in vanadium microalloyed steels processed by simulated thin slab casting and direct charging Part 1–Processing parameters, mechanical properties and microstructure. Materials science and technology. 2007;23:509-518.

[125] Jeanmaire G, Dehmas M, Redjaïmia A, Puech S, Fribourg G. Precipitation of aluminum nitride in a high strength maraging steel with low nitrogen content. Materials Characterization. 2014;98:193-201.
[126] Radis R, Kozeschnik E. Kinetics of AlN precipitation in microalloyed steel. Modelling and Simulation in Materials Science and Engineering. 2010;18:055003.
[127] Craven A, He K, Garvie L, Baker T. Complex heterogeneous precipitation in titanium–niobium microalloyed Al-killed HSLA steels—I.(Ti, Nb)(C, N) particles. Acta Materialia. 2000;48:3857-3868.
[128] Craven aJ, He K, Garvie LaJ, Baker TN. Complex heterogeneous precipitation in titanium-niobium microalloyed Al-killed HSLA steels - II. Non-titanium based particles. Acta Materialia. 2000;48:3869-3878.
[129] Jun HJ, Kang KB, Park CG. Effects of cooling rate and isothermal holding on the precipitation behavior during continuous casting of Nb-Ti bearing HSLA steels. Scripta Materialia. 2003;49:1081-1086.
[130] Hong SG, Jun HJ, Kang KB, Park CG. Evolution of precipitates in the Nb-Ti-V microalloyed HSLA steels during reheating. Scripta Materialia. 2003;48:1201-1206.
[131] Leap M, Brown E. Crystallography of duplex AlN–Nb (C, N) precipitates in 0.2% C steel. Scripta materialia. 2002;47:793-797.
[132] Jung JG, Park JS, Kim J, Lee YK. Carbide precipitation kinetics in austenite of a Nb-Ti-V microalloyed steel. Materials Science and Engineering A. 2011;528:5529-5535.
[133] Kundu A, Davis C, Strangwood M. Grain size distributions after single hit deformation of a segregated, commercial Nb-containing steel: Prediction and experiment. Metallurgical and Materials Transactions A: Physical Metallurgy and Materials Science. 2011;42:2794-2806.
[134] Gladman T. The physical metallurgy of microalloyed steels: Maney Pub; 1997.
[135] Lifshitz IM, Slyozov VV. The kinetics of precipitation from supersaturated solid solutions. Journal of physics and chemistry of solids. 1961;19:35-50.
[136] Manohar P, Dunne D, Chandra T, Killmore C. Grain growth predictions in microalloyed steels. ISIJ international. 1996;36:194-200.
[137] Saito Y, Enomoto M. Monte Carlo Simulation of Grain Growth. ISIJ international. 1992;32:267-274.
[138] Akamatsu S, Senuma T, Hasebe M. Generalized Nb (C, N) Precipitation Model Applicable to Extra Low Carbon Steel. ISIJ International. 1992;32:275-282.
[139] Priadi D, Napitupulu R, Siradj E. Austenite grain growth calculation of 0.028% Nb Steel. Journal of Mining and Metallurgy B: Metallurgy. 2011;47:199-209.
[140] Akbay T, Reed R, Atkinson C. Modelling reaustenitisation from ferrite/cementite mixtures in Fe□ C steels. Acta metallurgica et materialia. 1994;42:1469-1480.
[141] Yue C, Zhang L, Liao S, Gao H. Kinetic analysis of the austenite grain growth in GCr15 steel. Journal of materials engineering and performance. 2010;19:112-115.
[142] Wu S, Davis C. Effect of duplex ferrite grain size distribution on local fracture stresses of Nb-microalloyed steels. Materials Science and Engineering: A. 2004;387:456-460.
[143] Dong D, Chen F, Cui Z. Modeling of Austenite Grain Growth During Austenitization in a Low Alloy Steel. Journal of Materials Engineering and Performance. 2016;25:152-164.
[144] Gladman T. On the theory of the effect of precipitate particles on grain growth in metals. Proceedings of the Royal Society of London A: Mathematical, Physical and Engineering Sciences: The Royal Society; 1966. p. 298-309.
[145] Zener C. Private communication to CS Smith. Trans AIME. 1949;175:15.

[146] Manohar P, Ferry M, Chandra T. Five Decades of the Zener Equation. ISIJ international. 1998;38:913-924.
[147] Gladman T, Dulieu D. Grain-size control in steels. Metal Science. 1974;8:167-176.
[148] Gladman T, Pickering F. Grain-coarsening of austenite. Iron Steel Inst J. 1967;205:653-664.
[149] Enloe CM, Findley KO, Speer JG. Austenite grain growth and precipitate evolution in a carburizing steel with combined niobium and molybdenum additions. Metallurgical and Materials Transactions A. 2015;46:5308-5328.
[150] Hannerz N, KAZINCZY F. Kinetics of Austenite Grain Growth in Steel. J IRON STEEL INST. 1970;208:475-481.
[151] Nes E, Ryum N, Hunderi O. On the Zener drag. Acta Metallurgica. 1985;33:11-22.
[152] Hundert O, Nes E, Ryum N. On the zener drag—Addendum. Acta Metallurgica. 1989;37:129-133.
[153] Hillert M. Inhibition of grain growth by second-phase particles. Acta Metallurgica. 1988;36:3177-3181.
[154] Rudnizki J, Zeislmair B, Prahl U, Bleck W. Prediction of abnormal grain growth during high temperature treatment. Computational Materials Science. 2010;49:209-216.
[155] Tao S-F, Wang F-M, Sun G-L, Yang Z-B, Li C-R. DICTRA Simulation of Holding Time Dependence of NbC Size and Experimental Study of Effect of NbC on Austenite Grain Growth. Metallurgical and Materials Transactions A. 2015;46:3670-3678.
[156] Sha Q, Sun Z. Grain growth behavior of coarse-grained austenite in a Nb-V-Ti microalloyed steel. Materials Science and Engineering A. 2009;523:77-84.
[157] Andersen I, Grong Ø, Ryum N. Analytical modelling of grain growth in metals and alloys in the presence of growing and dissolving precipitates—II. Abnormal grain growth. Acta metallurgica et materialia. 1995;43:2689-2700.
[158] Cuddy L, Raley J. Austenite grain coarsening in microalloyed steels. Metallurgical Transactions A. 1983;14:1989-1995.
[159] Illescas S, Fernández J, Guilemany J. Kinetic analysis of the austenitic grain growth in HSLA steel with a low carbon content. Materials Letters. 2008;62:3478-3480.
[160] Fernández J, Illescas S, Guilemany J. Effect of microalloying elements on the austenitic grain growth in a low carbon HSLA steel. Materials Letters. 2007;61:2389-2392.
[161] Manohar Pa, Dunne DP, Chandra T, Killmore CR. Grain Growth Predictions in Microalloyed Steels. ISIJ International. 1996;36:194-200.
[162] Hillert M. On the theory of normal and abnormal grain growth. Acta Metallurgica. 1965;13:227-238.
[163] Martín DS, Caballero FG, Capdevila C, García de Andrés C. Austenite Grain Coarsening Under the Influence of Niobium Carbonitrides. Materials Transactions. 2004;45:2797-2804.
[164] Rollett A, Srolovitz D, Anderson M. Simulation and theory of abnormal grain growth - anisotropic grain boundary energies and mobilities. Acta metallurgica. 1989;37:1227-1240.
[165] Chun Y, Hwang S, Kwun S, Kim M. Abnormal grain growth of Zr-1wt.% Nb alloy and the effect of Mo addition. Scripta materialia. 1999;40:1165-1170.

[166] Kundu A, Davis C, Strangwood M. Modeling of grain size distributions during single hit deformation of a Nb-containing steel. Metallurgical and Materials Transactions A. 2010;41:994-1002.